The Dynamics of Nitinol Langevin Ultrasonic Transducers

Yuchen Liu

Submitted in fulfilment of the requirements for the
Degree of Doctor of Philosophy

James Watt School of Engineering
College of Science and Engineering
University of Glasgow

April 2025

In loving memory of my grandparents,

Huaichun Qin and Shuli Liu.

Abstract

Langevin ultrasonic transducers, especially sandwiched-type piezoelectric devices, are essential in industry and medicine for applications like ultrasonic welding and surgery due to their high-power capability and design flexibility. This research focuses on adaptive Langevin transducers that enable multiple operating frequencies and tuneable resonances, responding to various operational environments. By integrating shape memory alloys, particularly nickel-titanium, Nitinol, these transducers can achieve continuous resonance tuning with temperature changes, distinguishing them from traditional multi-frequency designs.

The first section details the design, manufacturing, and characterisation of conventional Langevin transducers, introducing the incorporation of Nitinol into their structure. Mathematical models were built using one-dimensional (1D) and three-dimensional (3D) constitutive equations in piezoelectricity to simulate Nitinol transducer behaviours. While the 1D model offers advantages in computational efficiency and does not require complete material properties in 3D space, transducer dimensions and modes limit its accuracy. Following the simulations, this chapter outlines the considerations for integrating Nitinol into Langevin configurations while building on established methodologies for conventional transducers.

A core focus of this thesis is the practical fabrication of Nitinol Langevin transducers and their tuneable dynamics. Prototypes were developed incorporating various transducer configurations. Characterisations validated the tuneable resonances derived from Nitinol's phase transformation, revealing two dynamics: active modal coupling and stable resonance. Notably, resonance stability under self-heating conditions was linked to the temperature-dependent properties of Nitinol's austenitic phase. These dynamics are influenced by the device geometry, martensitic transformation of Nitinol, self-heating within the piezoelectric elements and their temperature-dependent material properties.

In the final section, a case study on acoustic levitation using the Nitinol Langevin transducer is presented, aligned with the cascaded Nitinol configuration detailed in earlier in the thesis. The hypothesis is that by implementing a stable resonance condition under self-heating, a stable acoustic field can be generated. The results demonstrated that the stability in resonant frequency influences position, evaporation rate, and levitation time for water, acetone and isopropyl alcohol droplets, compared to a Langevin transducer in similar dimensions and made from conventional metals.

Contents

List of Tables

List of Figures

Acknowledgements

First, I would like to express my deepest gratitude to my principal supervisor, Dr Andrew Feeney, for his support, guidance, and patience throughout my PhD journey. I owe him a lot of 'cheers' for guiding me in my research. He celebrated my successes and offered support during my disappointments. I sincerely appreciate his encouragement to present my work at international conferences. Without his mentoring, it is impossible for me to complete this project. Additionally, I extend my gratitude to my secondary supervisor Prof Margaret Lucas. She was always supportive of my research by generously sharing her knowledge and experience.

I want to acknowledge the Engineering and Physical Sciences Research Council (EPSRC) for funding this project.

A special acknowledgement goes to Dr Lu Trong Khiem Nguyen, one of my closest friends and my 'Sifu' in finite element method and solid mechanics. He has consistently helped me whenever I asked him, even though explaining how an air-filled balloon pops or the recipe for a weird vegetable. His professionalism and curiosity about my work have always sparked me with practical yet unconventional (crazy) ideas. I wish him to remain 'out-of-range' throughout his career.

I thank my friends and lab mates in the Centre for Medical and Industrial Ultrasonics (C-MIU) group. We have shared many wonderful memories together. Also, I want to thank my colleagues at Nami Surgical Ltd. The knowledge I have gained from your expertise is truly valuable to me.

Finally, I want to thank my family for waiting over 29.3 years for me to grow up and finish my studies as a student. Your understanding and patience have provided me with confidence and peace in mind throughout my life. Especially, I would like to take a privileged moment to express my gratitude to Fan Yang, my beloved wife, whose support and encouragement are moving me forward. Our invaluable memories fill me with happiness and hope. This thesis would never have come to fruition without her love and sacrifice.

Declaration

I hereby declare that the research presented in this thesis is the result of original work undertaken by the author, under the supervision of Dr Andrew Feeney and Prof Margaret Lucas, within the James Watt School of Engineering at the University of Glasgow, United Kingdom, during the period from October 2021 to April 2025. This thesis is submitted in fulfilment of the requirements for the award of the degree of doctor of philosophy (PhD) and has not been submitted, in whole or in part, for any other academic qualification or degree at this or any other institution.

Chapter 1

Introduction

Ultrasound refers to acoustic waves that vibrate at frequencies greater than 20 kHz [1]. A simpler, more commonly used definition describes it as the high-frequency sound that is inaudible to humans [2, 3]. While this is adequate for general introductions, it lacks precision for ultrasonic engineering. For example, although the typical range of human hearing is reported to be between 20 Hz and 20 kHz [4], the upper limit can vary significantly among individuals. The author has observed this variability during outreach activities, where some younger participants demonstrated a higher upper hearing limit, though all remain below 20 kHz at low acoustic intensities. This discrepancy is influenced by factors like age, health, and acoustic intensity, as noted by researchers [5, 6]. Consequently, this leads to an ambiguous definition with uncertain frequency ranges that depend on individuals, complicating ultrasonic device design. Another example is between power ultrasonics, which deliver high acoustic power and generally operate at tens of kilohertz (about 20–100 kHz), and ultrasound imaging, which uses megahertz frequencies (about 1–20 MHz). This difference necessitates diverse techniques for designing and characterising devices. Therefore, a more precise definition of 'ultrasound' and 'ultrasonic' is essential, particularly for ultrasonic engineers. Recent research has proposed alternative definitions of ultrasound based on specific applications [7]. For the purposes of this thesis, 'ultrasound' refers mainly to power ultrasonics, specifically within the 20 kHz to 100 kHz window [8–10].

Power ultrasonics represents a specialised branch of high-power ultrasonic technologies utilising devices to generate ultrasound in industrial and medical applications, encompassing surgical devices, welding, and levitation [11]. These applications generally depend on generating high vibration amplitudes from device structures operating in various vibration modes. Devices are engineered to incorporate piezoelectric materials that convert a generator supplied and power amplified electrical signal into mechanical energy, primarily strain energy in vibrations (mechanical oscillations). The energy transformation explains why these devices are frequently referred to as transducers, a term employed throughout this thesis. Despite the progress in power ultrasonics over the past century, the standardised transducer configuration remains unclear. The reason is mainly attributed to the flexibility of transducer design, development of piezoelectric

materials, and varying application requirements [8, 12].

The bolt-clamped sandwich transducer, commonly called the Langevin transducer, is the most widely used narrow-band piezoelectric transducer in power ultrasonics. Its performance is assessed in both the frequency and time domains. For clarity, in this thesis, 'transducer dynamics' refers to the response of the transducer across both domains, including measures like resonant frequency, electrical impedance, and vibration amplitude. Recently, there has been a growing interest in optimising the dynamics of Langevin transducers, particularly regarding multi-frequency operation and modal coupling [13, 14]. This thesis concentrates on designing and characterising an innovative Langevin transducer incorporating shape memory alloys to achieve tuneable dynamics responding to varying temperatures. Drawing inspiration from the Nitinol cymbal transducer [15, 16] and the Nitinol fibre-enhanced composite rod [17, 18], which leverages phase transformations in Nitinol triggered by modest temperature changes to adjust resonant frequencies, this research suggests potential for achieving tuneable dynamics in a Langevin configuration. As a result, this new generation of Langevin transducer performs multi-functionality in real-world applications, such as actively controlled resonant frequencies and enhanced dynamics stability under varying operating conditions.

1.1 Langevin Transducers

The Langevin transducer has long been a favoured configuration for ultrasonic devices in power ultrasonics, widely utilised across various fields such as actuation [19], surgery [20], welding [21], and drilling [22]. This device was invented in 1916 by Paul Langevin, a professor at the Industrial College of Physics and Chemistry in Paris. In his design, small quartz crystals were positioned between metal segments, the first Langevin transducer. Initially conceived for underwater echolocation, the design faced manufacturing challenges such as dicing well-oriented bulk piezoelectric materials. Since then, the Langevin transducer has undergone significant developments with improved design and manufacturing techniques. Currently, in its most basic form, stacks of piezoelectric rings are sandwiched between two metallic end masses and compressed using a centrally pre-stress bolt, as illustrated in Figure 1.1.

1.1.1 Transducer Transduction

Piezoelectric materials are essential actuating units for ultrasonic transducers. Certain crystal materials, such as quartz, exhibit the piezoelectric effect. This effect represents that the mechanical stress applied to these crystals induces a surface charge, a phenomenon later termed the 'direct piezoelectric effect'. On the other hand, the phenomenon known as the 'converse piezoelectric effect' occurs when the application of an electric field produces mechanical strain in the material. The direct piezoelectric effect is distinct from the electrostriction, a quadratic

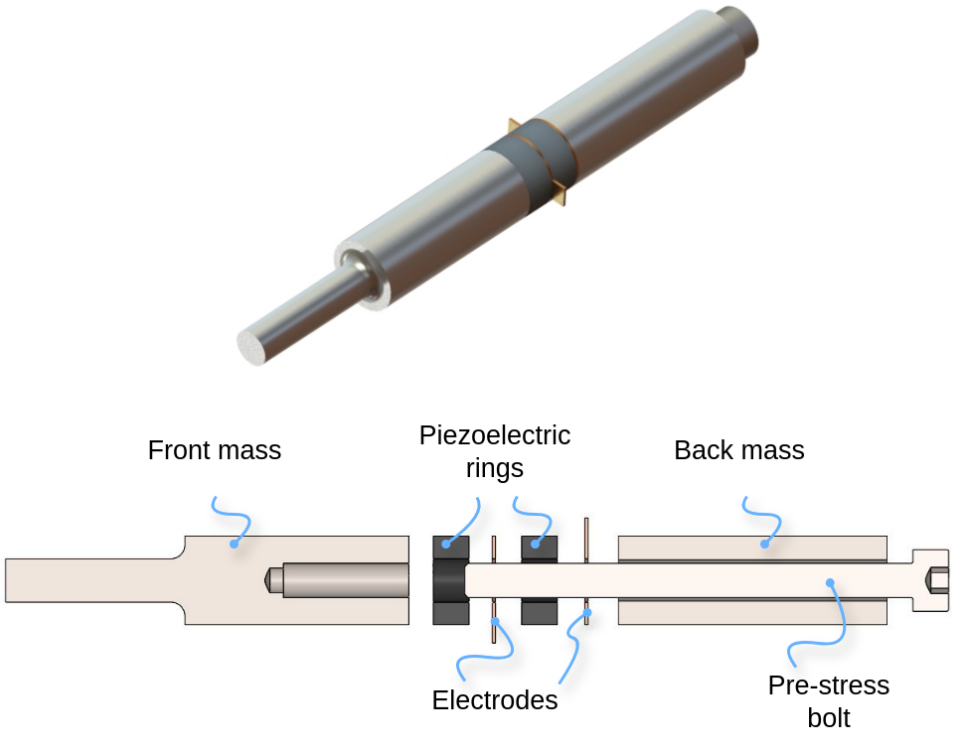

Figure 1.1: Configuration of a Langevin transducer with a stepped front mass.

and polarity-insensitive nature present in all dielectrics. Although both phenomena involve electromechanical coupling, they arise from fundamentally different mechanisms and can coexist in certain materials, such as ferroelectric materials. Lead zirconate titanate (PZT) is widely recognised as a preferred piezoelectric material for Langevin transducers. The Langevin configuration efficiently utilises the converse piezoelectric effect to convert input electrical energy into high-frequency mechanical vibrations. The transducer is designed to deliver vibration amplitudes on the micrometre scale at designated resonant frequencies, thereby addressing the specific requirements across various applications.

Typically, the Langevin transducer is operated at its resonant frequencies, which ensures a high mechanical quality factor. The quality factor measures how little energy is lost per cycle, representing the inverse of mechanical losses. Each resonance corresponds to distinct deformation patterns known as vibration mode shapes. Commonly employed mode shapes in Langevin transducers include longitudinal, bending, and torsional modes. To effectively excite these modes, carefully designing the piezoelectric components is essential. The transduction characteristics of the Langevin transducer about different vibration modes are illustrated in Figure 1.2, which further explains the underlying working principles based on referenced literature [23, 24].

Figure 1.2 illustrates the most efficient way to engineer piezoelectric segments, allowing the transducer to operate in specific mode shapes. However, regardless of the polarisation of the piezoelectric materials, these mode shapes naturally exist in the Langevin configuration. The

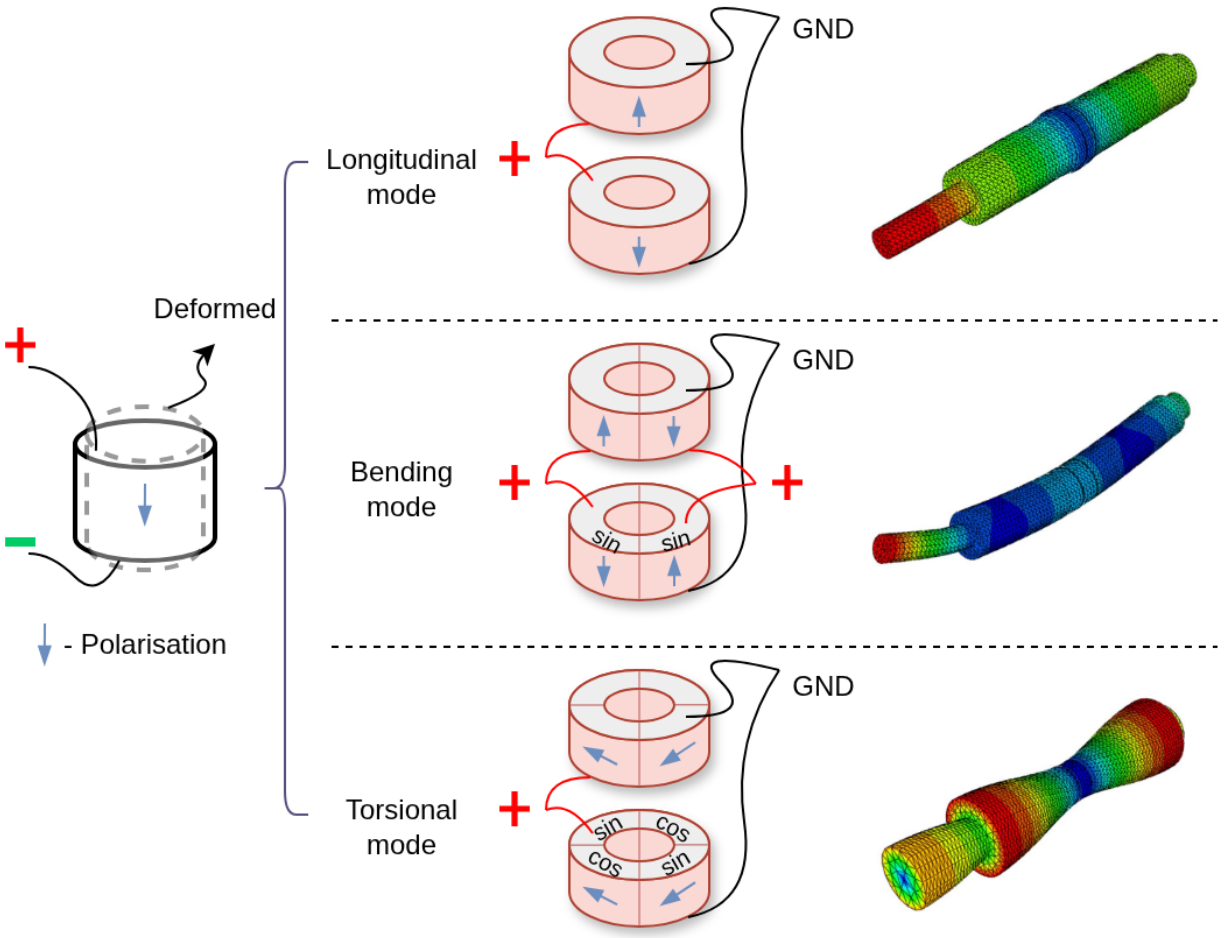

Figure 1.2: Transduction diagrams of piezoelectric ceramics incorporated into a Langevin transducer being operated in its longitudinal, bending, and torsional modes.

segmented piezoelectric stack in the figure is designed to excite selected modes and harmonics more efficiently, yielding high mechanical output.

1.1.2 Transducer Design and Fabrication

The design of an ultrasonic transducer heavily relies on understanding structural vibrations, material properties, operational parameters, and applications. Today, a range of analytical and numerical methods can predict transducer performance with high accuracy. Two standard analytical approaches are the equivalent-circuit model and the transfer matrix method [25, 26]. The former solves the Butterworth–Van Dyke (BVD) circuit, while the latter applies the constitutive relations. However, both methods suit low-dimensional theories, particularly one-dimensional (1D) problems. Most Langevin transducers are axisymmetric and have a consistent diameter throughout their structure. This allows the model to be simplified to a 1D representation and reduces calculation time, which is efficient for designing transducers with straightforward configurations. However, as the increasing demand for transducers capable of operating in complex dynamics and intricate configurations, such as ultrasonic motors vibrating in coupled modes,

there is a need for three-dimensional (3D) models to simulate transducer resonance behaviours accurately. Finite element analysis (FEA) is a widely used numerical tool for simulating problems based on a weak form of constitutive relations, which is suitable for complex configurations. Ultrasonic transducers involve multiple interacting physical phenomena, including coupled electrical and mechanical fields. FEA is particularly well-suited for managing the coupling of these physics within the scope of solid mechanics, enabling practical simulations of real-world behaviour where low-dimensional analytical models may be challenging to obtain in multi-physics scenarios. Given FEA is advantageous for transducer simulations, it has been the method discussed and utilised throughout this thesis.

The resonance behaviour of the transducer is highly sensitive to the dimensions of its segments, material properties, and the designed mode shapes. Therefore, dynamics simulations based on FEA are conducted iteratively by modifying segment dimensions and material combinations. The primary objectives of this design process include tailoring frequency responses, mode shapes, and nodal positions for clamping (where the amplitude is zero), all of which must be optimised. Typically, the sonotrode is often attached to the front mass in power ultrasonic applications to enhance the vibration amplitude. The gain, defined as the ratio of vibration amplitudes between the two ends of the sonotrode, is determined using FEA based on linear elasticity. Altering the sonotrode's material and dimensions allows tailoring this gain value, thus optimising transducer output performance.

Recently, researchers have incorporated new materials to achieve innovative functionalities, including multi-frequency and tuneable devices [27, 28]. Given the complexities of designing and manufacturing a Langevin transducer, integrating advanced materials adds further challenges that require careful consideration throughout the design process. Once the design satisfies all requirements, segments are fabricated according to the dimensions and materials, commonly through conventional mechanical machining methods, such as turning, milling, and drilling. For more intricate structures, advanced techniques like metal additive manufacturing are utilised [29]. Following the manufacturing process, a pre-stress characterisation is carried out to assemble the transducer, as the pre-stress value significantly impacts the transducer dynamics, particularly through the polarisation of piezoelectric materials. Methods of constant torque or constant stress assist to determine the optimal pre-stress value.

1.1.3 Applications of Langevin Transducers

While Langevin transducers have been proposed for more than a century, their versatile designs have made significant developments in applications. This adaptability encourages innovation across various industrial and medical fields, establishing Langevin transducers as a fundamental configuration of modern high-power ultrasonic technologies. The following section outlines several applications of power ultrasonics, with emphasis on areas informed by the author's doctoral experience. This discussion focuses on Langevin transducers that vibrate in their longitu-

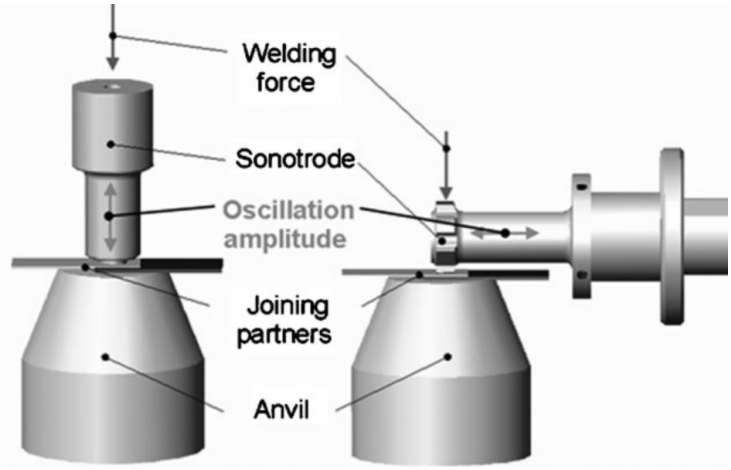

Figure 1.3: Types of ultrasonic welding setup: thermoplastic welding (left), metal welding (right) [31] (Reprinted from Advanced Engineering Materials, Copyright © 2009, with permission from Wiley).

dinal mode shapes with a basic configuration, although numerous transducer variants have been developed.

1.1.3.1 Ultrasonic Welding

Ultrasonic welding is a joining process that utilises high-frequency mechanical vibrations generated by a transducer to create strong and reliable bonds between materials, typically thermoplastics or metals, regardless of whether materials are similar or dissimilar. Its robustness highly depends on the material's geometric, mechanical, and physical properties and the transducer's dynamics [30]. In contrast to traditional fusion welding methods such as inductance and resistance welding, ultrasonic welding produces localised heat through friction between material sheets induced by transducer vibrations, thereby reforming the materials at the bonding interface. Minimal surface damage, clean, and fast processing are the primary advantages. Two distinct variants of welding systems are designed specifically for processing thermoplastics and metals, as illustrated in Figure 1.3 [31]. In thermoplastic welding, the transducer is positioned perpendicular to the bonding interface, whereas the transducer is aligned parallel to the welding zone in metal welding. This difference arises from their friction mechanisms: thermoplastic welding converts vibration energy into intermolecular friction within the material [32], leading to heat generation from mechanical losses, while metal welding relies on the heat due to friction at the interface.

Capabilities of ultrasonic welding have been well-documented. It was initially reported in the mid-20th century to join metals, such as copper, aluminium, and titanium, along with some of their alloys. The technology soon expanded to weld metals to non-metals [33]. Recent developments have allowed for joining between aluminium alloys and carbon fibre reinforced polymer (CFRP) [30], as well as aluminium alloys and glass fibre reinforced polymer (GFRP) [34],

with bonding occurring at the interface of the metal and the polymer matrix. Regarding the wide range of ultrasonically weldable materials, most processes adhere to the working principles illustrated in Figure 1.3. However, researchers have proposed that welding efficiency can significantly improve when using a metal welding setup for metal-to-GFRP applications [35,36]. The reason is that the perpendicular vibration can damage the glass fibres, which results in ineffective welding [35]. Therefore, the author suggests that the selection of system setups should consider each case individually.

1.1.3.2 Surgical Devices

The Langevin transducer, in its longitudinal modes, has been effectively utilised in various surgical devices. Its application in processing hard tissues spans oral maxillofacial, orthopaedic, neurosurgery, and spine surgery procedures. Unlike conventional surgical instruments, ultrasonic devices utilise high frequency vibration to improve cutting precision and enable selective tissue dissection. An insert, or end effector, is either directly attached to the transducer or connected to the sonotrode, depending on the transducer dynamics design and the surgical site access. The mechanical energy is delivered to the insert, removing hard tissue through physical contact at the tissue-insert interface. With a micro-meter scale vibration amplitude, these devices ensure minimal bone loss and precise incisions, promoting faster post-operation healing. The PIEZOSURGERY systems from Mectron, a leading company in ultrasonic surgery, utilise transducers that vibrate between 25 kHz and 30 kHz as handpieces, as shown in Figure 1.4(a), and are widely adopted for both dental and medical applications. Approximately 100 types of cutting inserts have been developed for the PIEZOSURGERY devices, with their types and dimensions engineered to specific surgical tasks [37]. The design of the inserts significantly influences the transducer dynamics and energy delivery efficiency. Recently, there has been a trend towards miniaturising the transducer and handpiece, which is important for broadening their application in various surgical procedures. However, this miniaturisation presents challenges, as the fabrication capability of piezoelectric materials constrains the dimensions, and the miniaturised transducer may lead to issues such as unstable dynamics and heat dissipation.

Electrosurgery has long been a conventional method for dissecting soft tissues. However, the significant heat generated during the process and the presence of electrical arcs can damage tissues. These damages may lead to adverse biological influences on nearby vulnerable structures, resulting in longer patient recovery. The ultrasonic scalpel addresses these issues by focusing output energy at the operational tip, minimising the charring injuries. For instance, in sealing renal arteries, hemostasis is achieved through focusing high power ultrasonic vibration at the instrument tip. This results from heat generated by friction and internal tissue losses, with cavitation contributing in fluids. The ultrasonic scalpel for soft tissue dissection has been in development for decades. The UltraCision scalpel, introduced in 1988, operates at a frequency of 55 kHz and was the first ultrasonic dissecting tool available on the market. Since then,

it has evolved from a scalpel design to include scissors-like (HARMONIC FOCUS, Ethicon, Johnson & Johnson MetTech) and grip-like (HARMONIC Shears, Ethicon, Johnson & Johnson MetTech) forms to accommodate both open and endoscopic surgical procedures. With developments in ultrasonic technology, both Ethicon (HARMONIC 1100 Shears [38], as illustrated in Figure 1.4(b)) and OLYMPUS (THUNDERBEAT Type S [39]) have introduced products that ensure secure hemostasis and sealing vessels with a diameter up to 7 mm. The versatility of modern devices allows them to dissect, seal, and grasp with a single instrument, resulting in shorter and more cost-effective surgical procedures. Nevertheless, the heat and smoke generated at the processing zone during the coaptation process remains a concern and is now a primary objective for pioneering companies.

(a)

(b)

Figure 1.4: Handpiece of PIEZOSURGERY touch from Mectron [37] and Harmonic 1100 Shears from Ethicon [38]

1.1.3.3 Acoustic Levitation

Various techniques for levitating objects, including electrostatic, magnetic, optical, and acoustic levitation, have been discovered. Among these, acoustic levitation takes advantage of the acoustic waves generated by an ultrasonic transducer to commonly create standing waves in mid-air, allowing the levitation for objects at their nodes. It is important to distinguish between acoustic levitation and acoustic tweezers. While both methods employ acoustic waves to manipulate objects, levitation specifically counteracts gravity, whereas gravity is not a concern in the

tweezer systems [40]. Acoustic levitation can levitate a diverse range of materials, encompassing liquids, solids, and even living organisms, and has found various applications in chemistry, materials science, pharmacy, and robotics.

From the perspective of transducers, two primary techniques are employed: phased arrays of flexural transducers and Langevin transducers. Transducer arrays employ multiple transducers aligning in matrices to generate standing waves in coupled acoustic fields, with each transducer controlled independently. This control method allows for manipulating the position of levitated objects in 2D or 3D spaces, with an outstanding application as acoustic holography [41, 42], as shown in Figure 1.5(a). In contrast, the Langevin transducer is typically used in single-axis levitation systems, which can operate in either the near field or far field. Near-field levitation occurs when the object is positioned close to the sound source, with high acoustic radiation force against the object's gravity [43]. Far-field levitation, on the other hand, involves forming a standing wave with a reflector or an additional transducer placed end-surface to end-surface, as illustrated in Figure 1.5(b). The spacing between the transducer and the reflector or the additional transducer must be an integer multiple of half the wavelength. Generally, the dimensions of levitated objects should be smaller than half the wavelength in a far-field single-axis system. However, research suggests that larger objects can also be levitated if the system is tailored to a near-field system with multi-axis setup [44] in Figure 1.5(c) or transverse travelling wave [45] in Figure 1.5(d).

1.2 Adaptive Ultrasonic Transducers

Adaptive ultrasonic transducers are innovative devices that actively or passively tune their dynamics in response to changing operational environments and purposes. These transducers are multi-functional, particularly regarding multiple resonant frequencies, a growing trend in ultrasonic device research. Multi-frequency operation in non-destructive testing (NDT) exploits the trade-off between scanning resolution and penetration depth [47]. Higher frequencies provide finer resolution but shallower penetration, whereas lower frequencies penetrate deeper at the expense of resolution. Multi-functionality is typically achieved through novel structures or the integration of advanced materials. An example is multi-frequency piezoelectric micromachined ultrasonic transducers (pMUTs), designed for biomedical imaging and NDT applications, where a popular approach involves altering structures and dimensions [48, 49].

In the Langevin configuration, a known technique is to adjust the positioning of multiple piezoelectric stacks, allowing for tuning the resonant frequency based on a single vibration mode shape [50]. Alternatively, the resonant frequencies of the Langevin transducer can also be tuned by electrical methods. By actively and independently controlling the open/short statuses of multiple piezoelectric units, one can shift resonant frequencies and modify electromechanical coupling factors, as illustrated in Figure 1.6 [51]. This capability allows the transducer to ad-

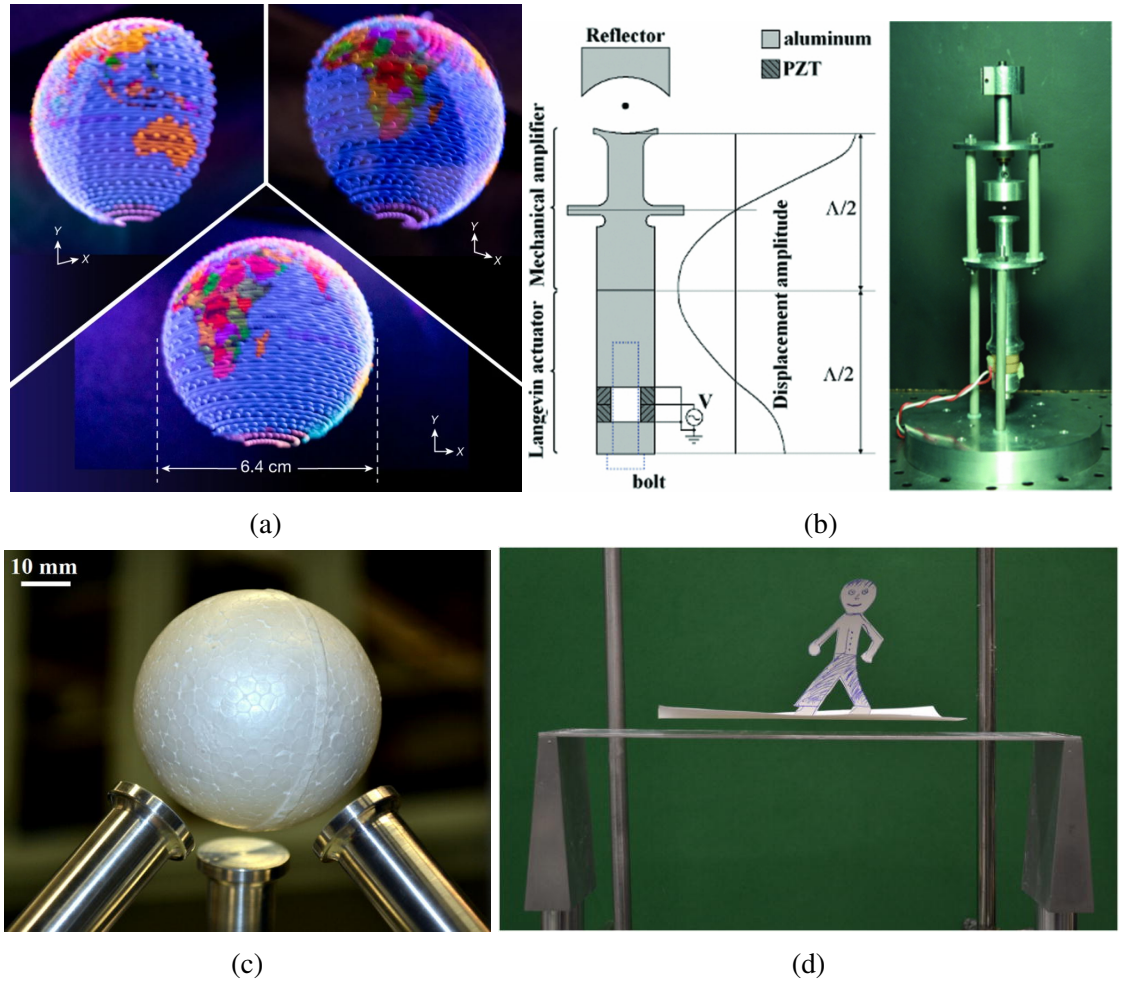

Figure 1.5: (a) An example of ultrasonic holography for a 3D globe [41] (Reprinted from Nature, Copyright © 2019, under exclusive licence to Springer Nature Limited), (b) Schematic of an acoustic far-field levitation system [46] (Reprinted from Review of Scientific Instruments, Copyright © 2011, with permission from AIP Publishing), (c) acoustic levitation of an expanded polystyrene sphere of 50 mm diameter [44] (Reprinted from Applied Physics Letters, Copyright © 2016, with permission from AIP Publishing), and (d) acoustic levitation of a large object via transverse travelling waves [45] (Reprinted from The Journal of the Acoustical Society of America, Copyright © 2017, with permission from AIP Publishing).

just its resonant frequency instantaneously without requiring multiple transducers or a complex structure. However, the rapid alterations in transducer dynamics cause mechanical and electrical fluctuations, which necessitate additional efforts in designing the control system.

A novel approach involves integrating shape memory materials, primarily nickel titanium, or Nitinol, into ultrasonic devices [16, 27, 52]. These devices tune their dynamics by changes in the material's mechanical properties due to the martensitic transformation in response to varying ambient temperatures. In radar applications, researchers have proposed an ultrasonic device based on Nitinol [28]. By selectively increasing the temperature in specific regions of the Nitinol metamaterial, the device manipulates the transmission direction of sound waves through martensitic transformations, as illustrated in Figure 1.7 (a). Exciting the guided wave at 68 kHz

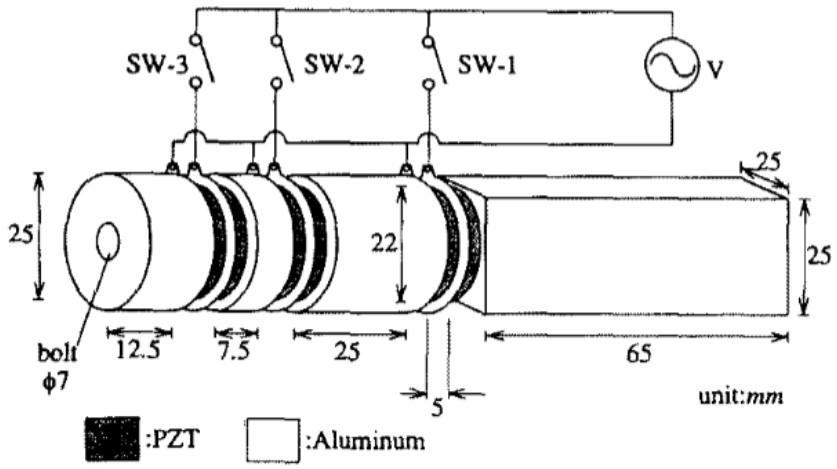

Figure 1.6: Diagram of the multi-frequency Langevin transducer [51] (Reprinted from IEEJ Transactions on Electronics, Information and Systems, Copyright © 1994).

yields the maximum difference in displacement amplitude between martensite and austenite. At this frequency, the metamaterial becomes partially transmissive, allowing the wave to propagate through one selected part of the metamaterial and effectively escape the structure. Another example is the Nitinol cymbal transducer [16, 27, 53], shown in Figure 1.7 (b). Integrating Nitinol end caps into cymbal transducers has demonstrated the ability to tune resonant frequencies effectively. Results indicate that resonant frequencies and corresponding modes can shift by several kHz at different temperatures [27], as depicted in Figure 1.7 (c).

The primary motivation for this research is to explore mechanisms by which transducers with adaptive dynamics could be achieved using materials with phase-transformational behaviours or with environment-sensitive properties. Specifically, the elastic moduli of Nitinol are highly sensitive to even modest changes in temperature. Accordingly, Nitinol can be integrated into ultrasonic devices, potentially in a Langevin configuration. This enables adaptability under varying operating conditions. To the best of the author's knowledge, such implementations into Langevin transducers have not yet been reported in the academic or industrial literature. In ultrasonic surgery, the tuning of the resonant frequency allows low-frequency (about 20 kHz) operation for hard tissues and high-frequency operation for soft tissues (about 55 kHz). These strategic operations improve a single transducer's versatility and efficiency.

1.3 Characteristics of Nitinol

Shape memory alloys are smart metallic alloys that can undergo reversible shape changes in response to various stimuli, such as temperature, mechanical stress, magnetism, and electricity. These shape changes occur due to martensitic phase transformations, rather than the conventional deformation based on elasticity or plasticity. One of the most common shape memory

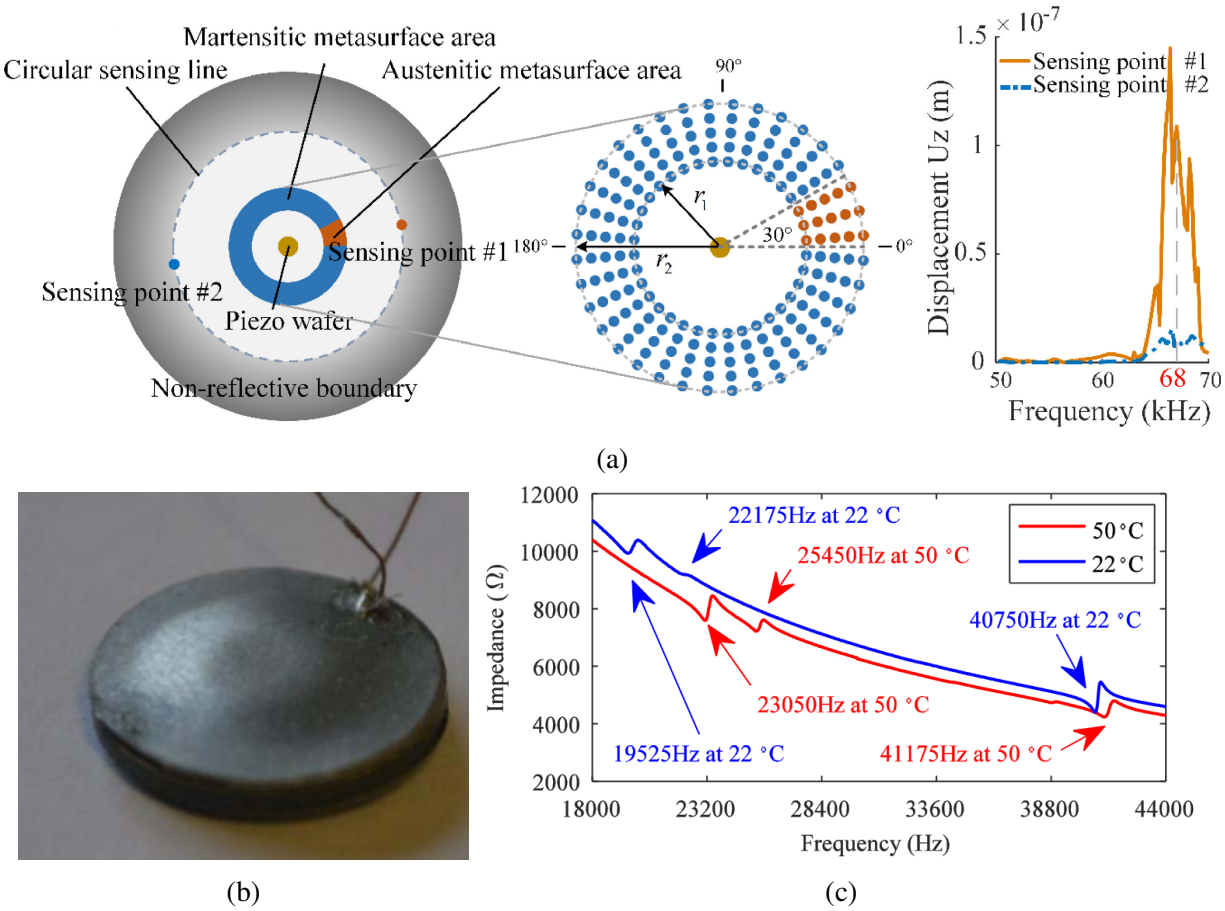

Figure 1.7: (a) Annular configuration of the metasurface radar system for steering wave radiations [28] (Reprinted from Journal of Sound and Vibration, Copyright © 2022, with permission from Elsevier). (b) Nitinol cymbal transducer and its impedance-frequency response at temperatures of 22 °C and 50 °C [27] (Reprinted from IEEE Transactions on Ultrasonics, Ferroelectrics, and Frequency Control, Copyright © 2018, with permission from IEEE).

alloys is an intermetallic compound called Nitinol, which consists of ~ 50 at% nickel. Nitinol is utilised in various applications, including actuators, antennas, and biomedical stents, due to its excellent abrasion resistance, corrosion resistance, and biocompatibility. However, its high cost presents a challenge to its broader use.

Nitinol possesses two key mechanical properties which are dependent, in part, on temperature or stresses. One is the shape memory effect, the ability of the material to recover a particular set shape in response to temperature, and the other is superelasticity, which is the ability of the material to recover from relatively high levels of applied stress [54]. Both phenomena arise from the phase transformation between martensite and austenite microstructures, as shown in Figure 1.8. As temperature decreases, phase stability shifts from austenite to martensite, while as it increases, from martensite to austenite. The fundamental principle is that the martensitic phase has a lower Gibbs free energy below the equilibrium temperature between martensite and austenite. Therefore, martensitic phase is thermodynamically stabilised lower than the equilibrium temperature, whereas austenite is stable above this temperature. An intermediate or-

thorhombic phase, known as the R-phase, can also be generated, depending on the composition of the alloy and heat treatments. These microstructures all possess different elastic properties, varying from a modulus in the order of 30-40 GPa for martensite [55, 56], towards 70-90 GPa for austenite [57, 58]. Fundamentally, the temperatures at which these microstructures can be generated depend on the alloy composition and the hot and cold working conditions. Variations in modulus have been studied using techniques such as nanoindentation [59], resonant ultrasound spectroscopy (RUS) [60], and tensile testing [55]. Measurement of the modulus change in a specimen of Nitinol thus enables the design of ultrasonic transducers with adaptive dynamic characteristics, given the dependence of frequency on elastic properties. To understand Nitinol deeper, the following subsections detail its shape memory effect and superelasticity.

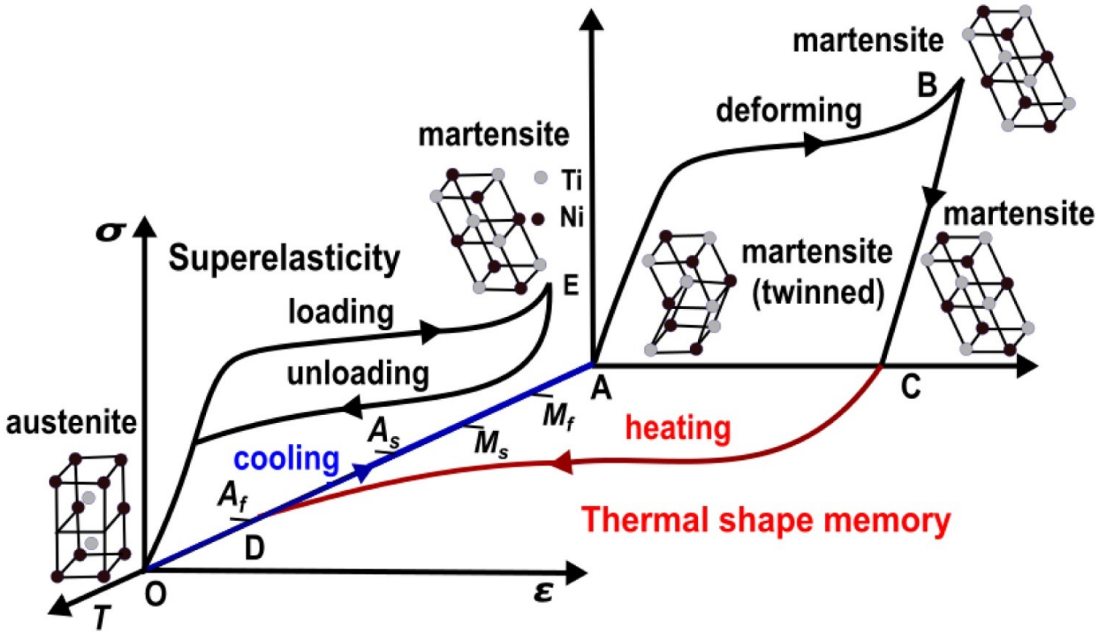

Figure 1.8: Stress–strain–temperature diagram for Nitinol [61] (Reprinted from Journal of Manufacturing Processes, Copyright © 2009, with permission from Elsevier).

1.3.1 Shape Memory Effect

The shape memory effect of Nitinol is a macro phenomenon of the martensitic transformations, which represent a solid-to-solid phase transition between two distinct phases: martensite (B19'), a low-temperature monoclinic crystallography, and cubic austenite (B2). Temperature changes primarily induce transformations between B19' and B2, including forward transformation (B2 - B19') and reverse transformation (B19' - B2). The key transformation temperatures considered for this effect include the martensite start (M_S), martensite finish (M_F), austenite start (A_S), and austenite finish (A_F). Four processes are involved in achieving a complete shape memory effect, particularly as the 'Thermal shape memory' illustrated in Figure 1.8.

The shape memory effect requires the initial operating temperature to be lower than M_S. At

this temperature, the twinned B19' phase naturally predominates in Nitinol when no external stress is applied. A trained shape of Nitinol is achieved through prior heat treatment, where the material is subjected to a mechanically constrained shape, or a parent shape, at temperatures exceedingly above A_F, followed by a cooling process below M_F. When external stresses are applied to twinned B19' with its inelastic state, the twin boundaries within the lattice begin to reorient, transitioning to monoclinic de-twinned B19', a process known as de-twinning that allows the material to accommodate additional strain energy. This de-twinning mechanism occurs gradually and partially in Nitinol, depending on the magnitude of the applied stress. Upon releasing the external stress, the stable phase remains as de-twinned B19' until the material is heated to A_S. Once the deformed Nitinol is over A_S, it transforms from de-twinned B19' to the B2 phase and ultimately becomes fully austenitic when the temperature exceeds A_F. Notably, the B2 phase retains the trained parent shape since both B2 and twinned B19' exhibit the same macroscopic parent shape. During a stress-free cooling process that ends up lower than the martensite finish temperature, the material reverts to the original twinned B19' phase, keeping the parent shape.

Furthermore, the two-way shape memory effect has been observed in Nitinol, enabling the material to remember its shape at both high and low temperatures. Unlike the conventional shape memory effect (one-way shape memory), the two-way shape memory effect does not necessitate a resetting force during operation [62]. This phenomenon is achieved through the thermo-mechanical training of Nitinol, where the material undergoes repeated cycling between its martensitic and austenitic phases under applied stresses. Additionally, it can be realised through engineering Nitinol with compositional gradient microstructures, even with multi-stage shape memory phenomena [63, 64]. In the shape memory effect, the phase transformation temperatures of Nitinol are influenced not only by the material composition [65] but also by the application of stress and cyclic thermal loading [66]. For instance, in the case of Ni60Ti40 (wt.%), as illustrated in Figure 1.9, the transformation temperatures are functions of the applied stress, with experiments conducted using an isobaric system that applies cyclic thermal loading to the samples [66]. It is important to note that the martensite represented in this graph may exist as fully twinned B19' or as a combination of twinned and de-twinned B19'. In this case, a stress of 140 MPa is required for twinned B19' to start transforming to de-twinned B19', while the stress needed to transform from B2 to de-twinned B19' exceeds 300 MPa. The shape memory behaviour can also be engineered through heat treatments conducted with or without applying stresses. This alteration in the material properties, such as precipitate formation, grain size, and internal stress state, enhances the flexibility in the design of Nitinol-based devices [67].

The martensitic transformations of Nitinol can exhibit a rhombohedral martensitic phase referred to as the R-phase, which forms an intermediate stage. Although R-phase is inherently a variant of B19', it does not contribute to the shape memory effect or superelasticity. Instead, R-phase formation impedes the transformation to the final phases, B2 or B19'. For instance, in

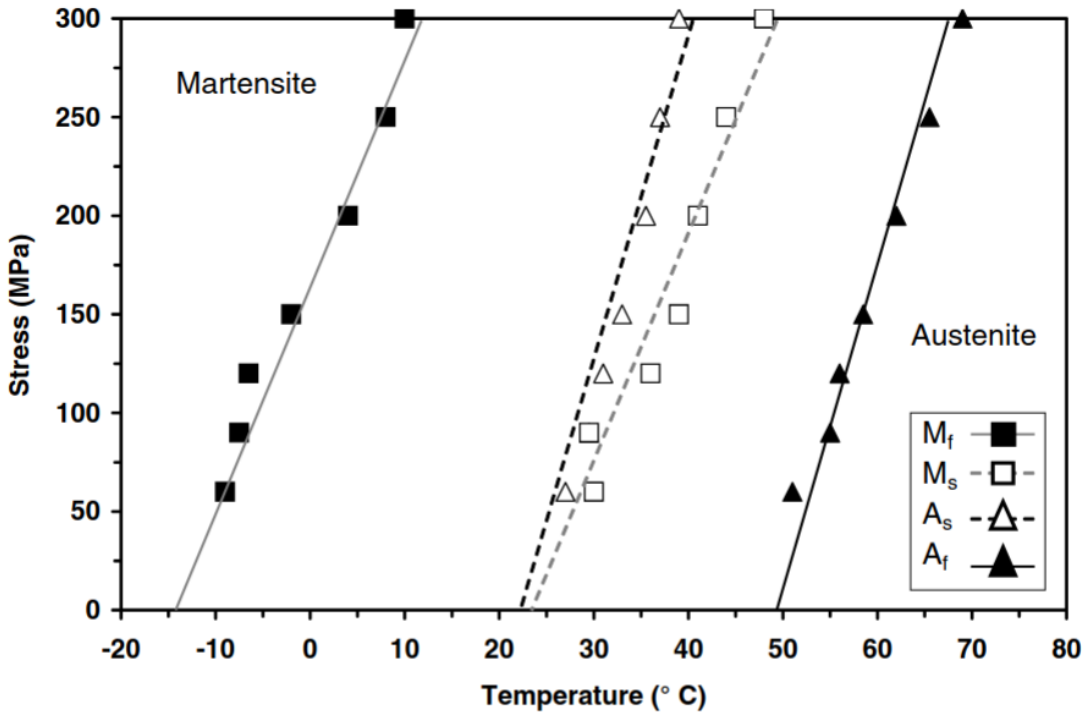

Figure 1.9: Phase diagram of Ni60Ti40 (wt.%) material derived from isobaric thermal cycling results [66] (Reprinted from Shape Memory Alloys: Modeling and Engineering Applications, Copyright © 2008, with permission from Springer Nature).

the transformation from B2 to twinned B19' triggered by temperature, the total energy transforming to twinned B19' decreases due to extra energy consumed through the B2 - R-phase and R-phase - B19' processes. Consequently, a noticeable phase transformation hysteresis results in decreased operational efficiency. Not all Nitinol contains R-phase, as its presence depends on material composition and heat treatment conditions. Additionally, the formation of the R-phase is suppressed through standard heat treatment at specific temperatures and ageing time [68]. Recent research focuses on controlling the transformation temperatures of the R-phase and exploring its potential applications. For example, using the R-phase in a Nitinol-based helical spring system effectively narrows the actuation temperature window compared to the system based on the martensitic phase transformation [69].

1.3.2 Superelasticity

Superelasticity arises in Nitinol, involving the phase transformation between de-twinned B19' and B2, enabling the material to undergo large and reversible deformations under stress. This normally adds up to 6–8% recoverable strain [70], compared to 0.2–0.5% for most metals. The superelasticity is based on external stresses without any changes in material temperature. The fundamental principle utilises the stress-induced martensite phase transformation and the instability of martensite at high temperatures. Therefore, the operation temperature usually slightly

exceeds A_F. There are four critical stresses to indicate the stress-induced phase transformations, which are martensite start stress (σ_{MF}), martensite finish stress (σ_{MF}), austenite start stress (σ_{AS}), and austenite finish stress (σ_{AS}). The phase transformation diagram is illustrated as the stress-strain relationship shown in Figure 1.8. Firstly, the external stress increases from zero to σ_{MS}, behaving as a linear elastic deformation of the material with the fully austenitic phase. When the stress above σ_{MF}, the B2 phase transforms to de-twinned B19' and the material has fully de-twinned B19' phase at σ_{MF}. An elastic behaviour of de-twinned B19' follows this process. Irreversible plastic deformation may occur if the material is strained much higher than σ_{MF}. Similar to this loading process, the unloading process involves the start of phase transformation from de-twinned B19' to B2 at σ_{AS}, and transforming fully B2 when the stress is lower than σ_{AF}. In the schematic, two stress-strain plateaus indicate the phase transformation is happening. Nitinol exhibits a lower elastic modulus during this transformation than the B2 and B19' phases. This reduced modulus is attributed to the energy consumption associated with the phase transformation, which allows the material to rearrange its crystallographic structure. Additionally, the region between these two plateaus demonstrates the hysteresis of the phase transformations, which can be determined by the interfacial energy at phase boundaries [71].

The chemical composition, heat treatment, and external stresses significantly affect the typical phase transformation behaviours associated with superelasticity [66, 72]. For example, it has been suggested that the annealing temperature engineers the transformation stresses and the hysteresis region [73]. As the annealing temperature increases, transformation stresses decrease, reaching a minimum hysteresis at around 600 K. However, superelasticity is no longer observed when the temperature is as high as 900 K. This phenomenon can be attributed to changes in microstructural properties, such as the material internal defects and residual stresses [74]. The superelasticity could also be influenced by material temperature independent of the annealing process. The tensile experiment at different temperatures, as reported in literature [66], demonstrates that superelasticity is a function of the material temperature. All phase transformation stresses tend to increase linearly with temperature, reflecting a higher required stress to cause the phase transformation from B2 to de-twinned B19'. While this phenomenon is graphically similar to Figure 1.9, they involve different transformations: B2 - twinned B19' and B2 - de-twinned B19', respectively.

Additionally, one could tailor the hysteresis through tensile experiments at different material temperatures [75]. The stress for producing two stress-strain plateaus increases with temperature, where the stress difference between plateaus decreases. Similar to the shape memory effect, the R-phase can be observed during the phase transformation in superelasticity [75]. Even though the transformation between B2 to R-phase narrows the transformation strain and decreases the hysteresis effect [75], the R-phase does not provide a strong superelastic effect. Given the difficulty of controlling the presence of the R-phase, it has limited potential in applications.

1.4 Original Contributions to Knowledge

Up to now, the integration of Nitinol into ultrasonic transducers for tuneable resonances has primarily been limited to flextensional type configurations, such as the cymbal transducer [27]. While Nitinol enhances the tuneability of the transducer, the observed non-linear vibration responses and the limited consistency of epoxy interfaces highlight critical considerations for high-power applications. Given the popularity of the Langevin transducer, where epoxy is not necessary in sandwiching segments, and the continuing challenges associated with performance degradations to temperature, Nitinol presents a promising and practical solution to adapt or compensate for the influence of temperature on the dynamics of the transducer. In this research, Nitinol is incorporated in the Langevin transducer for the first time, with thorough studies about transducer dynamics in response to temperature and its application.

The properties of piezoelectric materials are temperature dependent, where parameters such as the charge and voltage constants, d and g, and compliance and permittivity, s and ε, respectively, are highly sensitive to temperature [76, 77]. Hence, both the dynamic characteristics of the Langevin ultrasonic transducer, including resonant frequency and vibration amplitude, and electromechanical parameters, including impedance, are highly temperature dependent [78–80]. Although introducing Nitinol to the Langevin configuration complicates its dynamic characteristics, this increases the tuneability and changes the non-linearity in transducer dynamics, showing high adaptivity at varying temperatures. Following the previous research in Nitinol cymbal transducers, adaptive dynamic behaviours of Nitinol Langevin transducers have been identified and measured, including the tuneability of transducer dynamics, the adaptive modal coupling technique, and the resonance stability at elevated temperatures, which has significant implications for practical device applications.

In conjunction with relevant material characterisation methods, including differential scanning calorimetry (DSC), thermal and mechanical characteristics of the Nitinol have been characterised. Mathematical models have been developed to explain the dynamic behaviour of Nitinol Langevin transducers at room temperature. Electrical discharge machining (EDM) has been used to fabricates Nitinol components, followed by transducer assembly undertaken and tailored for different functionalities, including frequency tuneability, modal coupling, and resonance stability. Given these findings are frequency-based, acoustic levitation was chosen as the case study owing to its strong dependence on drive frequency. The subsequent measurements of transducer dynamics demonstrate that integrating a phase-transforming material like Nitinol offers advantages in the acoustic levitation based on stable resonance. The key original contributions of this doctoral project are outlined below, each of which has been delivered for the first time through this research endeavour.

- Development of a design and manufacture methodology for Langevin transducers incorporating Nitinol.

- The development of 1D and 3D mathematical models according to piezoelectricity to explain the dynamic behaviours of Langevin transducers.
- Fabrication of Nitinol Langevin prototypes comprising conventional configurations and variant cascaded structures.
- The complete characterisation of these prototypes demonstrates a range of novel dynamic behaviours, including resonance tuneability, active modal coupling, and resonance stability.
- The practical application of a Nitinol Langevin transducer as a case study via adaptive acoustic levitation.

1.5 Structure of the Thesis

This thesis begins with a concise overview of the relevant scientific literature, highlighting key developments in the field. It then presents the principles of Langevin transducer design and manufacturing, beginning with the proposition of a 1D mathematical model based on Timoshenko-Ehrenfest beam theory to simulate Langevin transducer dynamics, followed by an extended model for 3D piezoelectricity. Based on fundamentals in fabricating conventional Langevin transducers, specific recommendations for Nitinol Langevin transducers are provided prior to chapters about novel contributions related to adaptive resonance, active modal coupling, and stable resonance. The following chapter discusses the latest developments in utilising Nitinol Langevin transducers for adaptive acoustic levitation.

Chapter 2

Literature Review

2.1 History of Acoustics and Ultrasound

The study of acoustics was recorded as early as ancient Greece, with philosopher Pythagoras, in the 6th century B.C. A likely legendary story suggested that he observed the relationship between harmonious sound and the length of stretched strings with fixed ends. A shorter string emitted a higher pitch, which is the perceptual analysis of the fundamentals of acoustics in elastic bodies where the geometry and dimension decide the resonant frequency. However, the scientific word 'frequency' was not introduced. Pythagoras and his followers, such as Archytas (435/410–360/350 B.C.), an ancient scientist and philosopher, developed the concept of the harmonic mean. Here, 'harmonic' refers to consonant integer ratios between pitches, which were foundational in ancient music theory. Then, a Roman senator and philosopher, Boethius (480–524 A.D.) developed music theory. He wrote in *De Institutione Musica* [81], one of the first musical texts, that the music, or sound, can be produced by the motion of a string, the wind or water passing through a pipe, or the percussion of a brass hollow bar. From the modern scientific perspective, the depiction described that both mediums and excitations are required to generate sound.

However, it was not until the 17th century that the scientific study of acoustics gained momentum. In 1636, French scientist Marin Mersenne (1588-1648) published his representative work, *Harmonie universelle* [82], one of the earliest comprehensive works on a wide range of music theories. In his work, he proposed the formula to calculate the oscillation frequency of a stretched string, known as Mersenne's laws. He determined the frequency of an audible tone for the first time, laying the groundwork for further exploration into sound behaviours. At almost the same time, Galileo Galilei (1564-1642) discussed in his *Two New Sciences* in 1638 about the kinematics and the strength of materials, discussing the frequency of vibration for a simple pendulum [83]. By varying the speed at which a chisel was scraped and employing different spacing schemes when scratching the brass plate, Galileo established a direct relationship between the pitch of the produced sound and the spacing of the chisel's skips, thereby creating a frequency

measure. Many endeavours were also made by later experiments, for example, by Robert Hooke (1635-1703) and Joseph Sauveu (1653-1716), to connect pitch to sound frequency [84].

French philosopher Pierre Gassendi (1592-1655) proposed that pitch and propagation speed are important properties of sound [85]. He made the earliest known attempt to measure the speed of sound with about 25 % accuracy by roughly clocking the time elapsed between the flash and the hearing of a gunshot, assuming the light is transmitted instantaneously. He also proved that the speed of sound is independent of pitch. In 1660, Vincenzo Viviani (1622-1703) and Giovanni Alfonso Borelli (1608-1679) repeated the experiment to determine the speed of sound but with a cannon instead, obtaining a more accurate value of 350 m/s [86]. In 1738, the Academy of Sciences in Paris measured the precise speed of sound for the first time, where the value is 332 m/s, less than 1 % difference from the present value [87]. However, the speed of sound depends on temperature, wind and other environmental factors which have been considered in experiments since the 18^{th} century. In 1826, Swiss physicist Jean-Daniel Colladon (1802-1893) conducted an experiment that enhanced the understanding of sound waves [88]. By submerging a church bell, a so-called hydrophone, underwater, he discovered that sound travels faster in water than in air. Subsequently, research about measuring sound speed has flourished in various materials, including solids.

The history of ultrasound traces back to the late 18^{th} century. Lazzaro Spallanzani (1729-1799), an Italian physiologist and biologist, first studied the concept of echolocation in 1793 [89]. He observed that bats navigate using sound rather than sight, where the bat's deafness failed navigation, a phenomenon that would later form the foundation of ultrasound technology. His pivotal work set the stage for further discoveries about the properties of inaudible sound. This observation contributed significantly to developing sonar and other underwater acoustic technologies. Later, in 1842, Austrian physicist Christian Doppler (1803-1853) introduced the concept of the Doppler effect, which described how the frequency of a sound wave changes depending on the movement of its source and the observer [90]. This principle would later become essential for Doppler ultrasonography, which is widely used today in medical imaging to assess blood flow.

Although the public noticed inaudible sounds back then, detecting and generating ultrasound was still challenging. In 1858, John LeConte (1818-1891) recorded that a gas burner's jumping flame is sensitive to sound frequency, thus providing the potential to detect sound even with high frequency [91]. To produce ultrasound, Francis Galton (1822-1911) invented the dog whistle, which emits sound in the ultrasonic range to detect the hearing range of humans and animals purely mechanically [92]. Until the late 19^{th} century, Pierre Curie (1859–1906) and Paul-Jacques Curie (1855–1941) discovered the piezoelectric effect in 1880 [93]. They demonstrated that certain crystal materials, such as quartz, generate an electric charge when subjected to mechanical stress. This process is also reversible, named the converse piezoelectric effect, and has been predicted by Gabriel Lippmann (1845-1921) in 1881 and proven later by the Curie

brothers experimentally [94]. The direct and converse piezoelectric principles became the basis for the transducers used in modern ultrasound techniques, of which devices convert electrical signals into sound waves and vice versa.

2.2 Ultrasonic Transducers

2.2.1 Piezoelectric Materials

Throughout the early 20th century, research in piezoelectricity mainly focused on natural piezoelectric materials, including quartz, tourmaline and Rochelle salt. These materials exhibited electric polarisation when subjected to mechanical stress due to their non-centrosymmetric crystal structures. To understand the relationship between material piezoelectricity and crystal symmetry, German physicist Woldemar Voigt explained this in his published work in 1910 through a mathematical framework based on the theoretical foundation for piezoelectricity provided by Lippmann. Although extensive research characterised piezoelectricity back then, it was not until 1916 that Paul Langevin and Chilowsky introduced the first piezoelectric device for submarine echolocation. Subsequently, natural piezoelectric materials, especially quartz, have flourished extensively in applications such as radio transmitters and receivers. A representative example is that Walter Guyton Cady designed the first quartz crystal resonator and circuit to control exciting frequency in 1921.

By the mid-20th century, the development of synthetic piezoelectric ceramics revolutionised the field, providing materials with superior piezoelectric properties compared to natural crystals. In the 1940s, barium titanate ($BaTiO_3$) became the first widely used piezoelectric ceramic, which is primarily credited to A. von Hippel [95], offering high piezoelectric coefficients and straightforward fabrication. This finding was followed in the 1950s by the discovery of PZT, a solid solution of $Pb[Zr_xTi_{1-x}]O_3$, at the Tokyo Institute of Technology. Compared to $BaTiO_3$, PZT exhibits a higher Curie temperature, the temperature above which piezoelectric materials lose their polarisations and sensitive electrical parameters, resulting in the PZT essentially replacing $BaTiO_3$.

Soft PZT (donor doping) and hard PZT (acceptor doping) are two popular forms of commercial products, differentiated by their respective doping techniques. Soft PZT exhibits high piezoelectric coefficients, dielectric permittivity, and electromechanical coupling factors, making it ideal for applications requiring high sensitivity to voltage, such as precision actuators and energy harvesters. However, it is less suited for high-power applications due to its high dielectric losses. Conversely, hard PZT materials demonstrate lower dielectric losses and higher mechanical quality factors, enhancing their sensitivity to frequency and making them suitable for high-power applications, such as ultrasonic welding and motors. Since the 1970s, extensive research focused on improving the durability and temperature stability of hard PZT, enabling its

use in extreme environments like aerospace and defence technologies.

In the late 20th and early 21st centuries, researchers focused on lead-free piezoelectric materials due to environmental concerns over lead toxicity, leading to the development of materials such as sodium potassium niobate (KNN) and bismuth sodium titanate (BNT). Recent advancements include nano-engineered piezoelectric materials, thin-film piezoelectrics, and flexible polymer-based piezoelectrics, which are expanding the applications of piezoelectricity into wearable electronics, energy harvesting, and biomedical devices. The development of high-performance and environmentally friendly piezoelectric materials continues to push the boundaries of modern technology's sensors, actuators, and microelectromechanical systems (MEMS).

2.2.2 Development of Langevin Transducers

As introduced in Section 1.1, the first Langevin transducer was designed by Paul Langevin featured a sandwich structure, where metal segments hold the central thin quartz crystal. When exposed to high-frequency electrical signals, the quartz crystal generated ultrasonic waves through the converse piezoelectric effect. The Langevin transducer design was refined throughout the early to mid-20th century, incorporating multiple stacked crystal elements and various designs for metal parts to improve wave transmission. While quartz provided reliable piezoelectric properties, its performance was limited in efficiency, electromechanical coupling, and operational frequency range, driving researchers to explore alternative piezoelectric materials.

The mid-20th century saw significant advancements in Langevin transducer technology with the introduction of barium titanate and PZT. These materials exhibited higher piezoelectric coefficients and higher operating temperatures, making them superior alternatives to quartz. The design of modern Langevin transducers was subsequently revealed in the 1950s, where its configuration involved a central pre-stress bolt to clamp metal segments, called end masses, and piezoelectric material as a whole. However, the exact attribution of the bolt-clamped modification to the Langevin transducer remains unclear. The closest patent was published by Thomas J Scarpa in 1961 and granted in 1964 [96], which identified PZT as the piezoelectric element. This multilayered configuration with bolt-clamping, commonly referred to as the bolt-clamped Langevin transducer, continues being used till now. Due to the applied pre-stress increased stability of the connection between transducer segments, transducer performance was enhanced, enabling their widespread use beyond echolocation.

Since the 1960s, the Langevin transducer has been widely operated within the ultrasonic range under high-power conditions. Additionally, PZT was primarily selected as the piezoelectric element because of its high electromechanical coupling factor, high Curie temperature, and low dielectric loss [97]. Research has largely focused on optimising transducer configurations to maximise output intensity. Boucher and Kreuter modified the Langevin configuration with different types of horn geometries to investigate the influence of horn on acoustic output intensity when high power input was used [98]. In 1973, A.P. Hulst developed a symmetric sandwich

transducer prototype for potential applications of welding, drilling, and cleaning [99]. The designed frequency is 15 - 100 kHz, and the maximum output power density is above 40 W/cm^2.

Before this period, most geometry parameters were defined experientially, resulting in challenges in predicting transducer performance. Since the 1980s, advances in finite element analysis (FEA) in solid mechanics have allowed engineers to predict transducer dynamics accurately before manufacturing [100]. The flexibility in the design process accelerated the development of the Langevin transducer. In 1997, Koikel discovered that the contact area between the piezoelectric ring and the end masses influences the resonant frequency in the torsional mode and the pre-stress state [101]. He also explored how both external and internal bolting influence the transducer's electrical properties, including the electromechanical coupling factor. While externally bolted transducers exhibit higher angular velocity at the same current input than internally bolted ones, their lower output torque restricts their application in ultrasonic motors. Therefore, defining the bolt connection and the optimal pre-stress value is crucial. Later, Kazunari, in 1999, published the relationship between transducer dimensions and the pre-stress value applied to the piezoelectric element using an electromechanical finite element model [102].

In the 21st century, fundamental research on the design of Langevin transducers has experienced significant growth. Although no standardised dimensions or geometries have been established for designing Langevin transducers, extensive research has identified key patterns linking geometric parameters, novel structures, and advanced materials to transducer dynamics. Before this time, horns were widely integrated into transducers to enhance mechanical output in high-power applications, particularly in welding [103]. However, most of the horn shapes were stepped, and their design principles were poorly understood. After 2000, numerous studies explored the impact of different horn geometries on transducer dynamics and application performance. Representatively, Baraya and Hossam investigated how horn geometry influences transducer characteristics, including resonant frequency, vibration amplitude, and stress distribution [104]. Their findings indicate that the stepped horn exhibits the highest amplification factor among various geometries but possesses the lowest resonant frequency. However, comparing amplification factors at the same vibration frequency across different transducers is important. The amplification factor and resonant frequency are strongly dependent on transducer dimensions, so the amplification factor is inherently related to resonant frequency. As a result, meaningful comparisons of amplification factors can be made when evaluating transducers operating at identical resonant frequencies, which was the method in [105].

As the use of Langevin transducers continues to grow, significant enhancements in their functionality have been achieved through modifications in configurations. One area of research is to achieve a coupled mode based on a single device. This interest stems from the need for ultrasonic motors, where coupled motion is required to drive the mover continuously, which cannot be achieved by a single vibration mode. For example, in 1994, a torsional-longitudinal ultrasonic motor had been proposed by Shimanuk [106]. In his design, both the torsional and

longitudinal modes of the transducer are excited independently by two piezoelectric stacks with different polarisation directions. By tuning the pre-stress value, the torsional mode's frequency approached that of the longitudinal mode, resulting in a fully coupled mode at a single frequency. Over the years, the development of modal coupling has led to several novel coupled modes based on the fundamental modes of Langevin transducers, which are longitudinal, bending, and torsional modes. Although coupled modes based on two fundamental modes are shown in Table 2.1 with references, several studies were carried out in three-mode coupling [107]. For example, a 3D ultrasonic elliptical vibration transducer was proposed by Kurniawan [107]. By coupling the longitudinal mode to two orthogonal bending modes, 3D elliptical motions were achieved by exciting three independent piezoelectric stacks with typical phase differences, a concept that has been experimentally validated using optical displacement sensors. The micro-grooving results highlighted the excellence of using this coupled mode.

Table 2.1: Coupled modes for Langevin transducers.

	Longitudinal (L)	Bending (B)	Torsional (T)
Longitudinal (L)	-	L-B [23]	L-T [14]
Bending (B)	L-B	B-B [108]	B-T [109]
Torsional (T)	L-T	B-T	-

'-' means not applicable.

Most of the Langevin transducers in the early years had metal materials as end masses. However, in 2018, Wu designed polymer-based Langevin transducers and characterised their resonance properties [110]. All fabricated transducers had identical dimensions but were made from aluminium and different polymers. By operating the polymer-based transducers continuously in their first longitudinal mode, the temperature profile results illustrated that the mechanical losses are maximised at polymer end masses. In contrast, the piezoelectric element experienced the highest losses in the aluminium transducer. The mechanical quality factor of polymer-based transducers was significantly lower than that of the aluminium transducer and was more sensitive to variations in strain. It appears that the polymer-based Langevin transducers underperformed the conventional Langevin transducers. However, this research opens the potential for incorporating advanced materials into the Langevin configuration. As the natural advantages of polymers over metals, especially low density and corrosion resistance, the polymer-based transducers broaden their applications, including lightweight design and use in corrosive environments.

2.2.3 Multi-frequency Langevin Transducers

Multi-frequency transducers operate at multiple resonant frequencies, often characterised by the same vibration mode shape or related mode shapes. Due to their broad applicability, longitudinal modes are favourably tuned in the Langevin transducers, especially the first order. In 1983,

Keisuke Honda patented his work in multi-frequency Langevin transducers [111]. The objective was to address challenges about the crosstalk between adjacent fish boats when they used the same frequency in the sonar system for echolocation within the same area. Consequently, he designed a Langevin transducer capable of operating at multiple resonant frequencies. In his design, three piezoelectric stacks were sandwiched by four metal masses. Later on, this variant of the Langevin transducer was named the cascaded transducer. The resonant frequencies and electrical impedance of this transducer were tuned by exciting the piezoelectric stacks or using different combinations, effectively controlling the short and open states. This pioneering design allows the Langevin transducer to behave multifunctionally and enhances design flexibility.

Following Honda's design, research into the multi-frequency Langevin transducer was inspired. However, several studies have been conducted based on the cascaded transducer, as the configuration and functionality were undervalued. In 1994, M.J. Kim and N. Chubachi manufactured a cascaded transducer featuring three piezoelectric stacks [51]. They characterised the electric properties of the transducer by exploring different combinations of the short and open circuit conditions applied to the stacks. The short/open circuit not only tuned resonant frequency and admittance but also the electromechanical coupling factor and electroacoustic efficiency in the water tank. Subsequently, S. Lin and C. Xu further researched the electric properties and dynamics of a cascaded transducer [112]. They developed an electromechanical model based on the equivalent circuit for simulating the electric responses of the transducer with frequency. Based on this model, resonant frequencies and electromechanical coupling factors were finely tuned by adjusting the radius ratio between end masses under different short/open circuit conditions. This suggested that multi-frequency vibrations with cascaded transducers could be achieved by either separately exciting piezoelectric stacks or tailoring the transducer's dimensions.

Before 2020, there was no significant development on multi-frequency approaches for Langevin transducers and their applications. In 2023, a dual-frequency ultrasonic aspirator based on the cascaded transducer was proposed by Z. Liao et al. [113]. This design aligned broadly with the conventional cascaded configuration, except a horn replaced one end mass to facilitate cavitation. The unique and novel operating method made this design outstanding. Each piezoelectric stack was operated independently and simultaneously with frequencies in different orders of mode shapes, resulting in the transducer vibrating in a coupled dual-frequency mode. Consequently, the output signal of the transducer produced a coupled waveform according to sinusoidal signals at two frequencies. While the authors proposed that the coupled waveform promoted cavitation, no cavitation characterisation or theoretical analysis was presented, underscoring the need for further study. This novel and investigative work expands the possibilities for achieving simultaneous multi-frequency operation in Langevin transducers and has the potential to enhance transducer performance.

2.3 Integration of Ultrasonic Devices with Nitinol

2.3.1 History of Nitinol

Shape memory alloys (SMAs) have a history dating back to the 1930s, when Swedish chemist Arne Ölander first observed the shape memory behaviour in a gold-cadmium (Au-Cd) alloy. This shape memory effect is identified as the martensite transformation, which was first found experimentally by Adolf Martens in the 1890s and then explained by G.V. Kurdjumov based on a thermoelastic phase equilibrium in 1949 [114]. Kurdjumov also predicted that the martensite transformation is reversible in his work [114], a prediction that was confirmed through experiments involving the crystallography of Cu-Al alloys during heating and cooling cycles [115]. During the 1950s to 1960s, the characterisations of martensite transformation were developed in different alloys, representatively Fe-Ni [116, 117] and Cu-Al-Ni [118]. The most significant breakthrough then came in 1962 when William Buehler and his co-workers at the Naval Ordnance Laboratory discovered the extraordinary shape memory effect of nearly equiatomic Nitinol [119], which F. Levis first reported its existence [120]. The Nitinol expresses the shape memory effect by remembering its original shape when heated. Through manipulating the martensite transformation process by temperatures, the material properties, such as thermal expansion and hardness, varied drastically [119, 121]. Additionally, the composition, especially nickel atomic content, influenced the damping behaviours of Nitinol. This discovery of the shape memory effect in Nitinol and the sensitivity of its material properties to temperature sparked the subsequent research on a deeper understanding of Nitinol's phase transformation and thermal behaviours.

Around the 1970s, given the sensitivity of material properties of Nitinol to chemical composition, processing methods, and heat treatments, extensive research had been carried out aiming to correlate material behaviours to manufacturing, thus increasing its repeatability [122]. To assess the phase transformation behaviours of Nitinol, researchers characterised electrical resistance as a function of temperature. The variations in resistance versus temperature curves provided insights into transformation temperatures [122]. This resistance identification was widely used until introducing the commercial DSC [123]. DSC allowed the measurement of the energy required to increase or decrease the temperature of the material, allowing for precise identification of phase transformation behaviours. Numerous studies have been conducted to investigate Nitinol's mechanical properties based on these transformation characteristics. For example, the stress-strain relations of Nitinol in different phases were performed using tensile tests at different temperatures [124]. The results revealed that the austenitic phase of Nitinol can undergo larger strain than conventional metals and return to their original shape upon unloading. This phenomenon was then recognised as superelasticity due to the stress-induced martensite transformation [125]. Additionally, K.N. Melton and O. Mercier investigated the fatigue of Nitinol with different phase transformation temperatures [126]. As M_s decreased, the fatigue limit in-

creased. Because the mechanical tests were conducted at room temperature, specimens with different M_s were in different phases. Therefore, the results correlate the fatigue behaviours with phases of Nitinol.

Since the 1980s, advances in metallurgy and materials science have enabled better control of Nitinol composition, heat treatment, and mechanical properties. With improved understanding of the martensitic and austenitic phases, characterisation has focused on the temperature window between M_F and A_F to capture the full phase transformation. In 1996, J.G. Boyd and D.C. Lagoudas proposed a thermodynamical constitutive model which successfully simulated shape memory effect and superelasticity [127]. The superelasticity paved the way for later research and commercial applications, particularly in medicine, where Nitinol's ability to return to a predetermined shape after deformation proved highly valuable. Between 1980 and 2000, there was an increasing trend in applying Nitinol for biomedical uses, with the research focus being on industrial and military applications. Along with the popularity of Nitinol in biomedical applications, especially stent based on shape memory effect, the biocompatibility and corrosion resistance were extensively studied [128, 129].

Entering the 21^{st} century, the manufacturing and machining of Nitinol has been significantly improved via modern techniques. For example, H. Hou et al. manufactured Nitinol through additive manufacturing [130]. Contrary to conventional additive manufacturing, they discovered that incorporating intermetallic phases within the Ni-Ti matrix, forming nanocomposite structures, enhanced the electrocaloric performance. This unique microstructure resulted in a stress-strain behaviour with minimal hysteresis. This study demonstrates the potential to utilise additive manufacturing for the fabrication of Nitinol with a complex structure and the possibility of tailoring the microstructure in performing certain mechanical behaviours [130]. In manufacturing, the work hardening of Nitinol makes it challenging to be machined in conventional ways, such as milling and turning [131]. Alternatively, advanced machining techniques are suitable in this scenario, including laser cutting, EDM, photo-chemical etching, and water jet cutting [132], achieving high-quality final products with mitigated stress and improved heat dissipation during machining processes. These developments make Nitinol more reliable, versatile, and accessible across multiple industries.

2.3.2 Nitinol Ultrasonic Devices

Throughout the history of Nitinol, limited research has focused on Nitinol ultrasonic transducers. Both shape memory effect and superelasticity could be applied to practical ultrasonic devices, depending on the operating conditions and design purposes for end uses. One of the earliest patented Nitinol ultrasonic devices, developed by Russell Pflueger and colleagues in 1994, involved a Nitinol transmission member equipped with an ultrasonic transducer to perform ultrasonic angioplasty [133]. In their design, the superelasticity of Nitinol was employed to increase the flexibility of the angioplasty device during operation.

The foundation for incorporating Nitinol into ultrasonic devices could date back to the 1990s. Research on the thermodynamic behaviours of Nitinol fibre-reinforced composites suggested that the temperature of Nitinol significantly influences the efficiency of sound wave propagation within the structure [134]. However, it was not within the ultrasonic range. Later, the experiment was extended to the rod-shaped beam, showing changes in Nitinol elastic modulus actively controlled the propagation and frequency of longitudinal wave via varying temperatures [17,18]. From a solid mechanics point of view, the tuning in structural dynamics resulted from changing Nitinol properties, including elastic modulus, density, and Poisson's ratio. These findings form the foundation for later incorporating Nitinol into tuneable ultrasonic devices through the thermodynamic behaviours of Nitinol. It was not until 2000 when the first Nitinol flextensional transducer based on shape memory effect was developed by R.J. Meyer and R.E. Newnham [53]. In their design, two Nitinol end caps sandwiched a piezoelectric plate, bonding via epoxy. The transducer significantly tuned its resonant frequency based on Nitinol phase transformations with temperature compared to a minimal tuneability for transducers with brass and titanium end caps. The results demonstrated that the Nitinol transducer had a frequency increase of 25.5 % from 0 °C to 80 °C, whereas that of the brass and titanium transducers are 7 % and 2 %, respectively. Additionally, based on the shape memory effect, deformation occurred in the martensitic phase under hydrostatic pressure can be recovered by heating the transducer above A_F. This self-recovery capability enhances device reliability in applications.

Following the concept proposed by Meyer and Newnham, A. Feeney investigated the dynamics of cymbal transducers fabricated from Nitinol. Both shape memory and superelastic Nitinol were used in his designs, where the phase transformation temperatures were characterised through DSC. Transducers were fabricated by sandwiching Nitinol end caps with a piezoelectric circular plate. By applying thermal loadings to these transducers, tuneability in resonant frequencies in symmetric or asymmetric modes has been observed compared to cymbal transducers made from conventional metals. Additionally, the phase transformation of Nitinol not only tunes the frequency but also the nonlinear behaviours. However, the piezoelectric element also contributed to changes in non-linearity as responses to temperatures, and it is challenging to decouple the influences between the Nitinol and piezoelectric materials. Integrating Nitinol into a cymbal transducer shows potential for frequency selective ultrasonic scalpels, where low frequency for hard tissue, high for soft.

Recently, in 2022, Y. Song and Y. Shen introduced an innovative meta-surface radar system that enables active steering of ultrasonic waves using Nitinol unit cells [28]. The key concept is to use thermally activated Nitinol-based meta-surfaces to control wave propagation and guide it in specific directions dynamically. Each unit cell of the meta-surface consisted of a Nitinol stub and an aluminium substrate, forming a multiple mass-spring resonator system. The Nitinol's ability to change elastic properties between its low-temperature martensitic and high-temperature austenitic phases under thermal loading resulted in different vibration displacements

among phases, allowing the acoustic wave generated from the central transducer to escape from a desired direction on the meta-surface. The experimental results validated the finite element model and demonstrated that the ultrasonic waves at 68 kHz were steered actively. This study offers a novel method for implementing Nitinol into ultrasonic applications, such as structural health monitoring, where precise control of wave directionality enhances the flexibility in detecting localised damage in the structure.

Chapter 3

Design and Manufacture Principles

The key outcomes shown in this chapter appear in the following publication:
[135] Liu, Y., Nguyen, L.T.K., Li, X., and Feeney, A. (2024) A Timoshenko-Ehrenfest beam model for simulating Langevin transducer dynamics. *Applied Mathematical Modelling*, 131, 363-380.

This chapter initially outlines the conventional Langevin transducer's fundamental design and manufacture principles, including material selection, FEA, manufacturing, and assembly. The following section on mathematical modelling provides a theoretical framework for interpreting the dynamics of the Langevin transducer, mainly its resonant frequency and modal shape, by utilising linear piezoelectricity. A 1D electromechanical model was developed using Timoshenko-Ehrenfest beam theory to reduce the computational time required for simulating transducer dynamics. While the 1D model demonstrates superior performance in terms of time efficiency compared to a 3D model by Abaqus, its accuracy is closely tied to the structure and dimensions of the transducer, which restricts its applicability. Therefore, a 3D model was proposed to simulate transducer dynamics with more complicated structures. Furthermore, considering that the functionality of Nitinol Langevin transducers relies significantly on temperature influences on Nitinol elastic properties, the following sections describe experimental characterisations for conventional Langevin transducers while considering thermal loadings. Both electrical and physical measurements were employed to assess the dynamics under static or changing voltages and temperatures. Based on the methodology detailed above, the final section provides considerations on design, manufacturing, and experiments for achieving Nitinol Langevin transducers with tuneable dynamics with temperature.

3.1 Design for Conventional Langevin Transducers

In Chapter 1, the structure of the Langevin transducer, comprising the front mass, back mass, PZT stack, and central pre-stress bolt, is described. The choice of materials and their dimensions have a significant impact on the dynamics of the transducer. This section details the fundamental approach for constructing a conventional Langevin transducer, including material selection, dimension design, manufacturing, and related theoretical backgrounds. The structure of the Nitinol Langevin transducer developed in this thesis adheres to these established principles for conventional Langevin transducers while also taking into account the phase transformation behaviours of Nitinol. As a result, these fundamental approaches provides a basic framework for designing and fabricating Langevin transducers that incorporate SMAs, particularly Nitinol.

3.1.1 Material Selection

The material properties significantly influence a transducer's mechanical and acoustical performance. Material selection is, therefore, closely related to the desired transducer dynamics and intended applications. Additionally, given the broad family of piezoelectric materials available, selecting the appropriate ones to align with actuation requirements and dynamic considerations necessitates thorough discussion. This section explained the material choices for end masses and piezoelectric materials in power ultrasonic applications. In the design of a Nitinol Langevin transducer, although the influence of changing temperature on material properties is acknowledged, the initial transducer design is based on the properties of Nitinol at a constant temperature. In this scenario, the initial selection of Nitinol aligns with the material selection framework discussed in this section. Subsequent investigations on transducers are required concerning tuneable resonance as variations of material properties to temperature.

3.1.1.1 End Mass Materials

The resonance characteristics of the Langevin transducer heavily rely on the materials and dimensions of its constituent parts, especially piezoelectric materials [136]. This dependency arises not only from the dynamic stress-strain relationship within the framework of linear elasticity but also from the acoustic properties. Acoustic impedance, for example, is an acoustic parameter reflecting a material's ability to impede acoustic wave propagation through the material [137]. It can be expressed by either density and acoustic velocity or density and Young's modulus, from a physical or mechanical standpoint, respectively:

$$\begin{aligned} Z_A &= \rho \cdot c \qquad (physical) \\ Z_A &= \sqrt{\rho \cdot E} \qquad (mechanical) \end{aligned} \tag{3.1}$$

where Z_A is acoustic impedance, ρ is density, c is acoustic velocity, and E is Young's modulus. In the Langevin configuration, the acoustic impedance of two connected components should be matched to efficiently transmit acoustic energy from one component to another. This matching could be determined by achieving a minimum acoustic reflection [138], which is given:

$$\Gamma = (Z_A^{[2]} - Z_A^{[1]})/(Z_A^{[1]} + Z_A^{[2]}) \tag{3.2}$$

where the acoustic wave flows from component 2 to component 1. If there is a mismatch between components, their interface, typically perpendicular to the acoustic pressure gradient in the conventional Langevin configuration, will significantly reflect acoustic energy. Therefore, mismatched acoustic impedance leads to resistance against material vibrations induced by sound waves. To this end, the materials for the front and back masses are selected, ensuring acoustic impedance matching. Values of acoustic impedance for metal and piezoelectric materials used are provided in Table 3.1.

Table 3.1: Acoustic impedances of metal and piezoelectric materials used in this study.

Material	Acoustic impedance (Pa·s/m^3)
Aluminium alloy (6082)	16.57e6 [139]
Titanium alloy (Ti6Al4V)	25.694e6 [140]
Stainless steel 304	45.45e6 [141]
Copper	42.39e6 [141]
PIC181	36.1e6 [142]
PZ26	32.3e6 [143]

**Throughout this thesis, aluminium and titanium refer to their respective alloys.*

In power ultrasonics, the aim is to maximise the mechanical output at the working tip, typically the end face of the transducer or sonotrode. Achieving this involves employing a gradient of acoustic impedance across structure [144] or incorporating matching layers [137]. For instance, an impedance gradient is achieved using aluminium and stainless steel as the materials for the front and back masses, respectively. This material selection results in a gradual decrease in acoustic impedance from the back mass to the piezoelectric stacks and the front mass. Consequently, this configuration enhances the acoustic energy transmitted to the front mass, producing higher amplitudes at the working tip. Titanium is used when the front mass or the sonotrode reciprocates against the workpiece. It provides superior wear resistance, excellent biocompatibility, and a high mechanical quality factor. The trade-off is lower output amplitude than aluminium.

Stainless steel, titanium, and aluminium are frequently selected as end masses for Langevin transducers not just because of their affordability but also due to the ease of manufacturing and the inherent low mechanical losses associated with these metals, which contribute to a high mechanical quality factor (Q) value in the final transducer product. Mechanical losses of material also indicate the energy lost in deformation, and this loss is converted into heat, leading to a tem-

perature increase. However, this amount of heat is generally negligible for metals manufactured using conventional methods considering their high Q values.

When the temperature of the metal components in a transducer is increased, the heat typically originates from ambient temperature and dielectric heating from piezoelectric materials. Therefore, the properties of selected materials, including elastic modulus, density, and Poisson's ratio, are expected not significantly to change with increased temperature, thus consistent dynamics while operating. However, Nitinol is an exception because its temperature-dependent properties are concerned with tuneable resonance in the transducer.

3.1.1.2 Piezoelectric Materials

The typical choice for the piezoelectric material in the Langevin transducer is hard PZT, which the Navy Type classifies as US military standard MIL-STD-1376B. The hard PZT is renowned for its low dielectric loss and high Q, which enhances power transfer efficiency from electrical to mechanical energy. However, the narrow half-power bandwidth increases the dynamic sensitivity, making it unsuitable for off-resonance applications like sensing systems. In this study, normal commercial hard PZT such as PIC181 (PI Ceramic GmbH, Germany) and PZ26 (CTS Corporation, Ferroperm Piezoceramics, USA) have been used, which are selected for their proven high figure of merit (FOM) [145], as shown in Figure 3.1.

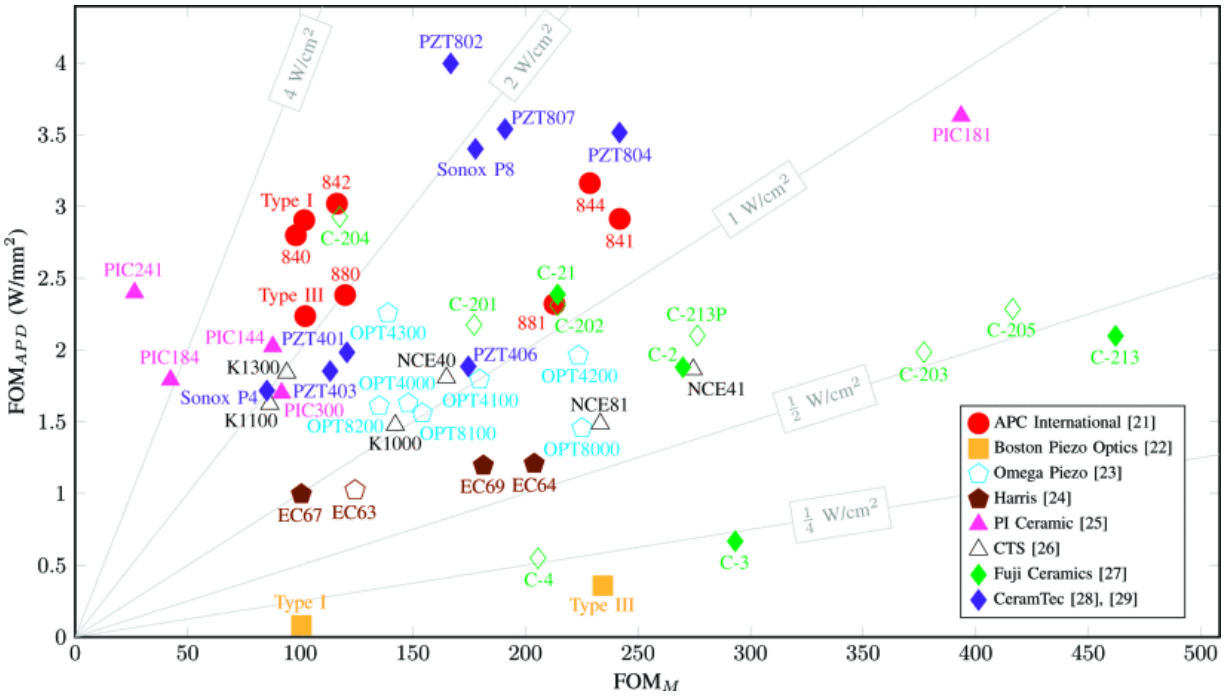

Figure 3.1: Comparison of hard PZT materials for power conversion based on volumetric power density FOM (FOM$_{APD}$) versus mechanical efficiency FOM (FOM$_M$) [145] (reprinted from 2020 IEEE 21st Workshop on Control and Modeling for Power Electronics, Copyright © 2020 IEEE).

Although PZ26 is not shown in Figure 3.1, its properties closely match CTS NCE41, indicat-

ing comparable high power performance. Together with PIC181, both deliver high volumetric power density and mechanical efficiency for power ultrasonic applications. The choice of PZT materials in a ring configuration ensured compatibility with the Langevin assembly, featuring an outer diameter identical to that of the front and back masses and an inner diameter larger than that of the central bolt.

Loss factors are important for selecting proper piezoelectric materials. In high-power applications, the temperature increases drastically in the piezoelectric segments during operation as the internal losses, including mechanical, dielectric, and coupling losses. If the segments are over the Curie temperature, the materials lose their polarisation and degrade transducer output. Therefore, the transducer's design should ensure that the piezoelectric material's maximum temperature is much lower than the Curie temperature and that the material has low loss factors or high Q. However, the magnitude of temperature increases is challenging to be predicted and simulated in the transducer design stage. Estimating heat generation relies on the electrical impedance of the transducer. However, variations in mechanical machining and assembly can lead to inaccuracies in predicting impedance. Therefore, piezoelectric materials with high Curie temperatures are preferred, reducing the chance of operation failure.

3.1.2 Finite Element Analysis

Abaqus, a FEA software by Dassault Systèmes, has been utilised in this study to adjust the dimensions of segments, ensuring that a typical mode shape vibrates at a required frequency. For instance, the first longitudinal mode of a bar-shaped transducer is commonly employed in applications, with its resonant frequency as a function of the structural length-to-diameter (L/D) ratio, a term in civil engineering to describe a bar structure [146]. By modifying the L/D ratio appropriately, the resonant frequency of the first longitudinal mode can be tailored to the expected value. Moreover, the flange is placed at the nodal plane (zero amplitude plane) so it can be clamped rigidly with minimal mechanical energy loss. It is crucial to position the PZT stack at or near the nodal plane to minimise strain and losses. The mechanical gain of the horn set ratio of tip displacement to stack displacement, then maximising output amplitude. The total gain, a product of the transducer mechanical gain and sonotrode gain defines the capability of generating high vibration amplitude. The FEA process is the identical for a transducer, whether it includes a sonotrode or not, as illustrated in Figure 3.2.

An approach in designing the electromechanical model in FEA involves considering the coupling between mechanical and electrical fields when applying electric potentials to the PZT material, owing to its linear piezoelectricity [147, 148]. However, practical challenges arise in obtaining the electrical properties of the PZT material due to changes in polarisation at high voltages. Furthermore, high excitation inputs generate parasitic dielectric losses [149], leading to a temperature rise in PZT stacks, which alters the material modulus and permittivity and, therefore, resonant frequencies. The involvement of the temperature field is also a concern when

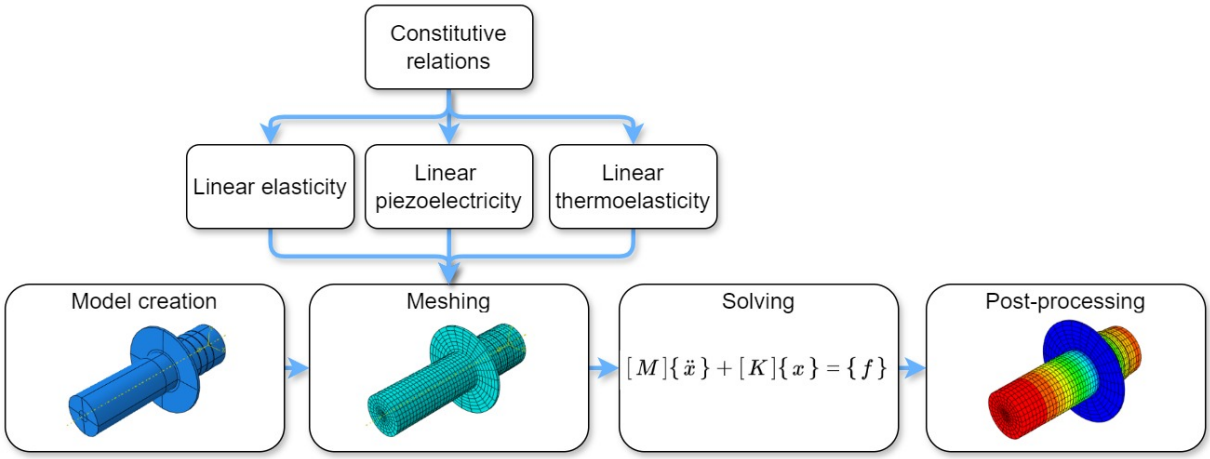

Figure 3.2: Linear FEA process of an ultrasonic transducer as per solid mechanics in Abaqus.

designing the Nitinol Langevin transducer, as the tuneable resonance behaviours are achieved through the applied heat on the Nitinol segment, inducing the martensitic transformation. Hence, it is preferred to initially design a purely mechanical model to determine the expected resonant frequency in a typical mode rather than an electromechanical one. Once the resonant frequency range and mode shape are defined, the optimisation process involves the electrical field, which is necessary as it alters effect stiffness matrix. The mechanical model tackles an eigenfrequency problem based on linear elasticity, with the elastic modulus, density, and Poisson's ratio being the key properties in FEA for tuning the resonance. However, the predefined and rigid calculation procedure limits the flexibility in creating FEA models through commercial software. To address this, mathematical models by the finite element method (FEM) in linear piezoelectricity were explored in Section 3.2. These models provide the flexibility to customise them from the basic constitutive laws and enable a comprehensive understanding of the problem theoretically.

3.1.3 Transducer Fabrication

Once the materials and dimensions of the segments are determined, conventional machining methods, such as turning and milling, are typically employed for fabrication when dealing with standard metals with straightforward configurations. However, in cases where the configuration is intricate, additive manufacturing becomes an alternative option [150]. For instance, direct metal laser sintering was suggested for producing the Ti-6Al-4V front masses, one featuring a conical taper with helical slots, while the other is planar twice folded [29]. The direct metal laser sintering is a powder fusion process in which a laser melts metal powder layer by layer. Benefits include manufacture of complex features, precise mass and stiffness tuning, and reduced machining and waste.

Although additive manufacturing addresses the challenges in complex geometries, the formation of imperfections between fabricated layers leads to fatigue failures under high-frequency cyclic loadings. Other advanced manufacturing methods like electrochemical machining (ECM)

and EDM offer non-contact precision shaping of hard-to-machine metals, such as Nitinol, with good surface finish. The Nitinol manufacturing discussion is detailed later in Section 3.4.2.

3.1.4 Transducer Assembly

Following fabrication, a central pre-stress bolt securely fastens the transducer segments and PZT stacks. Two primary methods for assembling the Langevin transducer based on different measuring techniques have been proposed: applying constant torque to the central bolt [151,152] or applying constant stress [153] to the PZT materials.

Constant torque: When employing constant torque, changes in the dimensions and polarisation of the PZT due to induced strain influence the resonance properties, including resonant frequency and electrical impedance. As torque values increase, resonance and impedance change until reaching a converged value at an optimal torque. However, deviations may occur if the bolt thread is damaged or lubricated, resulting in applied torque differing from the calculated value. Hence, ensuring high-quality bolt and front mass threading is necessary when utilising this method.

Constant stress: Alternatively, to apply constant stress to the PZT stack, the charge generated during the pre-stress process is measured. Based on Maxwell's equation in dielectric displacement, the generated charge can be converted into stress through the piezoelectric constants. However, applying stress to the PZT changes the induced strain, affecting polarisation and consequently impacting the piezoelectric constants [154]. This underscores the dependency of piezoelectric constants on stress, potentially misleading the final stress results when there is a limitation in obtaining the piezoelectric constants under different stresses.

3.2 Mathematical Modelling

Mathematical modelling has several advantages over employing finite element software based on Langevin transducer dynamics. First, the modelling process and results provide an in-depth understanding of the dynamic behaviours of the Langevin transducer. Furthermore, it allows for enhanced flexibility in modifying the Langevin model at the constitutive law level. This section explores the mathematical models for the Langevin transducer, which form the basis for simulating the Nitinol Langevin transducer in the electromechanical problem.

Here, the 1D model is presented firstly based on the Timoshenko-Ehrenfest beam theory, a reduced form of the 3D theory. The motivation for developing the 1D model lies in its reduced time costs for simulations over the FEA software and the degradation dimensions of material properties, particularly for the Nitinol Langevin transducer when addressing temperature-dependent problems. The 1D model eliminates the need to characterise Nitinol and PZT material properties concerning temperature in 3D space, simplifying the material characterisation

process. However, low accuracy can arise naturally due to the reduced theory regarding the dimensions of transducers. Therefore, a followed 3D model is developed to analyse the dynamics of Nitinol Langevin transducers with intricate configurations under customised boundary conditions.

3.2.1 Voigt Notation

The Voigt notation is a useful tool where the order of symmetric tensors in engineering problems is reduced. For example, the Cauchy stress tensor σ and the linear strain tensor ε in solid mechanics can be described according to the Hooke's law as given:

$$\sigma = \mathbb{C} : \varepsilon \tag{3.3}$$

where $\mathbb{C}$ is the stiffness tensor. The double dot denotes the double contraction between two tensors. In a Cartesian coordinate system, such as (x, y, z), the stress and strain tensors are expressed as:

$$\sigma = \begin{bmatrix} \sigma_{xx} & \sigma_{xy} & \sigma_{xz} \\ \sigma_{yx} & \sigma_{yy} & \sigma_{yz} \\ \sigma_{zx} & \sigma_{zy} & \sigma_{zz} \end{bmatrix}, \quad \varepsilon = \begin{bmatrix} \varepsilon_{xx} & \varepsilon_{xy} & \varepsilon_{xz} \\ \varepsilon_{yx} & \varepsilon_{yy} & \varepsilon_{yz} \\ \varepsilon_{zx} & \varepsilon_{zy} & \varepsilon_{zz} \end{bmatrix} \tag{3.4}$$

Due to the inherent symmetry of material stiffness tensor $\mathbb{C}$, the stress and strain tensors are symmetric as $\sigma_{ij} = \sigma_{ji}$ and $\varepsilon_{ij} = \varepsilon_{ji}$, where $i, j = 1, 2, 3$. Then, σ and ε can be reduced into vectors by using Voigt notation, as given:

$$\begin{aligned} \hat{\sigma} &= \begin{bmatrix} \sigma_{xx} & \sigma_{yy} & \sigma_{zz} & \sigma_{yz} & \sigma_{xz} & \sigma_{xy} \end{bmatrix}^{\mathrm{T}} := \begin{bmatrix} \sigma_1 & \sigma_2 & \sigma_3 & \sigma_4 & \sigma_5 & \sigma_6 \end{bmatrix}^{\mathrm{T}} \\ \hat{\varepsilon} &= \begin{bmatrix} \varepsilon_{xx} & \varepsilon_{yy} & \varepsilon_{zz} & \varepsilon_{yz} & \varepsilon_{xz} & \varepsilon_{xy} \end{bmatrix}^{\mathrm{T}} := \begin{bmatrix} \varepsilon_1 & \varepsilon_2 & \varepsilon_3 & \varepsilon_4 & \varepsilon_5 & \varepsilon_6 \end{bmatrix}^{\mathrm{T}} \end{aligned} \tag{3.5}$$

Throughout Section 3.2, the Voigt notation has been employed to implement anisotropic material property tensors in the constitutive laws, resulting in computational flexibility. It is convenient to suppress the hat in the vectors in the form of $\sigma := \hat{\sigma}$ and $\varepsilon := \hat{\varepsilon}$, as the scalar invariance $\sigma \cdot \varepsilon = \hat{\sigma} \cdot \hat{\varepsilon}$.

3.2.2 Constitutive Equations

3.2.2.1 Linear Elasticity

The constitutive equations are derived from the physical fields of the problem and the intrinsic characteristics of the materials involved. For example, metals and piezoelectric materials are primarily constructed the Langevin configuration, which can be further grouped into homogeneous elastic materials and transversely isotropic piezoelectric materials, respectively. The

stress-strain relationship of homogeneous elastic materials is described using linear elasticity, while linear piezoelectricity characterises piezoelectric materials. This section focuses on discussing the constitutive equation of linear elasticity, which is based on Hooke's law for continuous elastic materials, as given in (3.6), where $\mathbf{u}\nabla = (\nabla\mathbf{u})^{\mathrm{T}}$. In this equation, the linear strain tensor is defined as a gradient of the displacement vector field $\mathbf{u}$, according to:

$$\varepsilon = \frac{1}{2}(\nabla\mathbf{u} + \mathbf{u}\nabla) \tag{3.6}$$

When the material is a homogeneous material, such as stainless steel, titanium, and aluminium which are used in this study, the constitutive law can be rewritten as:

$$\sigma = 2\mu\varepsilon + \lambda\mathbf{tr}(\varepsilon)\mathbf{I} \tag{3.7}$$

where $\mathbf{tr}(\cdot)$ is the trace function of a matrix, and the $\mathbf{I}$ is the identity matrix. λ and μ are the first and second Lamé parameters, respectively, and are given by:

$$\begin{aligned} \lambda &= \frac{E\nu}{(1+\nu)(1-2\nu)} \\ \mu &= \frac{E}{2(1+\nu)} \end{aligned} \tag{3.8}$$

where E and ν are Young's modulus and Poisson's ratio for isotropic materials.

As the energy method is adopted in this study, the entropy energy describes deformations of homogeneous materials, where the elastic strain energy density is considered:

$$\psi(\varepsilon) = \mu\varepsilon : \varepsilon + \frac{1}{2}\lambda(\mathbf{tr}(\varepsilon))^2 \tag{3.9}$$

Then, the constitutive law has been given in (3.3) is obtained by considering the following:

$$\sigma = \frac{\partial\psi}{\partial\varepsilon} \tag{3.10}$$

3.2.2.2 Linear Piezoelectricity

To allow a comprehensive overview of the problem, an account of the basic theory of piezoelectric materials relevant to this research is provided here, which adheres to the IEEE Standard on Piezoelectricity [155]. In this theory, there are four distinguishable forms of constitutive relationships, comprising Stress-Charge; Stress-Voltage; Strain-Charge; and Strain-Voltage, with regards to input variables and their corresponding outputs, as detailed in Table 3.2. In this table, the $\mathbf{E}$ and $\mathbf{D}$ denote the vector electric field and the induced electric displacement vector field, respectively. The electric field is defined as a gradient of the electric potential field ϕ, according to:

$$\mathbf{E} = -\nabla\phi \tag{3.11}$$

Table 3.2: Four forms of constitutive relationships relevant to this study.

Form	Constitutive relationship
Stress-Charge	$(\varepsilon, \mathbf{E}) \xrightarrow{\mathbb{C}_{\mathbf{E}=0}, \chi_{\varepsilon=0}} (\sigma, \mathbf{D})$
Strain-Charge	$(\sigma, \mathbf{E}) \xrightarrow{\mathbb{S}_{\mathbf{E}=0}, \chi_{\sigma=0}} (\varepsilon, \mathbf{D})$
Stress-Voltage	$(\varepsilon, \mathbf{D}) \xrightarrow{\mathbb{C}_{\mathbf{D}=0}, \chi^{-1}_{\varepsilon=0}} (\sigma, \mathbf{E})$
Strain-Voltage	$(\sigma, \mathbf{D}) \xrightarrow{\mathbb{S}_{\mathbf{D}=0}, \chi^{-1}_{\sigma=0}} (\varepsilon, \mathbf{E})$

For comparison with the experimental setup described in Section 3.2.3.15, the constitutive law in Stress-Charge form is employed, given as follows:

$$\begin{aligned} \sigma &= \mathbb{C}_{\mathbf{E}=0} : \varepsilon - \mathbf{e}^T \cdot \mathbf{E} \\ \mathbf{D} &= \mathbf{e} : \varepsilon + \chi_{\varepsilon=0} \cdot \mathbf{E} \end{aligned} \tag{3.12}$$

The tensors of the constitutive coefficients in this constitutive relation are explained as follows. The fourth-order tensor $\mathbb{C}_{\mathbf{E}=0}$ is the elastic stiffness obtained in the absence of an electric field ($\mathbf{E} = 0$). The second-order tensor $\chi_{\varepsilon=0}$ is the electric permittivity tensor obtained in the absence of mechanical strain ($\varepsilon = 0$). The third-order tensor $\mathbf{e}$ is the piezoelectric coupling coefficient for the Stress-Charge form. The single dot denotes the dot product between two tensors. It is convenient to suppress the subscripts in the tensors of material properties and thus the following can be written: $\mathbb{C} := \mathbb{C}_{\mathbf{E}=0}$, $\chi := \chi_{\varepsilon=0}$.

On the other hand, the material properties for PIC181 provided from the manufacturer specifications correspond to the constitutive law in the Strain-Charge form:

$$\begin{aligned} \varepsilon &= \mathbb{S}_{\mathbf{E}=0} : \sigma + \mathbf{d}^T \cdot \mathbf{E} \\ \mathbf{D} &= \mathbf{d} : \sigma + \gamma_{\sigma=0} \cdot \mathbf{E} \end{aligned} \tag{3.13}$$

In this constitutive formulation, $\mathbb{S}_{\mathbf{E}=0}$ is the compliance stiffness in the absence of the electric field ($\mathbf{E} = 0$), $\gamma_{\sigma=0}$ is the electric permittivity in the absence of mechanical stress ($\sigma = 0$), and $\mathbf{d}$ denotes the piezoelectric coupling coefficients for the Strain-Charge form. Again, the shorthand $\mathbb{S} := \mathbb{S}_{\mathbf{E}=0}$ and $\gamma := \gamma_{\sigma=0}$ can be used. Comparing (3.13) with (3.12), one can readily derive:

$$\mathbb{C} = \mathbb{S}^{-1}, \quad \mathbf{e} = \mathbf{d} : \mathbb{S}^{-1}, \quad \chi = \gamma - \mathbf{d} \cdot \mathbb{S}^{-1} \cdot \mathbf{d}^T \tag{3.14}$$

where $\mathbb{S}^{-1}$ represents the inverse of the fourth-order tensor of $\mathbb{S}$.

Just as for hyperelastic materials, the constitutive law in (3.12) can be derived as partial derivative of an enthalpy density function. It is given by:

$$\psi(\varepsilon, \mathbf{E}) = \frac{1}{2}\varepsilon : \mathbb{C} : \varepsilon - \mathbf{E} \cdot \mathbf{e} : \varepsilon - \frac{1}{2}\mathbf{E} \cdot \chi \cdot \mathbf{E} \tag{3.15}$$

The constitutive relation (3.12) can be obtained by identifying:

$$\sigma = \frac{\partial \psi}{\partial \varepsilon}, \quad \mathbf{D} = -\frac{\partial \psi}{\partial \mathbf{E}} \tag{3.16}$$

Here, by considering (3.12), the enthalpy density function can be rewritten as follows:

$$\psi = \frac{1}{2}(\varepsilon : \sigma - \mathbf{E} \cdot \mathbf{D}) \tag{3.17}$$

3.2.3 Development of the 1D Electromechanical Model

Longitudinal and bending modes are commonly employed modal shapes in Langevin transducers. To develop a numerically effective tool for simulating the dynamics of the Langevin transducer considering longitudinal and bending modes, a 1D Timoshenko-Ehrenfest beam model is proposed as a reduction of the full 3D model. It is important to note that this beam consists of several segments made of three different materials, two of which can be modelled as isotropic elastic materials and the other as a transversely isotropic piezoelectric material. These segment structures are generalised as a solid beam with a circular cross-section, a solid beam with an annular cross-section, and a composite beam with a combination of circular and annular cross-sections.

3.2.3.1 Configuration of the Langevin Transducer

The Langevin transducer utilised for this section is a cylindrical configuration without a horn-type sonotrode, as shown in Figure 3.3, showing the transducer's front mass, a back mass, a PZT stack with electrodes, and a pre-stress bolt. The electrodes are orders of magnitude thinner than the PZT rings and the front and back masses, and contribute an insignificant effect on the transducer dynamics. Therefore, this section does not consider them to reduce the calculation complexity and computation time. In response to this assumption, the PZT stack is designed as a homogeneous hollow cylinder made of piezoelectric materials in the modelling (see Figure 3.3).

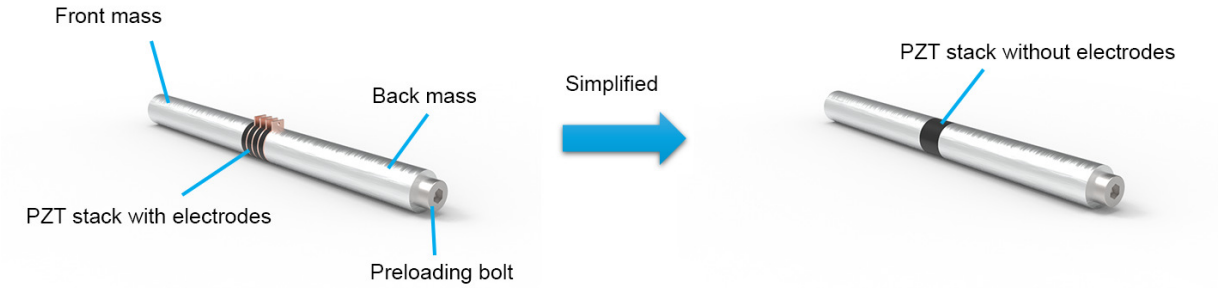

Figure 3.3: The cylindrical Langevin transducer of the form used in this study.

Each part of the Langevin transducer can be simplified into a straight beam due to its axial symmetry. It will be demonstrated later in this section that the transducer can be split into five different beam segments, each of which can be effectively modelled by a composite beam made of two orthotropic piezoelectric materials with poling directions along the symmetric axis, or the beam axis.

3.2.3.2 Problem Definition

The transducer with the configuration as shown in Figure 3.3 can be modelled using five different beam segments with different geometries and different materials, yielding a practically representative case. In this section, the geometries and materials of these segments are described in detail.

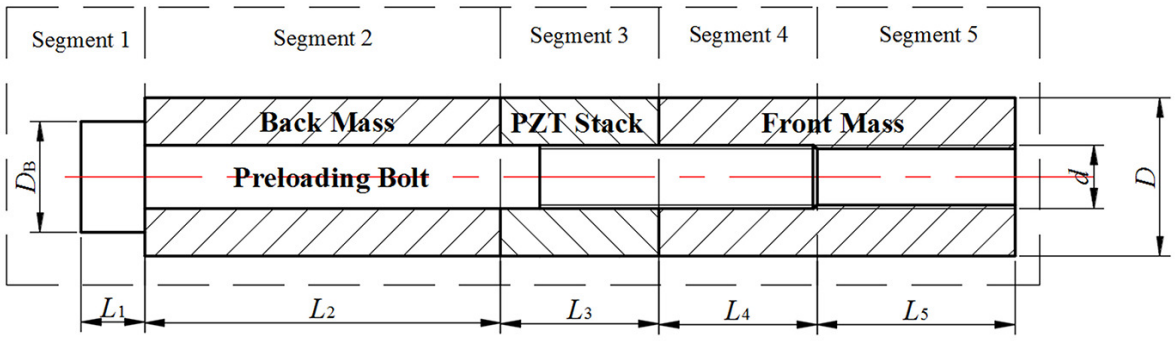

Figure 3.4: Configuration of the Langevin transducer with respect to different segments.

First, from Figure 3.4 the dimensions of each component in one beam segment can be readily identified. For example, the j^{th} segment, denoted as S_j, has the length l_j for all $j = \overline{1,5}$. The bolt contains the bolt head as a cylinder with the diameter D_B and the bolt screw as a cylinder with the diameter d. The back mass, the PZT stack, and the front mass are all hollow cylinders with annulus-type cross sections. They share the same outer diameter D and the same inner diameter d and connect to each other to make up one full hollow cylinder. Since this hollow cylinder is longer than the bolt screw, the entire transducer must be divided into five beam segments to enable accurate numerical modelling.

The bolt, including the bolt head and bolt screw, is made of A2 tool steel. The back mass and the front mass are made of titanium Ti6Al4V. The PZT stack is made of PIC181, following the standard specification of the manufacturer. The properties of these materials has been given in detail in Appendix A.

3.2.3.3 Variational Framework

As the poling of the PZT material is in the direction of the beam axis, the axial displacement of the beam cross-section must also be considered. It is important to note that this is different from

the classical Timoshenko beam theory, which normally only considers the bending [156, 157]. Let us assume that the beam axis is in the z-direction and the beam cross-section is the xy-plane. The starting point here is the assumption of the displacement field $\mathbf{u} = (u_1, u_2, u_3)$ of the material in the beam as follows:

$$\begin{aligned} u_1(x,y,z,t) &= 0 \\ u_2(x,y,z,t) &= w(z,t) \\ u_3(x,y,z,t) &= u(z,t) - y\varphi(z,t) \end{aligned} \tag{3.18}$$

where u_1, u_2, u_3 are the components of the displacement vector $\mathbf{u}$ in the three coordinate directions, u is the axial displacement of the cross-section, φ is the angle of rotation of the normal to the cross-section surface, and w is the deflection of the neutral axis in the z-direction. According to this, the strain field is given by revisiting (3.6):

$$\varepsilon = \frac{1}{2}(\nabla\mathbf{u} + \mathbf{u}\nabla) = \begin{bmatrix} 0 & 0 & 0 \\ 0 & 0 & \frac{1}{2}(w_{,z} - \varphi) \\ 0 & \frac{1}{2}(w_{,z} - \varphi) & u_{,z} - y\varphi_{,z} \end{bmatrix} \tag{3.19}$$

Therefore, the non-zero components of the strain field ε are ε_{23}, ε_{32}, and ε_{33}.

3.2.3.4 Reduction of the 3D Constitutive Law to 1D

To derive the variational formulation for the beam model of transducer, the 1D reduction of the aforementioned 3D laws is required. By using the Voigt notation following the IEEE Standard [155], the tensors of material properties in (3.12) can be represented as matrices. In particular, the elastic tensor and the piezoelectric coupling tensor are given as matrices $\mathbb{C} \in \mathbb{R}^{6\times6}$, $\mathbf{e} \in \mathbb{R}^{3\times6}$ and $\chi \in \mathbb{R}^{3\times3}$.

In general, reduction of the 3D constitutive law (3.12) to the lower-dimensional law also depends on the electric field, because the non-zero components of $\mathbf{E}$ can influence the form of the reduced law. In this work, the electric potential field is applied along the beam axis direction so that $E_3 \neq 0$ is the only non-zero component. Following this assumption, the non-zero stress and electric displacement components can be derived as follows:

$$\sigma_{33} = C_{33}\varepsilon_{33} - e_{33}E_3, \quad \sigma_{23} = 2\kappa C_{23}\varepsilon_{23}, \quad D_3 = e_{33}\varepsilon_{33} + \chi_{33}E_3 \tag{3.20}$$

where κ is the shear correction coefficient [158, 159]. As for the computation, the shear correction coefficient for a circular cross-section is employed:

$$\kappa_{\text{circular}} = \frac{6(1+\nu)}{7+6\nu} \tag{3.21}$$

and this can also be applied for an annular cross-section:

$$\kappa_{\text{annular}} = \frac{6(1+\nu)(1+\alpha^2)^2}{(7+6\nu)(1+\alpha^2)^2+(20+12\nu)\alpha^2}, \quad \alpha = \frac{d_{\text{o}}}{d_{\text{i}}} \tag{3.22}$$

where d_{i} and d_{o} are the inner and outer diameters of the annulus. The material constants appearing in (3.20) are obtained using the relation (3.14) and the material properties provided by PI Ceramic GmbH. Then, only the relevant material constants are used. One important point to note here is that for isotropic elastic materials, only $\sigma_{33} = C_{33}\varepsilon_{33}$ and $\sigma_{23} = 2\kappa C_{23}\varepsilon_{23}$ are required.

Therefore, consistent with the 1D law (3.20), the enthalpy density function reduces to the 1D version:

$$\psi_{1\text{D}}(\varepsilon, \mathbf{E}) = \frac{1}{2}(\sigma_{33}\varepsilon_{33} + 2\sigma_{23}\varepsilon_{23}) - \frac{1}{2}D_3E_3 \tag{3.23}$$

3.2.3.5 Derivation of the Equations of Motion

The variational equation for a beam segment made of transversely isotropic piezoelectric materials is derived, from where the equations of motion for the Langevin transducer can then be derived. In particular, the beam geometry is described by a cylinder assumed to be ideally bonded with a right circular hollow cylinder, or a cylindrical shell. These two cylinders are made of two different piezoelectric materials with poling in the z-direction. Although no beam segment in the simulated transducer has the above-mentioned material and geometrical description, the derivation can still be applicable to all five beam segments for two reasons:

1. The constitutive model for an isotropic elastic material can be specified as the reduced model for a transversely isotropic piezoelectric material.

2. A composite beam with the cylinder perfectly bonded with a right circular hollow cylinder, or a cylindrical shell, is a generalisation of the homogeneous cylinder beam.

The geometrical and material setup for five beam segments are shown in Figure 3.5. For the above reasons, the variational equation for a homogeneous beam of isotropic elastic material or a composite beam of elastic and piezoelectric materials has been incorporated in the subsequent derivation.

3.2.3.6 Total stored and kinetic energies

First, the formulation for one beam segment can be detailed. Let the coordinates of the two ends of the beam segment be $z = a$ on the left and $z = b$ on the right $(a < b)$. Then, the total stored

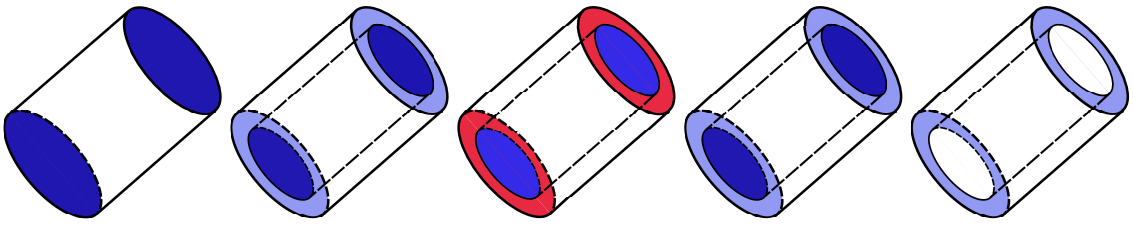

(a) (b) (c) (d) (e)

Figure 3.5: Geometrical and material definitions for the five beam segments representing the entire Langevin transducer, where the colours on the cross-sections designate the following: (1) dark blue for steel; (2) light blue for titanium; and (3) red for PIC181, showing (a) Segment 1: Cylinder made of isotropic elastic material, (b) Segment 2: Cylinder wrapped by a hollow cylinder made of two different isotropic elastic materials, (c) Segment 3: Cylinder made of isotropic material wrapped by hollow cylinder made of transversely isotropic piezoelectric material, (d) Segment 4: Cylinder wrapped by a hollow cylinder made of two different isotropic elastic materials, and (e) Segment 5: Hollow cylinder composed of isotropic material.

energy of the beam is given by:

$$\begin{aligned} W &= \int_a^b \int_A \frac{1}{2}(\sigma_{33}\varepsilon_{33} + 2\sigma_{23}\varepsilon_{23} - D_3E_3)\mathrm{d}A\mathrm{d}z \\ &= \int_a^b \int_A \frac{1}{2}(C_{33}\varepsilon_{33}^2 - 2e_{33}E_3\varepsilon_{33} + 4\kappa C_{23}\varepsilon_{23}^2 - \chi_{33}E_3^2)\mathrm{d}A\mathrm{d}z \end{aligned} \tag{3.24}$$

where A denote the cross-section area of the beam segment. The total stored energy W is a functional of the functions u, w, φ and ϕ, or alternatively expressed as $W = W[u, w, \varphi, \phi]$, by recalling that:

$$\varepsilon_{23} = (w_{,z} - \varphi)/2, \quad \varepsilon_{33} = u_{,z} - y\varphi_{,z}, \quad E_3 = -\phi_{,z} \tag{3.25}$$

Substituting (3.25) into (3.24), it can be shown that:

$$\begin{aligned} W = \int_a^b \int_A \Bigg[&\frac{1}{2}C_{33}(u_{,z}^2 + y^2\varphi_{,z}^2) + e_{33}u_{,z}\phi_{,z} \\ &+ \frac{1}{2}\kappa C_{23}(w_{,z}^2 - 2w_{,z}\varphi + \varphi^2) - \frac{1}{2}\chi_{33}\phi_{,z}^2 \Bigg] \mathrm{d}A\mathrm{d}z \end{aligned} \tag{3.26}$$

where the following identity has been taken into account:

$$\int_A y\mathrm{d}A = 0 \tag{3.27}$$

Note that equation (3.27) is valid because the neutral axis is across the centre of the circular cross-section. If the cross-section is not a disk, the property (3.27) is not always true because a composite beam which is being studied is made of two out of three different materials (see,

e.g., [160]). The kinetic energy for the beam segment is given by:

$$\begin{aligned} T &= \int_a^b \int_A \frac{1}{2}\rho \sum_{i=1}^{3} u_{i,t}^2 \mathrm{d}A\mathrm{d}z = \int_a^b \int_A \frac{1}{2}\rho \left[w_{,t}^2 + (u_{,t} - y\varphi_{,t})^2\right] \mathrm{d}A\mathrm{d}z \\ &= \int_a^b \int_A \frac{1}{2}\rho (w_{,t}^2 + u_{,t}^2 + y^2\varphi_{,t}^2) \mathrm{d}A\mathrm{d}z \end{aligned} \tag{3.28}$$

where ρ is the material density distribution in the beam segment and again (3.27) has been used.

Since a beam segment made of one cylinder and one hollow cylinder is considered, each of which is modelled by different materials, the integral over the cross-section must be split according to the following:

$$\int_A (\diamond)\, \mathrm{d}A = \int_{A^{(1)}} (\diamond)\, \mathrm{d}A + \int_{A^{(2)}} (\diamond)\, \mathrm{d}A \tag{3.29}$$

where $A^{(1)}$ stands for the circular cross-section and $A^{(2)}$ for the annulus cross-section. Let r_1 and r_2 denote the radius of the inner cross-section and the outer cross-section, respectively. Then, the areas of the circular and the annulus cross-sections are given by:

$$A^{(1)} = \pi r_1^2, \quad A^{(2)} = \pi(r_2^2 - r_1^2) \tag{3.30}$$

Similarly, the moment of inertia for the two different cross-sections can be computed as:

$$I_1 = \int_{A^{(1)}} y^2 \mathrm{d}A = \pi r_1^4, \quad I_2 = \int_{A^{(2)}} y^2 \mathrm{d}A = \pi(r_2^4 - r_1^4) \tag{3.31}$$

In the following derivation, the superscripts $(\diamond)^{(1)}$ and $(\diamond)^{(2)}$ are used to designate the material constants for two piezoelectric materials, for example, $C_{33}^{(1)}, C_{33}^{(2)}$ and so on. With this denotation, (3.26) can be rewritten as:

$$\begin{aligned} W = \sum_{j=1}^{2} \int_a^b \Bigg[&\frac{1}{2} A^{(j)} C_{33}^{(j)} u_{,z}^2 + \frac{1}{2} C_{33}^{(j)} I^{(j)} \varphi_{,z}^2 + A^{(j)} e_{33}^{(j)} u_{,z} \phi_{,z} \\ &+ \frac{1}{2} A^{(j)} \kappa^{(j)} C_{23}^{(j)} (w_{,z} - \varphi)^2 - \frac{1}{2} A^{(j)} \chi_{33}^{(j)} \phi_{,z}^2 \Bigg] \mathrm{d}z \end{aligned} \tag{3.32}$$

Similarly, the kinetic energy then becomes:

$$T = \sum_{j=1}^{2} \int_a^b \frac{1}{2} \left[A^{(j)} \rho^{(j)} (u_{,t}^2 + w_{,t}^2) + I^{(j)} \rho^{(j)} \varphi_{,t}^2\right] \mathrm{d}z \tag{3.33}$$

The geometrical constants and the material constants appearing in the above stored energy and kinetic energy can be combined, to shorten the formulation and thus benefit the subsequent derivation. In particular, the following 'composite' constants are introduced:

$$
\begin{aligned}
AC_{33} &= \sum_{j=1}^{2} A^{(j)} C_{33}^{(j)}, \quad A\kappa C_{23} = \sum_{j=1}^{2} A^{(j)} \kappa^{(j)} C_{23}^{(j)} \\
Ae_{33} &= \sum_{j=1}^{(2)} A^{(j)} e_{33}^{(j)}, \quad IC_{33} = \sum_{j=1}^{2} I^{(j)} C_{33}^{(j)}, \quad A\chi_{33} = \sum_{i=1}^{2} A^{(j)} \chi_{33}^{(j)} \\
A\rho &= \sum_{j=1}^{2} A^{(j)} \rho^{(j)}, \quad I\rho = \sum_{j=1}^{(2)} I^{(j)} \rho^{(j)}
\end{aligned}
\tag{3.34}
$$

It is important to note that the composite constants introduced above should not be confused with the multiplication of two constants as if the beam is made of homogeneous material.

To derive the stored energy and the kinetic energy for the entire transducer, the stored and kinetic energy functionals must be added for all five segments. To this end, the superscript $(\diamond)^{[s]}$ shall be used to denote the quantities for the beam segment s, including the composite constants defined above and the energy functional. For example, $W^{[s]}$ and $T^{[s]}$ denote the stored energy and the kinetic energy for the beam segment s, respectively, and $AC_{33}^{[s]}$ is the composite constant for the segment s. Also, it is assumed that the beam segment s spans from the coordinate $z = z_s$ to $z = z_{s+1}$. Therefore, the integral limits a and b in (3.36) for the beam segment s will be replaced by z_s and z_{s+1}, respectively. The total potential, defined as the difference between the kinetic energy and the stored energy, is given as:

$$
\Pi = \sum_{s=1}^{N_s} (T^{[s]} - W^{[s]}) \tag{3.35}
$$

with $N_s = 5$ being the number of the beam segments. In this expression, the stored energy $W^{[s]}$ and the kinetic energy $T^{[s]}$, $s = \overline{1, N_s}$, are given by:

$$
\begin{aligned}
W^{[s]} = \int_{z_s}^{z_{s+1}} \Big[& \frac{1}{2} AC_{33}^{[s]} u_{,z}^2 + \frac{1}{2} IC_{33}^{[s]} \varphi_{,z}^2 + Ae_{33}^{[s]} u_{,z} \phi_{,z} \\
& + \frac{1}{2} A\kappa C_{23}^{[s]} (w_{,z} - \varphi)^2 - \frac{1}{2} A\chi_{33}^{[s]} \phi_{,z}^2 \Big] \mathrm{d}z \\
T^{[s]} = \int_{z_s}^{z_{s+1}} & \frac{1}{2} \left[A\rho^{[s]} (u_{,t}^2 + w_{,t}^2) + I\rho^{[s]} \varphi_{,t}^2 \right] \mathrm{d}z
\end{aligned}
\tag{3.36}
$$

3.2.3.7 Establishing the Variational Equation

Taking the variation of $W^{[s]}$ with respect to u, w, φ and ϕ, the following equation can be obtained:

$$
\begin{aligned}
\delta W^{[s]} = \int_{z_s}^{z_{s+1}} \frac{1}{2} \Big[& (AC_{33}^{[s]} u_{,z} + Ae_{33}^{[s]} \phi_{,z}) \delta u_{,z} + A\kappa C_{23}^{[s]} (w_{,z} - \varphi) \delta w_{,z} \\
& + IC_{33}^{[s]} \varphi_{,z} \delta \varphi_{,z} - A\kappa C_{23}^{[s]} (w_{,z} - \varphi) \delta \varphi \\
& + (Ae_{33}^{[s]} u_{,z} - A\chi_{33}^{[s]} \phi_{,z}) \delta \phi_{,z} \Big] \mathrm{d}z
\end{aligned}
\tag{3.37}
$$

where δu, δw, $\delta\varphi$, $\delta\phi$ are the test functions corresponding to u, w, φ, ϕ, respectively. Note that the variation $\delta W^{[s]}$ expressed above is the Gateaux derivative of the functional $W^{[s]}$ at (u,w,φ,ϕ) in the direction $(\delta u,\delta w,\delta\varphi,\delta\phi)$.

The variation of the kinetic energy (3.28) is given by:

$$\delta T^{[s]} = \int_{z_s}^{z_{s+1}} \frac{1}{2}\left[A\rho^{[s]}(u_{,t}\delta u_{,t} + w_{,t}\delta w_{,t}) + I\rho^{[s]}\varphi_{,t}\delta\varphi_{,t}\right]\mathrm{d}z \tag{3.38}$$

The motion of the transducer is governed by Hamilton's principle:

$$\delta\int_{t_0}^{t_1}\left[\sum_{s=1}^{N_s}(W^{[s]} - T^{[s]})\right] = \int_{t_0}^{t_1}\sum_{s=1}^{N_s}(\delta W^{[s]} - \delta T^{[s]}) = 0 \tag{3.39}$$

where t_0 and t_1 are the initial time and the end time of the motion and considered as given. Substituting (3.37) and (3.38) into (3.39), it is possible to obtain the variational equation governing the motion of the transducer. Solving the variational equation by the finite element method will be the topic of the next section.

3.2.3.8 Differential Governing Equations

Essentially, the variational equation described by (3.39) can be solved by the finite element method. However, for the purpose of completeness, the differential equations governing the motion of the transducer are also derived. By applying integration by parts to (3.37) with respect to the variable z, it can be shown that:

$$\begin{aligned}
\int_{t_0}^{t_1}\delta W^{[s]}\mathrm{d}t = &\int_{t_0}^{t_1}\frac{1}{2}\left[(AC_{33}^{[s]}u_{,z} + Ae_{33}^{[s]}\phi_{,z})\delta u\right]_{z_s}^{z_{s+1}}\mathrm{d}t \\
&- \int_{t_0}^{t_1}\int_{z_s}^{z_{s+1}}\frac{1}{2}(AC_{33}^{[s]}u_{,zz} + Ae_{33}^{[s]}\phi_{,zz})\delta u\,\mathrm{d}z\mathrm{d}t \\
&+ \int_{t_0}^{t_1}\frac{1}{2}\left[A\kappa C_{23}^{[s]}(w_{,z} - \varphi)\delta w\right]_{z_s}^{z_{s+1}}\mathrm{d}t \\
&- \int_{t_0}^{t_1}\int_{z_s}^{z_{s+1}}\frac{1}{2}A\kappa C_{23}^{[s]}(w_{,zz} - \varphi_{,z})\delta w\,\mathrm{d}z\mathrm{d}t \quad + \int_{t_0}^{t_1}\frac{1}{2}\left[IC_{33}^{[s]}\varphi_{,z}\delta\varphi\right]_{z_s}^{z_{s+1}}\mathrm{d}t \\
&- \int_{t_0}^{t_1}\int_{z_s}^{z_{s+1}}\frac{1}{2}\left[IC_{33}^{[s]}\varphi_{,zz} + A\kappa C_{23}^{[s]}(w_{,z} - \varphi)\right]\delta\varphi\,\mathrm{d}z\mathrm{d}t \\
&+ \int_{t_0}^{t_1}\frac{1}{2}\left[(Ae_{33}^{[s]}u_{,z} - A\chi_{33}^{[s]}\phi_{,z})\delta\phi\right]_{z_s}^{z_{s+1}}\mathrm{d}t \\
&+ \int_{t_0}^{t_1}\int_{z_s}^{z_{s+1}}\frac{1}{2}(A\chi_{33}^{[s]}\phi_{,zz} - Ae_{33}^{[s]}u_{,zz})\delta\phi\,\mathrm{d}z\mathrm{d}t
\end{aligned} \tag{3.40}$$

where the denotation $[f(z)]_{z_s}^{z_{s+1}} = f(z_{s+1}) - f(z_s)$ has been used. As for the contribution of kinetic energy from Hamilton's principle (3.39), integration by parts can be employed with

respect to t to obtain:

$$\int_{t_0}^{t_1} \delta T^{[s]} \mathrm{d}t = \int_{t_0}^{t_1} \int_{z_s}^{z_{s+1}} \frac{1}{2} \big[-A\rho^{[s]}(u_{,tt}\delta u + w_{,tt}\delta w) - I\rho^{[s]}\varphi_{,tt}\delta\varphi \big] \mathrm{d}z\mathrm{d}t \tag{3.41}$$

where the condition that δu, δw and $\delta\varphi$ vanish at both $t = t_0$ and $t = t_1$ has been applied.

Substituting (3.40) and (3.41) into (3.39), it can be demonstrated that:

$$\begin{aligned}
\sum_{s=1}^{N_s} \Bigg\{ & \int_{t_0}^{t_1} \Big[(AC_{33}^{[s]} u_{,z} - Ae_{33}^{[s]} \phi_{,z}) \delta u \Big]_{z_s}^{z_{s+1}} \mathrm{d}t \\
& + \int_{t_0}^{t_1} \int_{z_s}^{z_{s+1}} \Big[A\rho^{[s]} u_{,tt} - AC_{33}^{[s]} u_{,zz} - Ae_{33}^{[s]} \phi_{,zz} \Big] \delta u \, \mathrm{d}z\mathrm{d}t \\
& + \int_{t_0}^{t_1} \Big[A\kappa C_{23}^{[s]} (w_{,z} - \varphi) \delta w \Big]_{z_s}^{z_{s+1}} \mathrm{d}t \\
& + \int_{t_0}^{t_1} \int_{z_s}^{z_{s+1}} \Big[A\rho^{[s]} w_{,tt} - A\kappa C_{23}^{[s]} (w_{,zz} - \varphi_{,z}) \Big] \delta w \, \mathrm{d}z\mathrm{d}t \\
& + \int_{t_0}^{t_1} \Big[IC_{33}^{[s]} \varphi_{,z} \delta\varphi \Big]_{z_s}^{z_{s+1}} \mathrm{d}t \\
& + \int_{t_0}^{t_1} \int_{z_s}^{z_{s+1}} \Big[I\rho^{[s]} \varphi_{,tt} - IC_{33}^{[s]} \varphi_{,zz} - A\kappa C_{23}^{[s]} (w_{,z} - \varphi) \Big] \delta\varphi \, \mathrm{d}z\mathrm{d}t \\
& + \int_{t_0}^{t_1} \Big[(Ae_{33}^{[s]} u_{,z} - A\chi_{33}^{[s]} \phi_{,z}) \delta\phi \Big]_{z_s}^{z_{s+1}} \mathrm{d}t \\
& + \int_{t_0}^{t_1} \int_{z_s}^{z_{s+1}} (Ae_{33}^{[s]} u_{,zz} - A\chi_{33}^{[s]} \phi_{,zz}) \delta\phi \, \mathrm{d}z\mathrm{d}t \Bigg\} = 0
\end{aligned} \tag{3.42}$$

As δu, δw, $\delta\varphi$ and $\delta\phi$ can vary arbitrarily on each interval (z_s, z_{s+1}), $s = 1, \ldots, N_s$, the following system of equations can be obtained:

$$\begin{aligned}
A\rho^{[s]} u_{,tt} - AC_{33}^{[s]} u_{,zz} - Ae_{33}^{[s]} \phi_{,zz} &= 0 \\
A\rho^{[s]} w_{,tt} - A\kappa C_{23}^{[s]} (w_{,zz} - \varphi_{,z}) &= 0 \\
I\rho^{[s]} \varphi_{,tt} - IC_{33}^{[s]} \varphi_{,zz} - A\kappa C_{23}^{[s]} (w_{,z} - \varphi) &= 0 \\
Ae_{33}^{[s]} u_{,zz} - A\chi_{33}^{[s]} \phi_{,zz} &= 0
\end{aligned} \tag{3.43}$$

for all $z \in (z_s, z_{s+1})$ and $s = \overline{1, N_s}$. This system must be accompanied by the boundary conditions derived from the boundary terms appearing in (3.42).

3.2.3.9 Reduction of Differential Equations

Through deriving this system, it has been argued that the variables δu, δw, $\delta\varphi$ and $\delta\phi$ can vary arbitrarily in the sub-domain (z_s, z_{s+1}). However, it is important to note that the validity of this argument depends on the considered beam segments. The explanation for this is as follows.

1. As for the beam segments [1], [2], [4], [5], these beam segments are not made of piezoelec-

tric material but only isotropic elastic materials, and so the electric field potential ϕ can be neglected in the modelling. Thus, for these beam segments, only the mechanical displacement fields, namely u, w, φ, are the unknown fields in the system. Moreover, as these beam segments are modelled using the isotropic materials, $Ae_{33}^{[s]} = 0$ and $A\chi_{33}^{[s]} = 0$ for $s = 1,2,4,5$ can be readily set. The longitudinal displacement u in these beam segments persists and depends on the applied electric field on the boundaries of the beam segment [3] because the displacement u in this beam segment [3] will transfer to the others via the resultant forces.

2. As for the beam segment [3], the electric field potential ϕ is required for the modelling and thus the unknown variables involve not only the mechanical displacement fields mentioned above but also ϕ.

3.2.3.10 Electrical Boundary Conditions

The derivation of the boundary conditions for the transducer consisting of different beam segments is slightly more sophisticated than the derivation for one homogeneous beam. Indeed, the reason is that the resultant forces at the interfaces between the connecting beam segments must be in equilibrium. The boundary conditions at the two ends of the total beam, namely $z = 0$ and $z = z_{N_s+1} = L$ can be easily identified by setting the appropriate boundary terms in (3.42) to zero. However, at the interfaces between two connecting beam segments s and $s+1$, the boundary conditions are identified by equating the boundary terms evaluated at the right end of beam segment s to the boundary terms evaluated at the left-end of the section $s+1$. To this end, the following set of boundary conditions can be derived:

$$\begin{aligned}
\left[(AC_{33}^{[1]}u_{,z} - Ae_{33}^{[1]}\phi_{,z})\delta u\right]_{z=0} &= 0, & \left[(AC_{33}^{[N_s]}u_{,z} - Ae_{33}^{[N_s]}\phi_{,z})\delta u\right]_{z=L} &= 0 \\
\left[A\kappa C_{23}^{[1]}(w_{,z} - \varphi)\delta w\right]_{z=0} &= 0, & \left[A\kappa C_{23}^{[N_s]}(w_{,z} - \varphi)\delta w\right]_{z=L} &= 0 \\
\left[IC_{33}^{[1]}\varphi_{,z}\delta\varphi\right]_{z=0} &= 0, & \left[IC_{33}^{[N_s]}\varphi_{,z}\delta\varphi\right]_{z=L} &= 0 \\
\left[(Ae_{33}^{[1]}u_{,z} - A\chi_{33}^{[1]}\phi_{,z})\delta\phi\right]_{z=0} &= 0, & \left[(Ae_{33}^{[N_s]}u_{,z} - A\chi_{33}^{[N_s]}\phi_{,z})\delta\phi\right]_{z=L} &= 0
\end{aligned} \tag{3.44}$$

and

$$\begin{aligned}
\left[(AC_{33}^{[s]}u_{,z} - Ae_{33}^{[s]}\phi_{,z})\right]_{z=z_s^+} + \left[(AC_{33}^{[s]}u_{,z} - Ae_{33}^{[s]}\phi_{,z})\right]_{z=z_{s+1}^-} &= 0 \\
\left[A\kappa C_{23}^{[s]}(w_{,z} - \varphi)\right]_{z=z_s^+} + \left[A\kappa C_{23}^{[s]}(w_{,z} - \varphi)\right]_{z=z_{s+1}^-} &= 0 \\
\left[IC_{33}^{[s]}\varphi_{,z}\right]_{z=z_s^+} + \left[IC_{33}^{[s]}\varphi_{,z}\right]_{z=z_{s+1}^-} &= 0 \\
\left[(Ae_{33}^{[s]}u_{,z} - A\chi_{33}^{[s]}\phi_{,z})\right]_{z=z_s^+} + \left[(Ae_{33}^{[s]}u_{,z} - A\chi_{33}^{[s]}\phi_{,z})\right]_{z=z_{s+1}^-} &= 0
\end{aligned} \tag{3.45}$$

for $s = 2, \ldots, N_s - 1$, where the notation $[f(z)]_{z=a^{\pm}} = \lim_{z \to a^{\pm}} f(z)$ means the limit of $f(z)$ from the left and from the right of a, respectively.

3.2.3.11 Finite Element Setup

In this section, we can introduce not only the discretisation of the variational equation (3.39) by the finite element method but also the numerical procedure for computing the natural frequencies of the Langevin transducer. The first step is to establish the finite element model for (3.39), with $\delta W^{[s]}$ and $\delta T^{[s]}$ given by (3.37) and (3.41). The standard conforming finite element method is adopted, only focusing on constructing the stiffness and mass matrices at the element level (see [161]). Further to this, the spectral element method is used for the discretisation [162, 163].

Let us assume the problem domain $\Omega = (0, L)$ for the transducer beam is discretised into N_e non-overlapping finite elements $\Omega^{(e)}$, i.e., $\Omega = \bigcup_{e=1}^{N_e} \Omega^{(e)}$, $\Omega^{(m)} \cap \Omega^{(n)} = \emptyset$ for $m \neq n$. As for the shape functions on the finite elements, Lagrange polynomials of order $p-1$ are used. Let $H_j = H_j(\xi)$ for $j = \overline{1, p}$ denote the shape functions on the reference domain $\mathscr{R} = [-1, 1]$ supported by the Chebyshev points $\xi_j = -\cos\left(j\frac{\pi}{p}\right)$ (see Figure 3.6). Therefore, the shape functions are given as:

$$H_j = \prod_{0 \leq n \leq p-1, n \neq j} \frac{\xi - \xi_n}{\xi_j - \xi_n} \tag{3.46}$$

The isoparametric mapping from the reference domain $\mathscr{R}$ to the element $\Omega^{(e)}$ is defined by:

$$z^{(e)}(\xi) = \sum_{j=1}^{p} z_j^{(e)} H_j(\xi) \tag{3.47}$$

where $z_j^{(e)}$ are the coordinates of the nodes in the element $\Omega^{(e)}$. If the $\{z_j^{(e)}\}_{j=1}^{p}$ are defined following the same distribution pattern of $\{\xi_j\}_{j=1}^{p}$, then the reference-to-physical mapping (3.47) becomes a linear mapping. The mapping (3.47) changes from element to element and its inverse mapping from $\Omega^{(e)}$ to $\mathscr{R}$ will be denoted $\xi^{(e)} = \xi^{(e)}(z)$. The shape functions defined on the physical coordinate z are then given by:

$$N_j^{(e)}(z) = H_j(\xi^{(e)}(z)) \tag{3.48}$$

Next, the trial functions u, w, φ, ϕ and their corresponding test functions $\delta u, \delta w, \delta\varphi, \delta\phi$ defined on the element $\Omega^{(e)}$ are interpolated according to:

$$f^{(e)}(z) = \sum_{j=1}^{p} N_j^{(e)}(z) f_j^{(e)} \tag{3.49}$$

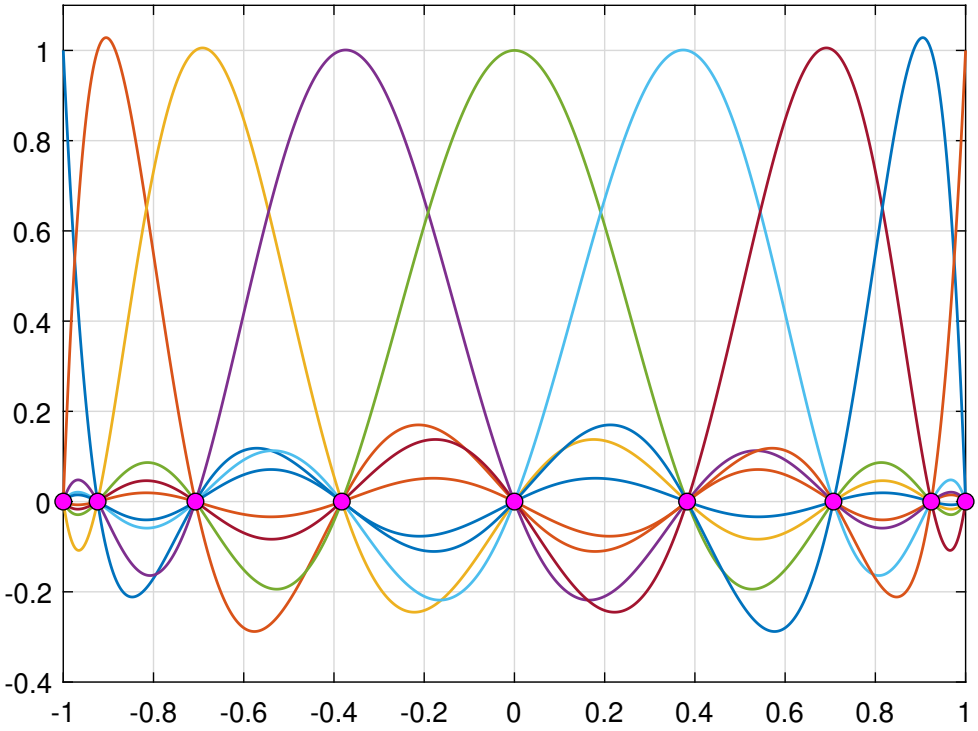

Figure 3.6: Chebyshev points and Lagrange polynomials supported by these points as shape functions. The Chebyshev supporting nodes are defined by $\xi_j = \cos(j\pi/p)$ with n being the number of nodes for one element (circles filled by magenta). In this figure, $p = 9$ and thus the shape functions are polynomials of order $p-1 = 8$.

where f stands for the trial functions as well as test functions and $f_j^{(e)}$ are the corresponding degrees of freedom associated with the element $\Omega^{(e)}$, In this work, we use the shape functions of the same polynomial order p for all the finite elements. Let us denote by boldface notation $\mathbf{f}^{(e)}$ the column vector of degrees of freedom $f_j^{(e)}$ in the element $\Omega^{(e)}$, i.e., $\mathbf{f}^{(e)} = \left[f_1^{(e)} \ \cdots \ f_p^{(e)}\right]^T$. This notation applies across the trial functions u, w, φ, ϕ and the test functions δu, δw, $\delta\varphi$, $\delta\phi$, e.g., $\mathbf{u}^{(e)} = \left[u_1^{(e)} \ \cdots \ u_p^{(e)}\right]^T$.

3.2.3.12 Element Stiffness and Mass Matrices

To derive the stiffness matrices at the element level, the variation in (3.37) is used, that is the variational equation before application of the integration by parts. Indeed, by substituting the interpolations of type (3.49) into (3.37), the following can be obtained:

$$\begin{aligned}\delta W^{[s],(e)} = {} & \delta\mathbf{u}^{(e)} \cdot \left[\mathbf{K}_{\mathbf{uu}}^{(e)}\mathbf{u}^{(e)} + \mathbf{K}_{\mathbf{u}\phi}^{(e)}\phi^{(e)}\right] + \delta\mathbf{w}^{(e)} \cdot \left[\mathbf{K}_{\mathbf{ww}}^{(e)}\mathbf{w}^{(e)} + \mathbf{K}_{\mathbf{w}\varphi}^{(e)}\varphi^{(e)}\right] \\ & + \delta\varphi^{(e)} \cdot \left[\mathbf{K}_{\varphi\varphi}^{(e)}\varphi^{(e)} + \mathbf{K}_{\varphi\mathbf{w}}^{(e)}\mathbf{w}^{(e)}\right] + \delta\phi^{(e)} \cdot \left[\mathbf{K}_{\phi\mathbf{u}}^{(e)}\mathbf{u}^{(e)} + \mathbf{K}_{\phi\phi}^{(e)}\phi^{(e)}\right]\end{aligned} \tag{3.50}$$

The element stiffness matrices in the above equation are given by:

$$\begin{aligned}
&\mathbf{K}_{\mathbf{uu}}^{(e)} = AC_{33}^{[s]}\widehat{\mathbf{K}}^{(e)}, && \mathbf{K}_{\mathbf{u}\phi}^{(e)} = Ae_{33}^{[s]}\widehat{\mathbf{K}}^{(e)}, && \mathbf{K}_{\mathbf{ww}}^{(e)} = AC_{23}^{[s]}\widehat{\mathbf{K}}^{(e)} \\
&\mathbf{K}_{\mathbf{w}\varphi}^{(e)} = -A\kappa C_{23}^{[s]}\widetilde{\mathbf{K}}^{(e)}, && \mathbf{K}_{\varphi\mathbf{w}}^{(e)} = \mathbf{K}_{\mathbf{w}\varphi}^{(e)T}, && \mathbf{K}_{\varphi\varphi}^{(e)} = IC_{33}^{[s]}\widehat{\mathbf{K}}^{(e)} \\
&\mathbf{K}_{\phi\mathbf{u}}^{(e)} = \mathbf{K}_{\mathbf{u}\phi}^{(e)T}, && \mathbf{K}_{\phi\phi}^{(e)} = -A\chi_{33}^{[s]}\widehat{\mathbf{K}}^{(e)}
\end{aligned} \tag{3.51}$$

where the matrices $\widehat{\mathbf{K}}^{(e)}$ and $\widetilde{\mathbf{K}}^{(e)}$ are defined by:

$$\widehat{K}_{ij}^{(e)} = \int_{\Omega^{(e)}} \frac{\mathrm{d}N_i^{(e)}}{\mathrm{d}z}\frac{\mathrm{d}N_j^{(e)}}{\mathrm{d}z}\mathrm{d}z, \quad \widetilde{K}_{ij}^{(e)} = \int_{\Omega^{((e))}} \frac{\mathrm{d}N_i}{\mathrm{d}z}N_j\mathrm{d}z \tag{3.52}$$

Note that in the notation $\delta W^{[s],(e)}$, the superscripts $[s]$ are used for the beam segment s, and (e) for the integration over the element $\Omega^{(e)}$. It is clear that the element stiffness matrices can be computed via two common matrices $\widehat{\mathbf{K}}^{(e)}$ and $\widetilde{\mathbf{K}}^{(e)}$.

As for the mass matrices, the variational formulation (3.41) is used. For one element, it is straightforward to derive:

$$\int_{t_0}^{t_1}\delta T^{[s],(e)}\mathrm{d}t = -\int_{t_0}^{t_1}\left[\delta\mathbf{u}^{(e)}\cdot\mathbf{M}_{\mathbf{uu}}^{(e)}\mathbf{u}_{tt}^{(e)} + \delta\mathbf{w}^{(e)}\cdot\mathbf{M}_{\mathbf{ww}}^{(e)}\mathbf{w}_{tt}^{(e)} + \delta\varphi^{(e)}\cdot\mathbf{M}_{\varphi\varphi}^{(e)}\varphi_{tt}^{(e)}\right]\mathrm{d}t \tag{3.53}$$

where:

$$\mathbf{M}_{\mathbf{uu}}^{(e)} = \mathbf{M}_{\mathbf{ww}}^{(e)} = A\rho^{[s]}\widehat{\mathbf{M}}^{(e)}, \quad \mathbf{M}_{\varphi\varphi}^{(e)} = I\rho^{[s]}\widehat{\mathbf{M}}^{(e)}, \quad \widehat{M}_{ij}^{(e)} = \int_{\Omega^{(e)}} N_i^{(e)}N_j^{(e)}\mathrm{d}z \tag{3.54}$$

3.2.3.13 Computation of Natural Frequencies

The global system of discretised governing equations can be obtained by the standard assembly procedure [161]. To this end, the following system for the $\delta\mathbf{u}$, $\delta\mathbf{w}$, and $\delta\varphi$ terms can be generated:

$$\begin{bmatrix}\mathbf{M}_{\mathbf{u}} & 0 & 0\\ 0 & \mathbf{M}_{\mathbf{ww}} & 0\\ 0 & 0 & \mathbf{M}_{\varphi\varphi}\end{bmatrix}\frac{\partial^2}{\partial t^2}\begin{bmatrix}\mathbf{u}\\ \mathbf{w}\\ \varphi\end{bmatrix} + \begin{bmatrix}\mathbf{K}_{\mathbf{uu}} & 0 & 0 & \mathbf{K}_{\mathbf{u}\phi}\\ 0 & \mathbf{K}_{\mathbf{ww}} & \mathbf{K}_{\mathbf{w}\varphi} & 0\\ 0 & \mathbf{K}_{\varphi\mathbf{w}} & \mathbf{K}_{\varphi\varphi} & 0\end{bmatrix}\begin{bmatrix}\mathbf{u}\\ \mathbf{w}\\ \varphi\\ \phi\end{bmatrix} = 0 \tag{3.55}$$

with the equation for $\delta\phi$ as follows:

$$\mathbf{K}_{\phi\mathbf{u}}\mathbf{u} + \mathbf{K}_{\phi\phi}\phi = 0 \tag{3.56}$$

One should recall the remark concerning the reduction of governing equations in Sec-

tion 3.2.3.8. Indeed, the argument therein applies also to the discretised system of equations. Accordingly, the degrees of freedom in φ only persist with the beam segment [3], while the degrees of freedom in **u**, **w** and φ are for the entire transducer beam. This is an important remark in the numerical implementation.

Let us group the degrees of freedom for **u**, **w** and φ into a master column vector **d** and group the corresponding stiffness matrices as follows:

$$\begin{aligned} \mathbf{M_{dd}}\mathbf{d}_{,tt} + \mathbf{K_{dd}}\mathbf{d} + \mathbf{K_{u\phi}}\phi = 0 \\ \mathbf{K_{\phi u}}\mathbf{u} + \mathbf{K_{\phi\phi}}\phi = 0 \end{aligned} \tag{3.57}$$

with:

$$\mathbf{d} = \begin{bmatrix} \mathbf{u} \\ \mathbf{w} \\ \varphi \end{bmatrix}, \quad \mathbf{M_{dd}} = \begin{bmatrix} \mathbf{M_{uu}} & 0 & 0 \\ 0 & \mathbf{M_{ww}} & 0 \\ 0 & 0 & \mathbf{M_{\varphi\varphi}} \end{bmatrix}, \quad \mathbf{K_{dd}} = \begin{bmatrix} \mathbf{K_{uu}} & 0 & 0 \\ 0 & \mathbf{K_{ww}} & \mathbf{K_{w\varphi}} \\ 0 & \mathbf{K_{\varphi w}} & \mathbf{K_{\varphi\varphi}} \end{bmatrix} \tag{3.58}$$

3.2.3.14 Boundary Conditions

The appropriate boundary conditions on the beam segment [3] must be applied to eliminate the singular mode in $\mathbf{K}_{\phi\phi}$. In this consideration, $\phi = V_1$ and $\phi = V_2$ are applied on the left and the proper boundaries of the PZT segment [3], where the left and right boundaries are assumed at a^{th} and b^{th} nodes, respectively. The idea here is to apply electrical boundary conditions to the second equation of (3.57) and then substitute it into the first one, as per linear condensation. The second equation of (3.57) is rewritten by moving the a^{th} and b^{th} columns of $\mathbf{K}_{\phi\phi}$ to the right-hand side, and then eliminating a^{th} and b^{th} rows for the whole equation as follows, where the total number of nodes is P:

$$\widehat{\mathbf{K}}_{\phi\mathbf{u}}\mathbf{u} + \widehat{\mathbf{K}}_{\phi\phi}\widehat{\phi} = -V_1 \cdot \begin{bmatrix} \mathbf{K}_{\phi\phi}^{1,a} \\ \vdots \\ \mathbf{K}_{\phi\phi}^{P,a} \end{bmatrix}_{P\neq a,b} - V_2 \cdot \begin{bmatrix} \mathbf{K}_{\phi\phi}^{1,b} \\ \vdots \\ \mathbf{K}_{\phi\phi}^{P,b} \end{bmatrix}_{P\neq a,b} \tag{3.59}$$

This equation can be rewritten as:

$$\widehat{\phi} = -\widehat{\mathbf{K}}_{\phi\phi}^{-1}(\widehat{\mathbf{K}}_{\phi\mathbf{u}}\mathbf{u} + V_1 \cdot \begin{bmatrix} \mathbf{K}_{\phi\phi}^{1,a} \\ \vdots \\ \mathbf{K}_{\phi\phi}^{P,a} \end{bmatrix}_{P\neq a,b} + V_2 \cdot \begin{bmatrix} \mathbf{K}_{\phi\phi}^{1,b} \\ \vdots \\ \mathbf{K}_{\phi\phi}^{P,b} \end{bmatrix}_{P\neq a,b}) \tag{3.60}$$

It has to be noted that the equation (3.60) can be substituted into the first equation of (3.57) as long as the vector ϕ is reduced to $\widehat{\phi}$. To this end, the first equation of (3.57) is rewritten by only moving a^{th} and b^{th} columns of $\mathbf{K_{u\phi}}$ to the right:

$$\mathbf{M_{dd}}\mathbf{d}_{,tt} + \mathbf{K_{dd}}\mathbf{d} + \widehat{\mathbf{K}}_{\mathbf{u}\phi}\widehat{\phi} = -V_1 \cdot \begin{bmatrix} \mathbf{K}_{\mathbf{u}\phi}^{1,a} \\ \vdots \\ \mathbf{K}_{\mathbf{u}\phi}^{P,a} \end{bmatrix} - V_2 \cdot \begin{bmatrix} \mathbf{K}_{\mathbf{u}\phi}^{1,b} \\ \vdots \\ \mathbf{K}_{\mathbf{u}\phi}^{P,b} \end{bmatrix} \tag{3.61}$$

Substituting (3.60) into the first equation of (3.57), the following can be obtained:

$$\begin{aligned} \mathbf{M_{dd}}\mathbf{d}_{,tt} + \mathbf{K_{dd}}\mathbf{d} - \widehat{\mathbf{K}}_{\mathbf{u}\phi}\widehat{\mathbf{K}}_{\phi\phi}^{-1}\widehat{\mathbf{K}}_{\phi\mathbf{u}}\mathbf{u} = V_1 \cdot (\widehat{\mathbf{K}}_{\mathbf{u}\phi}\widehat{\mathbf{K}}_{\phi\phi}^{-1} \begin{bmatrix} \mathbf{K}_{\phi\phi}^{1,a} \\ \vdots \\ \mathbf{K}_{\phi\phi}^{P,a} \end{bmatrix}_{P\neq a,b} - \begin{bmatrix} \mathbf{K}_{\mathbf{u}\phi}^{1,a} \\ \vdots \\ \mathbf{K}_{\mathbf{u}\phi}^{P,a} \end{bmatrix}) \\ - V_2 \cdot (\widehat{\mathbf{K}}_{\mathbf{u}\phi}\widehat{\mathbf{K}}_{\phi\phi}^{-1} \begin{bmatrix} \mathbf{K}_{\phi\phi}^{1,b} \\ \vdots \\ \mathbf{K}_{\phi\phi}^{P,b} \end{bmatrix}_{P\neq a,b} - \begin{bmatrix} \mathbf{K}_{\mathbf{u}\phi}^{1,b} \\ \vdots \\ \mathbf{K}_{\mathbf{u}\phi}^{P,b} \end{bmatrix}) \end{aligned} \tag{3.62}$$

This equation can be rewritten as, where $\mathbf{V}$ is the right hand vector:

$$\mathbf{M_{dd}}\mathbf{d}_{,tt} + \widehat{\mathbf{K}}_{\mathbf{dd}}\mathbf{d} = \mathbf{F}_{\phi} \tag{3.63}$$

with $\widehat{\mathbf{K}}_{\mathbf{dd}}$ being modified from $\mathbf{K_{dd}}$ to take into account of the last term $\widehat{\mathbf{K}}_{\mathbf{u}\phi}\widehat{\mathbf{K}}_{\phi\phi}^{-1}\widehat{\mathbf{K}}_{\phi\mathbf{u}}\mathbf{u}$ as follows:

$$\widehat{\mathbf{K}}_{\mathbf{dd}} = \begin{bmatrix} \mathbf{K_{uu}} - \widehat{\mathbf{K}}_{\mathbf{u}\phi}\widehat{\mathbf{K}}_{\phi\phi}^{-1}\widehat{\mathbf{K}}_{\phi\mathbf{u}} & 0 & 0 \\ 0 & \mathbf{K_{ww}} & \mathbf{K_{w\varphi}} \\ 0 & \mathbf{K_{\varphi w}} & \mathbf{K_{\varphi\varphi}} \end{bmatrix} \tag{3.64}$$

When the electric potential $V_1 = V_2 = 0$, the problem is degenerated to an eigenvalue problem. Therefore, the natural frequencies and mode shapes including both the bending and longitudinal modes are computed by solving the standard eigenvalue formula:

$$\left[\widehat{\mathbf{K}}_{\mathbf{dd}} - \omega^2\mathbf{M_{dd}}\right]\mathbf{d} = 0 \tag{3.65}$$

The natural frequencies ω_j and the corresponding natural displacement modes $\mathbf{d}_j$ are the square root of the eigenvalues and the eigenvectors, respectively, of the above eigenvalue prob-

lem:

$$\left[\widehat{\mathbf{K}}_{\mathbf{dd}} - \omega_j^2 \mathbf{M}_{\mathbf{dd}}\right] \mathbf{d}_j = 0, \quad j = 1,2,3,\ldots \tag{3.66}$$

The results ω_j and $\mathbf{d}_j$ will be compared with the eigenfrequencies and eigenmodes computed using the 3D model and the experimental results in the next section. If the electric potentials are non-zeros, the following equation is solved instead of (3.66) to obtain the responses of nodal displacement in the frequency domain:

$$\left[\widehat{\mathbf{K}}_{\mathbf{dd}} - \omega^2 \mathbf{M}_{\mathbf{dd}}\right] \mathbf{d} = \mathbf{F}_\phi \tag{3.67}$$

Harmonic analysis is commonly used to solve this equation by sweeping the frequency within a predefined range. It is important to note that the sweeping frequency cannot be the same as the eigenfrequencies in (3.66) if the system is undamped. When the sweeping frequency is equal to the eigenfrequency, two different scenarios for the rank of $[\widehat{\mathbf{K}}_{\mathbf{dd}} - \omega_j^2 \mathbf{M}_{\mathbf{dd}}]$ are given:

$$\begin{aligned} &r(\widehat{\mathbf{K}}_{\mathbf{dd}} - \omega_j^2 \mathbf{M}_{\mathbf{dd}}) < r(\widehat{\mathbf{K}}_{\mathbf{dd}} - \omega_j^2 \mathbf{M}_{\mathbf{dd}} | \mathbf{F}_\phi) \Rightarrow \text{No solution} \\ &r(\widehat{\mathbf{K}}_{\mathbf{dd}} - \omega_j^2 \mathbf{M}_{\mathbf{dd}}) = r(\widehat{\mathbf{K}}_{\mathbf{dd}} - \omega_j^2 \mathbf{M}_{\mathbf{dd}} | \mathbf{F}_\phi) < \text{System DOFs} \Rightarrow \text{Infinite solutions} \end{aligned} \tag{3.68}$$

Both situations result in unsolvable $\mathbf{d}$ at the eigenfrequencies in a harmonic analysis. Therefore, it is significant to avoid the sweeping frequency at the eigenfrequency. However, this raises another concern: the displacements approach infinity when the sweeping frequency is near the eigenfrequency, recalling the displacement responses in an undamped harmonic forced vibration [164]. The mathematical reason behind this holds that $\mathbf{A}^{-1} := \frac{1}{|\mathbf{A}|}\text{adj}(\mathbf{A})$ goes to infinity when the determinant of $\mathbf{A}$ closes to zero. The displacement vector $\mathbf{d}$ in (3.67) tends toward infinity near eigenfrequencies, as the determinant of $[\widehat{\mathbf{K}}_{\mathbf{dd}} - \omega_j^2 \mathbf{M}_{\mathbf{dd}}]$ approaches zero, causing $\mathbf{d}$ to depend on the fineness of the sweeping interval highly. In other words, simulating nodal displacement responses in this undamped and forced problem would be misleading, owing to the fact that the displacement of the transducer is always on the μm scale and can never be infinite in practice.

An alternative approach in the modal identification process involves incorporating the participation factor, which ascertains the number of modes to extract. This factor helps identify the most significant vibration modes instead of relying on displacement as an indicator. The modal participation factor measures the mass in motion in each direction for every mode. A high value in a specific direction signifies that the mode will be stimulated easily by forces or excitation in that particular direction. Although the participation factor approaches infinite as the displacement, using it as a modal indicator rather than an actual physical parameter is acceptable. Here,

Table 3.3: Structural dimensions.

Parameters	Dimension
l_1	$0.5D$
l_2	$0.5(L-l_1-l_3)$
l_3	$0.05L \sim 0.25L$
l_4	l_2
l_5	$0.5l_4$
d	$0.5D$
D_B	$0.75D$

the participation factor is given as:

$$\begin{aligned} &\gamma_j = \mathbf{d}_j^{\mathrm{T}} \cdot \mathbf{M} \cdot \mathbf{D}, \quad j = 1,2,3,\ldots \\ &\mathbf{M}_{eff,j} = \gamma_j^2 \end{aligned} \tag{3.69}$$

where vector $\mathbf{D}$ is the excitation direction vector, which is a norm vector, indicating the direction of excitation in each of the global Cartesian directions, and $\mathbf{M}_{eff,j}$ is the effective mass of the j^{th} eigenmode.

When doing modal identification, most of the significant modes should be extracted, indicating the need to assess how to select these modes. One way to judge this is by considering the ratio of effective mass in (3.69) to total mass. A ratio close to one suggests that most of the significant modes have been extracted.

3.2.3.15 Results and Discussion

As mentioned in Section 3.2.3.4, the relevant material constants for the 1D constitutive law can be derived using the piezoelectric material constants provided by the manufacturer of the PZT (PIC181, PI Ceramic GmbH). The material properties for the simulations are given in Appendix A.

It should be noted that C_{33} and C_{23} shown in Appendix A for the PIC181 material are not the Young's modulus and shear modulus, but instead are computed by (3.14). On the other hand, as for the isotropic elastic material, E can be assigned to C_{33} and $G = \frac{E}{2(1+\nu)}$ to C_{23} as above.

The dimensions of different beam segments are given in the Table 3.3. The total length of the transducer is $L = \sum_{i=1}^{5} l_i = 100$mm to match typical designs. The electric potentials $\phi = V_1$ and $\phi = V_2$ with $(V_2 > V_1)$ were applied on the two ends of the PZT stack, so the potential difference is $\Delta\phi = V_2 - V_1$. To demonstrate the robustness of the proposed computational framework as compared to the full 3D model, multiple simulations are performed corresponding to different geometrical settings by varying two ratios D/L and l_3/L and also the electric potential difference $\Delta\phi$.

The comparisons between the solutions of the 1D and 3D models are established by varying

the following parameters to reflect common industry practice:

- L/D in the set $\mathscr{D}_{L/D} = \{5, 10, 25/2, 20, 25\}$,
- l_3/L in the set $\mathscr{D}_{l_3/L} = \{1/20, 1/10, 3/20, 1/5, 1/4\}$,
- $\Delta\phi$ in the set $\mathscr{D}_{\Delta\phi} = \{0, 50, 100\}V$.

Thus, $5 \cdot 5 \cdot 3 = 75$ simulations are performed for both 1D and 3D model problems, where the first five bending modes and the first five longitudinal mode resonant frequencies for each problem setting are collected. In this study, harmonic analysis was utilised to determine the resonant frequency for longitudinal modes with non-zero electric potentials. However, as the electrical fields in this investigation are not completely coupled with the bending motions, the bending frequencies are obtained at either zero or non-zero potentials by solving (3.66). Also, the two ends of the transducer are set to be free. Assuming that the front mass and the back mass block have equal lengths, and the dimensions of the bolt follow the standard ISO 4762:2004 for a hexagon socket head cap screw, the structural parameters of the transducer can be deduced. The formulas in Table 3.3 express the correlation between all the structural parameters, namely d, D_B, D and l_j. The relative difference between the resonant frequency obtained by the 1D model and the corresponding value by the 3D model is then computed.

The natural frequencies of the first five bending modes and the first five longitudinal modes obtained by the proposed 1D model are compared with the corresponding counterparts obtained by the full 3D model. The relative difference between the frequency of the 1D and 3D models, denoted as $f_{1\mathrm{D}}$ and $f_{3\mathrm{D}}$, is computed according to $(f_{1\mathrm{D}} - f_{3\mathrm{D}})/f_{3\mathrm{D}}$. The relative differences shown in Figures 3.7 and 3.8 are generally below 5%, except for the relatively high longitudinal mode frequencies in the case of $L/D = 5$. The relative difference increases as the vibration modes increase, regardless of whether they are bending modes or longitudinal modes. Overall, the relative differences decrease with increasing ratio L/D and change insignificantly with the change of the ratio l_3/L. The relative differences are particularly high for the small ratio $L/D = 5$ but rather acceptably small for the ratio $L/D = 10$. Indeed, when L/D is small, the full 3D model should give a distinctive result from the 1D model.

However, both the L/D ratio and the l_3/L ratio of the transducer influence the accuracy of the results of the 1D model. It has been observed that the relative difference of the modes tends to significantly decrease with an increase in the L/D ratio, especially increasing the L/D ratio from 5 to 10. When the transducer is rather slender with $L/D \geq 12.5$, the computed natural frequencies of 1D model agree with the results of 3D model very well, which justifies the reliability of the proposed computational framework. Moreover, the l_3/L ratio has a smaller impact on the resonant frequency compared to that of the L/D ratio. Still, it has an obvious influence on resonant frequencies when the L/D ratio is 5. Furthermore, it is arguable that the applied electric voltage $\Delta\phi$ has little impact on the relative difference. In fact, it only affects resonant frequencies on a small scale.

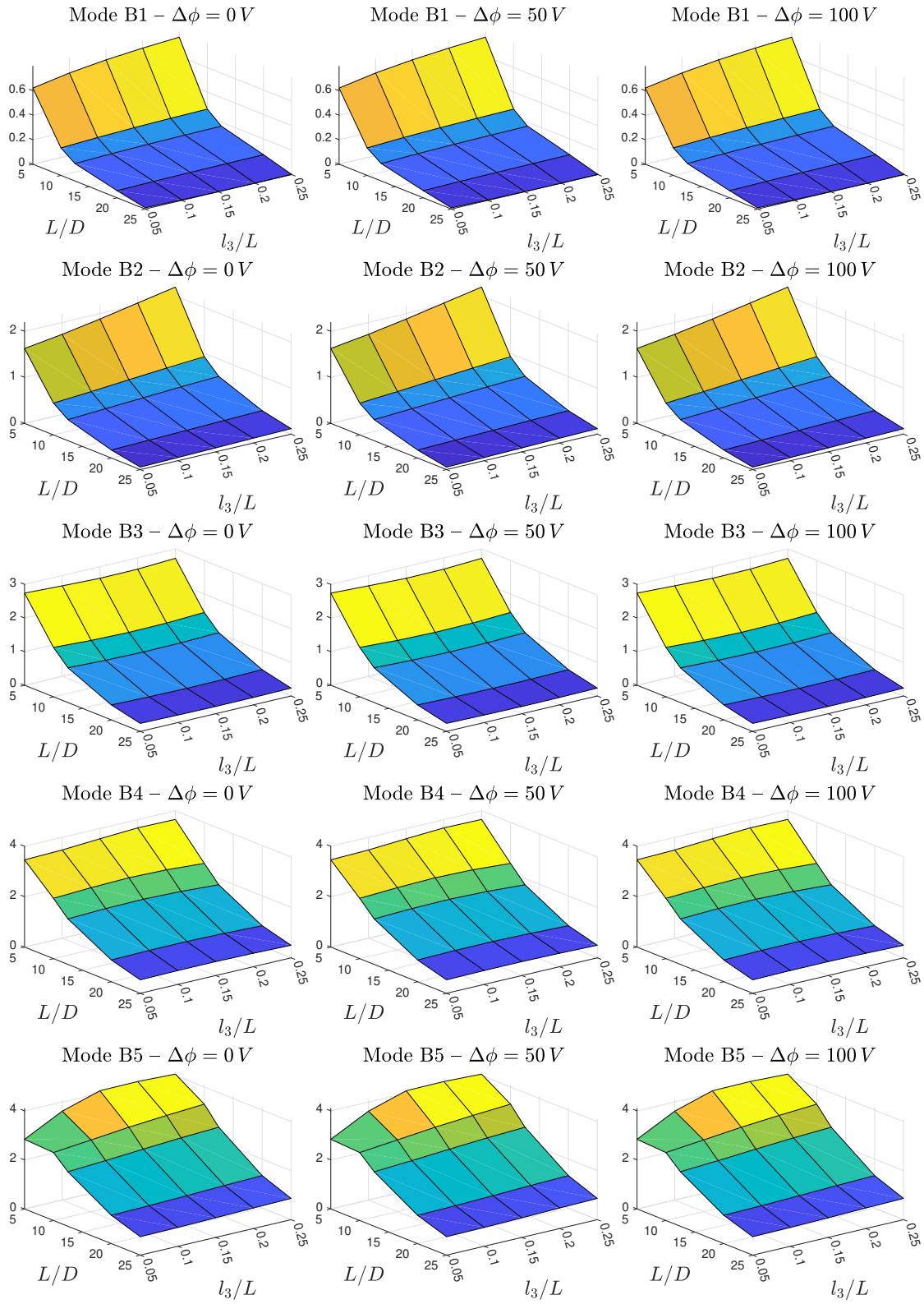

Figure 3.7: Relative differences between the results of 1D and 3D models for the first five bending modes with respect to the L/D ratio, l_3/L ratio, and electric potential $\Delta\phi$. In this figure, the letter B in the title stands for 'bending mode'. For example, B1 means the 1st bending mode.

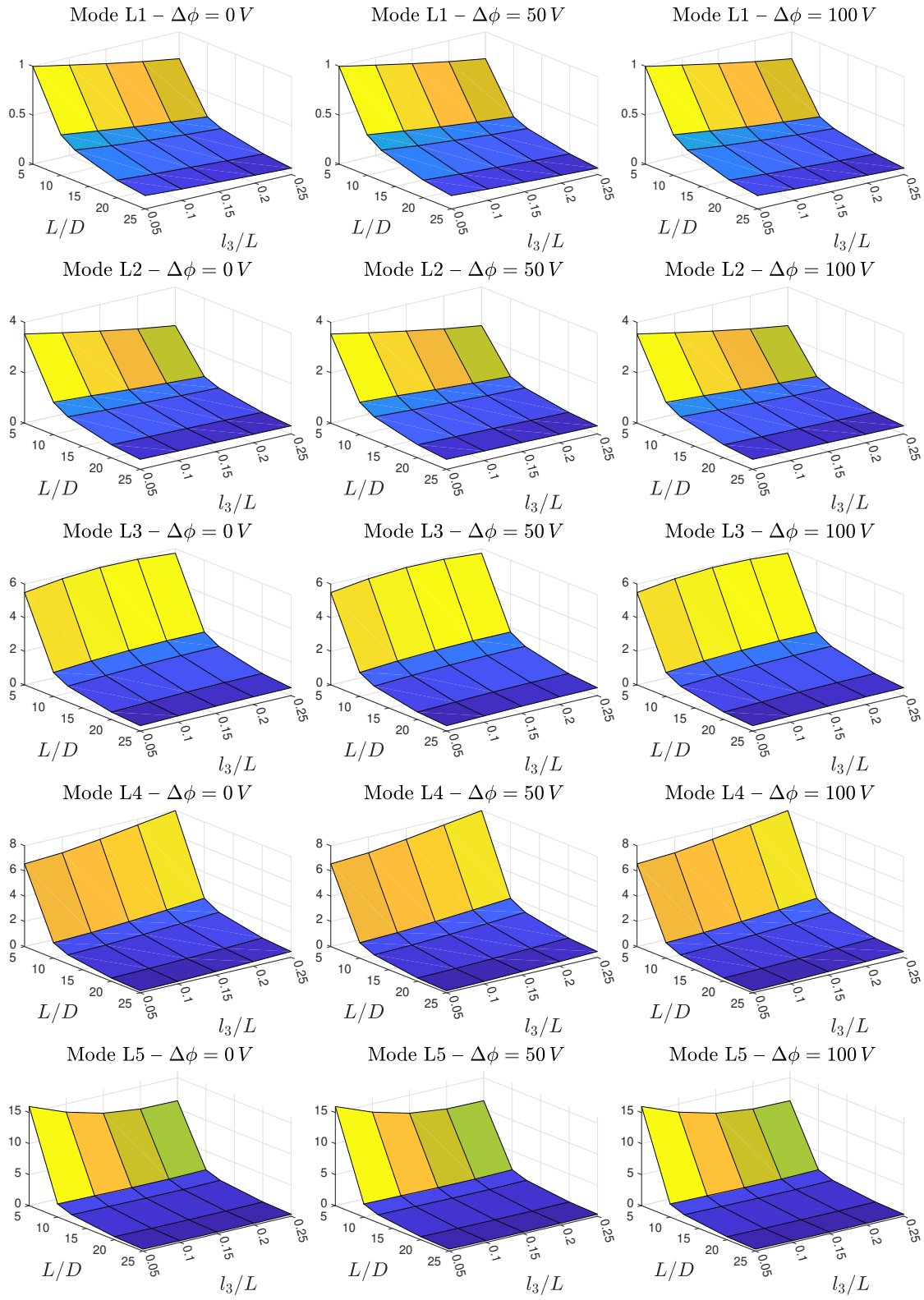

Figure 3.8: Relative differences between the results of 1D and 3D models for the first five longitudinal modes with respect to the L/D ratio, l_3/L ratio, and electric potential $\Delta\phi$. In this figure, the letter L in the title stands for the 'longitudinal mode'. For example, L1 means the 1st longitudinal mode.

Table 3.4: Dimensions of the Langevin transducer prototype.

Parameters	Dimension (mm)
l_1	4
l_2	51.5
l_3	9.2
l_4	40.5
l_5	19
D	8
d	4
D_B	7

To verify the 1D model for solving Langevin transducer dynamics, a Langevin transducer was designed and manufactured with an L/D ratio in the order of 12.5 and a l_3/L ratio of approximately 0.05. The transducer is shown in Figure 3.9. It consists of a titanium front mass, titanium back mass, PZT stack composed of PIC181, and pre-stress bolt made of A2 tool steel. All material properties are identical to those listed in Table A.1.

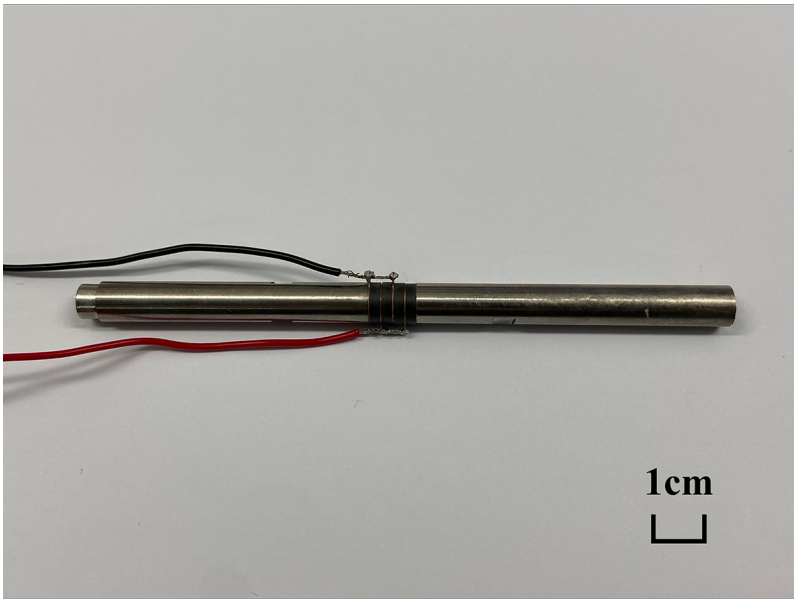

Figure 3.9: The Langevin transducer prototype.

The dimensions of the Langevin transducer prototype are listed in Table 3.4 In order to measure resonant frequencies, mode shapes, and vibration amplitudes, an optical measurement experiment was conducted using the scanning LDV (MSA100, Polytec GmbH, Germany) under an 8V excitation. The experimental characterisations, including LDV, are discussed later in Section 3.3. For this study, experimental measurements for the first ten longitudinal and bending modes were considered and extracted. Calculations were performed to obtain the resonant frequencies for the 1D and 3D models based on the physical structural parameters in Table 3.4. The comparison between the simulation results and the experimental measurements is shown Table 3.5. The symbols ‘L’ and ‘B’ in the table represent the longitudinal and bending modes,

respectively, and the number following the letter indicates the eigenmode order, where the reader is directed to the caption for examples.

Table 3.5: Comparison of resonant frequencies obtained by 1D model, 3D model and LDV measurements. In this table, the letter B in the column mode stands for 'bending mode' and L for the 'longitudinal mode'. For example, B1 and L1 mean the 1st bending and longitudinal modes, respectively. The second row shows how the relative differences in percentages are computed. The frequencies are listed in ascending order of magnitude.

Mode	1D Model (Hz)	3D Model (Hz)	LDV (Hz)	1D Model vs. 3D Model (%)	1D Model vs. LDV (%)	3D Model vs. LDV (%)
B1	2111.4807	2113.9980	2031	0.1191	3.9626	4.0866
B2	5926.9478	5933.2798	6230	0.1067	4.8644	4.7628
B3	10566.6597	10638.2324	10459	0.6728	1.0294	1.7137
B4	17649.8388	17748.2871	18770	0.5547	5.9678	5.4433
L1	20702.1092	20670.4668	19277	0.1531	7.3928	7.2286
B5	24481.3235	24880.9141	26045	1.6060	6.0037	4.4695
B6	33864.6709	34310.3633	34395	1.2990	1.5419	0.2461
L2	40195.6881	40012.6758	38213	0.4574	5.1885	4.7096
B7	42198.0625	43228.8828	44063	2.3846	4.2324	1.8930
B8	52180.8544	53183.7109	52285	1.8856	0.1992	1.7189

According to Table 3.5, it has been found that 1D and 3D models give results in excellent agreement, and both match with LDV results, indicating the accuracy and reliability of the 1D model in calculating resonant frequencies of a Langevin transducer. Except for the L1 mode, 1D and 3D models have a relative difference from LDV results of less than 5%. The results from the 3D model are closer to LDV results than the 1D model in most of the considered modes. The relative differences with LDV results are principally due to manufacturing inconsistencies and the inclusion of electrodes in the PZT stack. Additionally, the modelling theory presented here cannot capture all of the physical phenomena. For example, we did not consider the losses in piezoelectric materials, although this effect may have occurred in the experiment.

For further validation, the 1D model was compared to the 3D model and LDV results in terms of vibration mode shapes for the first ten modes. The results expressed in normalised amplitudes are shown in Figures 3.10 and 3.11.

The normalised amplitude calculated by the 1D model matches that of the 3D model, agreeing well with the LDV results. This confirms that the 1D model can accurately describe the dynamics of a Langevin transducer, either in terms of the resonant frequency or the vibration mode shapes. Overall, the performance of the proposed 1D model is particularly suitable for engineering applications that typically utilise low-order vibration modes.

When considering the application of high electric potentials to the transducer, the participation factor explains the significant modes that can be easily excited. However, the electrical

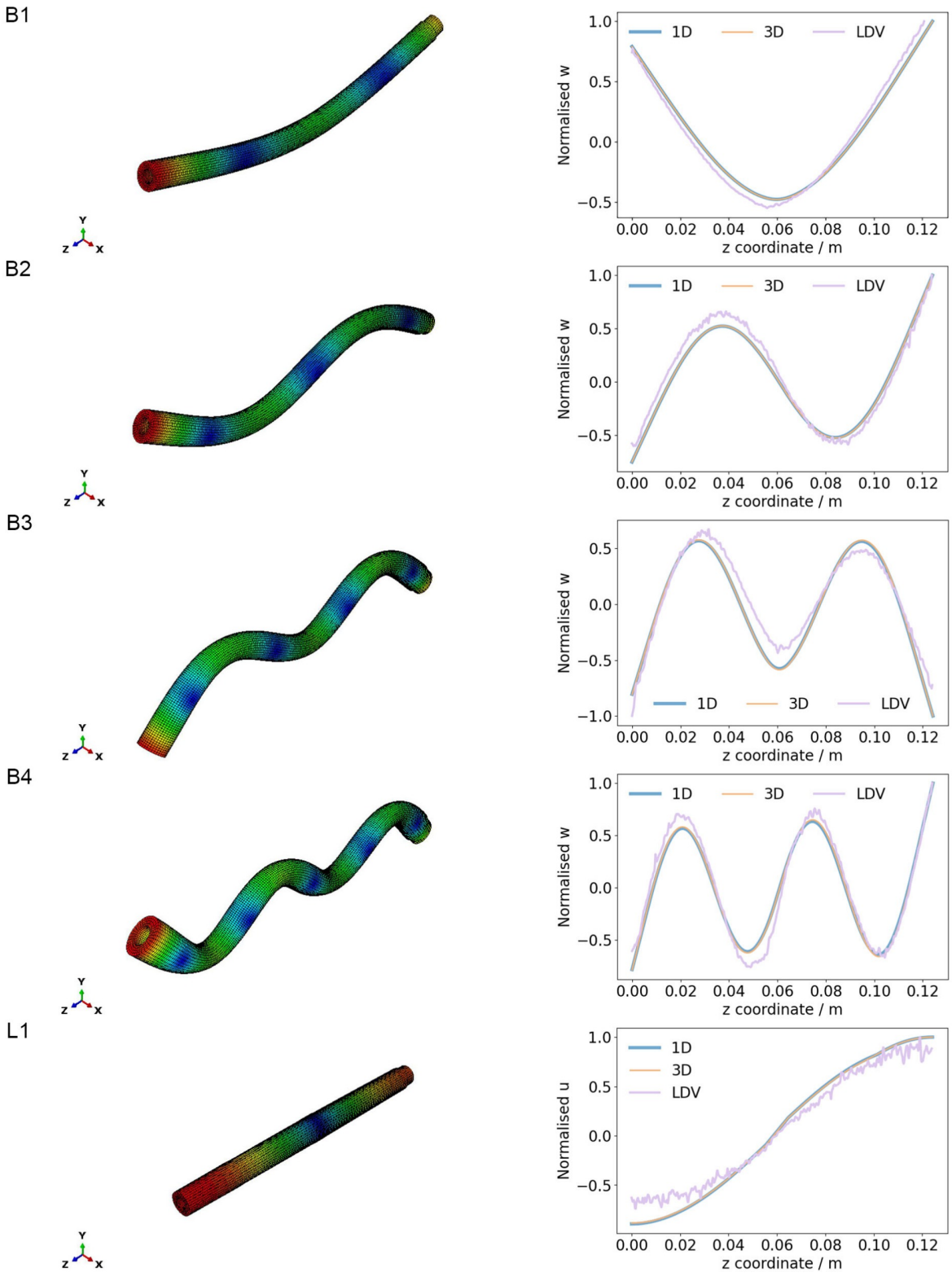

Figure 3.10: Normalised vibration amplitudes and mode shapes between 1D model (numerical), 3D model (FEA), and LDV results for the 1st to 5th modes, including B1, B2, B3, B4, and L1.

field only couples with longitudinal motions and not with the bending modes in this 1D model. Therefore, the participation factor can only be calculated for longitudinal modes by solving (3.69). For instance, the participation factor in the first five longitudinal modes at 50 V and 100

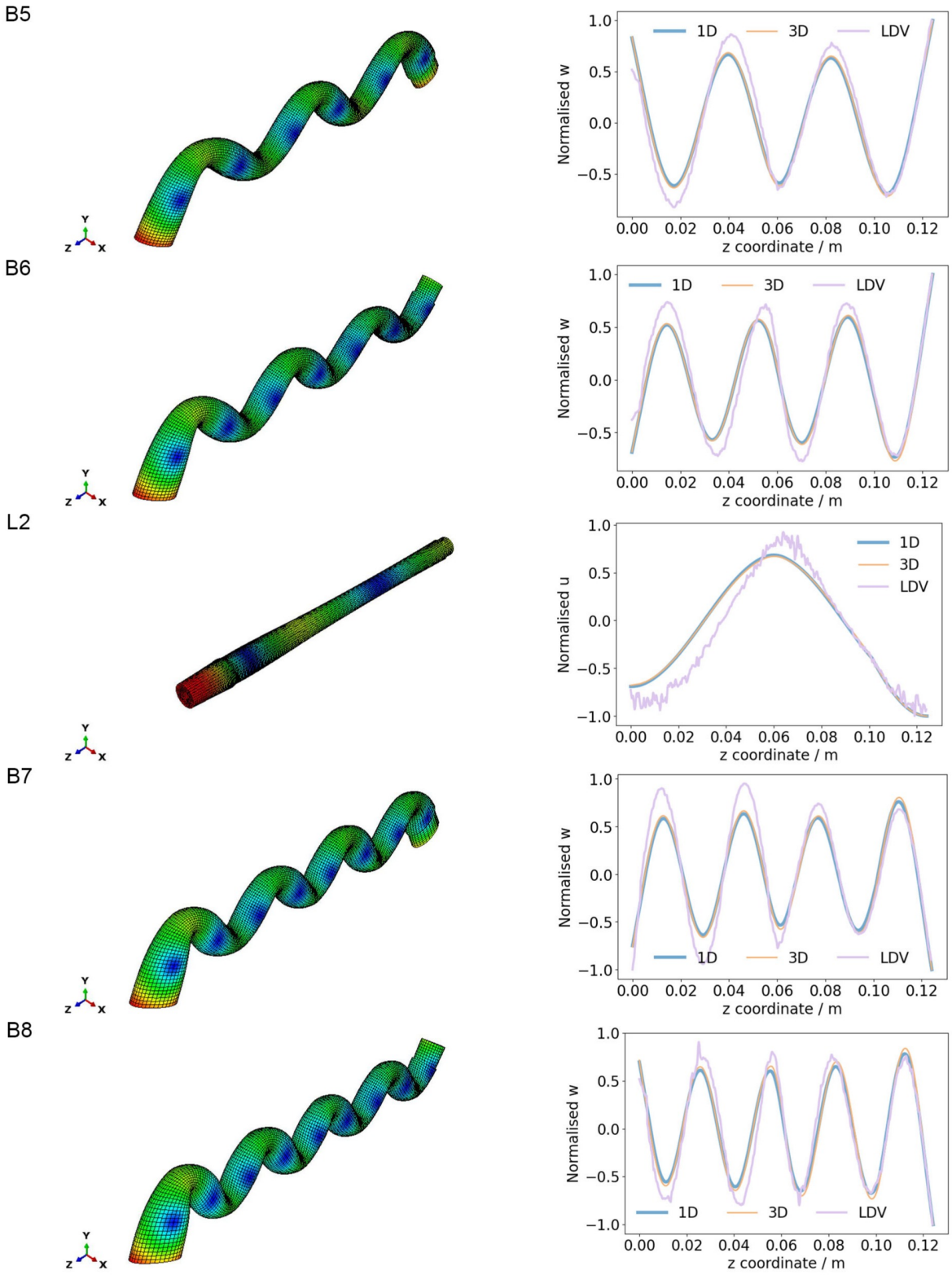

Figure 3.11: Normalised vibration amplitudes and mode shapes between 1D model (numerical), 3D model (FEA), and LDV results for the 6^{th} to 10^{th} modes, including B5, B6, L2, B7, and B8.

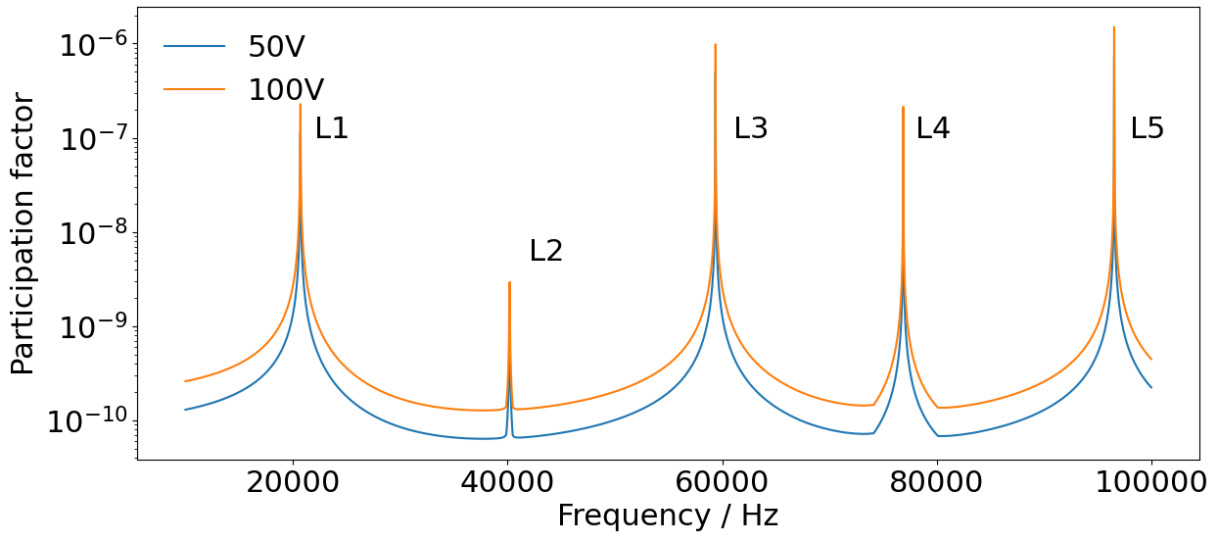

Figure 3.12: Participation factor spectrum in the first five longitudinal modes at 50 V and 100 V, where the frequency ranges from 10^4 Hz to 10^5 Hz with a 1 Hz interval.

V through harmonic analysis is shown in Figure 3.12. The frequency range extends from 10^4 Hz to 10^5 Hz with a one Hz interval. This illustrates that even-order modes (L2 and L4) are easier to excite than single-order ones (L1, L3, and L5). This technique is beneficial for identifying modes and indicating the vibration modes that can be utilised in power ultrasonics to generate high vibration amplitude.

The advantage of the 1D variational framework proposed in this section is that it simplifies the problem by reducing it to one dimension, as the transducer is axisymmetric. This allows for a more efficient and straightforward analysis of the linear piezoelectricity compared to higher-dimensional frameworks [165, 166]. However, the Timoshenko-Ehrenfest beam theory assumes that the cross-section remains in the plane when subjected to shear forces. It is a downside of the 1D variational framework for considering average shear deformation. Nevertheless, the frequency difference compared to the 3D model can be neglected if the L/D ratio is sufficiently large. Additionally, the 1D variational framework makes it easier to visualise the normalised deformation, making it a more accessible approach to understanding the dynamics of Langevin transducers.

3.2.4 Development of the 3D Electromechanical Model

3.2.4.1 Establishing the Variational Equation

The 3D constitutive equations of isotropic and piezoelectric materials have been discussed in (3.7) and (3.12). Regarding these constitutive relations, their strain energy density functions are in (3.9) and (3.15). Considering each segment in the cascaded transducer has the volume $\Omega^{[\mathrm{S}]} \subset \mathbb{R}^3$, where the superscript [S] denotes segment, segment strain energy $W^{[\mathrm{S}]}$ and kinetic energy $T^{[\mathrm{S}]}$ are expressed as:

$$\begin{aligned} W^{[\mathrm{S}]} &= \int_{\Omega^{[\mathrm{S}]}} \psi^{[\mathrm{S}]} \mathrm{d}\Omega \\ T^{[\mathrm{S}]} &= \frac{1}{2} \int_{\Omega^{[\mathrm{S}]}} \mathbf{u}_{,t} \rho^{[\mathrm{S}]} \mathbf{u}_{,t} \mathrm{d}\Omega \end{aligned} \tag{3.70}$$

As there is no work done by external forces, the total energy of the transducer involving n segments is:

$$\Pi = \sum_{\mathrm{S}=1}^{n} (T^{[\mathrm{S}]} - W^{[\mathrm{S}]}) \tag{3.71}$$

The state of transducer motion is obtained by using Hamilton's principle, aiming to minimise the energy in the variational problem:

$$\delta \int_{t_0}^{t_1} [\sum_{\mathrm{S}=1}^{n} (T^{[\mathrm{S}]} - W^{[\mathrm{S}]})] = \int_{t_0}^{t_1} \sum_{\mathrm{S}=1}^{n} (\delta T^{[\mathrm{S}]} - \delta W^{[\mathrm{S}]}) = 0 \tag{3.72}$$

where t_0 and t_1 are the given initial and final time, respectively.

3.2.4.2 Finite Element Process

Let $\mathrm{S} \in \{1, \ldots, \mathrm{S}_{\mathrm{seg}}\}$ index the transducer segments and let $\Omega^{[\mathrm{S}]} \subset \mathbb{R}^3$ denote the physical domain of segment S, with physical coordinates $\mathbf{x} = (x_1, x_2, x_3)$. The domain $\Omega^{[\mathrm{S}]}$ is partitioned into $n_e^{[\mathrm{S}]}$ finite elements. Each element is within the natural domain $\hat{\Omega} = [-1,1]^3 \subset \mathbb{R}^3$ under an isoparametric mapping $\mathbf{x} = \mathbf{F}^{[\mathrm{S}],(e)}(\xi)$, with $\xi = (\xi_1, \xi_2, \xi_3) \in \hat{\Omega}$. Therefore, the sum of strain energy $W^{[\mathrm{S}]}$ and kinetic energy $T^{[\mathrm{S}]}$ in (3.72) decompose additively over the mesh as $W^{[\mathrm{S}]} = \sum_{e=1}^{n_e^{[\mathrm{S}]}} W^{[\mathrm{S}],(e)}$ and $T^{[\mathrm{S}]} = \sum_{e=1}^{n_e^{[\mathrm{S}]}} T^{[\mathrm{S}],(e)}$, where $W^{[\mathrm{S}],(e)}$ and $T^{[\mathrm{S}],(e)}$ are the element contributions given in the variational form below:

$$
\begin{aligned}
\delta W^{[\mathrm{S}],(e)} &= \int_{\Omega^{[\mathrm{S}],(e)}} \frac{1}{2}\delta\boldsymbol{\varepsilon}(\mathbb{C}^{[\mathrm{S}]} : \boldsymbol{\varepsilon}^{[\mathrm{S}],(e)} + (\mathbf{e}^{[\mathrm{S}]})^{\mathrm{T}}\nabla\boldsymbol{\phi}^{[\mathrm{S}],(e)})\mathrm{d}\mathbf{x} \\
&+ \int_{\Omega^{[\mathrm{S}],(e)}} \frac{1}{2}\delta\nabla\boldsymbol{\phi}(\mathbf{e}^{[\mathrm{S}]} : \boldsymbol{\varepsilon}^{[\mathrm{S}],(e)} - \boldsymbol{\chi}^{[\mathrm{S}]}\nabla\boldsymbol{\phi}^{[\mathrm{S}],(e)})\mathrm{d}\mathbf{x} \\
&= \int_{\tilde{\Omega}} \frac{1}{2}\delta\boldsymbol{\varepsilon}(\mathbb{C}^{[\mathrm{S}]} : \boldsymbol{\varepsilon}^{[\mathrm{S}],(e)} + (\mathbf{e}^{[\mathrm{S}]})^{\mathrm{T}}\nabla\boldsymbol{\phi}^{[\mathrm{S}],(e)})\det(\mathbf{J}^{(e)})\mathrm{d}\xi \\
&+ \int_{\tilde{\Omega}} \frac{1}{2}\delta\nabla\boldsymbol{\phi}(\mathbf{e}^{[\mathrm{S}]} : \boldsymbol{\varepsilon}^{[\mathrm{S}],(e)} - \boldsymbol{\chi}^{[\mathrm{S}]}\nabla\boldsymbol{\phi}^{[\mathrm{S}],(e)})\det(\mathbf{J}^{(e)})\mathrm{d}\xi \\
\delta T^{[\mathrm{S}],(e)} &= \int_{\Omega^{[\mathrm{S}],(e)}} \frac{1}{2}\delta\mathbf{u}_{,t}\rho^{[\mathrm{S}]}\mathbf{u}_{,t}^{[\mathrm{S}],(e)}\mathrm{d}\mathbf{x} \\
&= \int_{\tilde{\Omega}} \frac{1}{2}\delta\mathbf{u}_{,t}\rho^{[\mathrm{S}]}\mathbf{u}_{,t}^{[\mathrm{S}],(e)}\det(\mathbf{J}^{(e)})\mathrm{d}\xi
\end{aligned}
\tag{3.73}
$$

where $\mathbf{J} = \det\left(\partial\mathbf{x}/\partial\xi\right) > 0$ denotes the Jacobian matrix, which defines a linear transformation between the natural and physical coordinate systems on elements which is commonly referred to as the reference-to-physical mapping. The element type is identical over the transducer problem domain and each element has p nodes, thus p shape functions $N_i : \Omega^{[e]}$ are obtained by linear approximations. For the geometric discretisation in a 3D FEM problem, four types of elements are typically applied, including tetrahedron, hexahedron, prism, and pyramid. Taking the linear tetrahedron and hexahedron elements as examples, which are the most widely used 3D elements, where the node numbering orders are shown in Figure 3.13.

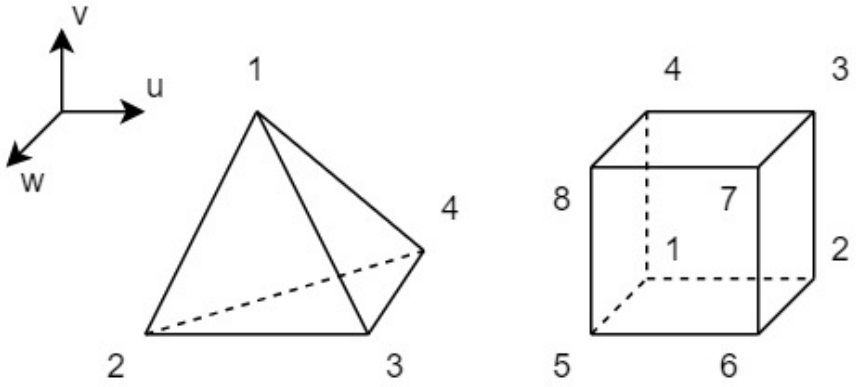

Figure 3.13: Numbering orders of linear tetrahedron and hexahedron elements.

Lagrange polynomials in $p-1$ order is used to derive the shape functions, as given:

$$
N_i(\xi_1, \xi_2, \xi_3, \hat{\xi}) = T_I(\xi_1) \cdot T_J(\xi_2) \cdot T_K(\xi_3) \cdot T_L(\hat{\xi}) \tag{3.74}
$$

where,

$$
\begin{aligned}
\hat{\xi} &= 1 - \xi_1 - \xi_2 - \xi_3, \\
T_I(r) &= \begin{cases} L_I^{I-1}(r)(\dfrac{2r}{r_I} - 1) & I \neq 1 \\ 1, & I = 1 \end{cases}
\end{aligned}
\tag{3.75}
$$

where $L(r)$ are the Lagrange polynomial.

$\mathbf{u}^{[\mathrm{S}],(e)}$ and $\nabla\phi^{[\mathrm{S}],(e)}$ can be rewritten by the nodal degree of freedoms as shown:

$$\mathbf{u}^{[\mathrm{S}],(e)} = \sum_{i=1}^{p} N_i \begin{bmatrix} u_i^{(e)} \\ v_i^{(e)} \\ w_i^{(e)} \end{bmatrix} = \begin{bmatrix} N_1 & 0 & 0 & \cdots & N_p & 0 & 0 \\ 0 & N_1 & 0 & \cdots & 0 & N_p & 0 \\ 0 & 0 & N_1 & \cdots & 0 & 0 & N_p \end{bmatrix} \begin{bmatrix} u_1^{(e)} \\ v_1^{(e)} \\ w_1^{(e)} \\ \vdots \\ u_p^{(e)} \\ v_p^{(e)} \\ w_p^{(e)} \end{bmatrix} = [N]_{(3,3p)} \hat{\mathbf{u}}^{(e)}$$

$$\nabla\phi^{[\mathrm{S}],(e)} = \sum_{i=1}^{p} \frac{\partial N_i}{\partial \xi} \phi_i^{(e)} = \begin{bmatrix} \frac{\partial N_1}{\partial \xi_1} & 0 & 0 & \cdots & \frac{\partial N_p}{\partial \xi_1} & 0 & 0 \\ 0 & \frac{\partial N_1}{\partial \xi_2} & 0 & \cdots & 0 & \frac{\partial N_p}{\partial \xi_2} & 0 \\ 0 & 0 & \frac{\partial N_1}{\partial \xi_3} & \cdots & 0 & 0 & \frac{\partial N_1}{\partial \xi_3} \end{bmatrix} \begin{bmatrix} \phi_1^{(e)} \\ \vdots \\ \phi_p^{(e)} \end{bmatrix} = [N]_{(3,3p),\xi} \hat{\phi}^{(e)} \tag{3.76}$$

where $[u_i^{(e)}, v_i^{(e)}, w_i^{(e)}]^\top \in \mathbb{R}^3$ is the nodal displacement vector of element e in segment S at reference coordinates $\xi = (\xi_1, \xi_2, \xi_3)$. Recalling the strain field ε is a function of the displacement field $\mathbf{u}$:

$$\varepsilon^{[\mathrm{S}],(e)} = \begin{bmatrix} \varepsilon_{11}^{(e)} \\ \varepsilon_{22}^{(e)} \\ \varepsilon_{33}^{(e)} \\ 2\varepsilon_{23}^{(e)} \\ 2\varepsilon_{13}^{(e)} \\ 2\varepsilon_{12}^{(e)} \end{bmatrix} = \begin{bmatrix} \partial u^{(e)}/\partial \xi_1 \\ \partial v^{(e)}/\partial \xi_2 \\ \partial w^{(e)}/\partial \xi_3 \\ \partial v^{(e)}/\partial \xi_3 + \partial w^{(e)}/\partial \xi_2 \\ \partial u^{(e)}/\partial \xi_3 + \partial w^{(e)}/\partial \xi_1 \\ \partial u^{(e)}/\partial \xi_2 + \partial v^{(e)}/\partial \xi_1 \end{bmatrix} \tag{3.77}$$

Substituting nodal displacements in (3.76) into (3.77), the element strain field is rewritten as:

$$\varepsilon^{[\mathrm{S}],(e)} = [B]\hat{\mathbf{u}}^{(e)} \tag{3.78}$$

Where $[B]$ is a $(6 \times p)$ matrix containing the first derivatives of shape functions with respect to the natural coordinate. Strain and kinetic energy for elements in (3.73) can be rewritten by substituting (3.76) and 3.78, as shown:

$$\begin{aligned} \delta W^{[\mathrm{S}],(e)} &= (\delta\hat{\mathbf{u}}^{(e)})^{\mathrm{T}} \cdot (\mathbf{K}_{\mathbf{uu}}^{(e)} \hat{\mathbf{u}}^{(e)} + \mathbf{K}_{\mathbf{u}\phi}^{(e)} \hat{\phi}^{(e)}) \\ &\quad + (\delta\hat{\phi}^{(e)})^{\mathrm{T}} \cdot (\mathbf{K}_{\phi\mathbf{u}}^{(e)} \hat{\mathbf{u}}^{(e)} + \mathbf{K}_{\phi\phi}^{(e)} \hat{\phi}^{(e)}) \\ \delta T^{[\mathrm{S}],(e)} &= -(\delta\hat{\mathbf{u}}^{(e)})^{\mathrm{T}} \cdot \mathbf{M}_{\mathbf{uu}}^{(e)} \hat{\mathbf{u}}_{,tt}^{(e)} \end{aligned} \tag{3.79}$$

where,

$$\begin{aligned}
\mathbf{K}_{\mathbf{uu}}^{(e)} &= \frac{1}{2}\int_{\Omega^{[e]}} [B]^{\mathrm{T}}\mathbb{C}^{[\mathrm{S}]}[B]\mathrm{d}\xi, & \mathbf{K}_{\mathbf{u}\phi}^{(e)} &= \frac{1}{2}\int_{\Omega^{[e]}} [B]^{\mathrm{T}}\mathbf{e}^{[\mathrm{S}]}[N]_{(3\times p),\xi}\mathrm{d}\xi \\
\mathbf{K}_{\phi\phi}^{(e)} &= -\frac{1}{2}\int_{\Omega^{[e]}} [N]_{(3\times p),\xi}^{\mathrm{T}}\boldsymbol{\chi}^{[\mathrm{S}]}[N]_{(3\times p),\xi}\mathrm{d}\xi, & \mathbf{K}_{\phi\mathbf{u}}^{(e)} &= \mathbf{K}_{\mathbf{u}\phi}^{(e)} \\
\mathbf{M}_{\mathbf{uu}}^{(e)} &= \frac{1}{2}[N]_{(3\times p)}^{\mathrm{T}}\boldsymbol{\rho}^{[S]}[N]_{(3\times p)}\mathrm{d}\xi
\end{aligned} \tag{3.80}$$

By substituting $\mathrm{d}\mathbf{x} = \det(\mathbf{J})\mathrm{d}\xi$ into (3.80), a linear mapping is established between the physical coordinate and the natural coordinate. In order to solve the integration over the domain $[-1,1]$, the stiffness matrices are computed using Gaussian quadrature. Therefore, finite element equations of the transducer motion are assembled in the following form:

$$\begin{aligned}
\mathbf{M}_{\mathbf{uu}}\hat{\mathbf{u}}_{,tt} + \mathbf{K}_{\mathbf{uu}}\hat{\mathbf{u}} + \mathbf{K}_{\mathbf{u}\phi}\hat{\phi} &= 0 \\
\mathbf{K}_{\phi\mathbf{u}}\hat{\mathbf{u}} + \mathbf{K}_{\phi\phi}\hat{\phi} &= 0
\end{aligned} \tag{3.81}$$

Taking $\mathbf{u} = \mathbf{U}e^{i\omega t}$ into account, where $\mathbf{U}$ is the vector which represents all nodal displacements in the mechanical field, the above equation is rewritten as:

$$\begin{aligned}
-\omega^2\mathbf{M}_{\mathbf{uu}}\hat{\mathbf{u}} + \mathbf{K}_{\mathbf{uu}}\hat{\mathbf{u}} + \mathbf{K}_{\mathbf{u}\phi}\hat{\phi} &= 0 \\
\mathbf{K}_{\phi\mathbf{u}}\hat{\mathbf{u}} + \mathbf{K}_{\phi\phi}\hat{\phi} &= 0
\end{aligned} \tag{3.82}$$

3.2.4.3 Boundary Conditions

In the context of boundary conditions in a mechanical and electrical system, we define the nodal indices for mechanical boundaries as $i,\ldots,j$ and for electrical boundaries as $k,\ldots,l$. It is important to note that the degrees of freedom (DOF) associated with mechanical nodes are quantified as 3, in contrast to the single degree of freedom attributed to electrical nodes. Let $\hat{n}$ represent the total number of nodes in the system. This framework clearly delineates the differing constraints and functionalities attributed to mechanical and electrical components within the model.

Two types of well-known boundaries are the Dirichlet and Neumann boundaries, indicating fixed and free in the mechanical field, respectively, while short and open circuits in the electrical field. Therefore, four situations are considered in this electromechanical model, which are fixed-short (Dirichlet-Dirichlet), free-short (Neumann-Dirichlet), fixed-open (Dirichlet-Neumann), and free-open (Neumann-Neumann). Here, the author exclusively details the static condensation in applying fixed-short boundaries as an example, with the rest of the situations presented as the final finite element equations.

Fixed (mechanical) & Short (electrical) The Dirichlet is applied to mechanical and electrical fields in this scenario. To minimise redundancy in the subsequent derivation, the nodal DOF indices for mechanical and electrical fields are $\hat{n}_m$ and $\hat{n}_\phi$, respectively. Subsequently, in-

dices that exclude boundary conditions are defined as follows: for mechanical fields, $\tilde{n}_m \in \hat{n}_m \neq [3i, 3i+1, 3i+2, \ldots, 3j, 3j+1, 3j+2]$, and for electrical fields, $\tilde{n}_\phi \in \hat{n}_\phi \neq [k, \ldots, l]$.

Applying boundary conditions to the first equation in 3.82, as given:

$$\begin{aligned} &-\omega^2 \tilde{\mathbf{M}}_{\mathbf{uu}} \tilde{\mathbf{u}} + \tilde{\mathbf{K}}_{\mathbf{uu}} \tilde{\mathbf{u}} + \tilde{\mathbf{K}}_{\mathbf{u}\phi} \tilde{\phi} = \\ &- \sum_{m \in \tilde{n}_m} \omega^2 U_m \begin{bmatrix} \mathbf{M}_{\mathbf{uu}}^{1,m} \\ \vdots \\ \mathbf{M}_{\mathbf{uu}}^{\hat{n}_m,m} \end{bmatrix} - \sum_{m \in \tilde{n}_m} U_m \begin{bmatrix} \mathbf{K}_{\mathbf{uu}}^{1,m} \\ \vdots \\ \mathbf{K}_{\mathbf{uu}}^{\hat{n}_m,m} \end{bmatrix} - \sum_{n \in \tilde{n}_\phi} V_n \begin{bmatrix} \mathbf{K}_{\mathbf{u}\phi}^{1,n} \\ \vdots \\ \mathbf{K}_{\mathbf{u}\phi}^{\hat{n}_m,n} \end{bmatrix} \end{aligned} \tag{3.83}$$

Then, applying boundary conditions to the second equation in (3.82), as given:

$$\tilde{\mathbf{K}}_{\phi\mathbf{u}} \tilde{\mathbf{u}} + \tilde{\mathbf{K}}_{\phi\phi} \tilde{\phi} = - \sum_{m \in \tilde{n}_m} U_m \begin{bmatrix} \mathbf{K}_{\phi\mathbf{u}}^{1,m} \\ \vdots \\ \mathbf{K}_{\phi\mathbf{u}}^{\hat{n}_\phi,m} \end{bmatrix} - \sum_{n \in \tilde{n}_\phi} V_n \begin{bmatrix} \mathbf{K}_{\phi\phi}^{1,n} \\ \vdots \\ \mathbf{K}_{\phi\phi}^{\hat{n}_\phi,n} \end{bmatrix} \tag{3.84}$$

where $\tilde{\mathbf{K}}_{\phi\mathbf{u}} \in \mathbb{R}^{\tilde{n}_\phi \times \tilde{n}_m}$, $\tilde{\mathbf{K}}_{\phi\phi} \in \mathbb{R}^{\tilde{n}_\phi \times \tilde{n}_e}$,$\tilde{\mathbf{u}} \in \mathbb{R}^{\tilde{n}_m \times 1}$, and $\tilde{\phi} \in \mathbb{R}^{\tilde{n}_\phi \times 1}$. The electric potential vector can subsequently be expressed by displacement, as provided:

$$\tilde{\phi} = -\tilde{\mathbf{K}}_{\phi\phi}^{-1} \tilde{\mathbf{K}}_{\phi\mathbf{u}} \tilde{\mathbf{u}} - \sum_{m \in \tilde{n}_m} U_m \tilde{\mathbf{K}}_{\phi\phi}^{-1} \begin{bmatrix} \mathbf{K}_{\phi\mathbf{u}}^{1,m} \\ \vdots \\ \mathbf{K}_{\phi\mathbf{u}}^{\hat{n}_\phi,m} \end{bmatrix} - \sum_{n \in \tilde{n}_\phi} V_n \tilde{\mathbf{K}}_{\phi\phi}^{-1} \begin{bmatrix} \mathbf{K}_{\phi\phi}^{1,n} \\ \vdots \\ \mathbf{K}_{\phi\phi}^{\hat{n}_\phi,n} \end{bmatrix} \tag{3.85}$$

The final step of static condensation replaces the potential vector in 3.83, and the finite element equation for the whole system is rewritten:

$$\begin{aligned} &[\tilde{\mathbf{K}}_{\mathbf{uu}} - \tilde{\mathbf{K}}_{\mathbf{u}\phi} \tilde{\mathbf{K}}_{\phi\phi}^{-1} \tilde{\mathbf{K}}_{\phi\mathbf{u}} - \omega^2 \tilde{\mathbf{M}}_{\mathbf{uu}}] \tilde{\mathbf{u}} = \\ &\sum_{m \in \tilde{n}_m} U_m \tilde{\mathbf{K}}_{\mathbf{u}\phi} \tilde{\mathbf{K}}_{\phi\phi}^{-1} \begin{bmatrix} \mathbf{K}_{\phi\mathbf{u}}^{1,m} \\ \vdots \\ \mathbf{K}_{\phi\mathbf{u}}^{\hat{n}_\phi,m} \end{bmatrix} + \sum_{n \in \tilde{n}_\phi} V_n \tilde{\mathbf{K}}_{\mathbf{u}\phi} \tilde{\mathbf{K}}_{\phi\phi}^{-1} \begin{bmatrix} \mathbf{K}_{\phi\phi}^{1,n} \\ \vdots \\ \mathbf{K}_{\phi\phi}^{\hat{n}_\phi,n} \end{bmatrix} \\ &- \sum_{m \in \tilde{n}_m} \omega^2 U_m \begin{bmatrix} \mathbf{M}_{\mathbf{uu}}^{1,m} \\ \vdots \\ \mathbf{M}_{\mathbf{uu}}^{\hat{n}_m,m} \end{bmatrix} - \sum_{m \in \tilde{n}_m} U_m \begin{bmatrix} \mathbf{K}_{\mathbf{uu}}^{1,m} \\ \vdots \\ \mathbf{K}_{\mathbf{uu}}^{\hat{n}_m,m} \end{bmatrix} - \sum_{n \in \tilde{n}_\phi} V_n \begin{bmatrix} \mathbf{K}_{\mathbf{u}\phi}^{1,n} \\ \vdots \\ \mathbf{K}_{\mathbf{u}\phi}^{\hat{n}_m,n} \end{bmatrix} \end{aligned} \tag{3.86}$$

Free (mechanical) & Short (electrical) Following the same static condensation method detailed above, the finite element equation for the system is expressed as follows:

$$[\mathbf{K_{uu}} - \widehat{\mathbf{K}}_{\mathbf{u}\phi}\tilde{\mathbf{K}}_{\phi\phi}^{-1}\widehat{\mathbf{K}}_{\phi\mathbf{u}} - \omega^2\mathbf{M_{uu}}]\mathbf{u} = \sum_{n\in\tilde{n}_\phi} V_n \widehat{\mathbf{K}}_{\mathbf{u}\phi}\tilde{\mathbf{K}}_{\phi\phi}^{-1}\begin{bmatrix}\mathbf{K}_{\phi\phi}^{1,n}\\ \vdots \\ \mathbf{K}_{\phi\phi}^{\hat{n}_\phi,n}\end{bmatrix} - \sum_{n\in\tilde{n}_\phi} V_n \begin{bmatrix}\mathbf{K}_{\mathbf{u}\phi}^{1,n}\\ \vdots \\ \mathbf{K}_{\mathbf{u}\phi}^{\hat{n}_m,n}\end{bmatrix} \tag{3.87}$$

where $\tilde{\mathbf{K}}_{\phi\phi} \in \mathbb{R}^{\tilde{n}_\phi \times \tilde{n}_\phi}$, $\widehat{\mathbf{K}}_{\mathbf{u}\phi} \in \mathbb{R}^{\hat{n}_m \times \tilde{n}_\phi}$, $\widehat{\mathbf{K}}_{\phi\mathbf{u}} \in \mathbb{R}^{\tilde{n}_\phi \times \hat{n}_m}$.

The electric potential is expressed as:

$$\tilde{\phi} = -\tilde{\mathbf{K}}_{\phi\phi}^{-1}\widehat{\mathbf{K}}_{\phi\mathbf{u}}\tilde{\mathbf{u}} - \sum_{n\in\tilde{n}_\phi} V_n \tilde{\mathbf{K}}_{\phi\phi}^{-1}\begin{bmatrix}\mathbf{K}_{\phi\phi}^{1,n}\\ \vdots \\ \mathbf{K}_{\phi\phi}^{\hat{n}_\phi,n}\end{bmatrix} \tag{3.88}$$

Fixed (mechanical) & Open (electrical) The finite element equation for the system is expressed as follows:

$$[\tilde{\mathbf{K}}_{\mathbf{uu}} - \widehat{\mathbf{K}}_{\mathbf{u}\phi}\mathbf{K}_{\phi\phi}^{-1}\widehat{\mathbf{K}}_{\phi\mathbf{u}} - \omega^2\tilde{\mathbf{M}}_{\mathbf{uu}}]\tilde{\mathbf{u}} = \sum_{m\in\tilde{n}_m} U_m \widehat{\mathbf{K}}_{\mathbf{u}\phi}\mathbf{K}_{\phi\phi}^{-1}\begin{bmatrix}\mathbf{K}_{\phi\mathbf{u}}^{1,m}\\ \vdots \\ \mathbf{K}_{\phi\mathbf{u}}^{\hat{n}_\phi,m}\end{bmatrix} - \sum_{m\in\tilde{n}_m} \omega^2 U_m \begin{bmatrix}\mathbf{M}_{\mathbf{uu}}^{1,m}\\ \vdots \\ \mathbf{M}_{\mathbf{uu}}^{\hat{n}_m,m}\end{bmatrix} - \sum_{m\in\tilde{n}_m} U_m \begin{bmatrix}\mathbf{K}_{\mathbf{uu}}^{1,m}\\ \vdots \\ \mathbf{K}_{\mathbf{uu}}^{\hat{n}_m,m}\end{bmatrix} \tag{3.89}$$

where $\tilde{\mathbf{K}}_{\mathbf{uu}} \in \mathbb{R}^{\tilde{n}_m \times \tilde{n}_m}$, $\tilde{\mathbf{M}}_{\mathbf{uu}} \in \mathbb{R}^{\tilde{n}_m \times \tilde{n}_m}$, $\widehat{\mathbf{K}}_{\mathbf{u}\phi} \in \mathbb{R}^{\tilde{n}_m \times \hat{n}_\phi}$, $\widehat{\mathbf{K}}_{\phi\mathbf{u}} \in \mathbb{R}^{\hat{n}_\phi \times \tilde{n}_m}$, and $\tilde{\mathbf{u}} \in \mathbb{R}^{\tilde{n}_m \times 1}$.

The electric potential is expressed as:

$$\phi = -\mathbf{K}_{\phi\phi}^{-1}\widehat{\mathbf{K}}_{\phi\mathbf{u}}\tilde{\mathbf{u}} - \sum_{m\in\tilde{n}_m} U_m \mathbf{K}_{\phi\phi}^{-1}\begin{bmatrix}\mathbf{K}_{\phi\mathbf{u}}^{1,m}\\ \vdots \\ \mathbf{K}_{\phi\mathbf{u}}^{\hat{n}_\phi,m}\end{bmatrix} \tag{3.90}$$

Free (mechanical) & Open (electrical) The finite element equation for the system is expressed as follows:

$$[\mathbf{K_{uu}} - \mathbf{K}_{\mathbf{u}\phi}\mathbf{K}_{\phi\phi}^{-1}\mathbf{K}_{\phi\mathbf{u}} - \omega^2\mathbf{M_{uu}}]\mathbf{u} = 0 \tag{3.91}$$

The electric potential is expressed as:

$$\phi = -\mathbf{K}_{\phi\phi}^{-1}\mathbf{K}_{\phi\mathbf{u}}\mathbf{u} \tag{3.92}$$

All simulations of (3.86), (3.87), (3.89), and (3.91) have been carried out using self-developed Python code based on the 3D mathematical models in this thesis. The results were compared against Abaqus, confirming both correctness and robustness. In addition, the custom implementation of above boundary conditions allows for more flexible and problem-specific

functionality beyond the scope of typical commercial solvers. Material properties applied in this study, including elastic modulus, Poisson's ratio, density for isotropic materials, stiffness, piezoelectric, and permittivity matrices for piezoelectric materials, are given in Appendix A.

The flexibility of the developed FEM is demonstrated typically based on L1 mode, where the eigenfrequency is solved under free-short and free-open conditions, followed by a single-frequency analysis at resonance under short-circuit conditions. The dimensions and materials of the model are consistent with the simplified configuration in the 1D model. This part applies four-nodes tetrahedral elements to mesh the entire transducer. The results for the eigenfrequency problem are plotted by ParaView and are shown in Figure 3.14.

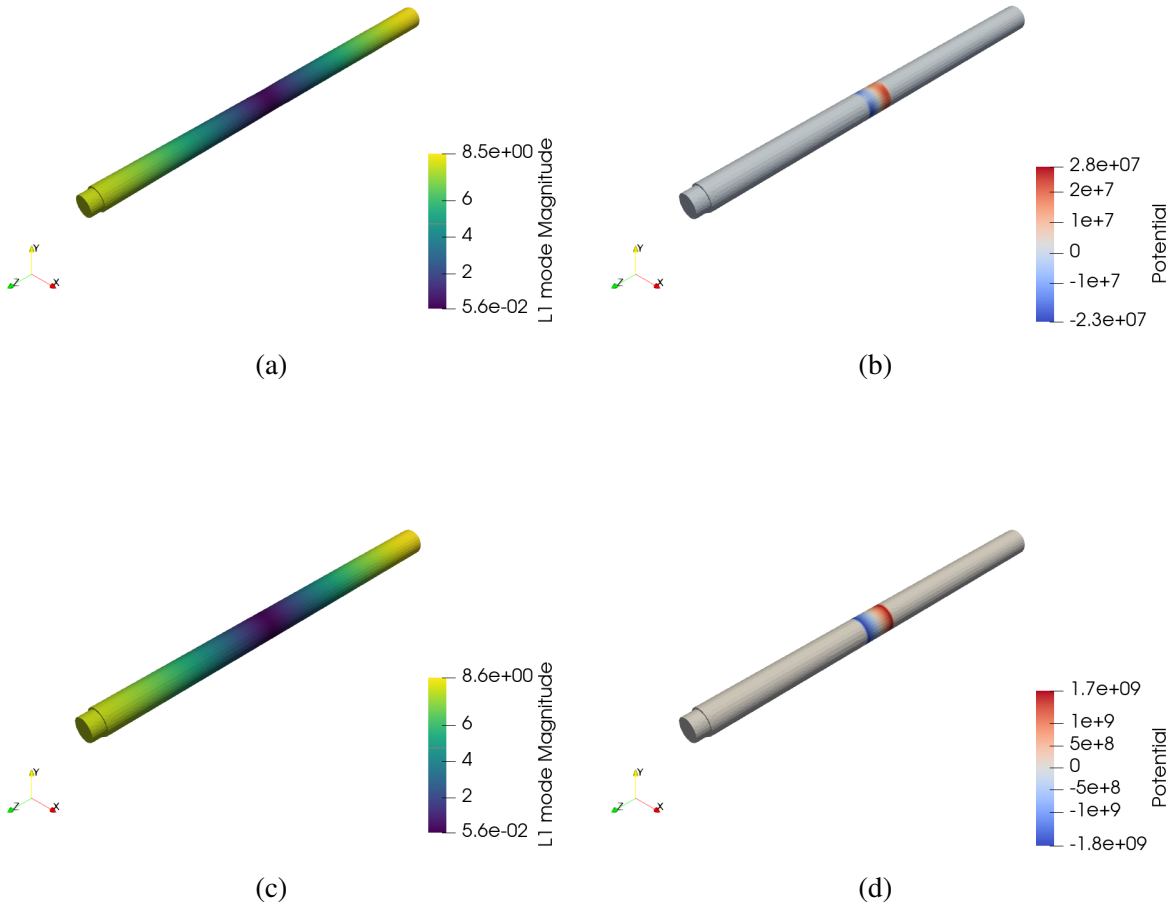

Figure 3.14: Demonstration of developed 3D electromechanical model based on a Langevin transducer in its L1 mode, illustrating (a) mode shape and (b) electric potential under free-short conditions at eigenfrequency of 20657 Hz (resonance), and (c) mode shape and (d) electric potential under free-open conditions at eigenfrequency of 20940 Hz (anti-resonance).

In Figure 3.14, the eigenfrequency of L1 mode at resonance is 20657 Hz, which is different from 20670 Hz in the 3D model by Abaqus shown in Table 3.5. The reasons are likely meshing quality and number of elements. Additionally, due to lack of parallelisation, crucial for

large-scale simulations, results in longer computation times. Although Abaqus is widely used for piezoelectric simulations, implementing custom electromechanical coupling, such as electric potential distribution, can be restrictive. Therefore, the proposed model has been used throughout the thesis, along with results obtained from Abaqus, to append the electric information for the designed Nitinol transducers.

3.3 General Overview of Experimental Characterisations

3.3.1 Electrical Impedance Analysis

An ultrasonic transducer can be operated at resonant or anti-resonant frequency, depending on the device's functionality in an application. For example, the resonant frequency, also named short circuit resonance or series resonance, is a common choice. Its low electrical impedance allows high vibration amplitudes during moderate loading. In contrast, when the transducer vibrates at its anti-resonant frequency, which is also called open circuit resonance or parallel resonance, it typically has high electrical impedance, where minimal current flows through the system. As a result, a high voltage input is needed to maintain vibration amplitudes, along with high loading resistance [167]. The piezoelectric transducer has electrical impedance characteristics, usually appearing capacitive away from the electrical resonance and anti-resonance while inductive between them. However, configurations and mode shapes affect phase properties, especially magnitude and window, as seen in flextensional transducers [168] and pMUT [169], showing capacitive impedance throughout resonance. An electrical impedance analyser (EIA) is used to characterise the electrical impedance of a transducer. Here, the measured electrical impedance is a complex number, where its value combines resistance and reactance, indicating opposition to alternating current (AC), and its phase demonstrates whether the transducer is conductive, inductive or resistive. Based on general Ohm's law for reactive elements, a single linear relationship between AC voltages and currents, the complex impedance is given by:

$$Z = \frac{V}{I} = \frac{|V|}{|I|} e^{\mathbf{j}(\theta_V - \theta_I)} \tag{3.93}$$

where $V = |V|e^{\mathbf{j}(\omega t + \theta_V)}$ and $I = |I|e^{\mathbf{j}(\omega t + \theta_I)}$ are the AC voltage and current with frequency ω. Generally, the phase difference $(\theta_V - \theta_I)$ in 3.93 demonstrates the phase that the current lags the voltage and has been widely rewritten as $\theta = (\theta_V - \theta_I)$.

The BVD model, an analogous equivalent circuit, approximately describes the electrical resonance behaviours of a transducer. A conventional BVD model consists of one mechanical and one electrical branch, representing a single mode. However, multiple modes exist in the piezoelectric transducer, and one mechanical branch does not demonstrate the whole system. These modes can be represented by modifying the BVD circuit model with additional mechanical branches, where each branch stands for a single vibration mode. The model comprises branches

of series of a capacitor, inductor, and resistor, with all shunted by a parallel capacitor, as shown in Figure 3.15 [170, 171].

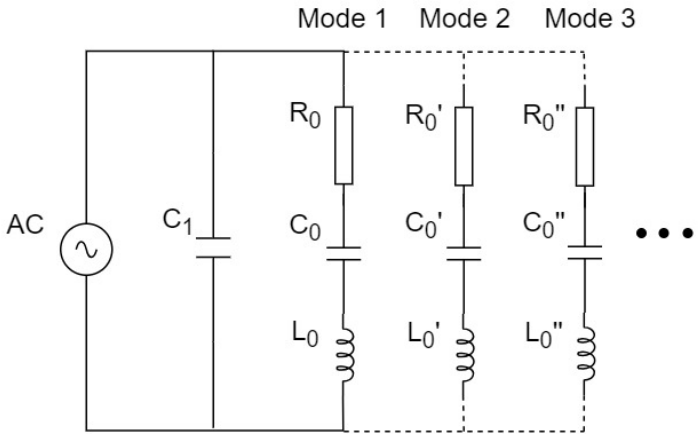

Figure 3.15: BVD equivalent circuit for piezoelectric transducers for multiple vibration modes.

In Figure 3.15, C_1 represents the dielectric capacitance, C_0 is the mechanical capacitance, L_0 is the mechanical inductance, R_0 is the mechanical resistance, and the branch of C_0, L_0, and R_0 is named a mechanical branch. For a piezoelectric transducer with a single vibration mode, only one mechanical branch remains. The mechanical branch indicates analogous mechanical properties of the transducer based on the electric field. Mechanical–electrical analogies represent mechanical systems as electrical networks and vice versa, showing similarity between mechanical and electrical fields [172]. A classic impedance analogy can explain the BVD model, showing relationships between electrical, mechanical, and acoustical parameters. Analogous parameters are listed in Table 3.6.

Electrical parameter		Mechanical parameter		Acoustical parameter
Electrical impedance	$\Leftrightarrow$	Mechanical impedance	$\Leftrightarrow$	Acoustic impedance
Capacitance	$\Leftrightarrow$	Mechanical compliance	$\Leftrightarrow$	Acoustic compliance
Resistance	$\Leftrightarrow$	Mechanical damping	$\Leftrightarrow$	Acoustic damping
Inductance	$\Leftrightarrow$	Mass	$\Leftrightarrow$	Inertance

Table 3.6: Classic impedance analogy between electrical, mechanical, and acoustical parameters.

Based the BVD model, which is a second order electrical circuits, impedance for a single vibration mode is given by:

$$Z_r = \frac{1 - \omega^2 C_0 L_0 + \mathbf{j}\omega C_0 R_0}{\mathbf{j}\omega(C_1 + C_0) - \omega^2 C_1 C_0 R_0 - \mathbf{j}\omega^3 C_1 C_0 L_1} \tag{3.94}$$

In (3.94), Z_r is the electrical impedance for a single vibration mode. The BVD is defined iteratively from (3.94) after measuring the electrical impedance, to achieve an optimal fitness between frequency responses of a BVD model and an experimental impedance spectrum. This

allows for indirect analysis of the mechanical behaviour of the piezoelectric transducer from its electrical properties. The advantage is that this technique enables the analysis of transducer dynamics when there are changes in the transducer temperature or excitation, which has limitations for physical measurements like LDV, primarily when the Nitinol Langevin transducer performs martensitic transformation under high excitation.

In this study, an impedance analyser (4294A, Keysight Technologies, CA, USA) has been principally used throughout the experiments, with its frequency range from 40 Hz to 110 MHz, a minimum one mHz resolution, and a maximum of 801 measurement points. One advantage of EIA is that it avoids the nonlinearity of PZT materials, which is a polarisation variation due to high excitation. As its low voltage signal ranges from 5 mV_{RMS} to 1 V_{RMS}, polarisation changes in PZT are negligible. Therefore, it measures the electrical response from the transducer in its static state. It is worth noting that the transducer must be grounded at elevated temperatures, such as Nitinol Langevin undergoing resonance tuning with temperature, before connecting to the EIA setup. This is because the temperature variation changes the PZT polarisation [173], thus generating charges. However, the current signal level of EIA ranges from 200 μA_{RMS} to 20 mA_{RMS}, meaning even a minimal burst of current from the transducer could damage the internal circuit module of EIA. A diagram showing the impedance spectrum of a piezoelectric transducer at resonance is presented in Figure 3.16, where electrodes of piezoelectric materials are connected to the impedance analyser probes.

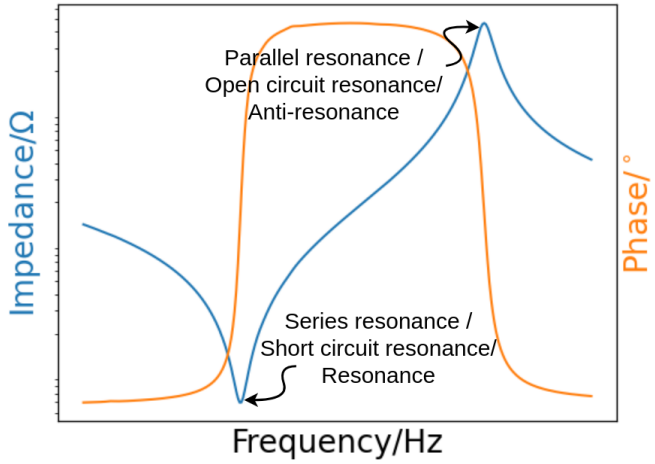

Figure 3.16: A diagram of electrical impedance spectrum.

The impedance spectrum approximately locate the resonance and anti-resonance. However, for an ultrasonic transducer, the resonant frequency includes electrical resonant frequency, which is at the zero phase, and mechanical resonant frequency, where the conductance reaches the maximum [174]. To obtain the mechanical and electrical resonant frequencies, the admittance loop is a widely used, a diagram example is shown in Figure 3.17.

In Figure 3.17, the susceptance is an imaginary part of admittance, a reciprocal of impedance, and the conductance is a real part. f_m, f_s and f_r represent frequencies of the piezoelectric

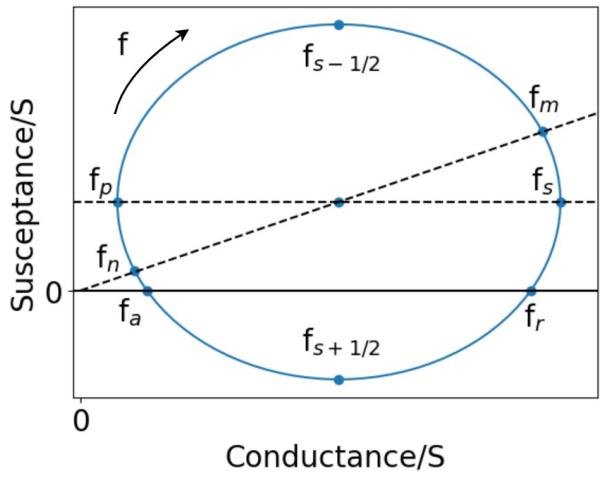

Figure 3.17: A diagram of a typical admittance loop.

transducer at maximum admittance, maximum conductance, and zero susceptance, respectively. Also, f_n, f_p, and f_a represent frequencies at maximum impedance, maximum resistance, and zero reactance, respectively. It is evident that the mechanical resonant frequency f_s differs from the electrical resonant frequency f_r. This is because mechanical and electrical losses lag the electrical resonance by a phase angle [175]. However, this phase lag is negligible in the Langevin transducer at a low excitation and constant temperature, which minimises the losses. The Q factor for a Langevin transducer in its first longitudinal mode is critically high, resulting in a fast phase shift near the electrical resonance. In this case, a small phase lag does not cause a significant frequency difference between mechanical and electrical resonant frequencies.

3.3.2 Experimental Modal Analysis

As mentioned above, EIA can obtain the resonance behaviours of the transducer, while the impedance spectrum only indicates the electrical properties and resonant frequencies rather than modal analysis. It is important to obtain such modal information, especially mode shapes, since it helps for understanding and optimising the structural dynamics of a transducer. For example, in ultrasonic applications, nodes and anti-nodes of a transducer, provided by the mode shapes, inform the positions of the working tip and mechanical clamping, respectively. Here, experimental modal analysis (EMA) determines the modal parameters of the piezoelectric transducer, such as resonant frequencies and mode shapes. In contrast to the analytical modal analysis, where the modal parameters are obtained theoretically, EMA uses modal identification algorithms to process experimental input-output data [176]. This input parameter represents the electric signal applied to the piezoelectric materials and involves sinusoidal, random, pseudo-random, or impulsive excitation [177]. According to DOF of the experimental setup measures, subsequent output is obtained from collecting modal parameters from multiple receiving channels. By constructing the modal parameters of all measured points in the frequency domain

to a model representing the scanned object, vibration mode shapes and modal vectors can be illustrated graphically. In this study, the modal parameters of transducers have been measured by LDV, including scanning (MSA100, Polytec GmbH, Germany) and 3D (CLV3000, Polytec GmbH, Germany) versions. The measuring principle of LDV is that the system analyses resolved Doppler frequency variations by collecting backscattered laser data from the transducer surface, as an example of the scanning LDV shown in Figure 3.18.

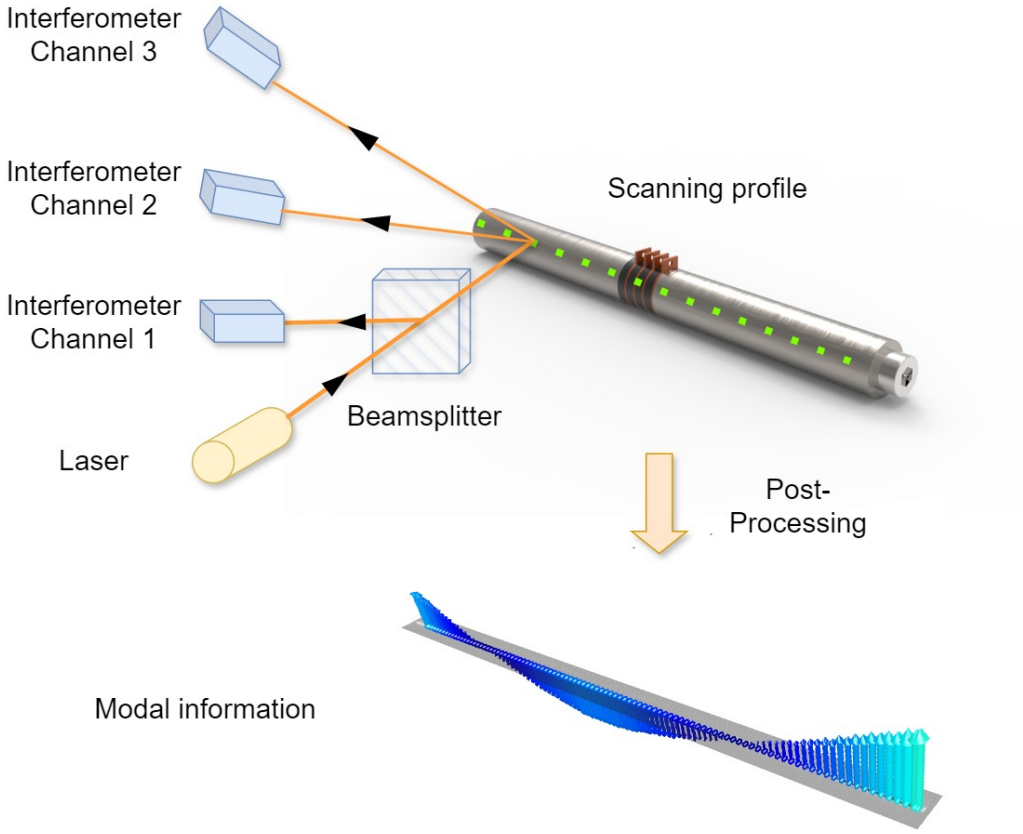

Figure 3.18: Working principle of the scanning LDV.

In Figure 3.18, each interferometer measures one off-axis in-situ vibration on the scanning profile, including amplitude, velocity, and acceleration, where the transducer is excited by a periodic chirp signal in this study. The collected broadband data concerning time is transformed in Cartesian coordinates, and the fast Fourier transformation is applied to process data to the frequency domain. By constructing data from scanned points on the transducer surface, the vibration mode shapes in all resonance modes within a defined frequency range can be demonstrated subsequently in a post-processing step. It is crucial to utilise the LDV techniques to validate the dynamics of the Nitinol Langevin transducer in its designed modes after manufacturing, emphasising consistency throughout the design process.

3.3.3 Harmonic Analysis

Power ultrasonic devices often operate at high power levels, inducing nonlinear dynamics. The amplitude–frequency and impedance–frequency responses become asymmetric about the resonance, exhibiting a 'shark-fin' profile. This is distinct to the dynamic results that obtained from both EIA and EMA which take low voltage input into account. Nonlinear behaviour in ultrasonic transducers causes the disproportionality between output amplitude and input excitation, resonance shifts, mechanical and electrical losses, and amplitude surges, resulting in unwanted degradation on transducer performance [178]. To understand the nonlinearity of a transducer, it is challenging to describe it by a mathematical model, as the nonlinear behaviours stem from either dimensional or material properties. Although some models have been proposed by adding extra terms to the constitutive law, the physical meaning of these terms are still unclear [179]. Therefore, to explore this nonlinear phenomenon, harmonic analysis becomes a practical method since it experimentally measures the transducer nonlinearity [180]. A harmonic system uses LDV to measure the vibration amplitude responses with frequency in a typical mode shape. As input voltage increases, the vibration response becomes strongly nonlinear and the resonance of the first longitudinal mode generally shifts to lower frequency. However, due to the amplitude saturation and frequency hysteresis proposed in the literature where unstable surges appear near the resonance, the nonlinearity can only be characterised by sweeping frequency upwards and downwards [178, 180, 181]. As the Langevin transducer is a complex system that involves materials, structures, and operations, any nonlinearities within these aspects should be considered as they contribute to the nonlinearity in the transducer dynamics. In a Nitinol Langevin transducer, nonlinearities in Nitinol properties caused by the martensitic transformation may lead to unique dynamic responses dependent on temperature and excitation. This highlights the need to characterise the designed transducers' nonlinear behaviour using harmonic analysis.

In this study, the harmonic system involves using an arbitrary waveform generator (33220A, Agilent, USA) to create a sinusoidal voltage signal as the input to operate the transducer, where voltage signals are magnified by a voltage amplifier (HFVA-62, Nanjing Foneng Technology Industry, China). The burst signal contains a finite number of sinusoidal cycles and is adjusted with a suitable duration to obtain the transducer dynamics at its steady state. Vibration is measured with a 1D LDV (OFV-303, Polytec, Germany). A laser controller converts Doppler frequency and phase shifts into velocity and displacement, respectively. After each burst signal operates the transducer, a period between bursts is introduced to minimise the heat generation as the dielectric loss and comparatively low Joule heating, given piezoceramics are minimally conductive. It has to be noted that the laser beam of the 1D LDV should be directed axially to the axis of the DOF to be measured. For example, this study researches the longitudinal modes for all transducers. Thus, the laser beam is on the same axis as the transducer and is focused on the centre of the end surface to ensure the collected vibration parameters only have longitudinal components. Automation is required to achieve the functionality of sweeping frequencies in the

system. It is done by using the combination of the LabVIEW software and a multifunction I/O module. Therefore, both input and output voltage, current and waveform could be programmed and recorded by the user interface in LabVIEW. The diagram of the harmonic analysis system is shown in Figure 3.19.

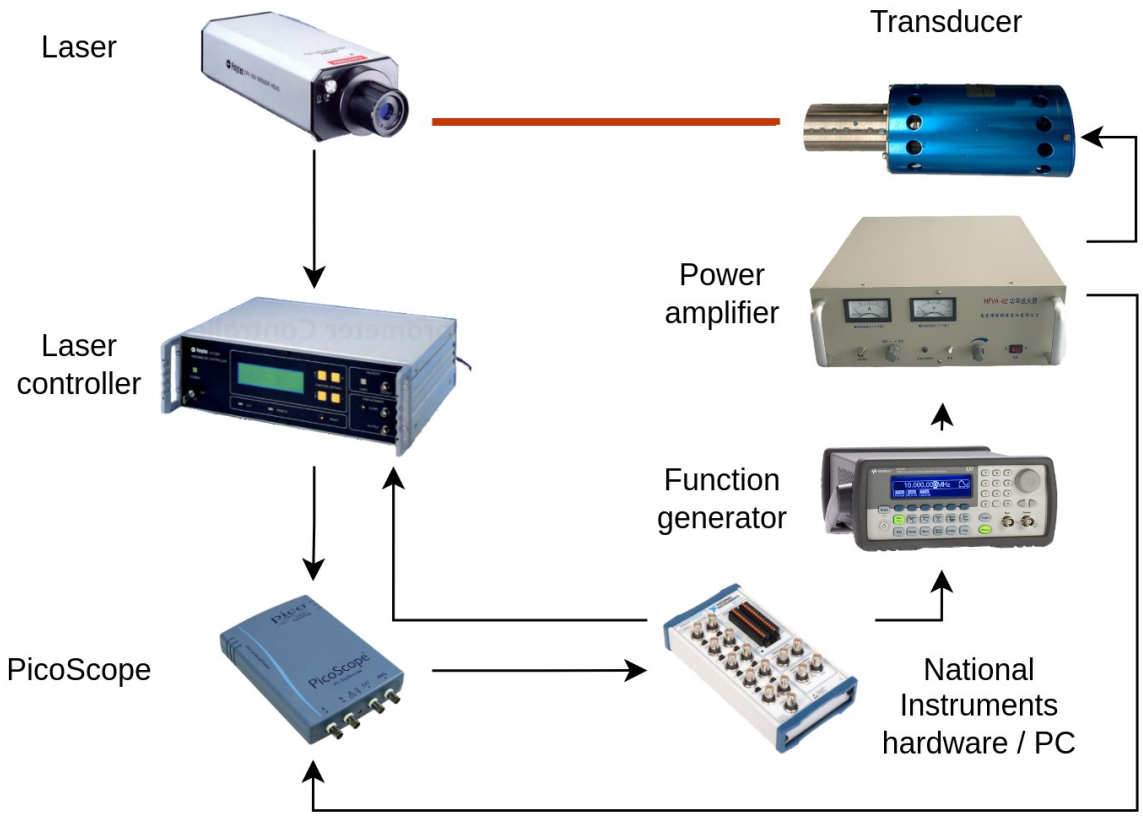

Figure 3.19: Diagram of the harmonic analysis system.

3.3.4 Continuous Operation under High Excitation

Another part of the experiments characterises the transducer dynamics under continuous operation with high electrical input, a common situation in power ultrasonics, which normally records voltage, current, and power over time. When continuously applying high excitation to the transducer, the heat generated due to dielectric loss of the piezoelectric material, widely called self-heating effect [182], degrades the transducer performance, where the piezoelectric properties are strongly dependent on temperatures. This dynamic degradation normally involves the decrease in resonant frequency and vibration amplitude [183]. Thus, it is important to measure the in-situ responses of a transducer to mimic the situation as closely as applications, especially for Nitinol Langevin transducers, where the inclusion of Nitinol further complicates the continuous operation. To accomplish this, an ultrasonic driver (PDUS210, PiezoDrive, Australia) has been used to operate the transducer. In an ideal case, the transducer maximises its output vibration

amplitude by driving at its mechanical resonant frequency. As mentioned before, mechanical resonance is normally collected by sweeping frequency, and the maximum conductance is found by fitting an admittance loop in a typical vibration mode. Therefore, tracking the mechanical resonance as an input for continuous operation is challenging. Instead, the electrical resonance is straightforward to track by analysing electrical signals. The electrical resonant frequency is approximately equal to the mechanical resonant frequency in a Langevin transducer as a high Q factor, achieving a high power consumption and an efficient driving procedure.

In order to ensure the transducer is driven at its electrical resonant frequency in a period, the driving system requires the ability to locate and track the resonance at zero phase. The phase tracking is widely used as it tracks the zero phase constantly to operate at the electrical resonant frequency [10]. Although phase tracking involves a complex combination of controllers and detectors, the fast and accurate control makes it an efficient and reliable technique. Furthermore, based on the phase tracking diagram, current and power tracking can be achieved to maintain the constant current and power by current and voltage probes. Using these functionalities, transducer in-situ properties, including resonant frequency, impedance, phase, current and power, are collected to evaluate the transducer dynamics. However, even with a minimum change in driving frequency, the significant phase variation results in the transducer vibrating at its off-resonance. Since the phase angle experiences a jump phenomenon at the resonance, the phase shifts from -90 to 90 when the frequency approaches the resonance from a lower frequency. Also, this procedure is inefficient when the transducer experiences varying loads, leading to a time-consuming process of using an algorithm to find the zero phase via the admittance loop. These could be optimised by implementing an advanced tracking algorithm and establishing efficient hardware interface communication [150, 184]. These tracking techniques greatly help monitor and understand variations in the resonance behaviours of the Nitinol Langevin transducer resulting from the martensitic transformation by managing constant excitation levels.

3.3.5 Thermal Loading

In the Nitinol Langevin transducer, the material properties of every segment are temperature dependent, not only on Nitinol and PZT but also on any other conventional metal for end masses and bolts. Elastic property variations significantly influence the transducer dynamics. Therefore, it is important to research the dynamic responses of a transducer at varying temperatures. Self-heating and thermal loading are ways to increase the transducer temperature passively and actively, respectively, which are both discussed in this work. As the self-heating situation does not involve temperature manipulations, only thermal loading is detailed in this section.

In order to evaluate the influence of Nitinol phase transformations on transducer dynamics, the Nitinol temperature is required to be constant, ensuring the phase transformation happens throughout the geometry and thus the constant elastic properties. To achieve this, the transducer needs to be positioned in a chamber-like facility, where heating/cooling units change the

temperature field inside which the thermostat controls. In this study, a commercial dehydrator (AJ-991, Andrew James, UK) and a laboratory oven (AX60, Carbolite Gero Ltd., UK) were utilised to realise the heating functionality, with a controllable heating functionality up to 70°C and 250°C, respectively. The apertures on them, as received, enable the use of LDV to measure the transducer dynamics at elevated temperatures, where the laser has been directed through the aperture. Also, a commercial climate chamber (MKF115, BINDER GmbH, Germany) has been used to create heating/cooling conditions. The programmed temperature window ranges from -40°C to 150°C, with a $\pm$2°C fluctuation. However, the aperture on the side of the chamber is unsuitable for laser tests at sub-zero temperatures since an opened window can cause severe temperature fluctuations and increases the humidity which results in an ice layer covering the transducer. Consequently, transducer dynamics become unstable during the test, increasing the risk that the temperature-induced charge of the piezoelectric material damages the impedance analyser module. Therefore, the aperture was closed through the measurement, which indicates that only impedance spectra could be measured. It must be noted that a thermocouple was used to measure the transducer surface temperature alongside, as the transducer's thermal loading may differ from the set value of the thermostat. This is primarily because there is always a temperature delay in the actual temperature of the input value. The experiment continues when the temperature on the transducer surface is stable, and its discrepancy to the set value is within the fluctuation range for 10 min to achieve a constant temperature field.

3.4 Integration of Nitinol into Langevin Transducers

3.4.1 Material Considerations

Regarding Nitinol selection, it is preferable to implement the material with its phase transformation temperatures close to room temperature. One reason is to maximise Nitinol's influence on transducer dynamics near room temperature, enabling accessible measurement which does not rely on facilities that apply a high thermal loading ability. Also, this starts from applying the Nitinol transducer to applications, as transducers are usually operated in room or close-to-room environments. For example, when high temperature is applied to the transducer, not only does the depolarisation of piezoelectric material degrade its electrical properties and thus operational efficiency, but elastic property shifts also influence resonance. Consequently, the driving system fails to track the resonance and causes a drastic drop in output power.

It has been widely proposed in the literature that the post-processing, such as heat treatments, significantly changes the phase transformation behaviours, especially transformation temperatures between martensite and austenite [185–187]. This enables Nitinol to be engineered to undergo phase transformation at prescribed temperatures. However, it increases the complexity of designing Langevin transducers, and more factors considered lead to inconsistency between

design and reality. Therefore, as-received Nitinol samples are not post-processed for this investigative research.

DSC characterises the thermal behaviours of materials, including polymers, metals, and organic chemicals [187]. In this study, DSC identifies Nitinol's phase transformation behaviours by monitoring a specimen's endothermic and exothermic processes in the heat flux format as a function of temperature. The working principle is that DSC measures the difference in the energy required to heat the specimen and reference by controlling heating rates. The specimen should be manufactured in an acceptable size and be encapsulated in an aluminium container, which is the reference in the test. The specimen and reference are then heated or cooled by positioning them in the furnace module at a constant and programmed heating/cooling rate. Internal thermocouples collect their in-situ temperatures. Thus, the heat flow to or from the specimen is calculated from their temperature profile differences. DSC is accurate and only requires small specimens on a millimetre scale. A proposed DSC result for Nitinol material is shown in Figure 3.20 as an example [188]. When the temperature reaches the transformation temperatures, changes in the baseline slope of the curve indicate the characteristic phase transformations.

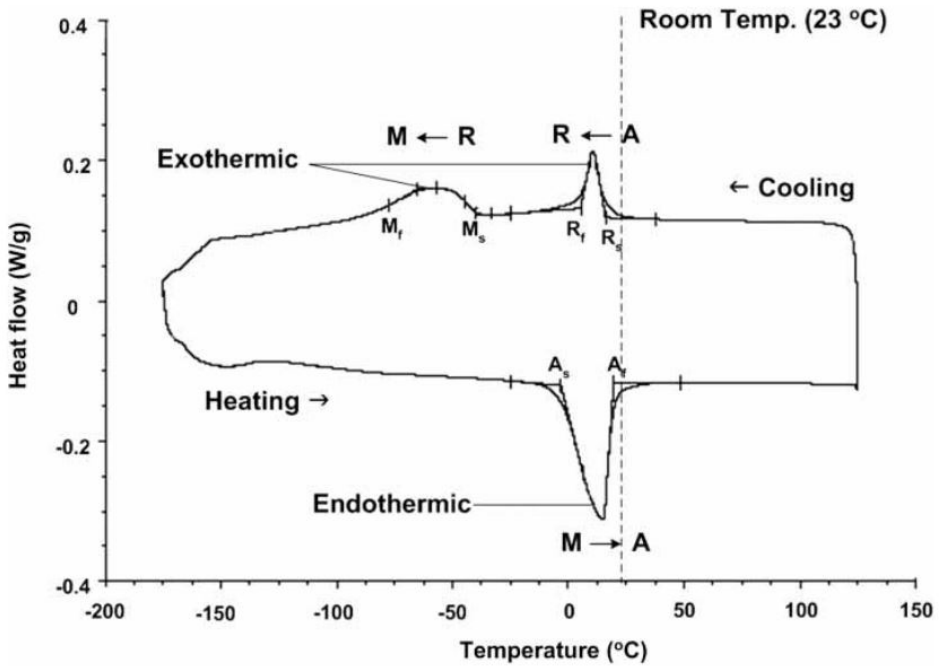

Figure 3.20: Heat flow characteristics of Nitinol measured by using DSC [188] (Reprinted from Proceedings of the Institution of Mechanical Engineers, Part C: Journal of Mechanical Engineering Science, Copyright © 2008 Institution of Mechanical Engineers).

Recalling that Nitinol's elastic properties are influenced by temperature and that transducer resonance behaviours are dependent on elastic modulus, it is important to characterise the elastic moduli of Nitinol with temperature in order to simulate Nitinol transducer dynamics. The complexities surrounding estimating the elastic moduli of Nitinol are well documented [189, 190]. For example, elastic moduli of the twinned martensite phase is highly dependent on detwinning

and reorientation [191], and it should be noted that a key determining factor of modulus difference between martensite and austenite is the grain size [192]. The larger the grain size, the larger the modulus difference within the temperature range of -100°C to 100°C [193]. Given these challenges, an attempt has been made by using a pulse-echo system, which involves the direct experimental determination of all independent components of the elastic tensor by measuring the velocity of ultrasonic waves in different directions of the samples [194]. The velocity travelling through the material was measured by a pulse-echo system (DPR300 Pulse/Receiver, JSR ultrasonics, USA) through recording the time of flight, the time delay of received signals to transmitted signals. Data was then collected in the following pattern: starting with the heating process from room temperature to 60°C, then cooling from 60°C to -40°C, and finally heating from -40°C to 20°C. The heating and cooling processes were carried out by a commercial dehydrator and a freezer with aerosol freeze sprays, respectively, and a thermocouple (RS PRO 1384, RS Components, UK) measured the sample temperature. One end surface of a designed Nitinol cylinder was connected to the ultrasonic transducer (I4-0506-R-SU, 5 MHz, Harisonics, USA) using ultrasonic transmission gel as the conductive agent. A digital storage oscilloscope (InfiniVision DSOX2014A, Keysight, USA) traced the pulse and echo signals. The acoustic velocity results is shown in Figure 3.21.

Similar results are illustrated above, in comparison to [195], with the acoustic velocity exceeding 5000 m/s throughout the complete phase transformation. However, the estimated modulus value for both martensitic and austenite phases ranges from 100 GPa to 120 GPa, which is significantly larger than what has been proposed in the literature [55–58]. This discrepancy is attributed to the anisotropic elastic evolution caused by microstructural orientations [196], where the crystallographic orientation of as-received materials is along the length of the rod [197]. Therefore, anisotropic microstructures influence the free vibration and sound transmission of the sample, indicating that that the acoustic velocity is unsuitable for determining Nitinol's elastic properties [196], without further research.

3.4.2 Fabrication Considerations

Nitinol Langevin transducers designed in this work feature a circular cross-section, and their axisymmetric configurations help reduce manufacturing inconsistencies. In order to implement Nitinol into the Langevin transducer, Nitinol material in cylindrical geometry is preferable to be machined into suitable configurations. Typically, a central hole or a thread is required to be introduced into the Nitinol segment. In terms of fabrication, the work hardening of Nitinol makes it challenging to be fabricated through conventional machining methods [198]. The strain-stress behaviour also affects the cutting process, which causes high tool wear, adverse chip form, and formation of burrs after turning and grinding [131]. One strategy is using EDM, a manufacturing process that uses sparks to erode material from a conductive workpiece. EDM has several advantages in manufacturing Nitinol material over conventional machining methods. It over-

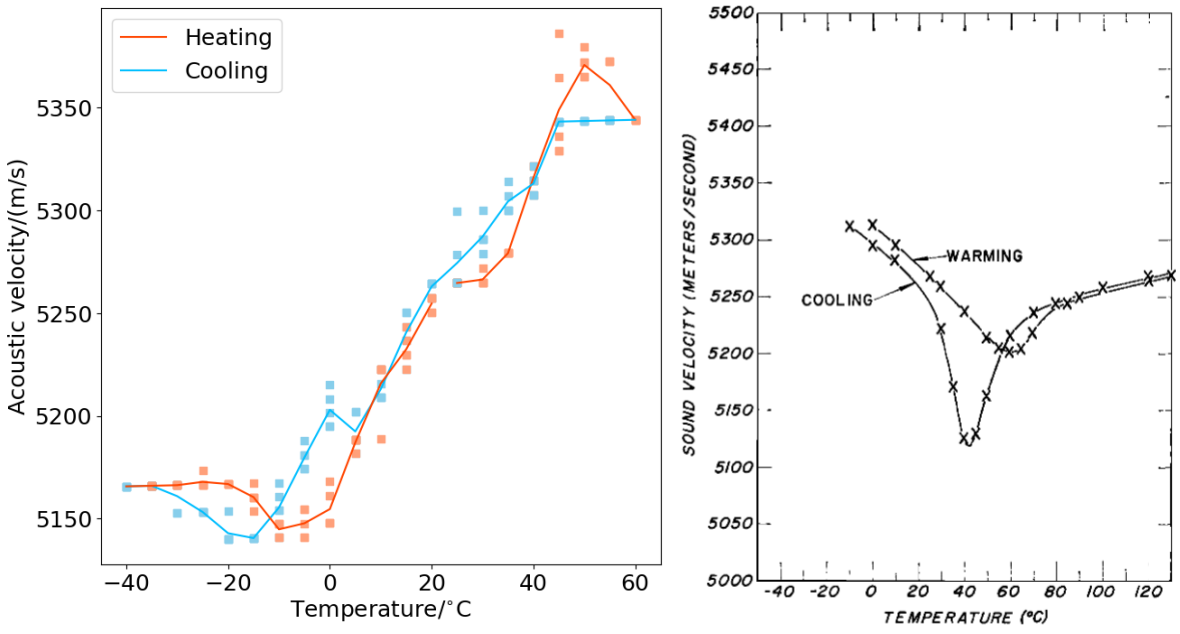

(a) (b)

Figure 3.21: (a) Preliminary pulse-echo results showing acoustic velocity of tested Nitinol sample, compared with (b) velocity results proposed in the literature [195] (Reprinted from The Journal of the Acoustical Society of America, Copyright © 1965, with permission from AIP Publishing).

comes defects such as strain hardening and poor surface finishes [199]. It is also known that a thin white layer can be formed because of the resolidification of molten Nitinol by quenching, resulting in a complex phase transformation and altered microstructure [200]. The white layer affects Nitinol's mechanical properties and benefits mechanical fatigue due to low surface tensile residual stress [201]. However, due to its relatively low thickness compared to the dimensions of fabricated samples, it makes only a minimal contribution to the elastic properties of the samples. Also, the zero-force applied in the EDM process keeps the residual stress at a very low level [202]. Another strategy is water-jet cutting, a cold process that prevents thermal damage to Nitinol. While the water-jet is effective for machining sheet materials, it limits the potential to fabricate bulk Nitinol mass segments.

In this study, EDM is primarily utilised. There are two types of EDM are commonly used in industry: wire EDM and sinker EDM. Unlike wire EDM, where the electrode is thin, sinker EDM uses a bulk electrode shaped into the expected final part configuration. In the process, the material is removed by a spark discharge between the workpiece and the electrode. Both methods' electrodes move along a programmed path to profile precise and intricate shapes in materials. Copper has been verified as the most suitable electrode material for manufacturing Nitinol because of its high thermal and electrical conductivity [203]. Sinker EDM is used in this study to fabricate Nitinol, and the workpiece is submerged in an oil coolant. The massive amount of heat is dissipated to the coolant instantly, ensuring a minimal phase transformation

of Nitinol. However, EDM can be time-consuming, as it depends on workpiece materials and designed working surface roughness. The efficiency is improved if the appropriate electrode material and process parameters are well managed, such as current, nanopowder size, and spark gap [204]. Many studies support the importance of parametric evaluation and optimisation [205, 206]. Overall, EDM is a suitable and accurate manufacturing strategy with many advantages in manufacturing Nitinol over conventional methods. A sinker EDM (AD35L, Sodick Europe Ltd., Warwick, UK) is used with copper selected as the electrode for the process to fabricate Nitinol parts in this study, as shown in Figure 3.22.

Figure 3.22: The sinker EDM (left) and the machining process for Nitinol (right).

An oxide film may appear after machining as a high temperature occurs on the working surface in the EDM process. Due to the high activity of Ti and Ni atoms, TiO_2 and $NiTiO_3$ commonly form the oxide film [207]. Although the mechanics of this film are different from the as-received Nitinol material, its relatively low thickness to the Nitinol part dimensions arguably makes a limited contribution to transducer dynamics, so it is not detailed in this research. After the EDM process, the Nitinol Langevin transducer was assembled by applying a pre-stress on the bolt using the constant torque method, forming the required robust and stable connection between parts. Then, EIA should be conducted to obtain local resonances, followed by modal identification to measure the vibration mode shapes. Based on the resonance properties, the elastic modulus of Nitinol is iteratively defined by using FEA. FEA is conducted at this step because elastic moduli of Nitinol phase microstructures are complicated to be experimentally determined [196].

Therefore, at present, the design of the prototype is limited to the estimations of the elastic moduli specified. However, by correlating the FEA model to the experimental results, an estimation of Nitinol elastic modulus at room temperature can be noted in the order of GPa. This also assumes the accurate definition of the other transducer components and their material

properties. However, the modulus magnitude is comparable with what would be expected.

3.4.3 Experimental Considerations

Experimental considerations for a Nitinol Langevin transducer involve characterising temperature-dependent dynamic properties concerning varied excitation levels, consequently showing tuneable transducer dynamics via the martensitic transformation. A thermal loading technique, based on the accessibility of facilities, is required and defines an appropriate temperature window aligned with the phase transformation temperatures, especially M_F and A_F. Typically, a wider temperature window of the thermal loading is ideal to include the complete phase transformation process, consequently tuning the resonance with a maximum. Moreover, an intricate phase transformation occurs when an unstable intermediary R-phase is involved. Therefore, only stable microstructures, martensite and austenite, are discussed to reduce complexity in designing and analysing Nitinol Langevin prototypes.

It is important to recognise that there are challenges in measuring transducer dynamics at different temperatures. This is primarily due to the difficulty of installing the experimental setups in those environments to obtain accurate results. For example, in the modal identification process, scanning LDV or 3D LDV cannot be performed at elevated temperatures, given the unsuitability of the instrumentation to those temperatures. As a result, the transducer mode shapes in this study are only measured at room temperature. These results are then used to reference the associated transducer resonance at different temperatures, assuming that the transducer mode shapes remain identical across the temperature range.

In order to conduct EIA and harmonic analysis at different temperatures, the Nitinol transducer needs to be placed inside thermal loading facilities where a uniformly distributed temperature field surrounds the transducer, achieving thermal equilibrium. A temperature window with constant interval steps is configured to include complete phase transformations. This enables the material to transform from martensitic phase at room temperature to austenitic phase at elevated temperatures or vice versa. It is worth noting that all measurements should be conducted with the assumed free-free boundary condition across the transducer, as the main focus is on the free vibration in longitudinal modes. Additionally, real-time temperature monitoring uses a thermocouple attached to the transducer surface and a thermal imager (TIM160, Micro-Epsilon, Germany) to ensure that the transducer is heated close to the surrounding environment.

3.5 Summary

This chapter initially investigated the way of how conventional Langevin transducer are designed, setting a pathway for integrating Nitinol. Material selection, FEA, transducer fabrication, and transducer assembly are discussed subsequently.

Certainly, the mathematical model enhances our comprehension of transducer dynamics at a fundamental level of constitutive relationships. A 1D electromechanical model has been attempted based on the Timoshenko–Ehrenfest beam theory, considering piezoelectricity. It should be noted that a good correlation with experimental results is achieved when the transducer L/D ratio exceeds 12.5. This limits the application of the proposed model in simulating the dynamics of Nitinol Langevin transducers despite the advantage of rapid calculation and minimal required temperature-dependent material properties. Therefore, a discussion is presented on the 3D model employing 3D constitutive laws under customised boundary conditions. Nevertheless, challenges in characterising material properties for both Nitinol and PZT at different temperatures have limited the development of temperature-dependent models. Therefore, the transducer dynamics in this study are simulated at room temperature using commercial FEM software and the proposed 3D electromechanical model.

The following section details the experimental characterisation processes for conventional Langevin transducers, including EIA, EMA, harmonic analysis, continuous operation under high excitation, and thermal loading. All characterisation methods focus on measuring the temperature-dependent data set, which is valuable for analysing the dynamics of the Nitinol Langevin transducers at varied temperatures. Subsequently, a method for integrating the Langevin transducer with Nitinol is proposed for the first time. The selection of Nitinol material is based on its key temperatures in primary phase transformations between martensite and austenite. Moreover, understanding Nitinol's elastic behaviours is important for simulations and for analysing transducer dynamics. It reveals that although the obtained acoustic velocities correlate well to the literature [195], the misleading elastic modulus calculated is due to the reorientation of the material microstructure. Thus, elastic properties from experimental results have been obtained by reverse engineering. Once the transducer has been designed, a sinker EDM is chosen to ensure accurate dimensions and a good surface finish for the manufacture of Nitinol. Following fabrication, the Nitinol Langevin transducer will be assembled and characterised using detailed approaches similar to those for a conventional Langevin transducer.

Chapter 4

Design for Adaptive Resonance

Following the procedures outlined in Chapter 3 about design and fabrication for a Langevin transducer incorporating shape memory alloys, this chapter aims to provide advice for the development of Nitinol Langevin transducers and to draw conclusions regarding their adaptive dynamics, tuneable resonance frequency and vibration amplitude, with temperature. Here, DSC measured accurate transformation temperatures of Nitinol samples, followed by the material being machined using EDM. Two prototypes have been manufactured, featuring Nitinol as end masses while with different dimensions. The transducer assembly and dynamics characterisation methods have been carried out as generalised in Sections 3.3 and 3.4. Based on the phenomena observed from the Nitinol Langevin prototypes, the chapter is separated into corresponding sections discussing resonance tuneability in longitudinal modes and modal coupling in flexing modes.

4.1 Transducer Design for Resonance Tuneability

4.1.1 Material Selection

Nitinol is chosen to be integrated into a Langevin transducer. It is a commonly used commercial shape memory material with manufactured to generally consistent standards in industry, which is ASTM F2063. On the other hand, its phase transformation behaviours provide a large, reversible elastic modulus change, enabling temperature induced tuneable resonance discussed in Chapter 3.

In the Langevin configuration, the pre-stress applied through a central bolt results in a strain in the Nitinol. However, Nitinol's elastic modulus is significantly affected by not only temperature but also strain [208], due to superelasticity effect, transformations between de-twinned martensitic and austenitic phases. This makes it challenging to decouple the effects of temperature and strain on elastic moduli of Nitinol and, as a result, the dynamics of transducers. Additionally, characterising the material elastic properties with temperature experimentally to

simulate practical conditions is difficult because the strain varies when the transducer is driven under a varying excitation. Therefore, the elastic modulus of Nitinol is not characterised in this study due to experimental limitations as discussed in Section 3.4.1, and the focus is primarily on phase transformation temperatures.

The phase transformation behaviours of Nitinol are influenced by multiple factors. Not only do the composition and aging processes impact temperature-induced phase transformations, but the presence of applied load or stress also plays a role [209]. As a result, the pre-stress, for example, in the transducer assembly also affects the transformation behaviours. This leads to variations in transformations between DSC results, where tested samples are stress-free, and practical operation with pre-stress. However, DSC remains a practical baseline for measuring the transformation temperatures of Nitinol because of difficulties in characterising thermal behaviours with controlled stress. Here, Nitinol samples with A_S and A_F slightly higher than room temperature are chosen to minimise the effort required to trigger the phase transformation from a low temperature martensite to a high temperature austenite. These samples are obtained from Kellogg's Research Labs (New Boston, NH, USA), and characterisation and fabrication are detailed in the following sections.

4.1.2 Transformation Behaviour Identification

Phase transformation behaviours of Nitinol were analysed using DSC as a suitable method for measuring the heat energy flows in and out of the target material within a specific temperature range. It was well documented that the rate of heating and cooling, referred to as the scan rate, determined the sensitivity and accuracy of the test [52, 210]. A higher scan rate resulted in more sensitive data with higher maximum and lower minimum heat flow values, but at the cost of decreased accuracy. In the literature, it has been suggested that a scan rate of 10°C/min was suitable for Nitinol [15, 52], and this rate was used for all DSC tests in this study. Cube-shaped Nitinol samples with dimensions of $1.5 \times 1.5 \times 1.5$ mm^3 were cut from the as-received samples for the DSC measurements. The DSC thermogram for the Nitinol sample is depicted in Figure 4.1, with the marked transformation temperatures.

In Figure 4.1, the onset and completion of the formation of each phase microstructure was marked by using individual temperature markers placed near the local maximum or minimum of the thermogram. These temperatures included M_S, M_P, M_F, A_S, A_P, and A_F. Since there was no distinct transformation from martensite and austenite to R-phase, R_S, R_P, and R_F were not indicated in the figure. Some key nominal transformation temperatures of the Nitinol sample are listed in Table 4.1. This section only considered the phase transformation from martensite to austenite to achieve resonance tuning. During the heating process at room temperature, the Nitinol sample exhibited a martensite phase as the A_S was higher, indicating that the phase transformation to austenite has not yet been triggered. Therefore, the temperature window for dynamic characterisations in the following sections was designed from 20°C to 100°C.

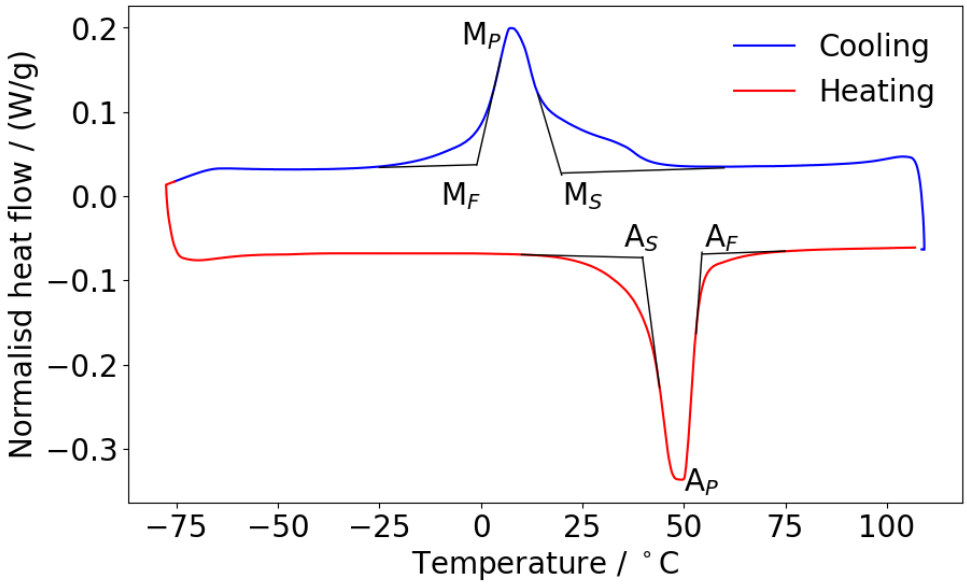

Figure 4.1: DSC thermogram for the Nitinol has been used for the Langevin transducer for achieving resonance tuneability, where the measured transformation temperatures are marked.

Table 4.1: Key nominal transformation temperatures of the Nitinol material for the resonance tuneability transducer.

Nominal transformation temperature	Value (°C)
M_S	19.76
M_P	7.43
M_F	-0.99
A_S	39.82
A_P	49.57
A_F	54.43

4.1.3 Transducer Fabrication

From a linear elasticity point of view, the resonance tuneablity is optimised by maximising the volume fraction of Nitinol in the transducer configuration, due to a greater contribution from Nitinol's stiffness to the system. Recalling that the PZT influences the resonant frequency in longitudinal modes oppositely to the Nitinol, when the volume of Nitinol is increased, the influence of PZT on transducer dynamics is relatively reduced. The explanation is detailed in Chapter 6. Therefore, the Nitinol material is integrated as the front and back masses of a Langevin transducer with a relatively large outer diameter of 25 mm and a length of 50 mm. EDM has been utilised to manufacture Nitinol front and back masses featuring a female thread and a through hole, respectively. The schematic of the manufacturing process is shown in Figure 4.2.

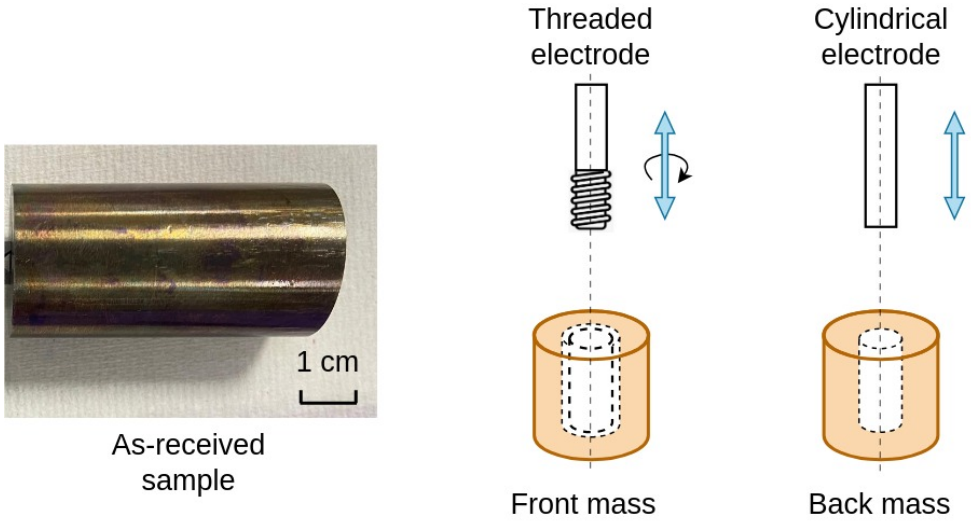

Figure 4.2: Schematic of the EDM manufacturing process for the front and back masses of the designed Nitinol Langevin transducer.

As the axisymmetric beam configuration of the designed Nitinol Langevin transducer, longitudinal vibration modes are dominant and are easily observed, especially the odd order modes if no nodal position is clamped. This research focuses on investigating the L1 and L3 modes, which are commonly used in power ultrasonic applications.

A 3D FEA model of the Nitinol Langevin transducer was created using Abaqus to predict the modal frequencies of L1 and L3. With Nitinol in its martensitic phase, the corresponding frequencies were approximately 13 kHz and 38 kHz, respectively. The choice of this modulus value was informed by existing literature [55, 56] when performing an initial design, as experimentally measuring the modulus presented challenges.

A more accurate modulus can be estimated by reverse optimising through FEA after identifying fundamental frequencies and mode shapes. Indeed, in this scenario, resonance information of the transducer is not precisely simulated for the first design, which is a downside of this study. The manufactured Nitinol front and back masses are pre-stressed to sandwich a PZT stack using a central A2 tool steel bolt. The steel bolt, featuring commercial standard thread quality, is suitable due to its high acoustic impedance within the structure. The resonant frequency and electrical impedance of L1 and L3 modes, close to the FEA frequencies, are monitored during the pre-stress procedure using EIA at room temperature, as shown in Figure 4.3.

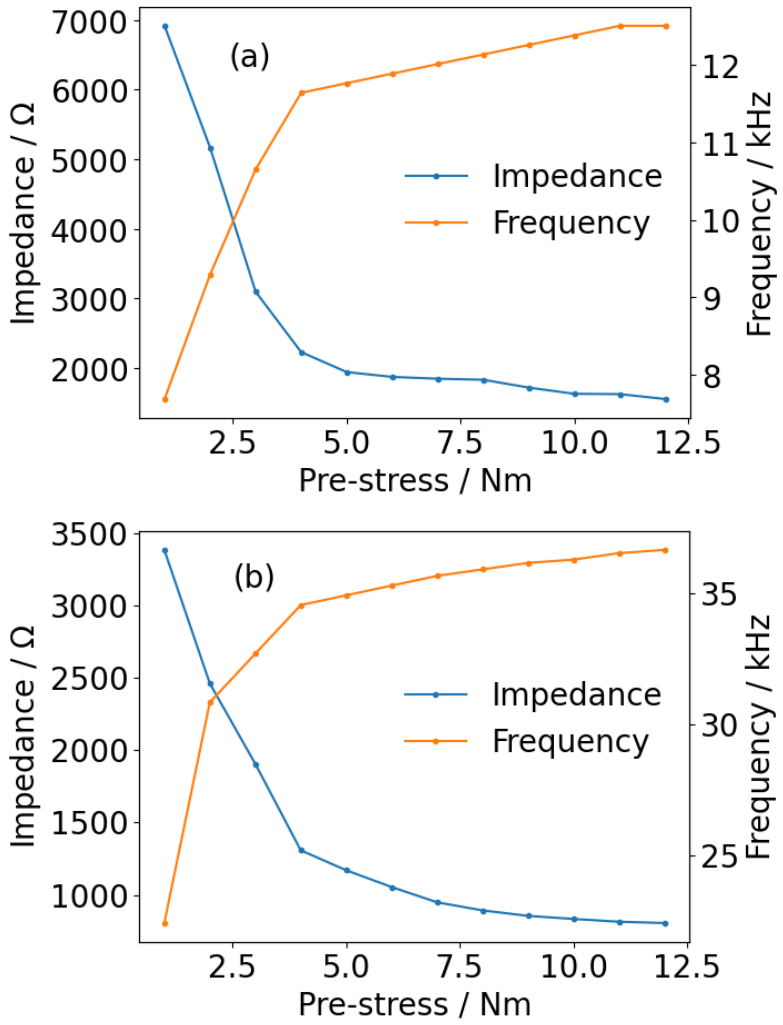

Figure 4.3: Impedance and frequency results of (a) L1 and (b) L3 modes for the Nitinol Langevin transducer during the pre-stress procedure at the room temperature.

The optimal pre-stress value of 12 Nm appeared to converge the resonant frequency and minimise the electrical impedance in both L1 and L3 modes, as shown in Figure 4.3 (a) and (b). The procedure was stopped at this point, and the manufactured Nitinol Langevin transducer is depicted in Figure 4.4. It is clear that a purple-like oxidation layer appears on the surfaces of the end masses. This thin layer, primarily composed of titanium dioxide, forms passively when the sample is exposed to air [211]. Given its thickness on the nanometre scale, it has minimal influence on the Nitinol's mechanical properties and the transducer's dynamics.

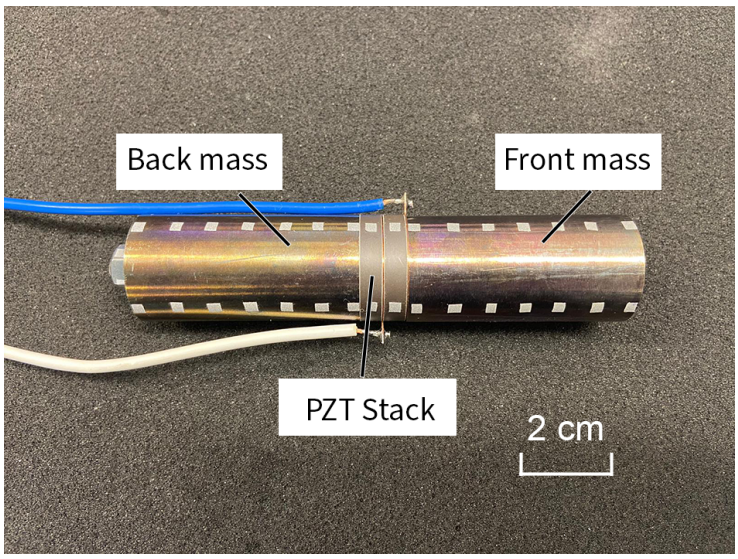

Figure 4.4: The manufactured Nitinol Langevin transducer with a 12 Nm pre-stress.

4.1.4 Transducer Characterisation

The EIA results in Figure 4.3 indicate the electrical resonant frequencies of L1 and L3 modes, but do not provide the vibration mode shapes. It is crucial to measure the mode shape as it reveals nodes and anti-nodes that should correlate with those from FEA. To accomplish this, mode shapes are measured using a 3D LDV for the entire configuration at room temperature. An input voltage of 10 $V_{P\text{-}P}$ has been set to ensure the detection of the vibration mode shape and to cancel out environmental noises. The obtained mode shapes for the Nitinol Langevin transducer through 3D LDV are compared to those from the FEA and are displayed in Figure 4.5. Using an eigenfrequency analysis, the electric potential distribution of both modes is calculated by the proposed 3D model under short circuit conditions as an example, as shown in Figures 4.6 and 4.7. The elastic moduli of Nitinol are iteratively defined in martensite due to its high dependency on frequency [212], microstructures [213], and grain size [214], leading to complexities and limitations in measuring its elastic properties in the 10 kHz scale cyclic loading. The mode shapes and resonant frequencies obtained from the 3D LDV closely match those from the FEA in Figure 4.5, with the iteratively defined Nitinol elastic modulus being 48 GPa in martensite, falling within the range between 30 GPa and 50 GPa as reported in the literature [55, 56]. These findings provide fundamental modal characteristics of L1 and L3 modes for the Nitinol Langevin transducer at room temperature, serving as an indicator for experiments at elevated temperatures.

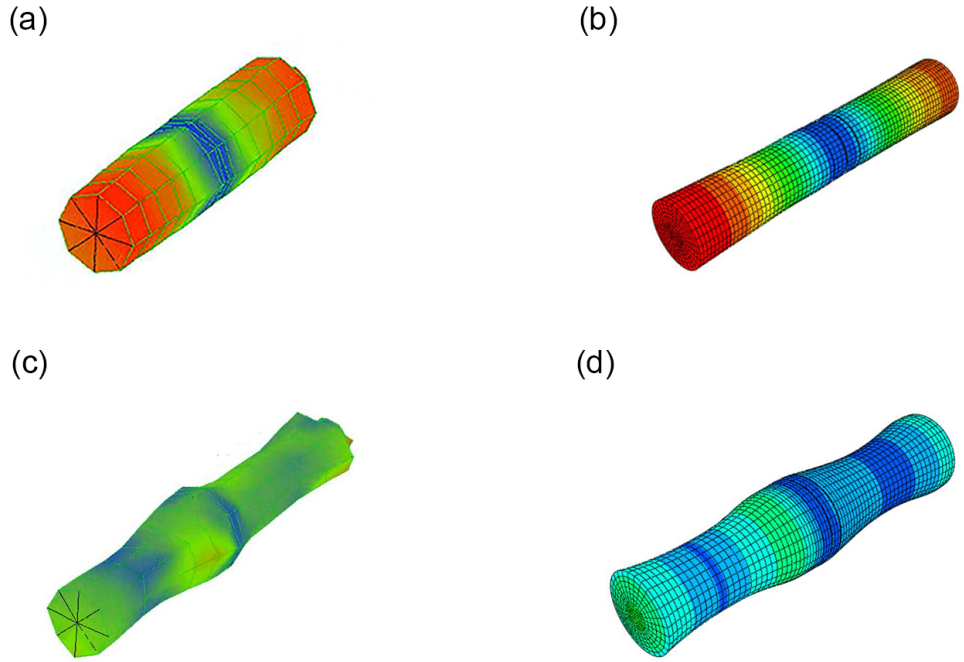

Figure 4.5: (a) 3D LDV and (b) FEA results of the L1 mode for the Nitinol Langevin transducer at 12.815 kHz and 12.560 kHz, and the following (c) 3D LDV and (d) FEA results illustrate the L3 mode for the Nitinol Langevin transducer, vibrating at 37.433 kHz and 38.934 kHz, respectively. Both modes were measured at room temperature. The Turbo colour map is used, with amplitude increasing from blue to red.

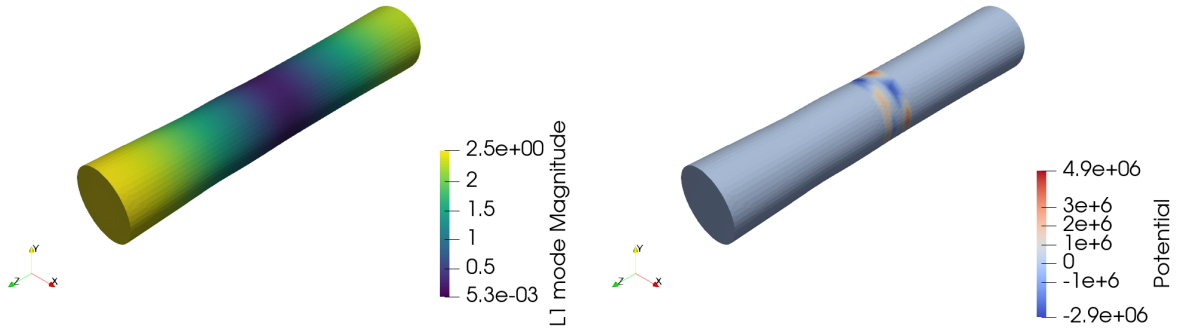

(a) (b)

Figure 4.6: (a) Mode shape and (b) electric potential of the L1 mode for the Nitinol Langevin transducer at 12.596 kHz under short circuit conditions.

The harmonic analysis system measured the vibration amplitude of the Nitinol Langevin transducer across a frequency window, and demonstrated nonlinearity under various excitations. In this experimental set-up, a function generator generates sinusoidal voltage signals with varying input frequencies, and a power amplifier amplifies this signal to achieve 10 V_{RMS} to 50

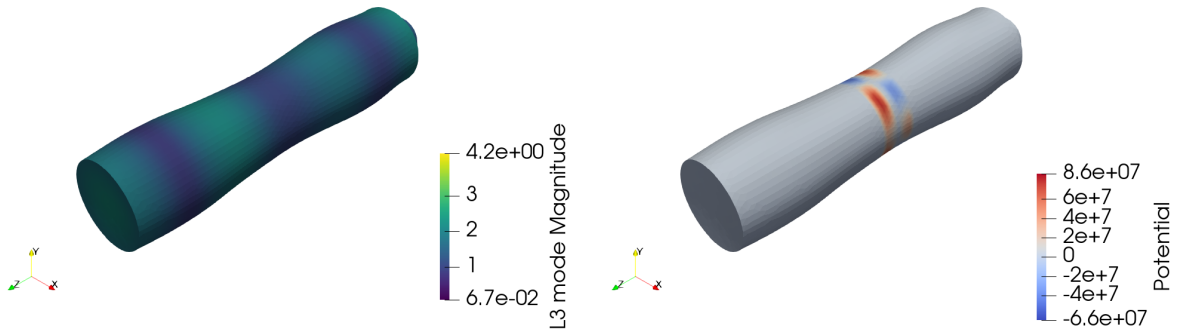

(a) (b)

Figure 4.7: (a) Mode shape and (b) electric potential of the L3 mode for the Nitinol Langevin transducer at 38.345 kHz under short circuit conditions.

V_{RMS}, then transmitting it to the Nitinol Langevin transducer. During the harmonic test, the transducer was positioned on polyurethane foam to closely simulate free mechanical boundary conditions. Subsequently, its vibration amplitude was measured using a 1D LDV, with the laser beam focused on the centre of the transducer end surface to ensure the collection of longitudinal vibrations. The harmonic results of L1 and L3 modes for the Nitinol Langevin transducer were recorded with a 5 Hz interval and are presented in Figure 4.8.

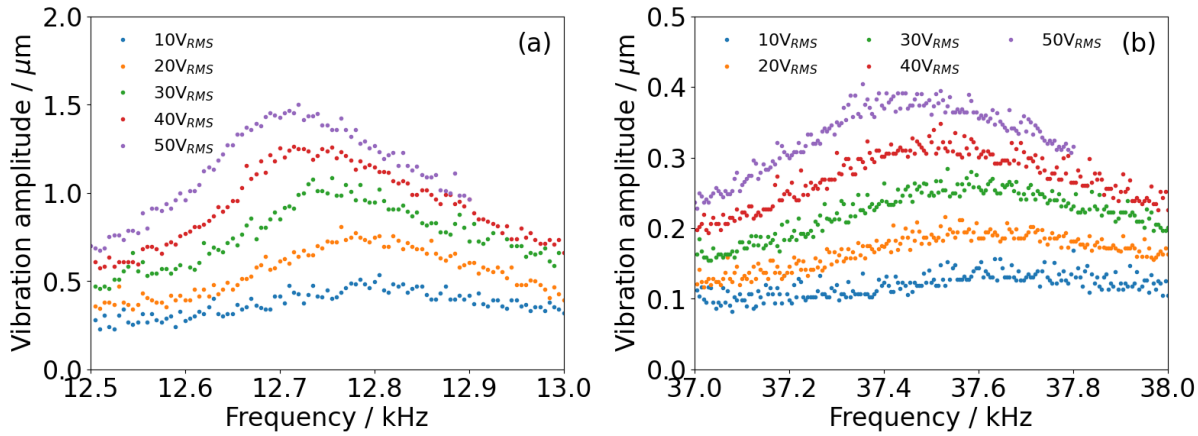

Figure 4.8: Vibration amplitude spectra of (a) L1 and (b) L3 modes for the Nitinol Langevin transducer from 10 V_{RMS} to 50 V_{RMS} at the room temperature.

The vibration amplitude of both modes increases with voltage, which is consistent with that of conventional Langevin transducers. The fluctuations in data points arise from the inherent errors of the laser and setup vibrations caused by imperfect damping of the optical table beneath, and the overall low amplitude promotes these jumping effects. Furthermore, at the same voltage input, the amplitude of the L1 mode surpasses that of the L3 mode, in line with the principle that higher-order modes exhibit lower longitudinal amplitudes. Additionally, the resonant

frequency decreases with voltage, showing the nonlinearity of resonance behaviours. This nonlinear phenomenon here, as discussed in Section 3.3.3, is a result of multiple factors, including nonlinear transformation of Nitinol, changes in the PZT electrical properties, and structural parameters. This phenomenon has been extensively studied in the literature based on conventional Langevin transducers [181, 215], but there is still a gap in quantifying it. All dynamic data at room temperature serves as the reference for subsequent experiments at elevated temperatures, where transducer frequency and amplitude are continuously and consistently monitored.

4.2 Validation for Resonance Tuneability

From here, the dynamics of the Nitinol Langevin transducer at elevated temperatures are studied using the harmonic analysis technique. A laboratory oven was utilised to maintain a constant temperature environment. Inside the oven, the Nitinol Langevin transducer was positioned on superwool, a flame-retardant calcium-magnesium silicate thermal insulating sheet, to ensure safety when high temperatures and voltages are applied during the experiment. Although the acoustic performance of the supercool is lower than that of polyurethane foam, it effectively eliminated the rigid boundary applied to the transducer. The harmonic system was kept outside the oven, with cables routed through the side window to the transducer. The 1D LDV measured the transducer vibration amplitude by directing the laser beam through the side window and pointing it at the transducer end surface. While the opened window is small, temperature uniformity inside the oven can be imparted. Hence, a thermal couple was used to measure the transducer surface temperature. The experimental setup developed from the harmonic analysis system is shown in Figure 4.9.

The experiment was initiated once the transducer temperature reached the set value and stabilised for 10 min to ensure homogeneous temperature distribution throughout the transducer. Input voltages ranged from 10 V_{RMS} to 50 V_{RMS}, consistent with the harmonic system settings at room temperature. The temperature window during the test was between 25°C and 100°C. The upper limit of 100°C was selected to exceed A_F and facilitate the phase transformation process, thereby enhancing the resonance tuneability of the Nitinol Langevin transducer. The harmonic analysis results, including vibration amplitude and electrical impedance, for the L1 mode of the Nitinol Langevin transducer at elevated temperatures and voltages are shown in Figure 4.10 and 4.11, as well as in Figure 4.12 and 4.13. Additionally, the harmonic analysis results for the L3 mode are presented in Figure B.1 and B.2, as well as in Figure B.3 and B.4.

The figures illustrate that temperature and voltage significantly influence the resonant frequency, vibration amplitude, and impedance of the L1 and L3 modes in the Nitinol Langevin transducer. A key finding is that the frequency shifts in response to temperature behave differently than those of traditional transducers in these modes. Specifically, for a traditional Langevin transducer vibrating in its longitudinal modes, the elevated temperature mainly affects the PZT

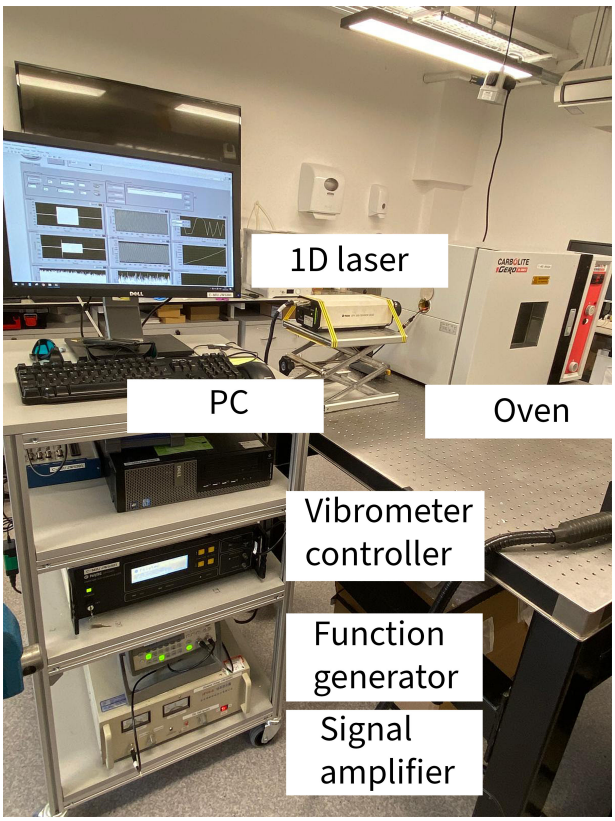

Figure 4.9: Experimental setup for studying the dynamics of the Nitinol Langevin transducer under constant temperature and voltage conditions.

material properties, subsequently a gradual decrease in resonant frequencies [216]. In contrast, the resonant frequencies of the Nitinol Langevin transducer in both L1 and L3 modes experienced a significant increase within a temperature range from 30°C to 55°C. This suggests that the change in Nitinol's material properties, particularly an increase in modulus, contributes to the rise in transducer frequency from a linear elasticity standpoint. The temperature window of frequency shifting closely aligns with the phase transformation from martensite to austenite in the heating process, where the A_S and A_F are 39.82°C and 54.43°C respectively. It is important to recall that the phase transformation temperatures of A_S and A_F are affected by applied stress, preventing them from precisely indicating frequency variations.

Additionally, considering the interplay between the properties of PZT and Nitinol on the transducer dynamics, the temperature range for frequency tuning should be discussed in the context of the assembly rather than strictly adhering to the transformation temperatures of Nitinol alone. Overall, this underscores that the phase transformation of Nitinol, particularly its modulus changes, plays a crucial role in the frequency tuning of the Nitinol Langevin transducer. To quantitatively evaluate the dynamic tuneability, the frequency variations are expressed as percentages relative to temperature and are depicted in Figure 4.14.

In Figure 4.14, the frequency at room temperature serves as the baseline for the elevated temperatures, allowing for quantification of tuneability in percentage format. The frequencies

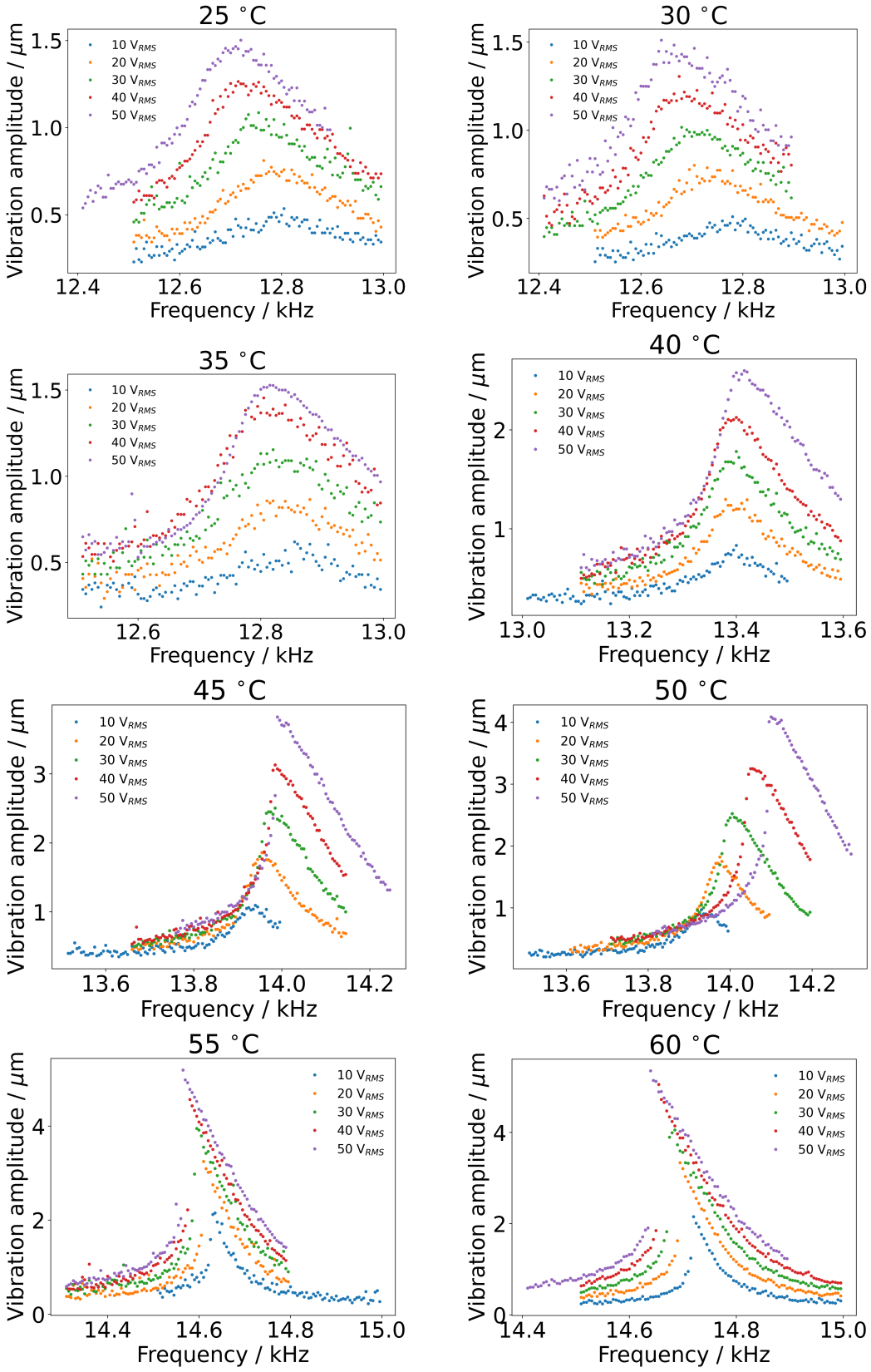

Figure 4.10: Vibration amplitude spectra of the L1 mode for the Nitinol Langevin transducer under static temperatures within a 25°C to 60°C temperature window with applied voltages of 10 V_{RMS} to 50 V_{RMS}.

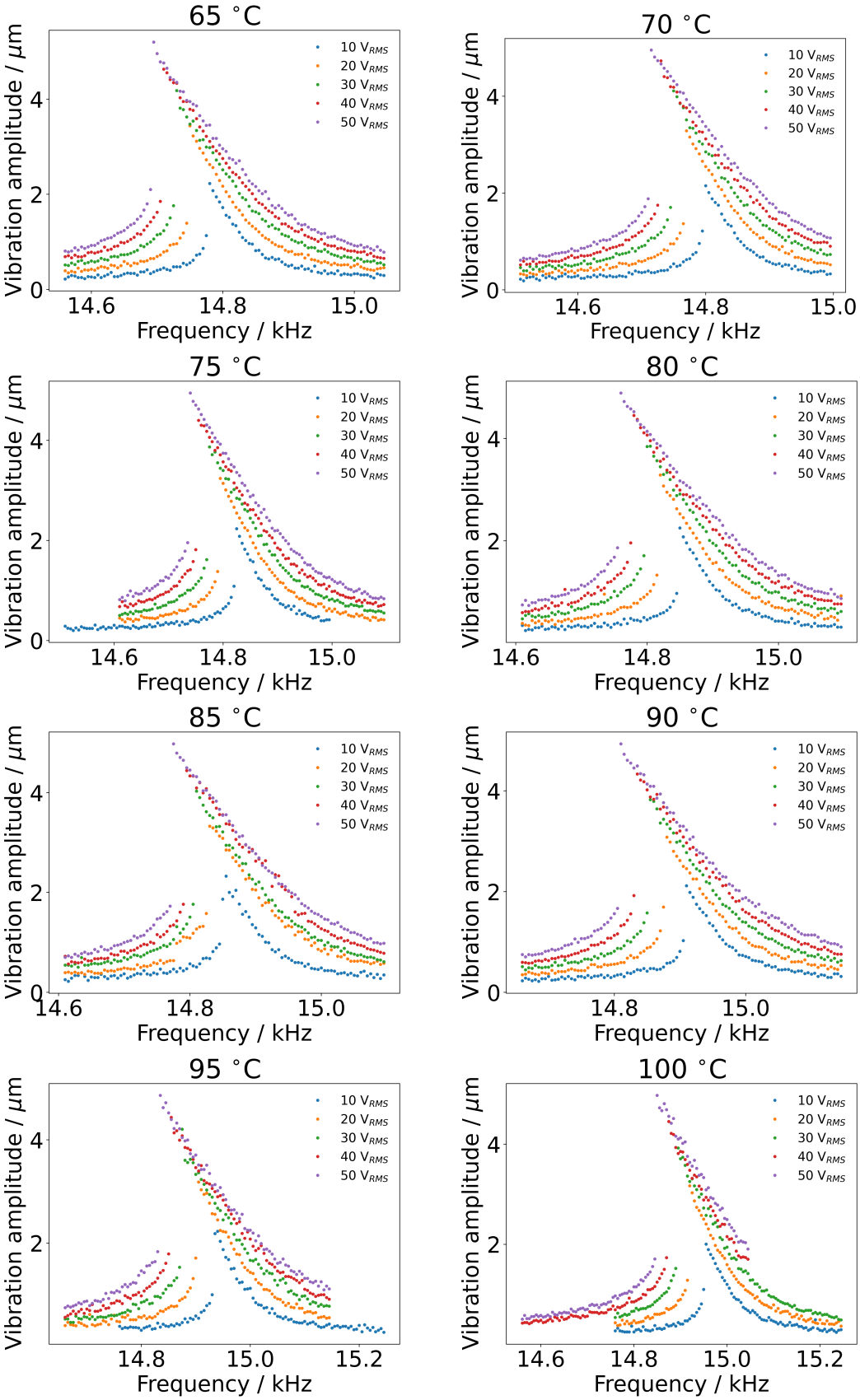

Figure 4.11: Vibration amplitude spectra of the L1 mode for the Nitinol Langevin transducer under static temperatures within a 65°C to 100°C temperature window with applied voltages of 10 V_{RMS} to 50 V_{RMS}.

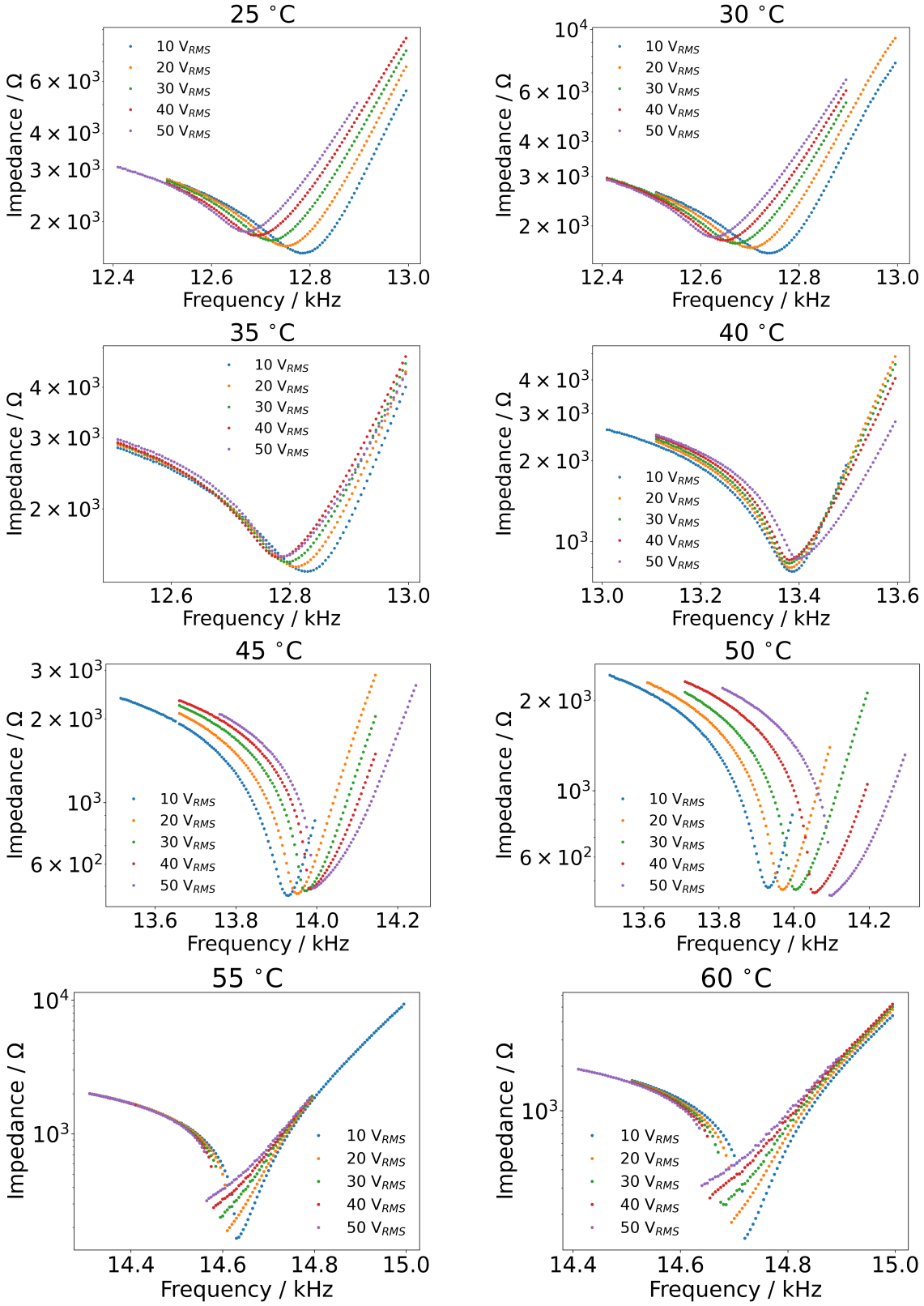

Figure 4.12: Impedance spectra of the L1 mode for the Nitinol Langevin transducer under static temperatures within a 25°C to 60°C temperature window with applied voltages of 10 V_{RMS} to 50 V_{RMS}.

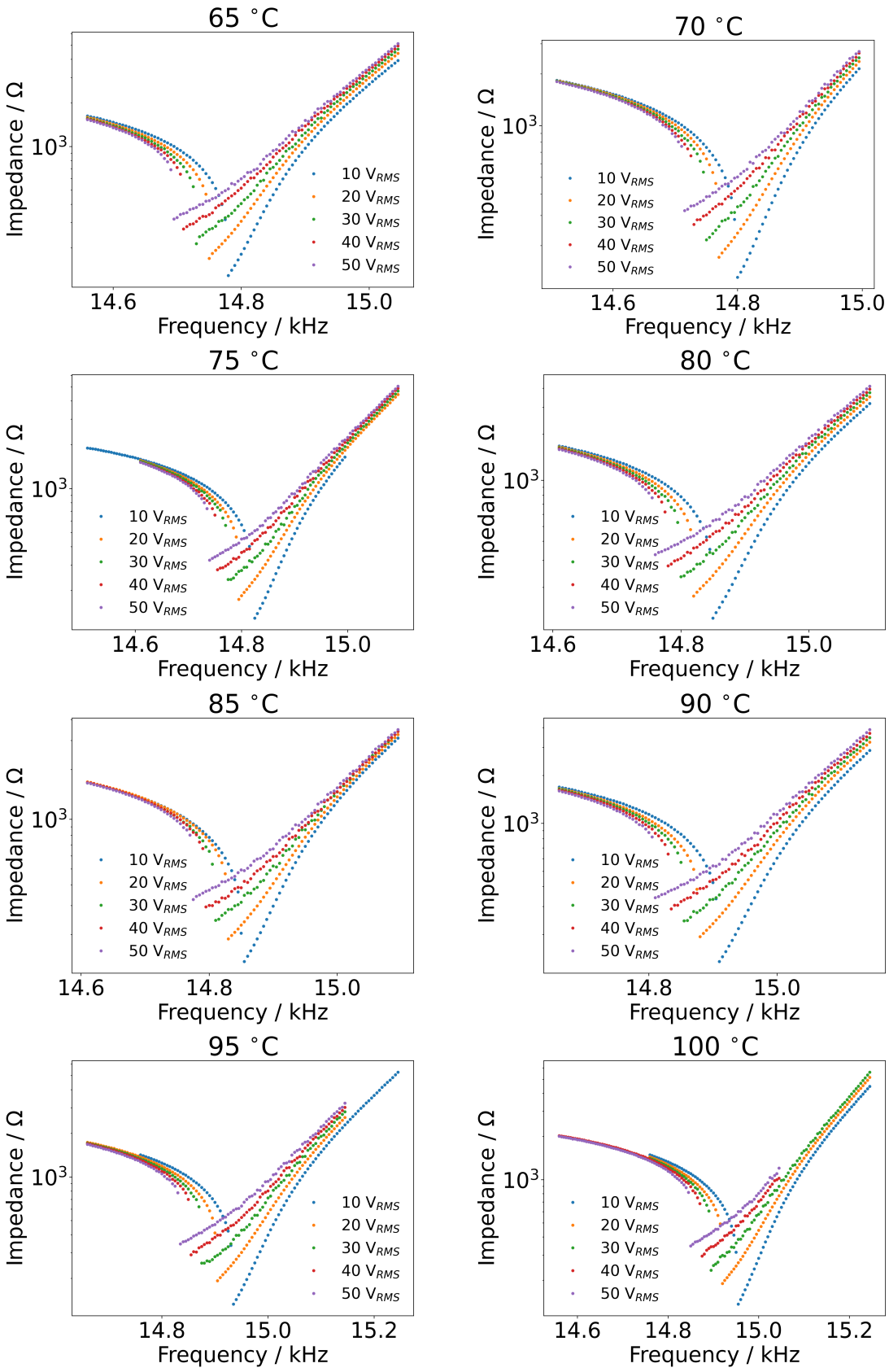

Figure 4.13: Impedance spectra of the L1 mode for the Nitinol Langevin transducer under static temperatures within a 65°C to 100°C temperature window with applied voltages of 10 V_{RMS} to 50 V_{RMS}.

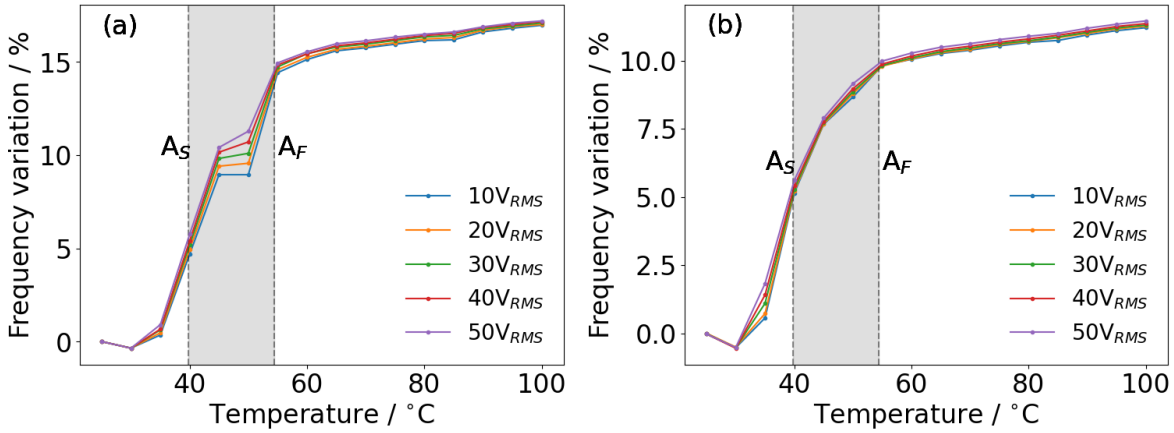

Figure 4.14: Resonant frequency variations in the (a) L1 and (b) L3 modes of Nitinol Langevin transducer at elevated temperatures within a temperature window from 25°C to 100°C and electric potentials of 10 V_{RMS}, 20 V_{RMS}, 30 V_{RMS}, 40 V_{RMS}, and 50 V_{RMS}

of L1 and L3 modes initially decreased from 25°C to 30°C, then rised drastically from 30°C to 55°C, followed by a gradual increase from 55°C to 100°C. The initial decrease can be attributed to changes in PZT properties, which have a more significant impact than the modulus increase in Nitinol, as the temperature is below A_S. From 30°C to 55°C, both resonant frequencies in (a) and (b) show a rapid increase, indicating that the Nitinol modulus was increasing faster due to the phase transformation from martensite to austenite. Once the temperature exceeds 55°C, the frequency continues to increase but at a slower rate. This is likely because, although the phase transformation appears complete, the Nitinol modulus remains temperature-dependent in its austenite phase, which still influences dynamics more than that of PZ26. This aligns with literature [55] that reports a modest modulus increase following the phase transformation process. It is promising to note that the frequency variations for the L1 and L3 modes within the measured temperature range exceed 10%, highlighting a significant temperature tuneability of the Langevin transducer incorporating Nitinol. As recorded in the literature, the tuneability of the Nitinol cymbal transducer is approximately 20% [15], suggesting that tuneability is associated with transducer configurations and vibration modes, and likely correlates with the volume percentage of Nitinol within the structure. From Figure 4.10, 4.11, B.1, and B.2, temperature not only affects the resonant frequencies of the L1 and L3 mode, but also their vibration amplitudes. The vibration amplitude variations are expressed as percentages and are shown in Figure 4.15.

In Figure 4.15 (a), the vibration amplitudes of the L1 mode increase with temperature from 30°C to 55°C, except for a drop at 50°C, and then stabilise from 55°C. This trend is likely attributed to the nonlinear contribution of the Nitinol modulus to the dynamics of the Nitinol Langevin transducer. However, in the L3 mode shown in Figure 4.15 (b), the amplitudes demonstrate a significant temperature dependency and reach a maximum at 40°C, which contrasts with the behaviour observed in the L1 mode. This difference can likely be explained by modal coupling effects, where the adjacent bending mode mitigates the longitudinal amplitude.

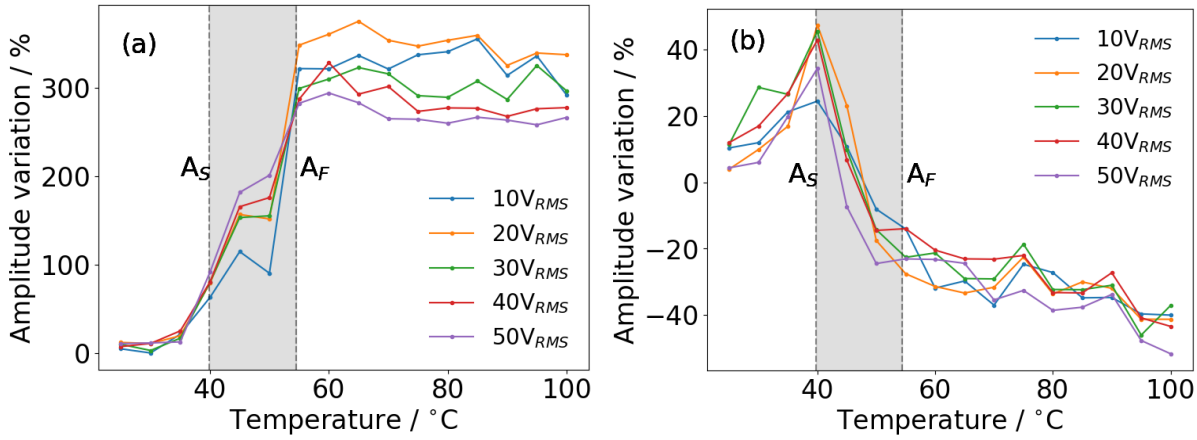

Figure 4.15: Vibration amplitude variations in the (a) L1 and (b) L3 modes of the Nitinol Langevin transducer at elevated temperatures within a temperature window from 25°C to 100°C and electric potentials of 10 V_{RMS}, 20 V_{RMS}, 30 V_{RMS}, 40 V_{RMS}, and 50 V_{RMS}

A fifth-order bending mode in FEA is close to the L3 mode at room temperature. The coupling effect could have emerged at elevated temperatures. This phenomenon, which could happen at low temperatures, will be discussed in the next section. However, proving this is challenging, given the complexity of the experimental setup required to obtain dynamics of coupled modes at elevated temperatures. As the temperature rises, the vibration amplitude recorded by the 1D LDV appears less converged, which can be attributed to limitations of the harmonic system and environmental noise from the oven. The harmonic system measures vibration velocity with a resolution of 1 mm/s, resulting in a vibration amplitude resolution of 0.004 μm at 40 kHz. Consequently, the low vibration amplitudes could not be measured accurately. This issue could be addressed using a more advanced harmonic system with a different laser vibrometer decoder.

Furthermore, it is important to mention that the amplitude of the L1 mode tripled when the temperature exceeded 60°C. This presents an opportunity to manufacture a multifunctional ultrasonic device where the low amplitude L1 mode can be adjusted to a high amplitude by heating the transducer. For instance, the low amplitude indicates a small mechanical quality factor suitable for high loads. However, adjusting to a high amplitude with a high mechanical quality factor would improve working efficiency with smaller loads. For a piezoelectric transducer, electrical parameters must be measured since they underscore the operational information for the driving system. In this part of the work, the electrical impedance at resonance has been measured with temperature and is shown in Figure 4.16.

In Figure 4.16 (a) and (b), the electrical impedance at resonance for both L1 and L3 modes are functions of temperature. The impedance values for the L1 mode decrease significantly from 30°C to 55°C, which aligns with the temperature range for frequency tuning. This suggests that the phase transformation in Nitinol also influences the electrical properties of the transducer. The decrease in impedance indicates an increase in the transducer's dielectric conductance at the zero-phase resonance point, resulting in a higher displacement current and, consequently, a

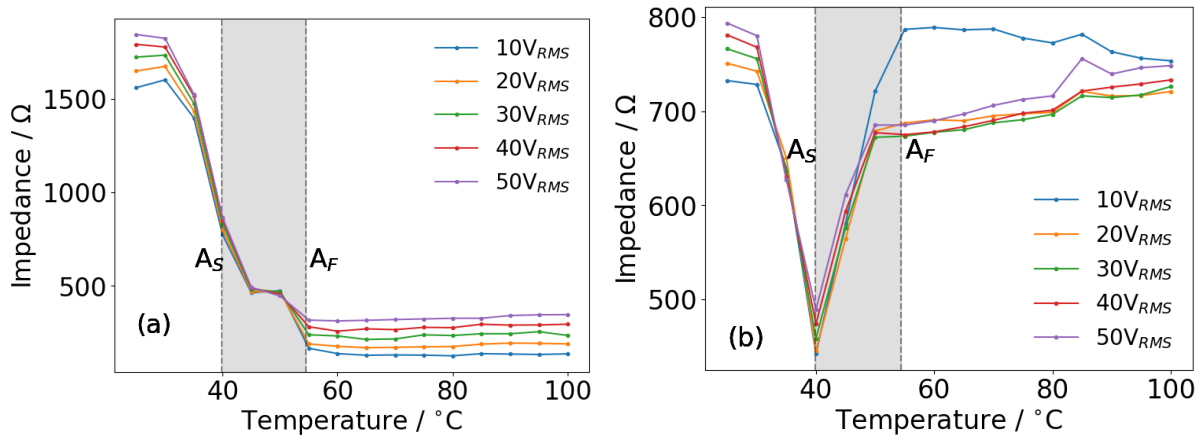

Figure 4.16: Electrical impedance in the (a) L1 and (b) L3 modes of the Nitinol Langevin transducer at elevated temperatures within a temperature window from 25°C to 100°C and electric potentials of 10 V_{RMS}, 20 V_{RMS}, 30 V_{RMS}, 40 V_{RMS}, and 50 V_{RMS}

greater vibration amplitude, according to mechanical-electrical analogies. This correlates with the changes in vibration amplitude across the temperature range. When the temperature exceeds 55°C, the impedance increases slightly, behaving similarly to a traditional Langevin transducer. In the L3 mode, impedance initially decreases from 30°C to 40°C, followed by a rapid increase to 50°C, and then gradually rises with temperature. The initial decrease is primarily due to the phase transformation in Nitinol, as observed in the L1 mode. However, the subsequent increase is likely a result of mode coupling with a nearby bending mode.

It has also been observed that the impedance spectra in Figure 4.12, 4.13, B.3, and B.4 exhibit minimal voltage dependence at 40°C. The impedance spectra for both L1 and L3 modes at 35°C, 40°C, and 45°C, with relative frequencies, are shown in Figure 4.17, where the resonance at 10 V_{RMS} serves as the reference. In traditional Langevin transducers, applying increased voltage to the electrodes of the piezoelectric unit or elevating the temperature generally results in a decrease in longitudinal frequency and an increase in electrical impedance. This phenomenon can be attributed to the influence of the electric field and temperature on the electrical properties of PZT, including both piezoelectric and dielectric characteristics [217], which consequently induce shifts in frequency and impedance. Additionally, variations in the mechanical properties of materials within the transducer at differing temperatures contribute significantly to the frequency variations. However, for the L1 mode, the Nitinol Langevin transducer behaves like a traditional transducer at temperatures of 35°C and below, exhibits minimal frequency dependence on voltage at 40°C, and thereafter, higher voltage leads to an increased resonant frequency. In the case of the L3 mode, the transducer frequency rises with voltage at 35°C, shows similar minimal frequency dependence at 40°C, and then subsequently functions as a traditional transducer at 45°C and upwards. Notably, the observed abnormal voltage dependency occurs exclusively during the phase transformation of Nitinol, indicating that rapid changes in the moduli of Nitinol may significantly influence the voltage response of transducer in relation to resonant frequencies.

There are two hypotheses proposed here to explain this phenomenon. The first suggests that the elastic properties of Nitinol at 40°C enables the transducer to exhibit maximum resistance to fluctuating electric potentials. In this interpretation, changes in the piezoelectric and dielectric properties have a limited impact on the resonance shift. The second hypothesis holds that elevated electrical fields induce greater stress on the PZT. Due to the presence of a pre-stress bolt, this stress is transferred to the Nitinol, potentially leading to a stress-induced phase transformation to de-twinned martensitic phase. The de-twinned martensitic phase possesses a higher modulus than twinned martensitic phase [218], thereby increasing resonant frequency that offsets any decreases caused by alterations in piezoelectric and dielectric properties. However, existing experimental setups do not provide conclusive evidence for either hypothesis. An advanced materials testing facility capable of measuring Nitinol's elastic properties or phase behaviours under constant pre-stress and voltage conditions at elevated temperatures would be beneficial for further investigation in this study.

Increases in temperature of the Nitinol segment are attributed to the surrounding environment, which induces a phase transformation and subsequently changes the elastic modulus. This change leads to variations in frequency and vibration amplitude for both the L1 and L3 modes. The results demonstrate that the tuneability of the Nitinol Langevin transducer is achieved, as its dynamic properties are significantly influenced by temperature. This was particularly evident when operating the transducer with excitation levels ranging from 10 V_{RMS} to 50 V_{RMS}. Moreover, within the temperature range associated with the phase transformation, the Nitinol Langevin transducer exhibited minimal voltage dependence of resonant frequency. Although the properties of PZT also exhibit temperature dependence, their impact on the dynamics is considerably less pronounced than that of Nitinol. The Nitinol Langevin transducer shows promising potential for dynamic tuning through temperature manipulations, and this could be further enhanced by modifying the transducer dimensions. This, in turn, enables the potential to use the Nitinol Langevin transducer to achieve multifunctionality for various applications.

4.3 Transducer Design for Modal Coupling

In the previous section, it is demonstrated that adjusting the temperature of a Nitinol Langevin transducer can actively control its dynamics, particularly the resonant frequencies and vibration amplitudes. This effect is mainly due to changes in the properties of both Nitinol and PZT. Building on this idea, a hypothesis suggests that different modes respond uniquely to variations in Nitinol and PZT properties. By altering temperatures, it may be possible to couple two adjacent modes. This could address issues such as the unwanted decoupling of a coupled mode, often stemming from manufacturing inconsistencies. Additionally, this approach could enable the active coupling of two dissimilar modes, resulting in complex vibration mode shapes. This would be advantageous for actuators, particularly in systems extensively utilising coupled modes.

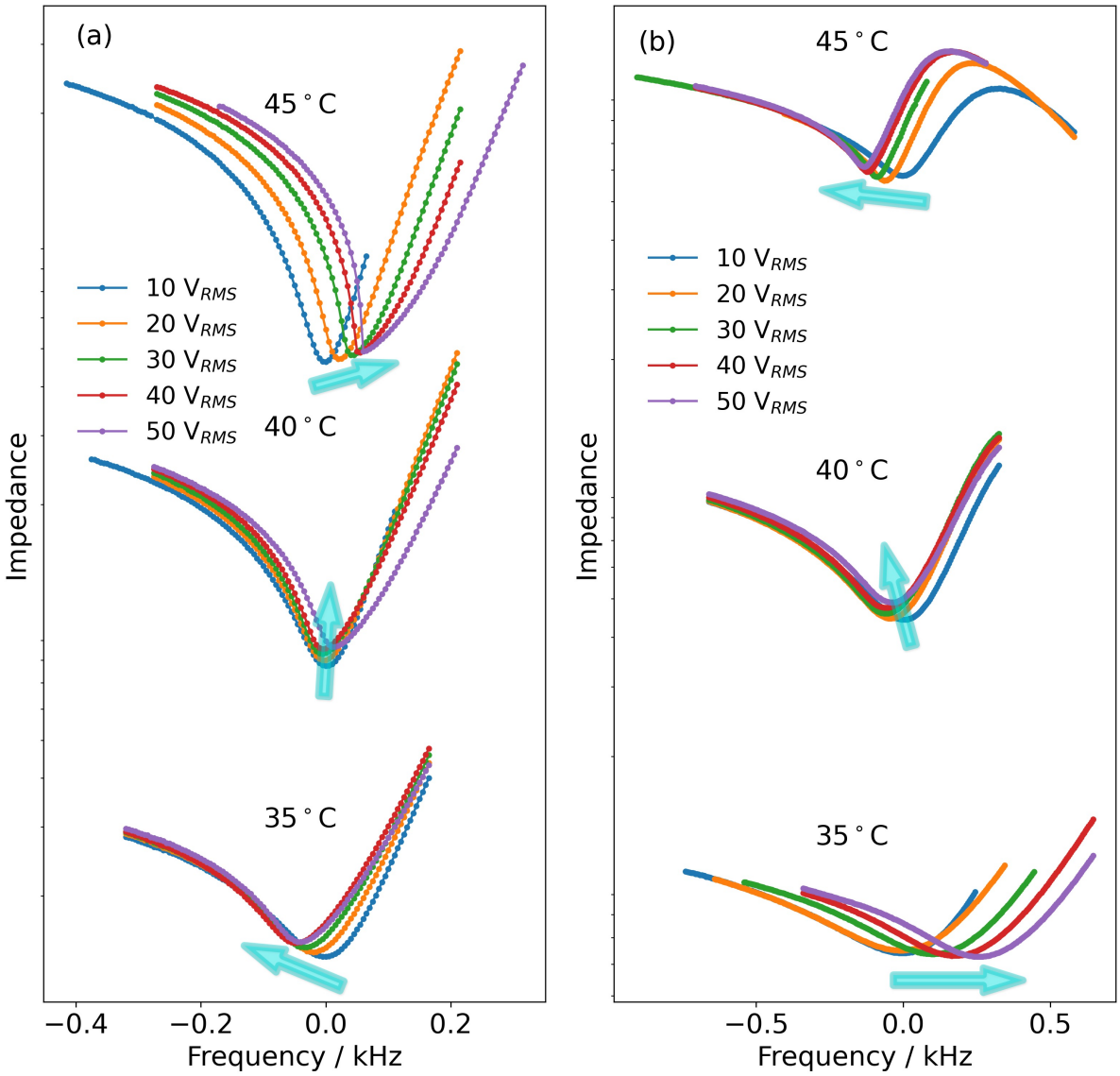

Figure 4.17: Impedance spectra in relation to relative frequency at 35°C, 40°C, and 45°C, ranging from 10 V_{RMS} to 50 V_{RMS}, showcasing the voltage dependence of impedance during the phase transformation of Nitinol from martensite to austenite, where the arrows indicate patterns of resonant frequencies with increasing voltages.

4.3.1 Transformation Behaviour Identification

This section made an effort to couple similar modes of a Nitinol Langevin transducer by utilising Nitinol's temperature-dependent phase microstructures. The transducer was characterised over a broad temperature range to encompass complete Nitinol phase transformations between martensite and austenite, allowing for the observation of interplays between Nitinol and PZT across these transformations. Nitinol from Kellogg's Research Labs, characterised by a broader phase transformation range between A_F and M_F, was chosen for this purpose. DSC was conducted to identify its transformation behaviours accurately in an unloaded condition, particularly the critical phase transformation temperatures, to provide practical operational guidance. The

thermogram is depicted in Figure 4.18.

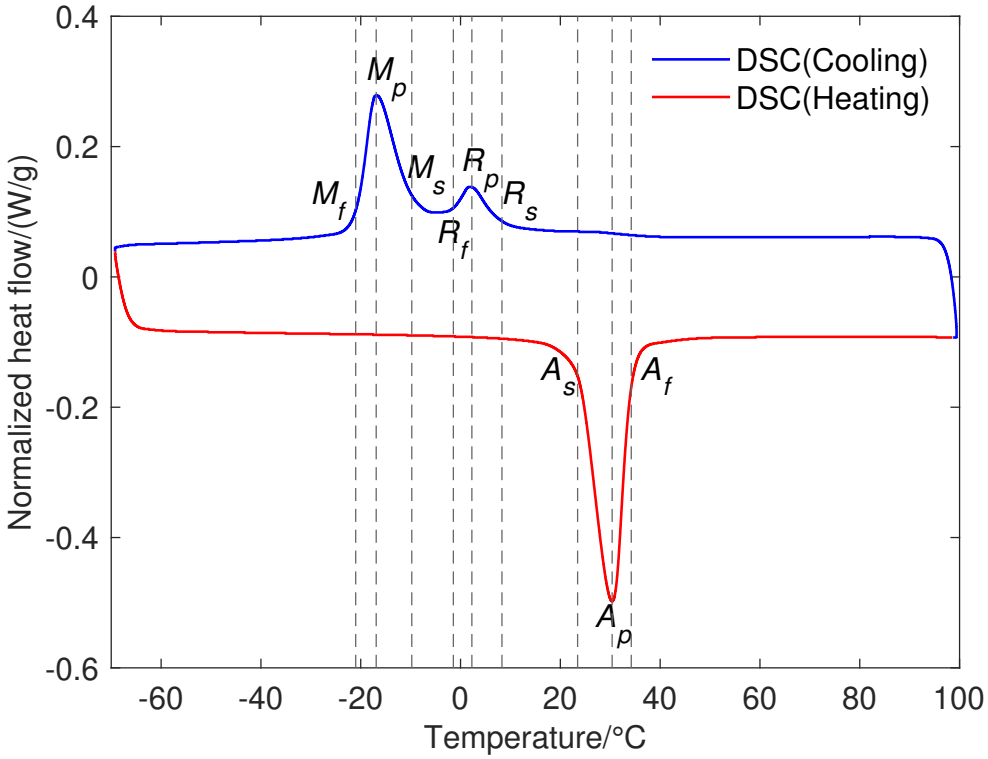

Figure 4.18: DSC thermogram for the Nitinol used for the NMCT, where the measured transformation temperatures are indicated.

Here, the heating and cooling rates for DSC were set at a rate of 10°C/min. The temperature range was specifically set from -70°C to 100°C, ensuring to effectively capture key transformation temperatures, particularly the A_F and M_F. Some key nominal transformation temperatures are listed in Table 4.2.

Table 4.2: Key nominal transformation temperatures of the Nitinol material for the modal coupling transducer.

Nominal transformation temperature	Value (°C)
M_S	-9.77
M_F	-21.01
A_S	23.46
A_F	34.21

A single transformation stage ‘martensite → austenite’ appears as the Nitinol sample is heated, whereas two transformation stages ‘austenite → R-phase’ and ‘R-phase → martensite’ appear while cooling. It is common for an intermediate phase such as the R-phase to manifest during the heating or cooling process, based on the fact that Nitinol is hysteretic in nature. This highlights the importance of considering the dynamics of the Nitinol Langevin transducer in

whether the heating or cooling phase.

4.3.2 Transducer Fabrication

The Langevin transducer designed in this section comprises Nitinol front and back masses fabricated from as-received cylinders. The bolt material is grade A2-70 stainless steel, and the PZT stack consists of two PZ26 rings and two ring-shaped copper electrodes. An initial design was simulated using FEM based on these material selections, with elastic properties of Nitinol obtained from the literature [55–58]. The transducer was found to have two adjacent out-of-plane (OP) modes near 45 kHz at room temperature. The designed dimensions of Nitinol front and back masses are 25 mm in outer diameter and 10 mm in length. The Nitinol front mass includes an M8 female thread through its length, while the back mass has an 8 mm hole through the component. The thread and hole are manufactured through EDM, with copper electrodes shaped into male thread and rod configurations. The manufacturing parameters are identical to those used to process the Langevin transducer for resonance tuneability. The fabricated front and back masses are shown in Figure 4.19.

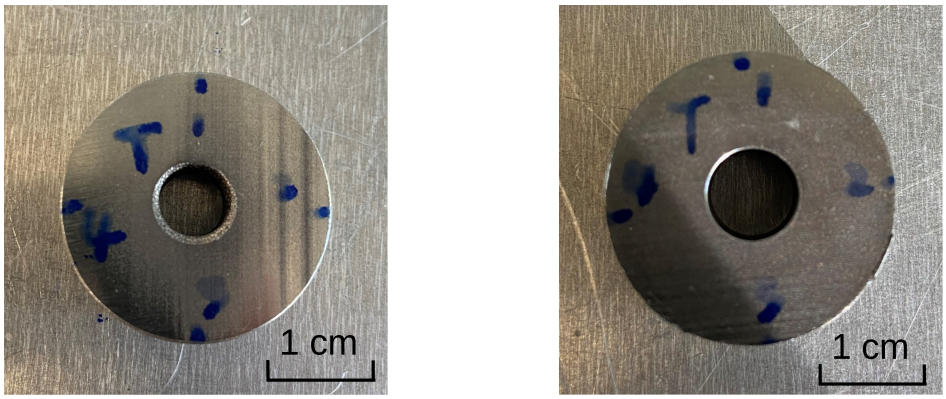

(a) (b)

Figure 4.19: Fabricated Nitinol (a) front mass and (b) back mass.

After Nitinol front and back masses have been fabricated, the transducer was assembled by sandwiching end masses and PZT stack between them through a central preloading bolt, as shown in Figure 4.20.

To ensure a stable assembly, one important step is to investigate the optimal pre-stress applied to the transducer. The constant torque method is utilised here, which is detailed in Section 3.1.4. The impedance analyser recorded the impedance spectra of the Nitinol transducer under the optimal pre-stress values at room temperature, as shown in Figure 4.21.

In Figure 4.21, the frequency sweep ranges from 35 kHz to 55 kHz, aiming to centralise the FEM frequencies for both adjacent OP modes. Two local resonance peaks are observed, indicating the presence of two vibration modes near 45 kHz. However, determining the actual

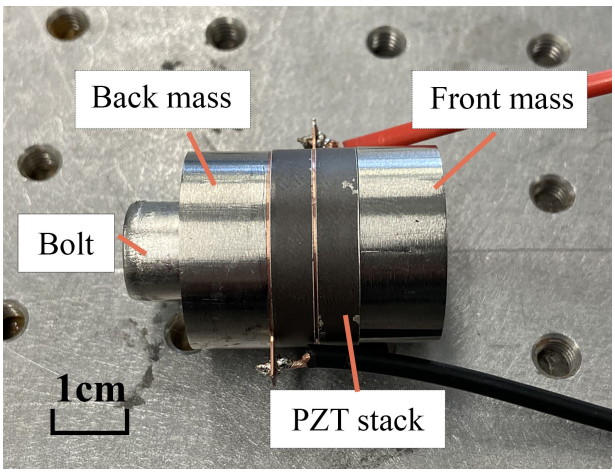

Figure 4.20: Manufactured Nitinol Langevin transducer for modal coupling.

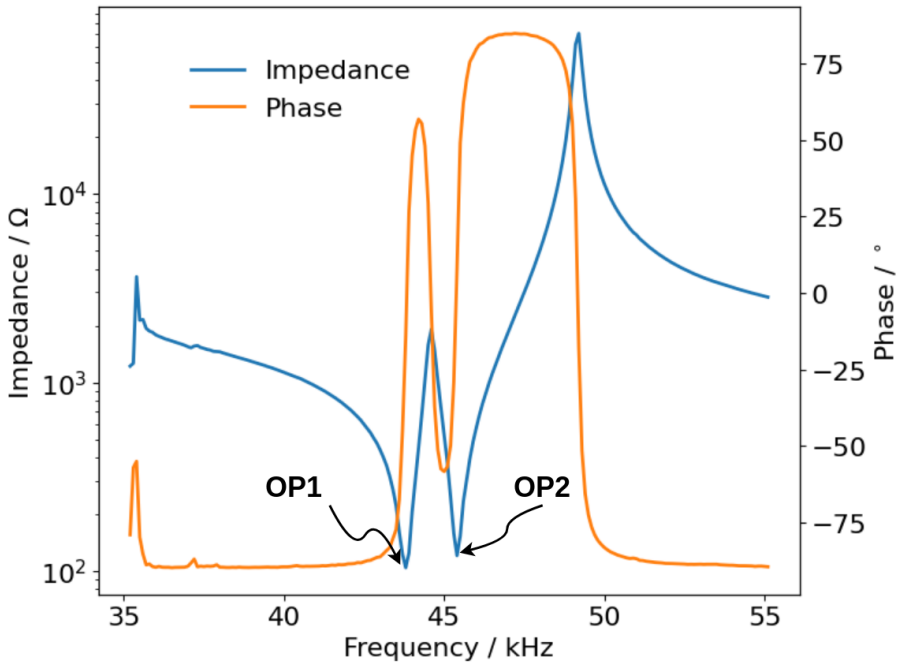

Figure 4.21: Impedance spectra of the Nitinol Langevin transducer with 10.5 N/m pre-stress.

vibration mode shapes requires the modal identification process, which is elaborated in the following section. Specifically, when the torque is 10.5 Nm, the impedance for both local resonant frequencies of OP modes reaches the minimum, signifying that the transducer exhibits maximum conductance at the zero phase electrical resonance. Consequently, the optimal pre-stress value for this Nitinol Langevin transducer is 10.5 Nm.

4.3.3 Transducer Characterisation

The impedance results reveal two distinct resonant frequencies labelled OP1 and OP2. To visualise their actual mode shapes, a scanning LDV measured the modal information of the trans-

ducer at 8 $V_{P\text{-}P}$, specifically displacement, velocity, and acceleration in the frequency domain. Two lateral surfaces and the end section surface were scanned to structure the mode shapes across the configuration, as shown in Figure 4.22 (a) and (c) for OP1 and OP2 modes, respectively. Subsequently, FEA was performed by reverse and iterative optimisation of the Nitinol properties to closely match the LDV results, as shown in Figure 4.22 (b) and (d). The LDV and FEA results for OP1 and OP2 modes, from here referred to only as OP1 and OP2, correlate closely in both cases. OP1 was induced by the OP mode associated with the front and back masses, whereas the mode shape of OP2 was induced by the OP mode associated with the PZT rings. Both modes have a similar mode shape but with a 90° spatial phase difference in the circumferential direction.

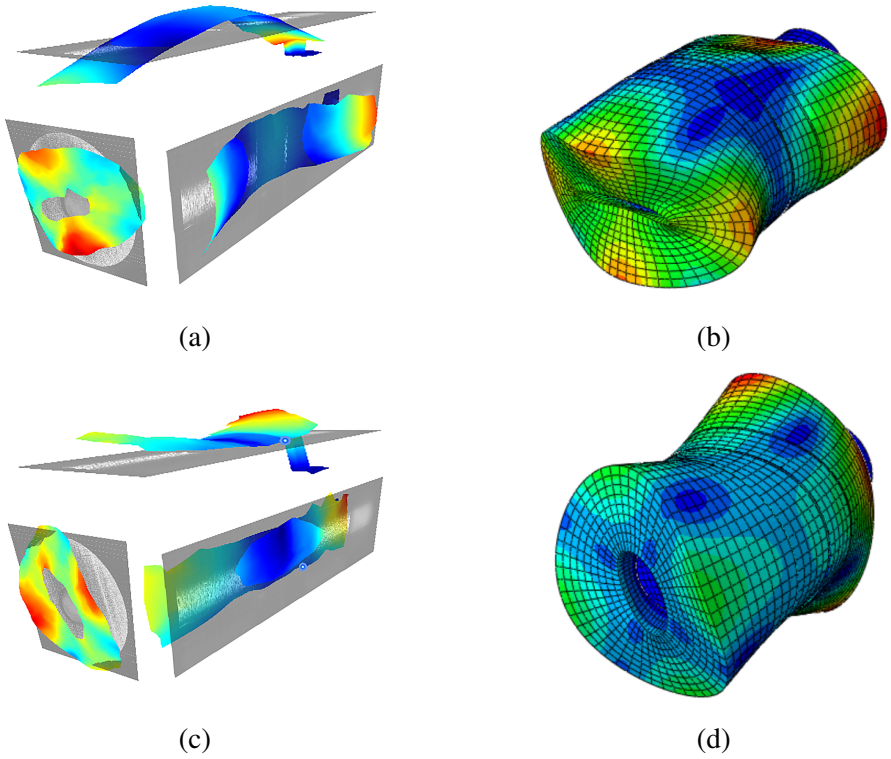

(a) (b)

(c) (d)

Figure 4.22: Mode shapes of OP1 mode from (a) LDV at 44.5 kHz and (b) FEA at 44.17 kHz and mode shapes of OP2 mode from (c) LDV at 45.70 kHz and (d) FEA results of OP2 mode at 47.11 kHz.

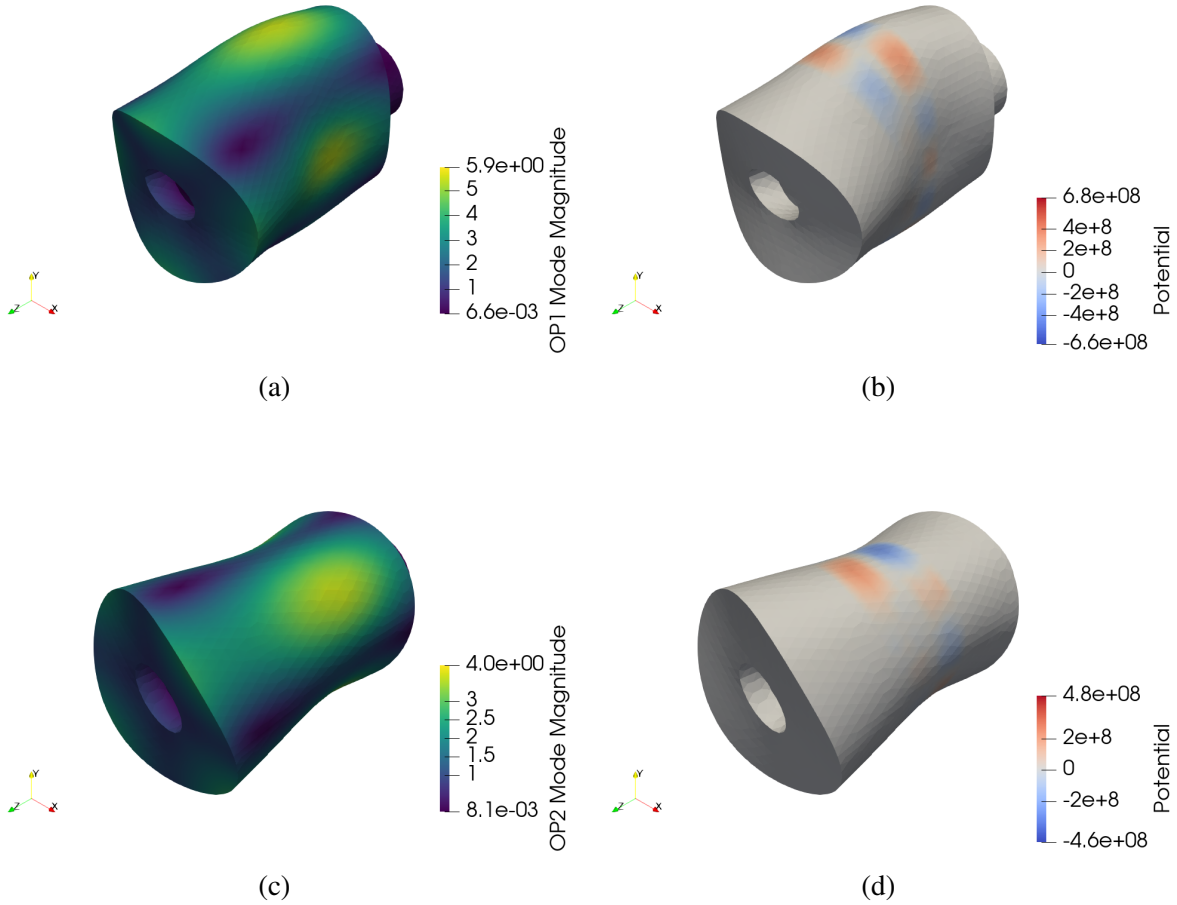

Figure 4.23: (a) Mode shape and (b) electric potential of OP1 mode for the Nitinol Langevin transducer at 44.227 kHz under short circuit conditions, and (c) mode shape and (d) electric potential of OP2 mode for the Nitinol Langevin transducer at 46.514 kHz under short circuit conditions.

The frequency response functions (FRF) for reference points on the end surface has been conducted to validate both modes are orthogonal but with similar mode shapes. FRF of a linear system is defined as the Fourier transform of the time domain response divided by the Fourier transform of the time domain input [219]. For an electromechanical system like ultrasonic transducers, the FRF explains the relationship between input in electrical parameters and outputs in vibrations measured by 3D LDV in acceleration, velocity, and displacement. FRF represent the response of a system per unit excitation as a function of frequency. As such, they are fundamental to the identification of modal parameters. Here, to prove the OP1 and OP2 are similar and orthogonal modes, FRFs of four reference points on the transducer end surface were captured, where positions of points represent maximum vibration amplitudes showing from the scanning LDV results in Figure 4.22. Assigned reference points were located near the circumference of the surface, as shown in Figure 4.24.

A 3D LDV was utilised against the transducer end surface to obtain the FRFs in a spa-

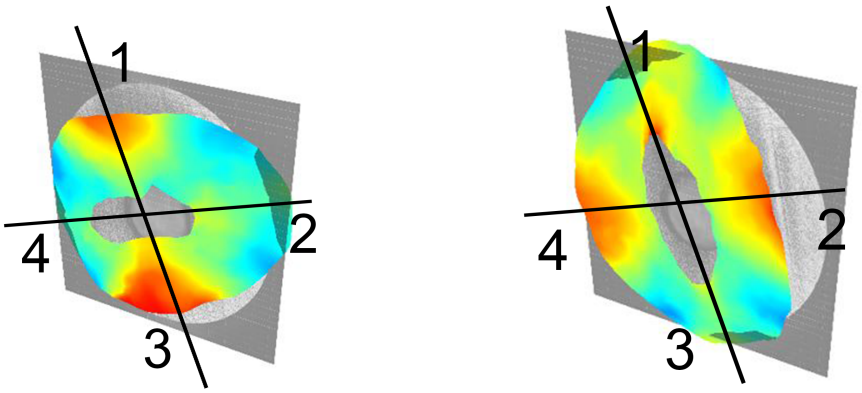

(a) (b)

Figure 4.24: Locations of four reference points on the end surface for both OP1 (a) and OP2 (b) modes.

tial coordinate system. A sine wave signal of fixed excitation amplitude is used as input, the excitation frequency of the sine wave signal changes from low to high or randomly to cover the resonant frequency window. The response amplitude is recorded for each given excitation frequency input of the sine wave signal. The response amplitude is then plotted against the excitation frequency, which presents the frequency response of the oscillator displacement versus the excitation frequency. The FRF magnitude concerning frequency is shown in Figure 4.25.

The FRF magnitudes demonstrate that OP1 performs at higher corresponding vibration amplitudes at points 1 and 3, whereas OP2 exhibits higher amplitudes at points 2 and 4. If OP1 and OP2 represent the same mode but vibrate in different planes, the four points on the end surface should display close FRF magnitudes for both modes due to the transducer's symmetric configuration. This observation shows that they are similar yet distinct modes, demonstrating their orthogonality.

4.4 Validation for Modal Coupling

In order to investigate how changes in Nitinol and PZT properties with temperature can lead to modal coupling of OP1 and OP2, this section provides a detailed characterisation of transducer dynamics at various temperatures. The relationship between frequency and temperature for OP1 and OP2 was assessed using EIA connected to a commercial dehydrator to control the temperature to which the Langevin transducer is exposed. Initially, the Langevin transducer was cooled from room temperature to -40°C using aerosol freeze spray (RS Components), kept at -40°C for 10 min, and then heated to 65°C by the dehydrator. Subsequently, the transducer was cooled from 65°C to room temperature to complete an entire cooling-heating-cooling cycle. Although a thermocouple measured the surface temperature of the transducer, it likely had sufficient time to reach thermal equilibrium. The resonant frequencies as a function of temperature for the two

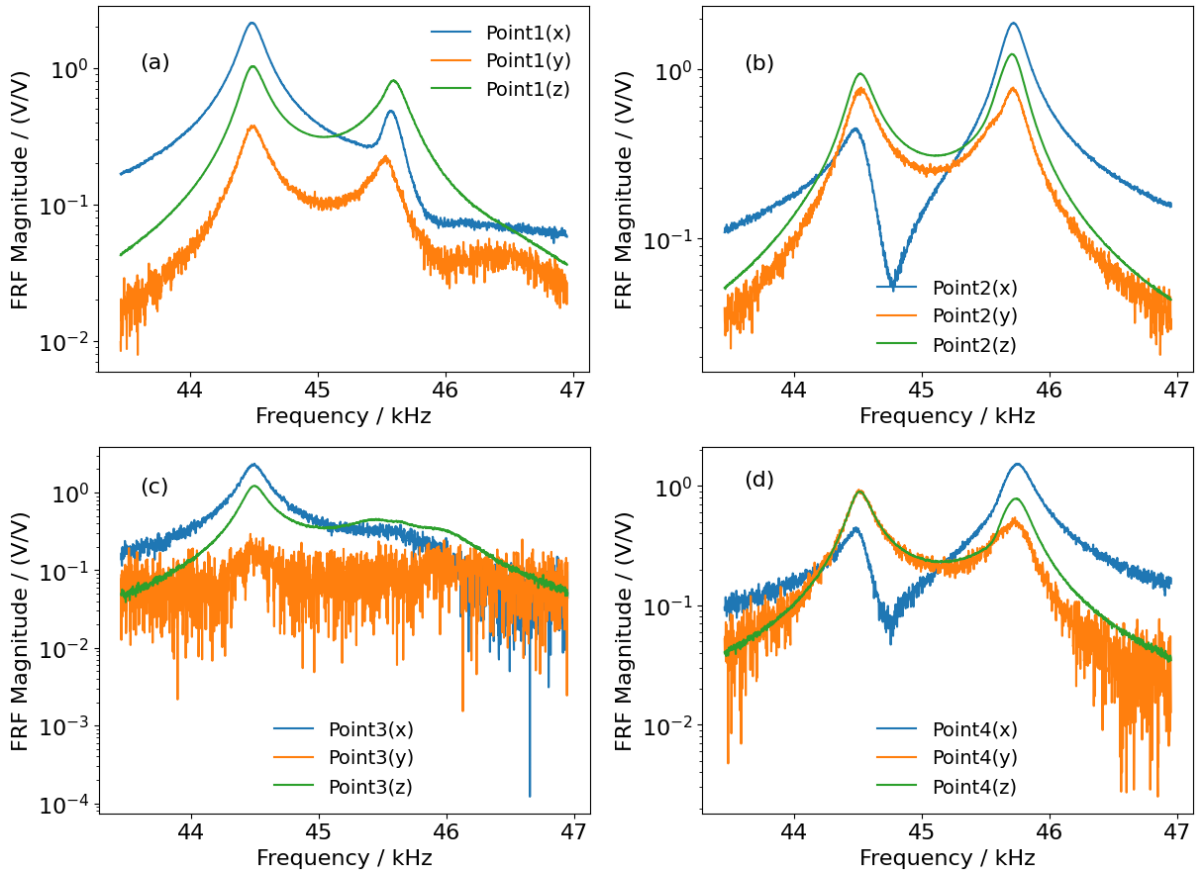

Figure 4.25: FRFs for (a) point 1, (b) point 2, (c) point 3, and (d) point 4 on the end section surface.

modes are depicted in Figure 4.26.

The maximum frequency difference of each mode in the heating-cooling loop is around 5 kHz. This is over 10% of the vibration frequency at room temperature. Although temperature can affect the resonant frequency of a transducer by changing the material properties of PZT materials, for example, in terms of softening in longitudinal modes of Langevin transducers, the total difference between maximum and minimum frequencies is generally about 5% within this temperature window. Thus, this phenomenon showcases the frequency tuning capability of a Nitinol Langevin transducer, providing additional evidence of its resonance tuneability as discussed in Section 4.1. The enclosed areas between the heating and cooling processes display the achievable frequency hysteresis for a Nitinol Langevin transducer across changing temperatures. It should be noted that the hysteresis area is related to the energy principally absorbed by the Nitinol material and subjected to an entire heating-cooling loop. This amount of energy is attributable to the transformations between the martensitic and austenitic phases.

As discussed in the previous section, the phase transformation of Nitinol results in an elastic modulus change, significantly influencing the resonant frequency of a Nitinol Langevin transducer. The frequency changes in heating and cooling processes for each mode indicate that the higher the slope, the faster the phase transformation process. These results demonstrate how

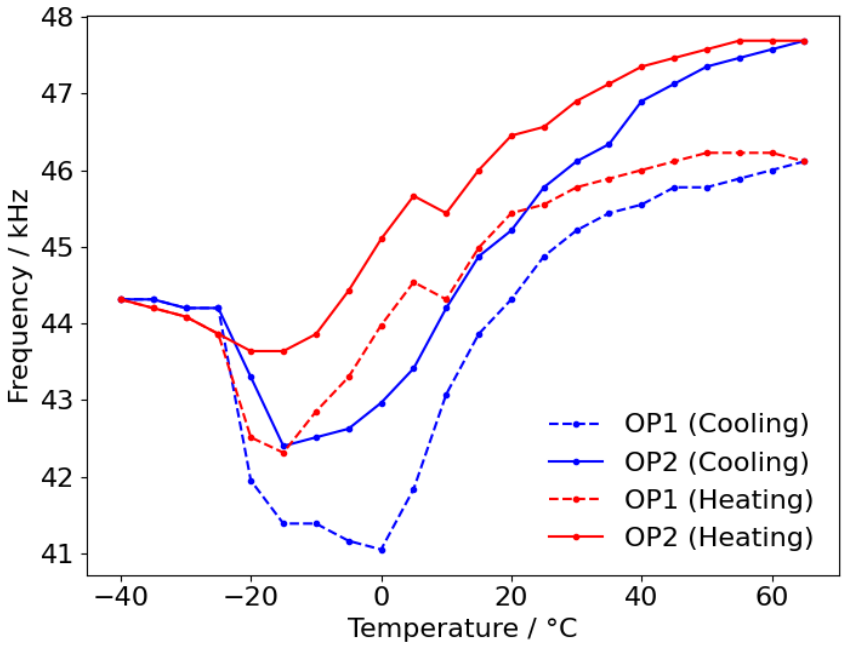

Figure 4.26: Resonant frequencies of the Nitinol Langevin transducer in its OP1 and OP2 modes at different temperatures.

the phase transformations of Nitinol embedded within the transducer contribute to a change in frequency. OP1 exhibits particularly significant frequency shifts from -15°C to -20°C in heating and cooling processes. However, this only occurs during the heating process for OP2. This can be interpreted as the critical temperature where coupling and de-coupling occur. When the temperature approaches -25°C, OP1 and OP2 are coupled. In order to gain a deeper insight into the modal coupling effect, Figure 4.27 illustrates the frequency intervals between OP1 and OP2 in the heating and cooling processes.

The results show the zero intervals for resonant frequency below -25°C, indicating that OP1 and OP2 are coupled. In the heating process, two frequency interval increases have been detected in results at temperatures lower than 0°C and higher than 35°C. It was noticed that 0°C and 35°C are close to A_S and A_F. These two increases, in each case, can therefore be explained in part by the changing Nitinol material properties. When the temperature is between 0°C and 35°C, the frequency intervals generally decrease. In the cooling process, the interval reaches the maximum at 0°C, close to R_F, indicating the contribution of R-phase transformation on transducer tuneability. To investigate how Nitinol and PZT properties also contribute to the electric parameters of the transducer, the electric impedance results were recorded as illustrated in Figure 4.28.

The notable variations observed near -20°C in both heating and cooling processes demonstrate that the phase transformation of Nitinol around this temperature has a substantial effect on the conductance. Recalling mechanical-electrical analogies, the phase transformation from martensite to austenite influences the damping of the Nitinol Langevin transducer. Although

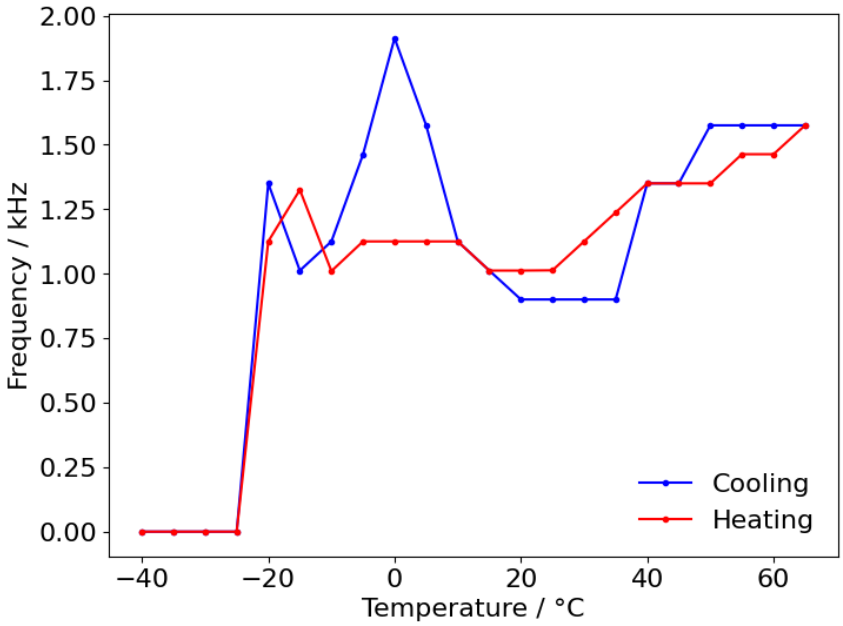

Figure 4.27: Frequency intervals between heating and cooling processes of the Nitinol Langevin transducer in its OP1 and OP2 modes at different temperatures.

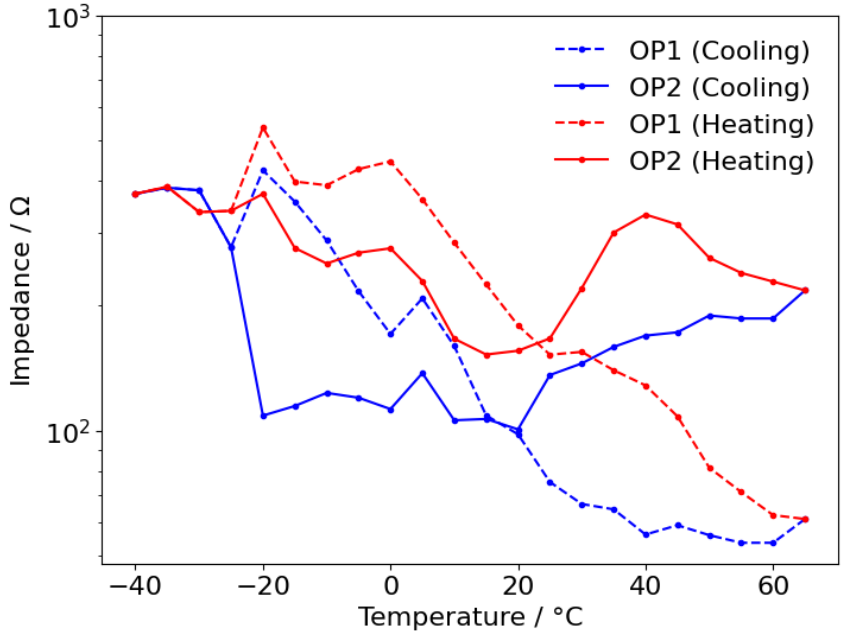

Figure 4.28: Impedance intervals between heating and cooling processes of the Nitinol Langevin transducer in its OP1 and OP2 modes at different temperatures.

the temperature increases, the electrical impedance does not greatly change for OP2, while a gradual decrease was shown in OP1. This indicates that the electrical properties were affected distinctly with different vibration modes.

The hysteresis of the OP1 and OP2 resonant frequencies is related to the energy in the system arising from the phase transformations. The significant frequency differences between

the heating and cooling processes can be applied to a tuneable ultrasonic device. From a mechanical-electrical analogue viewpoint, the martensitic transformation affects the conductance and, thereby, the damping of the mechanical system. The results demonstrate the promising potential of using temperature to realise active modal coupling for a Nitinol Langevin transducer, and there are new avenues of investigation open for progressing this research. Further investigation typically includes achieving the modal coupling near room temperature rather than an extreme temperature of -20°C demonstrated in this section. One possible method is to heat-treat the Nitinol, engineering its phase transformation temperatures close to room temperature. Also, the structure could be optimised to narrow the frequency difference between two fundamental modes.

Certainly, the modal coupling in this section aligns with the tuneability in resonances, differing from the first section through the interaction between two adjacent modes. The Nitinol prototypes in this chapter demonstrate they are capable of thermally tuning their resonances in an opposite pattern and a wide range to conventional Langevin transducers, where only PZT is the tuneable segment. However, the author hypothesises that the tuneability is limited by material properties and configurations, which has been validated in the next chapter and analysed in Chapter 6. Obviously, the resonant frequencies of the transducers in this chapter can only be tuned by between 10% and 15%, far less than aimed application in multifunctional surgical tools, where 20 kHz and 55 kHz are respectively expected for hard and soft tissue dissection. This chapter lays the groundwork for adaptive Langevin transducers incorporating shape memory alloys, specifically Nitinol, giving potential pathways to maximise tuning resonances and to control functional temperature, including modifications in phase transformation behaviours and optimisations in configuration designs.

4.5 Summary

In the initial section of the chapter, a Nitinol Langevin transducer featuring Nitinol as both front and back masses was fabricated and characterised to demonstrate its tuneable resonance. DSC was utilised to investigate the phase transformation behaviours of the Nitinol and to understand the operating temperature range of the transducer. EDM was successfully employed in manufacturing the Nitinol end masses to reduce the effects of work hardening and thermal aging. The assembled transducer was then characterised at room temperature to obtain modal information for both the L1 and L3 modes, including mode shapes, vibration amplitudes, and resonant frequencies. Using the developed harmonic system, the transducer dynamics were measured at elevated temperatures from 25°C to 100°C. The harmonic analysis revealed that the resonant frequency for both modes of the Nitinol Langevin transducer could be rapidly tuned when the temperature was from 35°C to 55°C, closely aligning with the temperature window for the phase transformation from martensite to austenite. This behaviour can be explained by linear elasticity,

where changes in the modulus of Nitinol primarily influence transducer dynamics, while PZT also plays a role in temperature variations. More than a 10% frequency variation with modest temperature changes demonstrates the frequency tuneability of the Nitinol Langevin transducer. Additionally, both vibration amplitude and electrical impedance of the transducer can be tuned with temperature. However, a likely modal coupling between the L3 mode and an adjacent bending mode compromised the vibration amplitude, limiting measurements with the 1D LDV. Therefore, careful design is essential for achieving a pure mode in the Nitinol Langevin transducer. It is interesting to note that the phase transformation also influences the voltage responses, reaching minimal frequency dependency on voltages at 40°C for both longitudinal modes. This suggests that the transducer can be fine-tuned in practical applications to remain stable in resonant frequency despite consistent voltage variations.

Active modal coupling was then introduced, showing that it can be induced by varying the transducer temperature. A second prototype of the Nitinol Langevin transducer was constructed using Nitinol with a broader transformation window, following the same method as the previous transducer for resonance tuneability, where both front and back masses were made of Nitinol. Two out-of-plane modes were identified using scanning LDV and 3D LDV, revealing that these modes are orthogonal but distinct. To consider the complete phase transformation from martensite to austenite, testing temperatures were set between -40°C and 60°C. OP1 and OP2 were tuned to demonstrate the potential for active modal coupling and decoupling at -25°C. The coupling effect could be designed for similar modes near room temperature by adjusting the transducer dimensions, achieving modal coupling without equipping an end-effector or attachment. However, the lack of suitable material properties for both Nitinol and PZT at different temperatures makes it difficult to realise the numerical analysis of the Nitinol Langevin transducer, which must be the focus of future investigation.

Chapter 5

Design for Stable Resonance

The key outcomes shown in this chapter appear in the following publications:
[216] Liu, Y., Hafezi, M. and Feeney, A. (2024) A cascaded Nitinol Langevin transducer for resonance stability at elevated temperatures. *Ultrasonics*, 137, 107201.
[183] Liu, Y., Hafezi, M. and Feeney, A. (2024) Dynamic stability of a nitinol Langevin ultrasonic transducer under power and current tracking conditions. *Applied Acoustics*, 225, 110188.

This chapter focuses on serendipitous work that originates from incorporating Nitinol into a modified Langevin configuration. As depicted in Chapter 4, although both prototypes demonstrated tuneability in their resonances, different dimensions and phase transformation behaviours have led to applicable adaptive resonance in different fundamental modes. This suggests that they still have an unclear effect on the longitudinal mode of the Nitinol Langevin transducers. Also, stress-induced phase transformation may occur due to the high strain of the Nitinol experienced when it is placed at antinodes. The design of the Nitinol segment is strategically positioned near a node to mitigate this influence. Therefore, the cascaded configuration was attempted, incorporating Nitinol as its middle mass. It has to be noted that the Nitinol used here is the back mass in the previous modal coupling transducer, which is different from that of the tuneable prototype. This is because one of the aims is to investigate different phase transformation behaviours on tuneability in longitudinal modes. Interestingly, during transducer characterisations with temperature, stable resonance was discovered near room temperature, which is the main topic of this chapter, which details a thorough characterisation and analysis to validate its unique dynamics.

Across power ultrasonics and sensing, piezoelectric ultrasonic transducers commonly experience changes in dynamic properties during continuous operation due to the dielectric heat of piezoelectric materials [26]. These changes, arising for example through high excitation voltages, can lead to nonlinear dynamic behaviours which compromise device performance. A commonly applied technique to mitigate the influence of temperature in the piezoelectric stack

is through pulse-excitation [26], where the time window for which the piezoelectric material is subjected to voltages causing temperature increases is minimised, and the measurement of the dynamic performance of the transducer is undertaken at steady-state. However, the principal disadvantage of this technique is that relatively long burst times can still be required to ensure steady state, and there remain temperature increases in the piezoelectric materials. An alternative approach is to compensate for temperature rises, and thus nonlinear behaviour, by phase tracking. Here, the changing resonance response of the transducer as a function of the excitation is monitored and the excitation adjusted accordingly. However, the dynamic properties of the transducer, including resonant frequency, are still a function of temperature. A further practical option is to apply a DC bias voltage across the transducer to compensate for the frequency shift in part generated by changes in temperature [220]. However, DC bias voltages can result in unstable load powers and vibration amplitudes with respect to temperature. In general, mitigating the influence of temperature on the performance of piezoelectric ultrasonic transducers remains a significant challenge for practical applications.

As a novel approach to mitigating the influence of temperature on the properties of piezoelectric materials, the phase-transforming shape memory alloy Nitinol is incorporated into the piezoelectric stack of a Langevin power ultrasonic transducer, in a cascaded configuration. The underlying principle is that the nonlinear changes in the elastic properties of Nitinol with increasing temperature can be utilised to dynamically compensate for the impact that variations in the mechanical and electrical properties of piezoelectric materials have on the resonance behaviour of a Langevin transducer in the longitudinal mode. Thus, the dynamic response of the transducer can be linearised at various excitation levels. In this chapter, two configurations of Langevin transducer were designed and characterised. One transducer incorporated a Nitinol middle mass, and in the second, titanium, creating a close acoustic impedance between the two materials. These designs result in similar resonance behaviours and dynamics at room temperature, emphasising comparisons between these transducers under thermal loadings. A combination of electrical and thermomechanical characterisation was undertaken to demonstrate the transducer dynamics through the martensitic transformation. The resulted stability of transducer dynamics, named as the resonance stability, were analysed at elevated temperatures under either stepwise isothermal or self-heating conditions.

5.1 Transducer Design and Fabrication

In this study, two transducers are designed and fabricated. The first is the NMCT, and the second incorporates a titanium middle mass in place of the Nitinol, called the titanium-middle cascaded transducer (TMCT). The purpose of fabricating the TMCT is to demonstrate the unique behaviours regarding compensation of the dynamics for the NMCT, as a comparison case.

The transducers were designed using FEA, where the resonant frequencies of the first longi-

tudinal modes of vibration were tuned to around 30 kHz. Following this, the transducer components, including piezoelectric ceramic rings, were acquired, before the end and middle masses of the configurations were machined. A conventional machining process can be utilised for titanium, but Nitinol experiences relatively severe work hardening, and so here EDM was applied instead, to machine the Nitinol ring to the required dimensions [221]. Prior to these steps, the transformation properties of the Nitinol used to fabricate the NMCT were characterised.

5.1.1 Design of the Transducers

The Nitinol back mass used in Section 4.3 has been repurposed into this chapter, with DSC results and transformation temperatures demonstrated in Figure 4.18 and Table 4.2, respectively. The objective is to design a Langevin transducer with a more intricate configuration aimed at minimising the strain on Nitinol during operation while leveraging its unique dynamics through martensitic transformation. Therefore, the Nitinol has been positioned as close to the nodal point as possible in the new design to reduce the chance of inducing stress-induced phase transformation. A cascade configuration of Langevin transducer was produced using Abaqus FEA, with one model incorporating Nitinol as the middle mass to form the NMCT, and the other comprising a titanium ring as the middle mass, constituting the TMCT. The first longitudinal mode of each transducer was tuned to approximately 30 kHz, consistent with operational frequencies for standard power ultrasonic applications, which are between 20 kHz and 100 kHz. The finite element results are shown in Figure 5.1, along with the resonant frequencies.

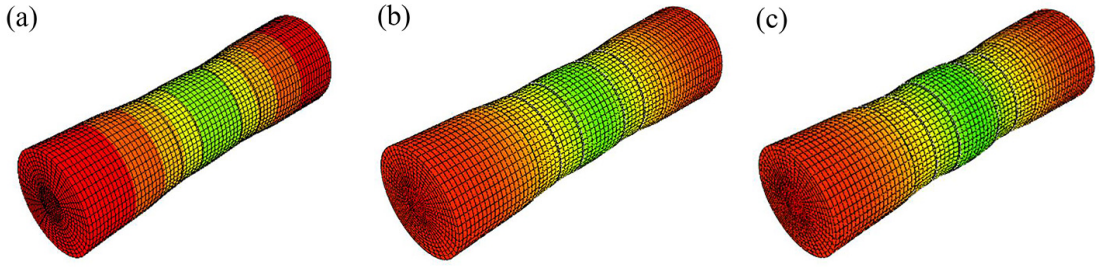

Figure 5.1: Finite element simulation results of the first longitudinal mode for (a) the NMCT in the heating cycle at 28.705 kHz, (b) in the cooling cycle at 29.515 kHz and (c) the TMCT at 31.214 kHz.

Recalling the discussion in Section 3.4.1, there are challenges in experimentally measuring elastic moduli of Nitinol. Therefore, at the outset, the finite element model for the NMCT was developed through an iterative trial approach using estimations of elastic moduli using the scientific literature [55–58], from where the models were later refined using experimental data, and this is what has been employed in Chapter 4. The material properties used in the final FEA models are shown in Table 5.1, which includes the iteratively defined elastic moduli for the Nitinol in its martensitic and austenitic phases.

Table 5.1: Iteratively defined elastic moduli for the Nitinol in FEA

Phase	Elastic moduli (GPa)
Mixed martensite and austenite (Room temperature in heating cycle)	60
Austenite (Room temperature in cooling cycle)	73

The detailed configuration of the transducers is shown in Figure 5.2, where the two end masses, the middle mass, and the two PZT stacks are indicated, alongside key dimensional labels which can be used for reference.

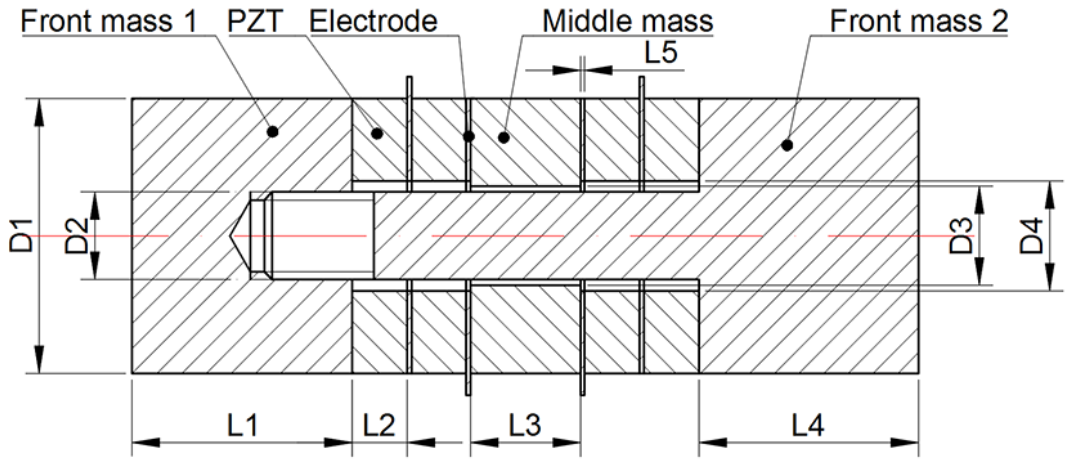

Figure 5.2: Detailed schematic of the configuration used for both the NMCT and the TMCT.

The electric potential distribution for both NMCT and TMCT is simulated based on the proposed 3D mathematical model, as shown in Appendix C. The resonance frequencies obtained from Abaqus were utilised to conduct these simulations. A 10 V electric potential input was applied as an example to illustrate the electric potential distribution when the transducers are excited.

The Nitinol middle mass is a ring manufactured by EDM, with copper used as the electrode material because of its high thermal and electrical conductivity [203]. Each PZT stack consists of one pair of PZ26 rings, and complemented by two copper electrodes. To ensure structural symmetry and uniformity, a bolt feature was fabricated on the front mass 2 to fit into each transducer assembly, where a threaded feature machined into the front mass 1.

A major challenge in the design of these transducers was accommodating differences in acoustic impedance between the end mass materials and the middle mass in each case. Acoustic impedance can be described as the product of material density and sound velocity, and it is known that an optimal acoustic performance is achieved when the sandwich structure possess a gradient acoustic impedance [222]. Measurements of longitudinal sound velocity through Nitinol were made using a pulse-echo system detailed in Section 3.4.1. This enabled acoustic

impedances for both mixed martensite and austenite (Heating cycle) and austenite (Cooling cycle) to be measured, where they are shown to be marginally higher than that of PZ26, as shown in Table 5.2 and 3.1.

Table 5.2: Acoustic impedances of transducer materials.

Material	Acoustic impedance ($kgm^{-2}s^{-1}$)
Nitinol (Heating)	33.1e6
Nitinol (Cooling)	34.9e6

The measurements of acoustic impedance compare well with observations in the literature [223], although material properties of Nitinol alloys can differ, depending on their specific compositions and processing conditions. Using these measurements, a material with acoustic impedance lower than PZ26 would be desirable for front mass 1, with reference to Figure 5.2, to ensure the necessary acoustic impedance gradient. An aluminium alloy (6082) was also selected, since its acoustic impedance is lower than that of both Nitinol and PZT, and because it has relatively low loss characteristics with high energy transmission [224]. Finally, titanium (Ti6Al4V) was selected for the TMCT since its acoustic impedance is close to that of Nitinol, and is a material commonly used in power ultrasonic transducers such as the Langevin configuration, like aluminium, in part because of its relatively high magnitude of quality factor. A summary of the dimensions for both transducers is shown in Table 5.3, with reference to Figure 5.2.

Table 5.3: Acoustic impedances of transducer materials.

Parameter	Dimension value (mm)
$L1$	20
$L2$	5
$L3$	10
$L4$	20
$L5$	0.38
$D1$	25
$D2$	8
$D3$	9
$D4$	10

The NMCT and TMCT were both assembled by loading the central bolt with a pre-stress of 10.5 Nm. It appears that a pre-stress of 10.5 Nm is optimal for achieving the lowest electric impedance for both transducers. The manufactured transducers are shown in Figure 5.3.

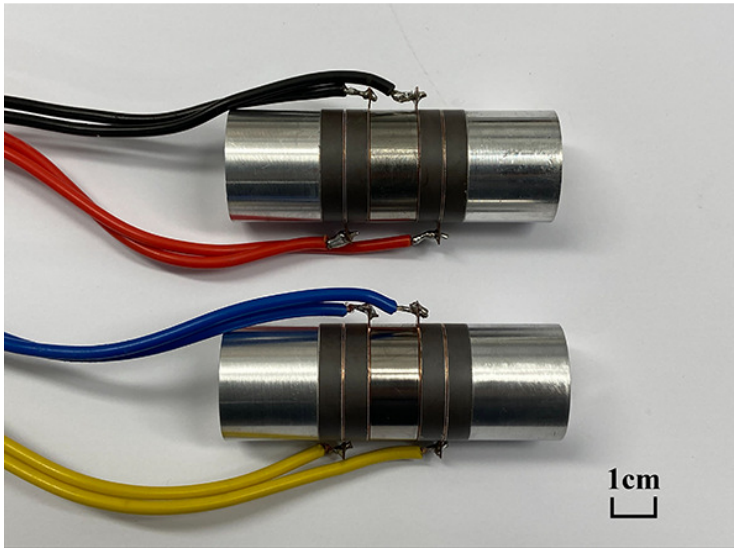

Figure 5.3: Manufactured NMCT (top) and TMCT (bottom).

5.2 Dynamic Characterisation in Controlled Isothermal Environments

5.2.1 Modal Identification at Room Temperature

Accurate mode identification is important during the experimental process because it should be ensured that the correct mode of vibration is being monitored as the associated resonant frequency changes with temperature. When the temperature of the transducer changes, the dynamic properties, particularly elastic moduli, of the transducers also change, thereby directly influencing resonant frequency. EIA generally only provides electrical data with respect to parameters including frequency, thus LDV is required to capture the modal behaviour which can be correlated with FEA. Here, the vibration modes of each transducer were measured at the room temperature using a 3D scanning LDV at an 8 $V_{P\text{-}P}$ excitation. The reason of measuring under 8 $V_{P\text{-}P}$ is to ensure a sufficiently clear and detectable vibration mode shape. The LDV results for two transducers at room temperature for the first longitudinal mode of vibration are shown in Figure 5.4.

During the heating cycle, the Nitinol undergoes a transformation from its low temperature martensite state to the high temperature austenite state. Conversely, during the cooling cycle, the Nitinol transitions from its high temperature austenite state to the low temperature martensite state. There is a hysteretic response inherent in shape memory materials such as Nitinol, as shown in Figure 4.18, and this explains the resonant frequency difference of the NMCT across the heating and cooling cycles. These mode shapes can be directly compared with those shown in Figure 5.1, where the measured resonant frequencies also closely match. Therefore, there is a high level of confidence in the estimations for the elastic moduli used for the NMCT model, provided in Section 5.1.1.

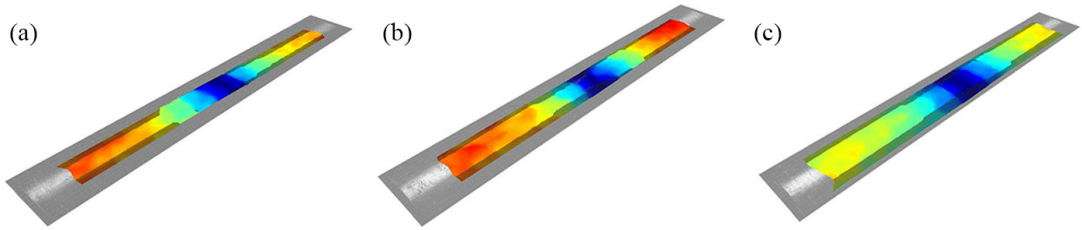

Figure 5.4: LDV results of the first longitudinal mode for NMCT in the heating cycle (a) at 28.719 kHz and cooling cycle (b) at 29.336 kHz, where the heating cycle denotes that the Nitinol is in the state of heating from low temperature martensite to high temperature austenite, and vice versa for the cooling cycle; and TMCT (c) at 31.338 kHz.

5.2.2 Resonance Stability in Stepwise Isothermal Regimes

5.2.2.1 Experimental Setup

With the longitudinal mode for each transducer measured, along with its resonant frequency, the dynamic response of each transducer could then be monitored as a function of temperature. The aim of this part of the study was to quantify the influence of changing temperature on the dynamic properties of the NMCT, with those for a transducer comprising a conventional Langevin transducer material, TMCT. To achieve this, resonant frequency and electrical impedance were monitored by an analogue circuit with an impedance analyser module (Analog Discovery 2, Digilent) which was connected to a commercial climate chamber as the mechanism for applying controlled temperature functions. Transducers were placed on a polyurethane foam inside the climate chamber to establish boundary conditions as close to free-free as is physically practical. The resonant frequency and electrical impedance of the first longitudinal mode for both NMCT and TMCT were measured by sweeping through a designated frequency range at 0.5 V_{RMS}. All data were measured within a $-40°C$ to $60°C$ temperature window, to capture all phase transitions of Nitinol as suggested through the DSC results shown in Figure 4.18. The temperature step interval was set as $5°C$. The temperature was stabilised at each step for 10 min, to ensure that the temperature of each transducer equilibrated with the environment and was homogeneous through the device. Temperature was continuously and consistently monitored throughout. The experimental setup is illustrated in Figure 5.5.

In an ultrasonic system, the temperature of the device and the applied voltage directly influence the dynamic properties, such as resonant frequency and impedance. The hypothesis here is that the material behaviours unique to shape memory materials, and nonlinearities, associated with the Nitinol in the NMCT will interact differently with the expected resonance behaviours associated with the PZT stack, as temperature and voltage change, for the NMCT compared to the titanium based TMCT. To quantify this, the temperature-voltage relationship was assessed by monitoring the dynamic properties of the transducers for different excitation voltages when the transducer temperature is stable. In each case, the resonant frequency, electrical impedance, and power are obtained by the PiezoDrive which was connected externally to the transducers

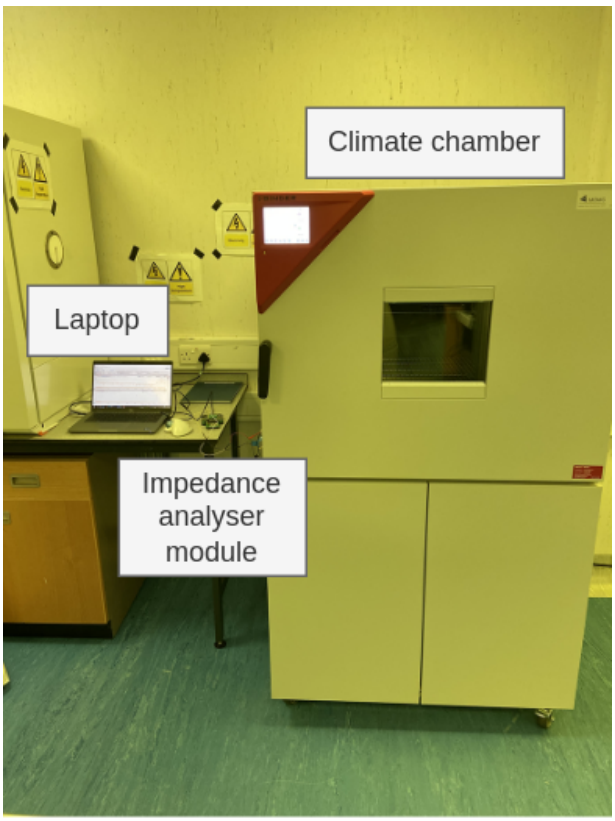

Figure 5.5: Image of experimental setup.

inside the climate chamber. The phase tracking function of the ultrasonic driver ensures that the transducers operate at their resonant frequency. To study the potential of the NMCT as a suitable candidate of power ultrasonic device for practical application, the vibration amplitude was obtained using the harmonic system via sinusoidal signals with voltages from 10 V_{RMS} to 50 V_{RMS}, applying a burst time interval of 3 s to minimise self-heating within the transducer where possible. By using a 1D LDV, the vibration amplitude of the first longitudinal mode is then collected.

5.2.2.2 Dynamic Characterisations

Before the experiment is conducted, the phase of the Nitinol material must be reset, ensuring the initial phase at the starting temperature is accurately known. Because of hysteresis, Nitinol's microstructure may be martensitic, austenitic, or a mixture, depending on whether it is on a heating or cooling path. This was done by using the aerosol freeze spray to cool the NMCT to -40°C for 10 min and then gradually heat in ambient conditions until it returns to room temperature (20°C). According to Figure 4.18, the initial phase of Nitinol is a combination of martensite and austenite, because A_f has not yet been passed. The experiment includes three temperature functions to realize a heating-cooling loop: (1) heating the transducers from room temperature to 60°C; (2) cooling the transducers from 60°C to -40°C; and (3) heating the transducers from

-40°C to room temperature. The first set of analyses aimed to evaluate the influence of static temperatures on NMCT dynamic properties, with particular focus on the resonant frequency. resonant frequency results for the NMCT and TMCT in their first longitudinal mode with respect to temperature are shown in Figure 5.6, extracted from the series resonance from EIA in each case.

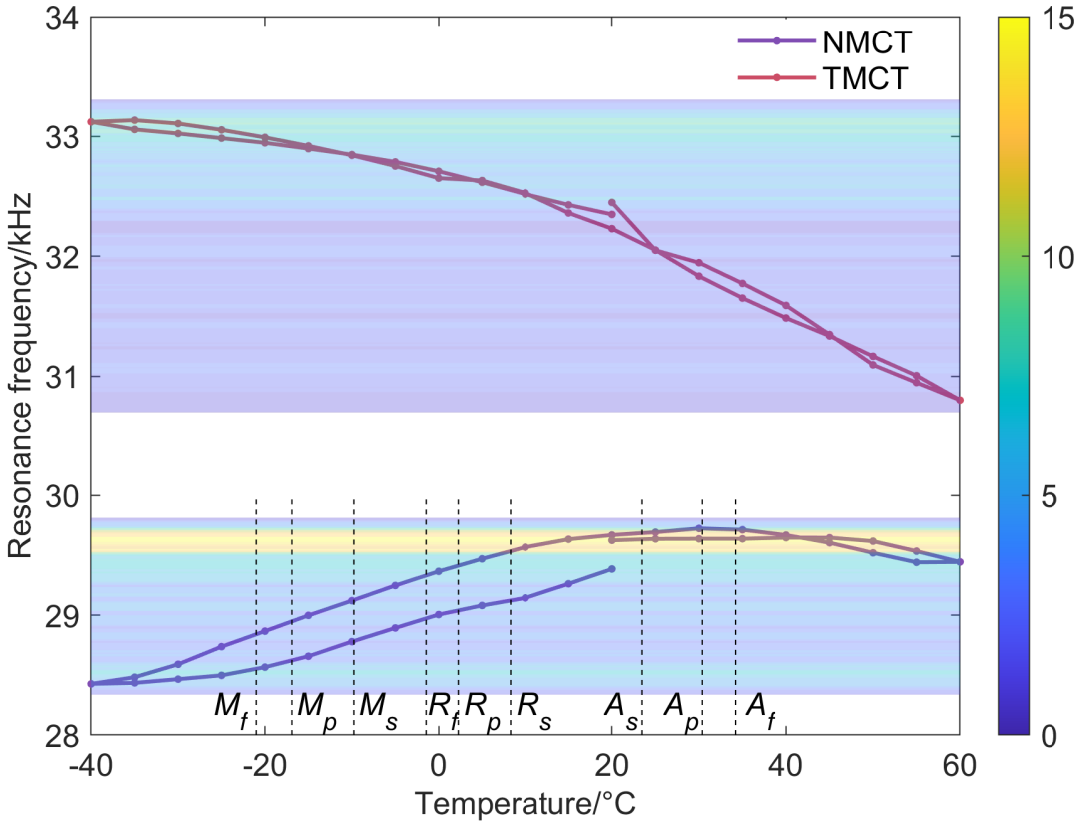

Figure 5.6: resonant frequencies of the NMCT and TMCT under the static temperature condition for the first longitudinal mode within a -40°C to 60°C temperature window. The background colour illustrates the number of superimpositions of half-power bandwidths across the temperature window for both transducers, as reference to the right-side colour bar.

The results show that the resonant frequencies of the TMCT monotonically decrease in the heating cycle, but increase in the cooling cycle. The experiment was conducted neglecting electrical losses, such as dielectric loss and piezoelectric loss [225], with low excitation. Therefore, the resonant frequency differences are primarily contributed by changes in PZ26 elastic and electric properties, especially c_{33} for longitudinal modes, and are partially influenced by the thermoelasticity. By contrast, the resonant frequencies of the NMCT do not exhibit this monotonical change across the heating-cooling loop. What is noticeable, is that there is a stability of resonant frequency at temperatures approximately higher than 20°C and 10°C in the heating and cooling cycles, respectively. The phenomenon can be likely attributed to changes in the elastic moduli of Nitinol, which compensates for the temperature-induced changes in the material properties of PZT.

In order to assess the resonance stability quantitatively, a half-power bandwidth superimposing technique is used. The half-power bandwidth is a measure of transducer performance in the frequency domain. Driving the transducer at any frequency inside the band, its power falls no lower than half of the peak value. Accordingly, it is acceptable in this study for NMCT and TMCT working in the half-power bandwidth. By superimposing bandwidth at two adjacent temperatures, the frequency range that satisfies driving at both temperatures can be obtained. Similarly, the superimposition can be undertaken across the entire temperature range, thus allowing measurement across a sufficiently wide heating-cooling loop. As shown in Figure 5.6, the background of the figure shows the number of superimpositions corresponding to the right-side colour bar. The maximum superimpositions of NMCT and TMCT are 15 and 8, respectively. This interestingly implies that the NMCT could be driven reliably throughout the frequency band between 29.609 kHz to 29.651 kHz within temperature ranges of 20°C to 50°C and 10°C to 45°C in the heating and cooling cycles, respectively. Comparing to results of the TMCT, the NMCT shows a prominent resonance stability. It should be noted that this significant observation applies to the case including elastic loss only.

As shown in Figure 5.7, electrical impedance results of NMCT and TMCT both exhibit strong temperature dependence. The impedance of TMCT increases and decreases during heating and cooling cycles, respectively. However, NMCT shows minimal variations within the temperature range from -40°C to 25°C. Above this range, NMCT's impedance undergoes similar rates of change to that of TMCT. Statistically, the smaller range of the data set of NMCT impedance compared to TMCT confirms that the former has a lower spread in the data, and thus is less sensitive to temperature. Moreover, phase transition temperatures in Figure 4.18 broadly align with the patterns in the data trends for the NMCT. This indicates the phase transitions influence the electrical properties in a transducer. It is worth noting that the larger area enclosed by curves of TMCT results indicate a higher hysteresis than that of the NMCT, and in general, it is evident that Nitinol phase transitions affect transducer electrical properties.

From here, dynamic properties including antiresonant frequency, half-power bandwidth, quality factor, and electromechanical coupling coefficient, are compared. As shown in Figure 5.8 (a) and (b), antiresonant frequency and half-power bandwidth results are consistent with the trends shown in Figure 5.6 and Figure 5.7, respectively. Both half-power bandwidth and quality factor are indicators of the resonance behaviour of an ultrasonic transducer in an underdamped condition. Since NMCT has a wider bandwidth and a lower quality factor than TMCT through the heating-cooling loop in Figure 5.8 (b) and (c), NMCT has greater damping. It shows significant potential for NMCT to be applied into sensing applications, in addition to power ultrasonic applications. Another indicator for analysing the dynamic response is the electromechanical coupling coefficient which is a measure of the fraction of electrical energy that can be converted into mechanical energy and vice versa in an ultrasonic transducer system. When assuming the transducer is a cylindrical piezoelectric element, the electromechanical cou-

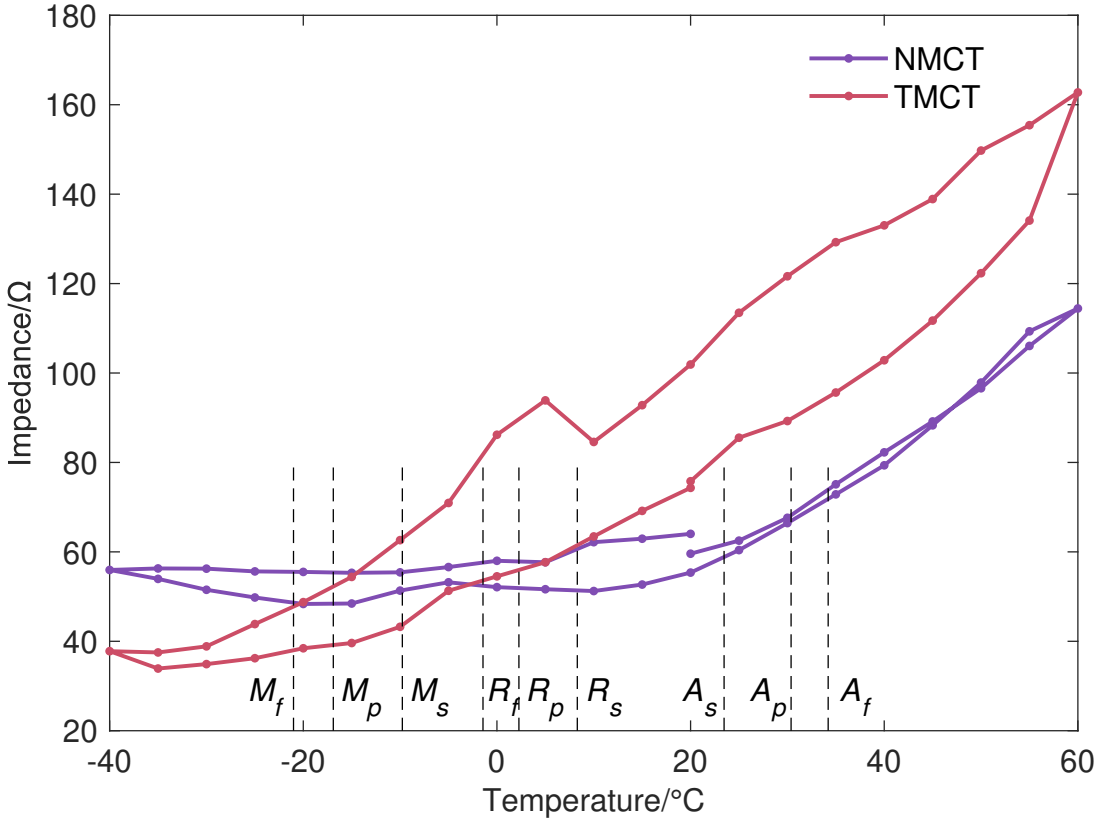

Figure 5.7: Electrical impedance results of NMCT and TMCT with respect to temperature.

pling coefficient for its longitudinal vibration can be obtained using IEEE 176-1987 [155], as shown in (5.1).

$$(k_{33}^{l})^2 = \frac{\pi f_s}{2f_p}\tan\left(\frac{\pi(f_p - f_s)}{2f_p}\right) \tag{5.1}$$

Here, k_{33}^{l} is the electromechanical coupling coefficient, f_s is the frequency of maximum conductance, and f_p is the frequency of maximum resistance. In Figure 5.8 (d), the electromechanical coupling coefficient of NMCT is almost constant over the entire temperature window, while that of TMCT is decreased with an increasing temperature. This implies that the resonance stability exists in the electromechanical coupling coefficient of NMCT. Thus, the incorporation of Nitinol enables a higher and stable energy conversion in the transducer.

A clearer understanding of the dynamic responses for the NMCT can be achieved by considering the unloaded conventional BVD equivalent circuit model, as mentioned in Section 3.3.1. This model describes the connection between mechanical and electrical properties for an ultrasonic transducer. In the equivalent circuit diagram, C_0 is the electrical static capacitance, C_1 is the mechanical equivalent capacitance, L_1 is the mechanical equivalent inductance, and R_1 is the mechanical equivalent resistance.

Based on the BVD model, the first parameter that can be obtained from experimental impedance spectra is R_1. At the resonant frequency, where its phase is zero, the transducer

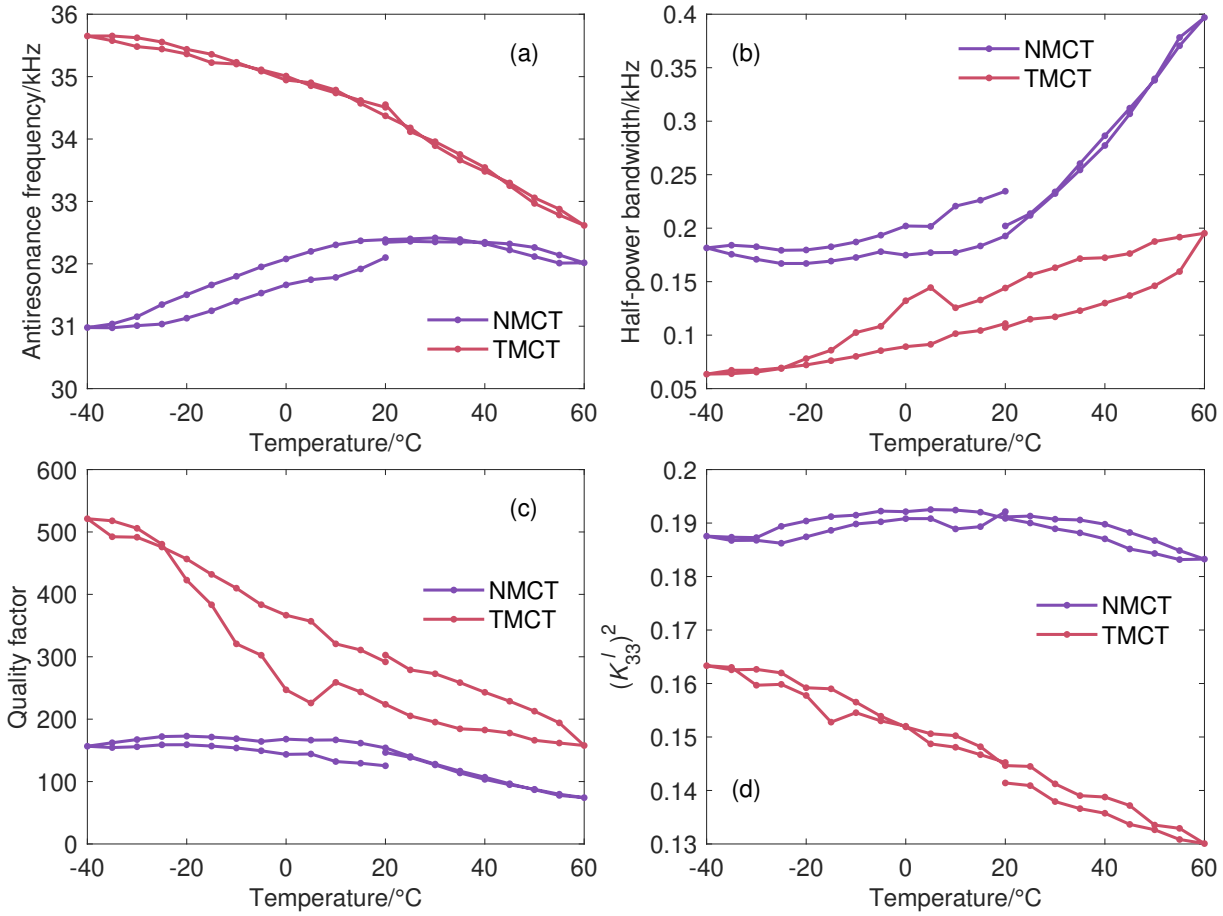

Figure 5.8: (a) Antiresonant frequency, (b) half-power bandwidth, (c) quality factor, and (d) electromechanical coupling coefficient of the NMCT and TMCT with respect to temperature.

becomes a transient and purely resistive system. Therefore, R_1 equals the resonance impedance, and the experimentally measured impedance at an off-resonant frequency is the sum of the impedance for C_0 and C_1. Relations of components in the BVD model are described through (5.2) to (5.4).

$$Q = \frac{1}{2\pi f_r R_1 C_1} \tag{5.2}$$

$$L_1 = \frac{1}{(2\pi f_r)^2 C_1} \tag{5.3}$$

$$Z_{off} = C_0 + C_1 \tag{5.4}$$

Here, Q is the quality factor, f_r is the resonant frequency, and Z_{off} is the impedance at the off-resonant frequency. Calculated results for C_0, C_1, L_1, and R_1 with respect to different temperatures are shown in Figure 5.9.

C_0 denotes the electrical capacitance of the transducer, which is defined by intrinsic electrical properties of PZT. As shown in Figure 5.9(a), NMCT capacitance remains higher than those of the TMCT across the temperature window, though in the same order of magnitude. The energy

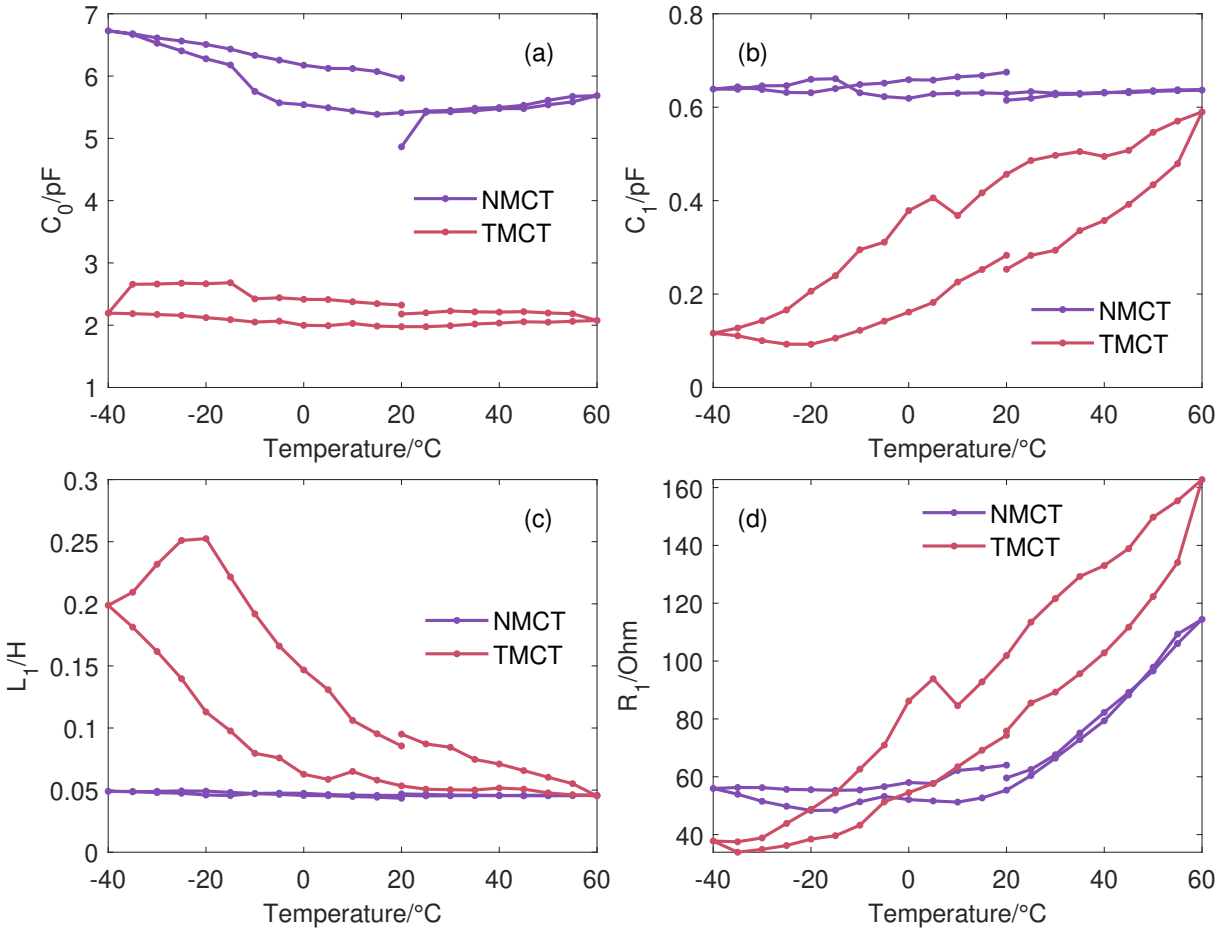

Figure 5.9: Calculated C_0 (a), C_1 (b), L_1 (c), and R_1 (d) results from the BVD model.

stored in the PZT is the product of C_0 and square of the voltage applied, divided by two. From this, it is evident that the NMCT can store more electrical energy for a given applied voltage. A practical method to analyse the results in Figure 5.9(b), (c), and (d) is to describe the mechanical system through the impedance analogy [226]. Equivalent mechanical parameters C_1, L_1, and R_1 represent compliance, mass inertia, damping, respectively [227]. The magnitude of C_1 in Figure 5.9(b) increases with a rise in temperature, and vice versa. This indicates that TMCT's compliance exhibits a similar variation with C_1, as its stiffness is the inverse of compliance, aligning with the thermal behaviours of PZT in Figure 5.6. However, the C_1 magnitude of the NMCT is effectively constant, showing that the change in Nitinol stiffness contributes to the compensation of the variations of the PZT properties. Besides, L_1 in Figure 5.9(c) suggests that the mass inertia of the TMCT decreases with a rise in temperature, and vice versa. However, the mass inertia of NMCT is generally constant, and lower than that of the TMCT. This can be explained by the fact that the TMCT can readily achieve higher vibration velocities than the NMCT, and it can be more significantly influenced by variations in this temperature window. In Figure 5.9(d), the R_1 analogized damping of both the NMCT and the TMCT increases with a rise in temperature, which corresponds to the half-power bandwidth shown in Figure 5.8(b).

The hysteresis of mass, compliance, and damping can explain the existence of impedance and resonant frequency hysteresis for both the NMCT and the TMCT.

5.2.3 Resonance Stability in Stepwise Isothermal and Stepwise Electric Potential Regimes

To introduce dielectric loss and piezoelectric loss effects, NMCT and TMCT are measured from 10 V_{RMS} to 50 V_{RMS} in a defined heating-cooling cycle. The resonant frequencies of the NMCT and TMCT are shown in Figure 5.10(a) as functions of both voltage and temperature. Multiple factors, including fatigue of PZT materials and slight temperature differences, can be attributed to the jump phenomenon of transducers at room temperature in the heating cycle. Changes of resonant frequency in the NMCT and TMCT follow a similar trend to that exhibited in Figure 5.6, across all applied voltage levels. In general, the higher the voltage applied, the lower the frequency of NMCT and TMCT, which is a nonlinear softening behaviour of ultrasonic transducers that has been widely reported in the literature over many years [228, 229]. Specific to the NMCT, resonance stability is detected at temperatures around ambient room temperature. Utilizing the half-power bandwidth superimposition method described earlier, the quantified resonance stability is shown in Figure 5.10(b). Coloured areas represent the frequency band and maximum temperature window that generated the associated level of resonance stability. As voltage increases, both the width of the frequency band and the temperature range rise. Comparing the results in Figure 5.6 and those for 10 V_{RMS} in Figure 5.10(b), stability was reduced, likely due to the introduction of electrical losses. However, stability was enhanced with an increase in applied voltage level. It should be noted that the stabilised temperature range in the cooling loop is significantly wider than that in the heating loop. Therefore, the austenite in the Nitinol microstructure appears to more favourably induce resonance stability, compared to the microstructure comprising a mix of austenite and martensite. It is also important to note that within the stabilised temperature window, the variation of resonant frequencies is within 1%.

The electrical impedance of both the NMCT and TMCT are shown to rise with increasing voltage, as shown in Figure 5.11. Comparing these results to those shown in Figure 5.7, there appears to be negligible hysteresis, likely due to the electrical losses in the PZT for rising applied voltage level. The electrical impedance of the NMCT is a function of temperature in the voltage range from 10 V_{RMS} to 50 V_{RMS}, when the temperature is above 15°C, but generally stable below this temperature. Additionally, the results also show the NMCT has a lower impedance spread than that of TMCT. Therefore, the NMCT demonstrates higher electrical stability than the TMCT.

This analysis can be extended to considering comparisons for antiresonant frequency, half-power bandwidth, quality factor, and electromechanical coupling coefficient. This data is summarised in Figure 5.12, and in general it is evident that the changes in these properties with

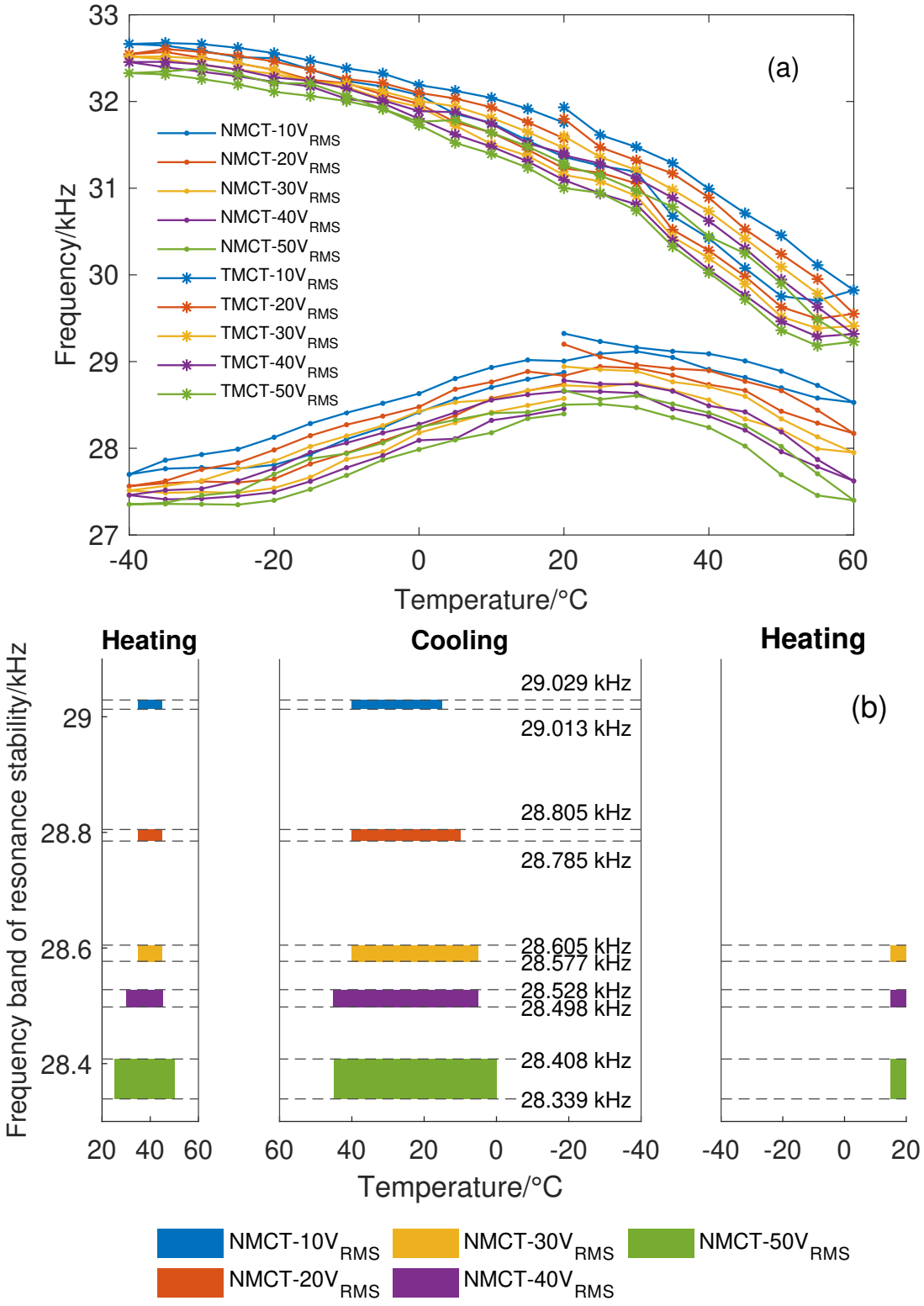

Figure 5.10: (a) resonant frequency and (b) the frequency band of resonance stability for the NMCT and TMCT under the static temperature-voltage condition for the first longitudinal mode within a -40°C to 60°C temperature window, and applied voltages of 10 V_{RMS} to 50 V_{RMS}.

temperature are consistent with the results presented in Figure 5.8, irrespective of applied voltage level. Antiresonant frequencies at different voltages, as shown in Figure 5.12(a), exhibit

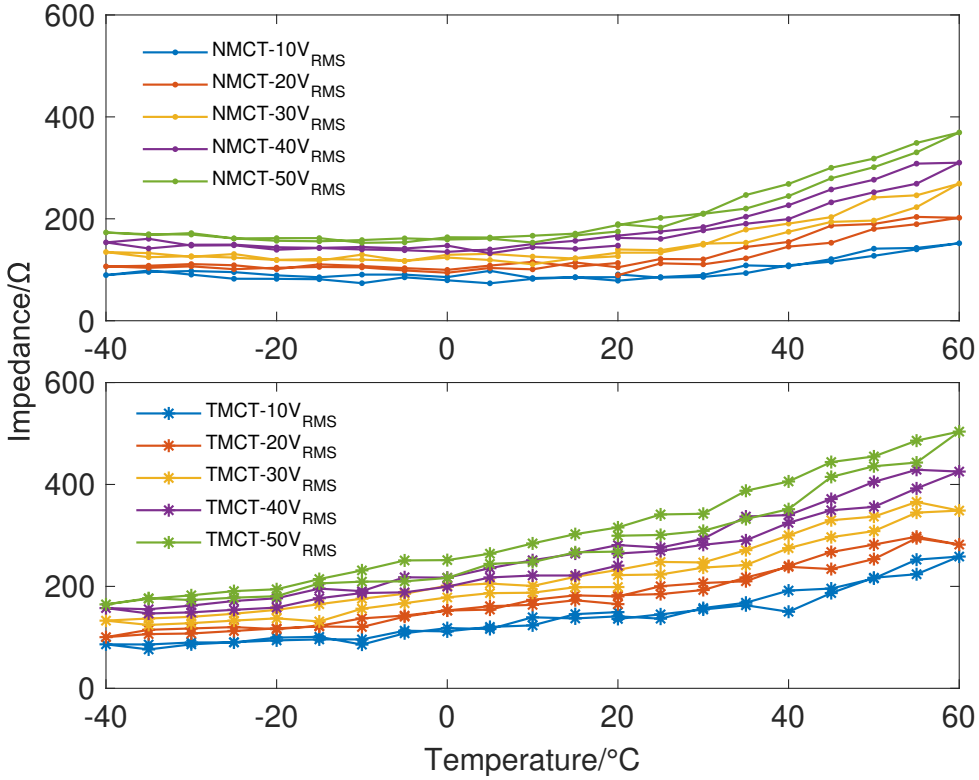

Figure 5.11: Impedance magnitudes of the NMCT and TMCT under the static temperature-voltage condition for the first longitudinal mode within a -40°C to 60°C temperature window, and applied voltages of $10V_{RMS}$ to 50 V_{RMS}.

resonance stability in the data around the room temperature. Thus, the phase transition of the Nitinol affects the resonance and antiresonant frequencies simultaneously. As shown in Figure 5.12(b), the NMCT has wider half-power bandwidth overall and higher spread of data at higher voltage excitation levels. This likely indicates that the NMCT has higher mechanical damping which is more readily influenced by the applied voltage level. Moreover, the quality factor of the NMCT in Figure 5.12(c) demonstrates that the damping of the NMCT system is a function of voltage, resulting in higher energy loss, and there appears to be a more significant reduction in quality factor for the TMCT compared to the NMCT for given applied voltage increases. Furthermore, it can be seen in Figure 5.12(d) that electromechanical coefficients of the NMCT and TMCT are functions of both voltage and temperature. Whilst the electromechanical coefficient of the TMCT appears to be relatively independent of applied voltage, unlike for the NMCT, there is a general stability of the electromechanical coefficient across the specified temperature window (heating or cooling) which is not detected for the TMCT, which progressively reduced as temperature rises. Although the electromechanical coefficient is generally stable for the NMCT, there are slight increases in both cycles, unlike the phenomenon depicted in Figure 5.8(d). Both hysteresis and temperature dependence can be attributed to variations in elastic and electrical losses in the system, under different applied voltages.

Next, the load power response of both the TMCT and NMCT were measured, and these are

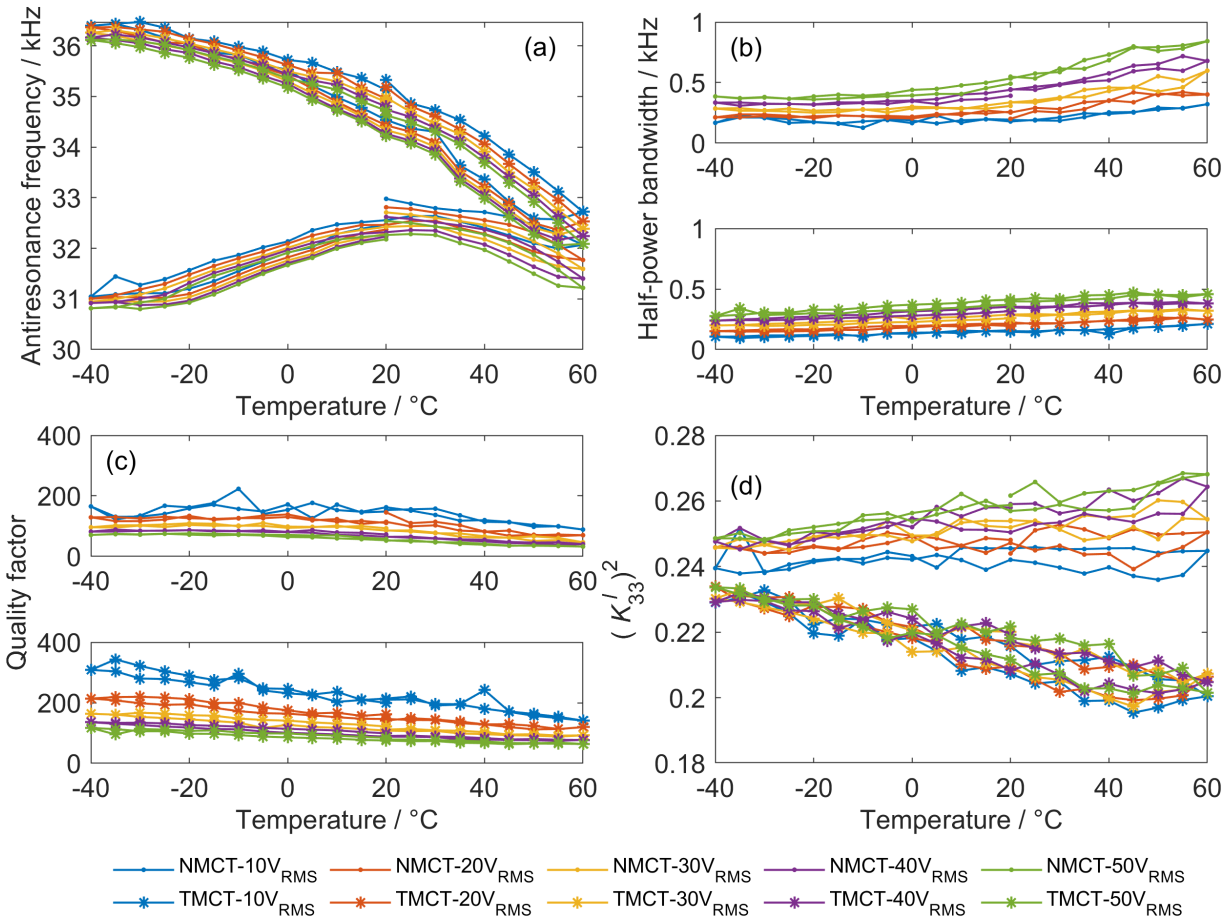

Figure 5.12: (a) Antiresonant frequency, (b) half-power bandwidth, (c) quality factor, and (d) electromechanical coupling factor results for the NMCT and TMCT under the static temperature-voltage condition for the first longitudinal mode within a -40°C to 60°C temperature window, and applied voltages of 10 V_{RMS} to 50 V_{RMS}.

shown in Figure 5.13. On the right side of the power cut-off line, the load power of the NMCT is shown to significantly reduce with temperature. However, on the left side of the line, the power remains constant at different voltages and is reversible. This is a notably different behaviour compared to the TMCT load power results, which all exhibit a general decrease as temperature rises, as shown in Figure 5.13(b). This verifies that the NMCT's electrical properties also exhibit a degree of stability. As voltage increases, the range of steady power gradually narrows, and the temperature window for stability is reduced. When the device is operated on the left-hand side of the cut-off line, the approximately constant load power and electromechanical coupling coefficient (Figure 5.12(d)) means power tracking is not required. This electrical stability can be potentially applied to cold working conditions, such as ultrasonic de-icing.

The vibration amplitude responses of the NMCT as functions of temperature were then measured for different applied voltages, and these results are shown in Figure 5.14. There were practical limitations on the environments in which the LDV could be operated, and so this harmonic analysis process was only performed at room temperature. As described in Section 5.1.1,

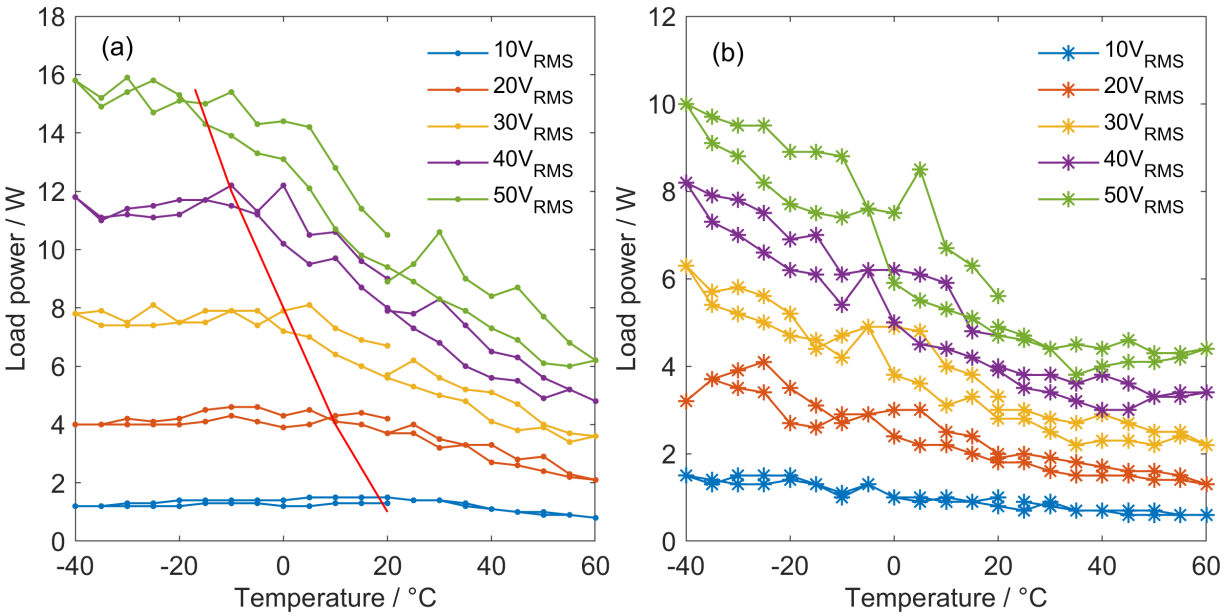

Figure 5.13: Load power results of (a) the NMCT and (b) the TMCT under the static temperature-voltage condition for the first longitudinal mode within a -40°C to 60°C temperature window, and applied voltages of 10 V_{RMS} to 50 V_{RMS}, where the red trend-line indicate stable load powers on its left.

the NMCT incorporates Nitinol existing in one of two states at room temperature. This is due to the hysteresis in the material, with differences depending on a heating or cooling cycle being applied. Measurements were made with Nitinol in each microstructure, with voltage increased from 10 V_{RMS} to 50 V_{RMS} in 10 V_{RMS} steps, then decreased back to 10 V_{RMS}.

In general, there is a high level of consistency and similarity between the data from both cycles, with nonlinear softening in resonance behaviours consistent with that reported in other research of Langevin transducer dynamics [29, 230], in addition to the nonlinear jump phenomenon [215]. As the applied voltage rises, the maximum displacement amplitude is higher for the NMCT after the cooling cycle (at almost identical resonant frequencies). Slight differences in impedance contribute to differences in amplitude, but also the microstructure of the Nitinol introduces mechanical damping to the system. In addition, the red dashed line in Figure 5.14 indicates the hysteresis of the rising and falling voltage, which is consistent with the polarisation versus electrical (P-E) hysteresis loop of PZT material due to internal field bias [231]. The NMCT in the heating cycle exhibits a more prominent hysteresis at higher voltages, which suggests that the NMCT in this condition has lower polarisation dissipation energy and less remnant polarisation. Hysteresis appears to be related to the microstructure of Nitinol, however, further investigation is necessary to confirm this.

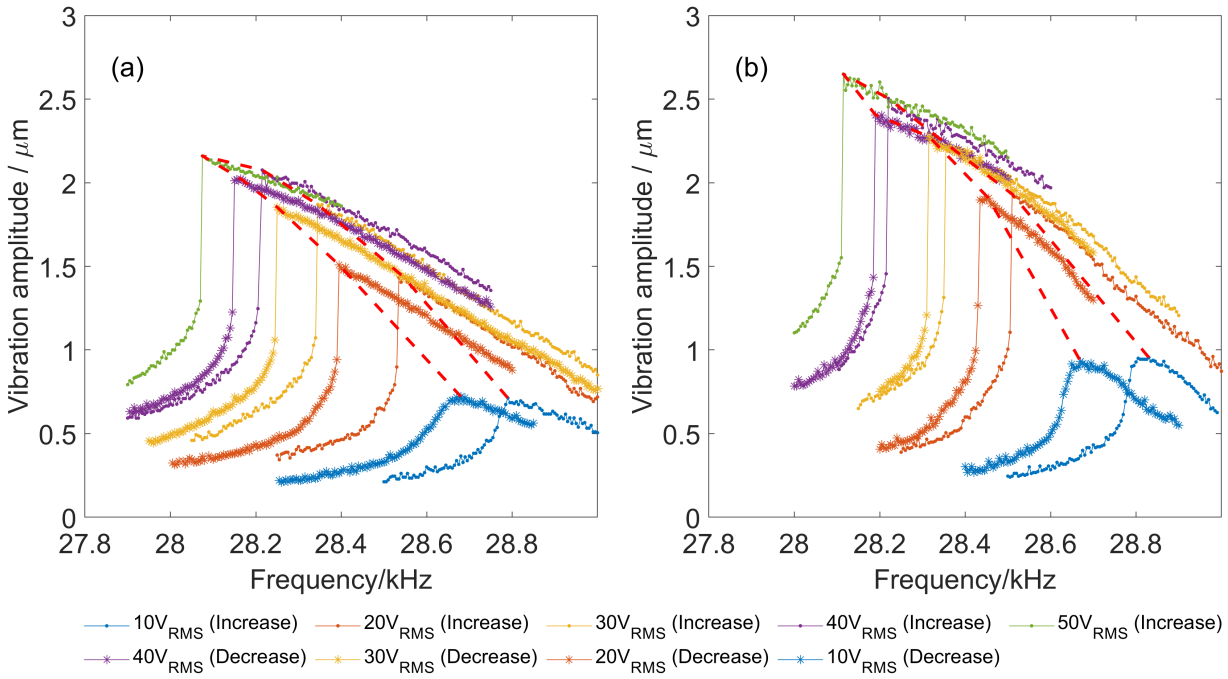

Figure 5.14: Vibration amplitude spectra of the NMCT from 10 V_{RMS} to 50 V_{RMS} after (a) the heating cycle (a) and (b) the cooling cycle.

5.3 Influence of Self-Heating on Dynamics

The experimental results detailed so far were obtained using static temperature conditions. However, in practical applications, the thermal conditions generated by dielectric loss in the PZT can induce an unevenly distributed temperature field, or self-heating, in the transducer. Therefore, quantifying and accounting for self-heating is important for studying the resonance stability of the NMCT. The self-heating was only explored for the NMCT in the cooling cycle, given its higher amplitude and lower hysteresis than that of the heating cycle, as shown in Figure 5.14. Here, the transducers are operated continuously until either the PZT stack temperature reaches 60°C or the elapsed measurement time is 300 s. The measurements for both transducers are shown in Figure 5.15, which are recorded using a thermal imager. It should be noted that during the experiment, only the temperature changes of the two PZT stacks and the middle mass are included, given the negligible changes in temperature of the end-masses. It is also clear that the PZT stacks generally reach higher temperatures than the middle mass.

The frequency as a function of time for the transducers are shown in Figure 5.16(a), it appears that the resonant frequency of NMCT can be stabilised within relatively short time spans when the voltage is lower than 50 V_{RMS}. The frequency difference at times from 4 s to 104 s at 20 V_{RMS} is only 10 Hz, which is indicative of a significant resonance stability performance. However, the resonant frequency of the TMCT as shown in Figure 5.16(b) decreases as the time increases, regardless of the voltage excitation level. Interestingly, the impedance of NMCT and TMCT exhibit almost the same behaviour, as shown in Figure 5.16(c) and (d). This may be

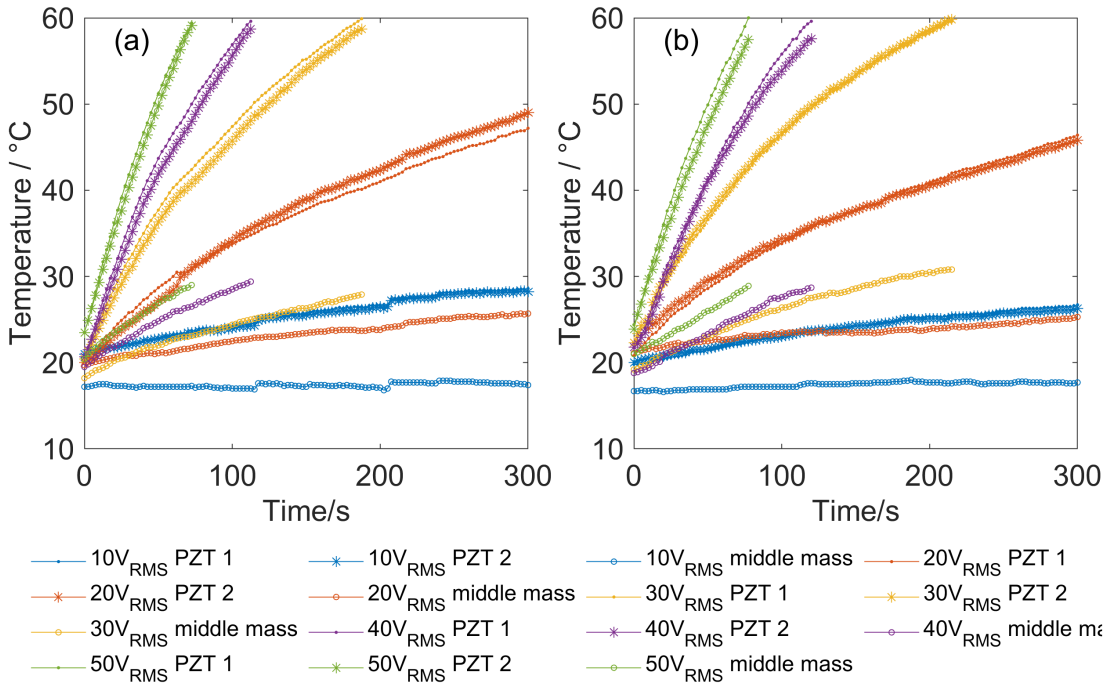

Figure 5.15: Temperature as a function of time of the two PZT stacks and the middle mass for (a) the NMCT and (b) the TMCT under self-heating conditions, and applied voltages of 10 V_{RMS} to 50 V_{RMS}.

because the temperature of the Nitinol is much lower than that of PZT stacks, which means that Nitinol cannot significantly influence the transducer's electrical properties . Moreover, both the NMCT and TMCT exhibit similar current RMS and load power responses as shown in Figure 5.16(e), (f), (g), and (h), suggesting that Nitinol does not have notable influence on the dynamics from self-heating.

A thermal imager was used to monitor the surface temperature distribution of the transducers. Because they comprised different materials, the camera's emissivity setting was adjusted for each material according to the literature [15, 232] and the instruction manual, as listed in Table 5.4. It should be noted that the transducers were not painted black to avoid adding mass that could influence their dynamic response.

Table 5.4: Emissivity of the materials used in this thesis.

Materials	Emissivity
Aluminium	0.2
Titanium	0.6
Steel	0.8
Nitinol	0.64 [15]
PZT	0.95 [232]

As shown in Figure 5.17(a) to (h), the temperatures of the PZT stacks and the middle mass of the NMCT have been monitored, where the PZT stacks are consistently observed to be the hottest. Although the temperature of the Nitinol middle mass does increase, it is significantly

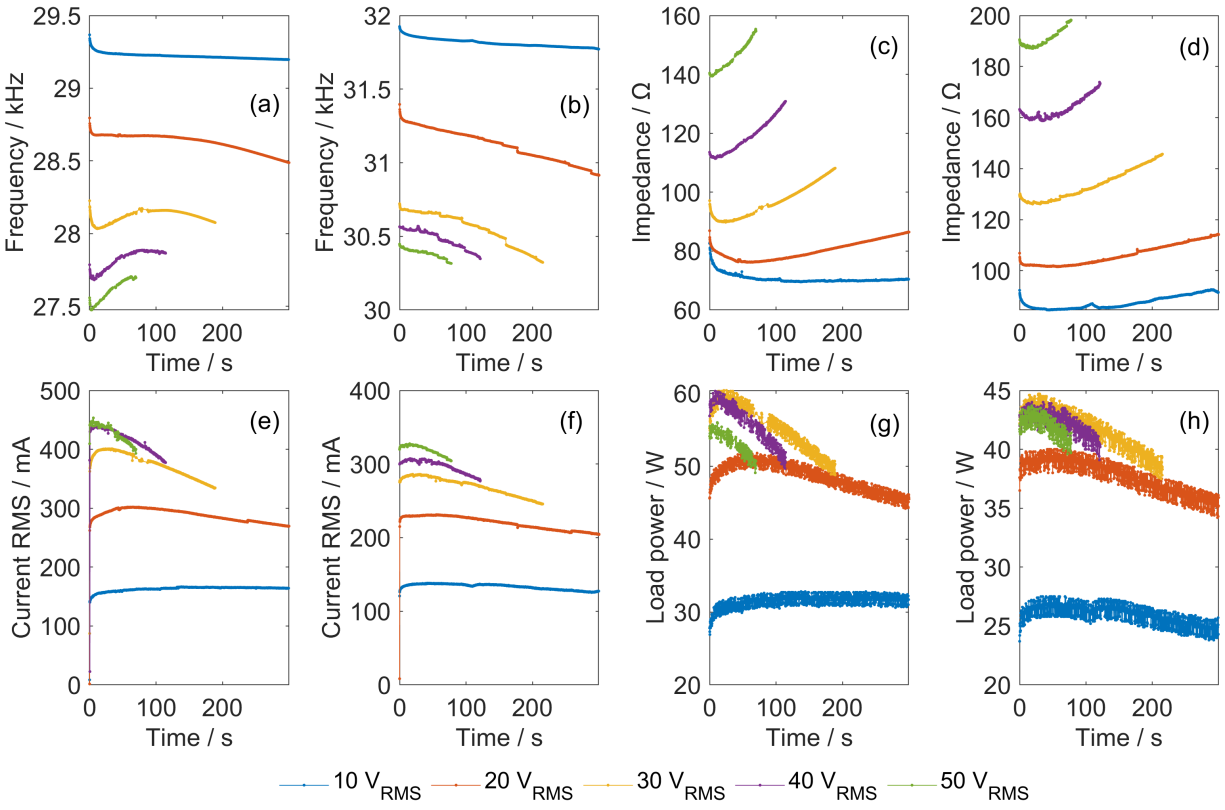

Figure 5.16: resonant frequency (a) and (b), impedance (c) and (d), current RMS (e) and (f), and load results (g) and (h) of the NMCT and TMCT under self-heating conditions, and applied voltages of 10 V_{RMS} to 50 V_{RMS}.

lower than that of the PZT stacks. To investigate further, the temperature of the PZT was used as a reference, where temperature was adjusted in intervals of 5°C as the NMCT was driven in a continuous mode from 10 V_{RMS} to 50 V_{RMS} before decreasing back to 10 V_{RMS}, in steps of 10 V_{RMS}. In Figure 5.18(i), vibration amplitude results are displayed with respect to resonant frequency, PZT temperature, and excitation voltage, which is indicated by the coloured areas. As the voltage increases, the vibration amplitudes between 25°C and 45°C remain generally stable, whereas the difference between the NMCT at 45°C and 50°C becomes more pronounced. This means that despite the non-uniform temperature distribution in the NMCT, resonance stability still exists in its vibration amplitude, and the applicable temperature range is larger compared to Figure 5.10(b). There appear to be optimal conditions to drive the NMCT, dependent on the transducer assembly. It is worth noting that under self-heating conditions, the vibration amplitude associated with a particular excitation voltage remains at a similar same level between 25°C and 45°C. Overall, this phenomenon reveals the potential of the NMCT being applied to power ultrasonic applications utilising continuous mode excitation at higher voltage levels, ensuring a stabilised output vibration amplitude within the 20°C to 45°C temperature range.

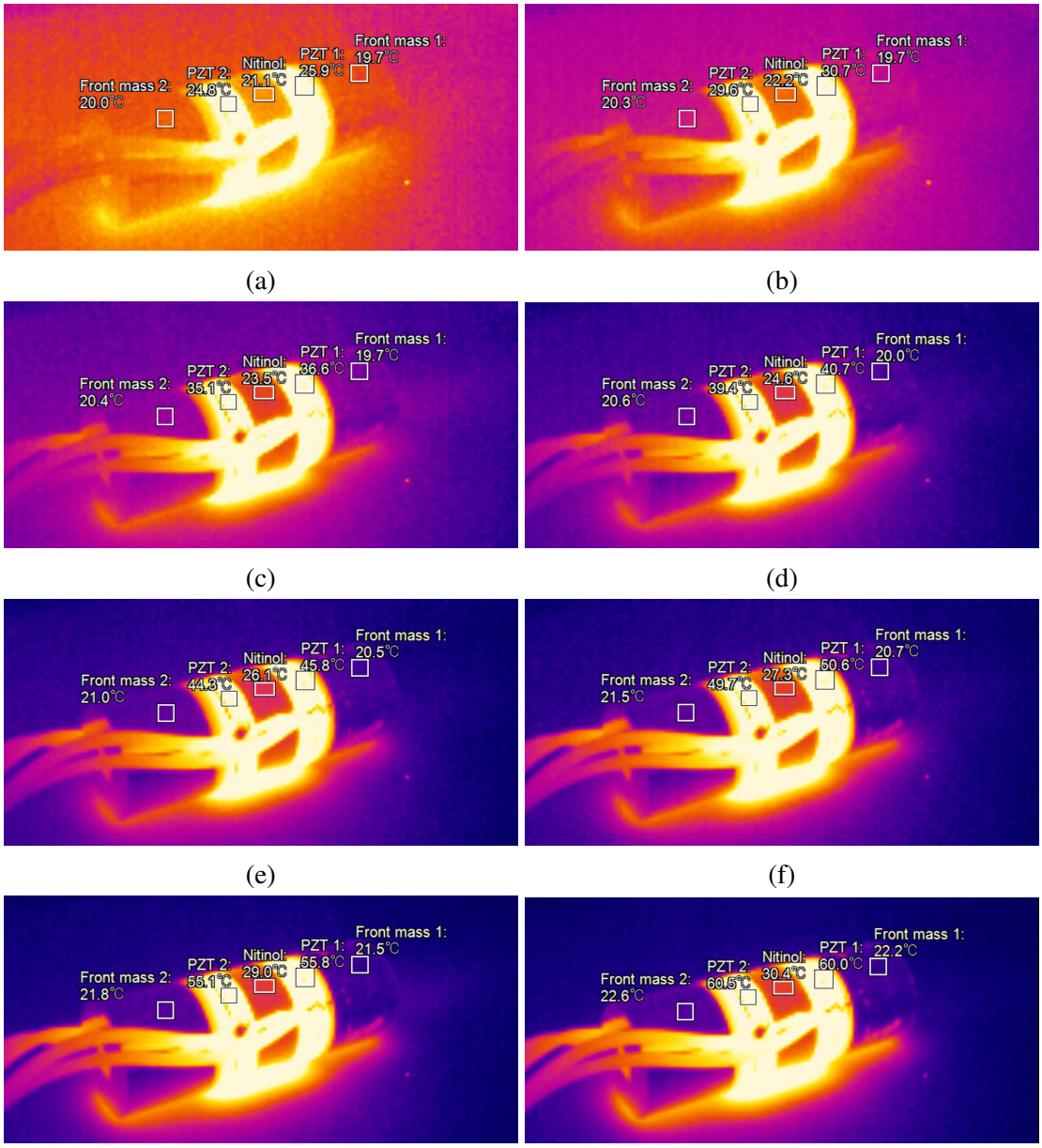

Figure 5.17: Thermal imaging maps showing self-heating in the NMCT, including PZT stack temperatures of (a) 25°C, (b) 30°C, (c) 35°C, (d) 40°C, (e) 45°C, (f) 50°C, (g) 55°C, and (h) 60°C

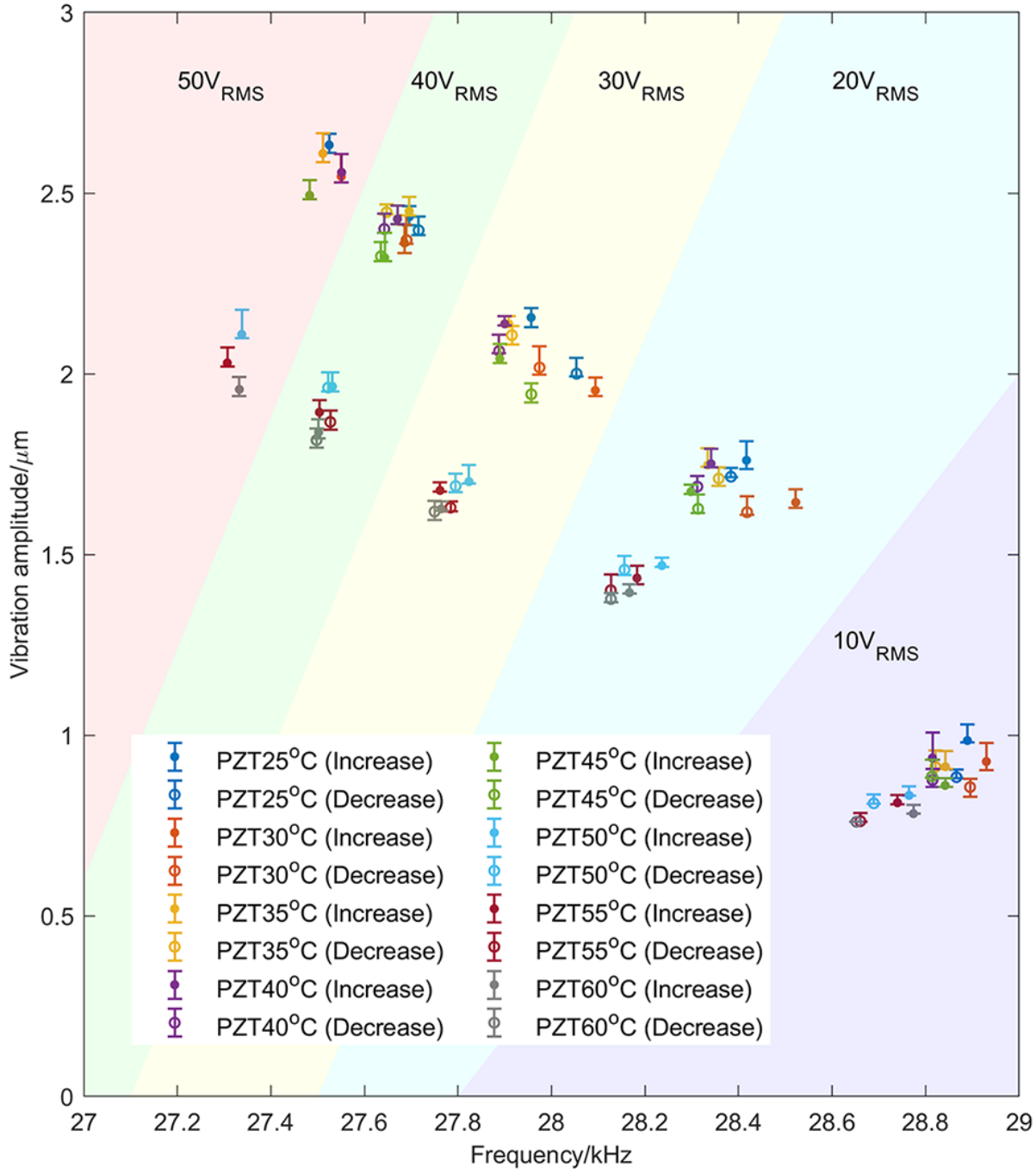

Figure 5.18: Vibration amplitudes with respect to resonant frequency, PZT stack temperature from 25°C to 60°C, and excitation voltage (coloured areas) from 10 V_{RMS} to 50 V_{RMS}.

5.4 Dynamic Stability under Power and Current Tracking

The dynamic stability of the NMCT has thus far been demonstrated for two cases, one at elevated temperatures from -40°C towards 60°C, and for a constant voltage excitation condition at ambient room temperature. In practical applications across medicine and industry, it is common to use power or current tracking to ensure stable operation of a Langevin transducer. This section focuses on the use of power tracking and the dynamic stability of the NMCT, where all experiments are conducted at ambient room temperature and for the NMCT alone. The transducer is positioned on polyurethane foam to realise as close to a free-free boundary condition as possible. The PiezoDrive system is used to perform both power and current tracking for continuous operation across 300 s. Under different excitation levels, parameters comprising monitored power, current, resonant frequency, and electrical impedance magnitude are measured in order to evaluate dynamic stability. Phase tracking is also applied to ensure that the transducer nominally vibrates at resonance throughout each test. Thermal imaging is used to collect temperature profiles, but it should be noted that the temperature increases of the aluminium end masses (1 and 2) are negligible, since their temperatures consistently remain close to ambient room temperature. As shown by the heat map shown in Figure 5.17 (h), even as the temperatures of the end-masses approach 60°C, the temperatures of the aluminium end-masses remain close to ambient room temperature. Therefore, the temperature data presented in this section relate to those of the PZT stacks and the Nitinol middle mass. As further confirmation and evidence of dynamic stability, the vibration amplitude of the first longitudinal mode of vibration is continuously monitored using a 1D LDV.

5.4.1 Power Tracking

To ensure that the transducer power reached the required set magnitudes within the designated time window, the power control gain was set to 20 % of the set load power. The temperature of the PZT stacks increased significantly over time, as shown in Figure 5.19(a), whereas the temperature of the Nitinol middle mass only displayed moderate increases by comparison. Due to marginal differences in the electrical properties of the two PZT stacks, there exists a temperature difference between them. Different excitation powers, as seen in Figure 5.19(b), lead to different temperature gradients. Despite the power tracking method stabilising the load power, it is not entirely stable at 10 W. This is most likely due to the dynamic properties of the transducer changing more rapidly at higher load powers. Thus, there is a delay in the tracking output result associated with the actual power magnitude, resulting in jumps and fluctuations for all collected results. In Figure 5.19(c), the current is stable when the power reaches set magnitudes of 2 W and 4 W. However, current linearly reduces as time increases when the load powers are 6 W, 8 W, and 10 W. This is likely because the impedance at these load powers increases with time, as seen in Figure 5.19(e), attributed to the increased temperatures of the PZT stacks.

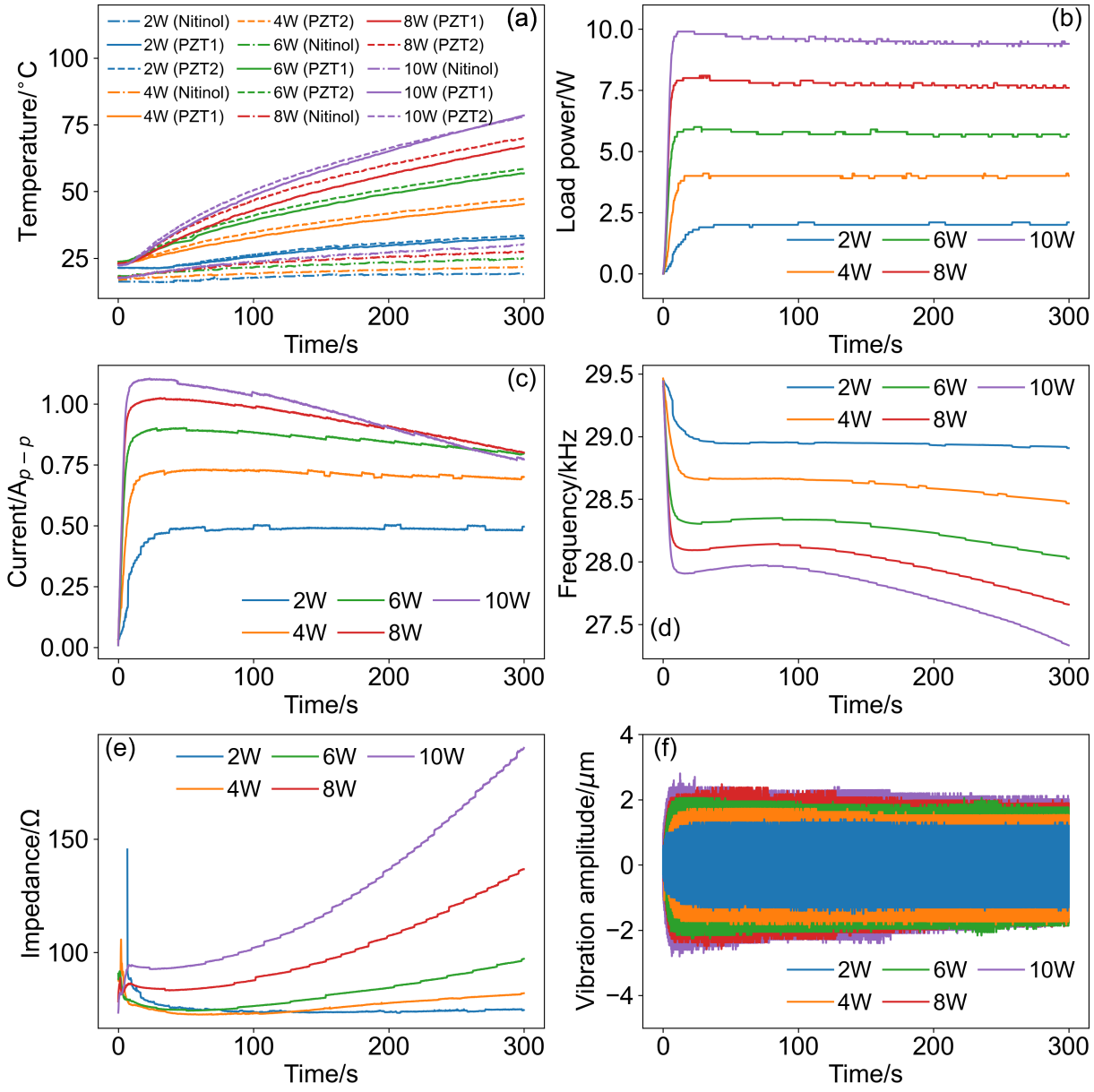

Figure 5.19: Dynamic characteristics in the first longitudinal mode of vibration for the transducer with the power tracking method, for a 300 s continuous operation and set load power magnitudes of 2 W, 4 W, 6 W, 8 W, and 10 W, showing (a) temperatures of the two PZT stacks and the Nitinol mass monitored by the thermal imager, and (b) load powers, (c) currents, (d) frequencies, and (e) electrical impedances, all collected using the PiezoDrive system, and (f) vibration amplitudes measured using the 1D LDV.

In Figure 5.19(d), the transducer's frequency exhibits dynamic stability when the load power is less than 6 W. Here, frequency stability is defined as the resonant frequency difference within a given time, equal to or less than 5 Hz. When the load power is 2 W, the frequency is stable from 38.217 s to 172.825 s, whilst there is stability from 22.047 s to 103.735 s when the load power is 4 W. This can be attributed to likely moduli increases of Nitinol, compensating for elastic moduli and polarisation changes in the PZT stacks with temperature. However, any

moduli increase of Nitinol in the austenite phase would be limited, resulting in a natural limit for dynamic stability, should the experiment time be sufficiently long or for the temperature to rise high enough. This phenomenon is different compared to traditional PZ26 or hard PZT based Langevin transducers, whose resonant frequency of the first longitudinal mode typically decreases as their PZT stack temperatures rise, and consequently where no dynamic stability can be observed [216]. When the load powers reach 6 W, 8 W, and 10 W, the resonant frequency initially increases before subsequently reducing. The likely reason is that the increases in Nitinol moduli overcompensate for the elastic moduli and polarisation changes associated with the PZT stacks. In general, the operational stability in this experiment is not only shown in terms of resonant frequency, but also electrical impedance. The impedance has a 2 Ω difference at 2 W load power, and a 1.9 Ω difference at 4 W load power, both within respective time windows of stable frequency. This indicates that the electrical properties of the transducer in either case are also stable. In Figure 5.19(f), the vibration amplitude also exhibits stability for powers of 2 W and 4 W. The overall amplitude results exhibit similar changing patterns to the current, shown via Figure 5.19(c), and are inverse to the electrical impedance, as indicated by Figure 5.19(e). These results strongly suggest that this transducer has significant potential to be used in applications requiring stable load power and vibration amplitude output, such as ultrasonic motors.

5.4.2 Current Tracking

The final part of this study presents the dynamic stability from the perspective of current tracking. Here, the current control gain is set at 20 % of the set magnitudes, where the test for 1 $A_{P\text{-}P}$ is stopped at around 150 s, where the excitation voltage reaches the maximum limit of 200 $V_{P\text{-}P}$ that the transformer can deliver. Consequently, the phase tracking becomes unstable, such that the phase cannot be locked as low as zero. As depicted in Figure 5.20(a), the temperatures of the PZT stacks and the Nitinol middle mass increase almost linearly, where the gradients highly depend on the applied current level. The load power can be stabilised with different set current magnitudes when the current is lower than 1 $A_{P\text{-}P}$. As shown in Figure 5.20(c), the current can be locked at magnitudes lower than 1 $A_{P\text{-}P}$. However, when the set current value is 1 $A_{P\text{-}P}$, it decreases with time and exhibits unstable fluctuations due to the practical limits associated with the phase tracking. The output power level increases nonlinearly as current rises beyond 0.8 $A_{P\text{-}P}$, as shown in Figure 5.20(b), where there is a transition to a level of instability for the transducer, from a trackable state around 0.8 $A_{P\text{-}P}$ to that which cannot be readily tracked at 1 $A_{P\text{-}P}$. Additionally, minor fluctuations at lower currents are attributed to the time delay, as previously discussed.

resonant frequency is observed to decrease over time with a 39.1 Hz difference from 27.72 s to 299.866 s, as shown by Figure 5.20(d), when the applied current is 0.2 $A_{P\text{-}P}$, consistent with traditional transducers. One possible reason is that only modest temperature increases of Nitinol in its set form do not fully compensate for the elastic modulus changes attributable to the PZT

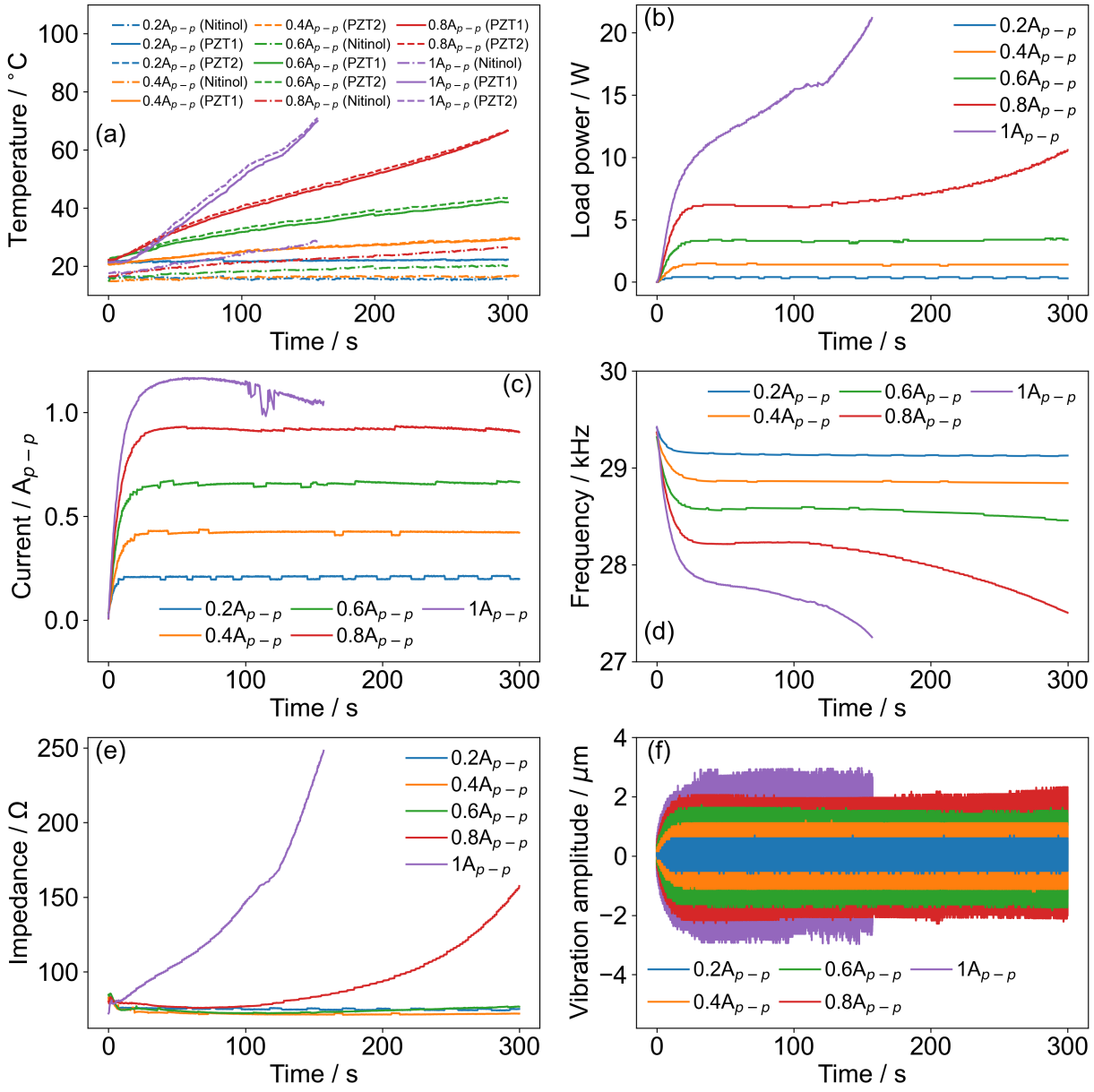

Figure 5.20: Dynamic characteristics in the first longitudinal mode of vibration for the transducer with the current tracking method, for a 300 s continuous operation and set current values of 0.2 $A_{P\text{-}P}$, 0.4 $A_{P\text{-}P}$, 0.6 $A_{P\text{-}P}$, 0.8 $A_{P\text{-}P}$, and 1 $A_{P\text{-}P}$, showing (a) temperatures of the two PZT stacks and the Nitinol mass monitored by the thermal imager, and (b) load powers, (c) currents, (d) frequencies, and (e) electrical impedances, all collected using the PiezoDrive system, and (f) vibration amplitudes measured using the 1D LDV.

stacks. Frequency stability is observed for current magnitudes of 0.4 $A_{P\text{-}P}$, 0.6 $A_{P\text{-}P}$, and 0.8 $A_{P\text{-}P}$, and their respective stabilised time windows are from 33.176 s to 212.298 s, from 47.46 s to 161.483 s, and from 57.325 s to 111.293 s. However, frequency decreases with time when the current is set to 1 $A_{P\text{-}P}$, due to the rapid temperature increases of the PZT stacks, restricting the ability of the Nitinol middle mass to compensate for the effects of elastic modulus changes. Electrical impedance remains stable when the set current magnitudes are lower than 1 $A_{P\text{-}P}$,

as shown in Figure 5.20(e), while it increases with time at 1 $A_{P\text{-}P}$. Although the impedance increases rapidly at 0.8 $A_{P\text{-}P}$ after the stability period, showing an unstable state, it is stabilised within the frequency stability window. Therefore, the transducer can be operated for a short period at 0.8 $A_{P\text{-}P}$, while it is not recommended at 1 $A_{P\text{-}P}$. It should be noted that the transducer exhibits electrical impedance stability at 0.2 $A_{P\text{-}P}$, with an impedance difference of 1.7 Ω from 7.981 s to 299.866 s. This is because modest heat generation does not appear to significantly affect the electrical properties of the transducer. The electrical impedance differences within the stability time windows of 0.4 $A_{P\text{-}P}$, 0.6 $A_{P\text{-}P}$, and 0.8 $A_{P\text{-}P}$ are 0.5 Ω, 1.1 Ω, and 1.5 Ω, respectively. The vibration amplitudes are stable within the defined time windows when the current is lower than 1 $A_{P\text{-}P}$, but unlike the power tracking results, the amplitudes rise almost linearly as the current increases.

Higher set magnitudes of load power and current result in rapid temperature increases of both the PZT stacks and the Nitinol middle mass, which subsequently lead to rapid changes in the dynamic properties of the transducer, as evident from the results in Figure 5.19 and Figure 5.20. It is noteworthy that the dynamic stability of the transducer based on frequency, electrical impedance, and vibration amplitude are significantly dependent on temperature gradient, either by power or current tracking. These gradients indicate the rate at which the temperature changes over time. The results show that it is likely when the changes of Nitinol moduli compensate for the elastic moduli and polarisation changes of PZT, dynamic stability can be achieved, and the power and current tracking approaches are effective. Discrepancies and an inability to compensate can be observed in the frequency results at 10 W load power and 0.2 $A_{P\text{-}P}$ current, respectively. Therefore, there is some potential to address this through dimensional modifications of the PZT stacks and Nitinol middle mass, to achieve dynamic stability for a wide range of operational test conditions, transducer configurations, and excitation levels.

The stability in resonance demonstrated in this chapter, either under isothermal or self-heating conditions, is a variant of resonance tuneability in the format of the influence of Nitinol on dynamics approximately compensates for that of the PZT. This proves that the Nitinol tunes the resonant frequencies more effectively than the PZT in the tuneable Langevin transducer in Chapter 4. The results presented in this chapter, as well as in Chapter 4, indicate that the tuneability and stability of the longitudinal modes are influenced by variations in transducer configurations and the volume of Nitinol. A detailed analysis of this will be provided in the next chapter based on FEA simulations. When comparing the NMCT prototype to the tuneable Langevin transducer, it is evident that different material phase transformation temperatures lead to varying functional temperatures. This demonstrates that the tuneability temperature depends on the phase transformation behaviours of Nitinol. Also, the differences in modulus between the martensitic and austenitic phases significantly impact tuneability from a solid mechanics perspective. This could be further validated by testing materials with different compositions but similar transformation temperatures, all being incorporated into the same configuration, which

will be explored in future work.

5.5 Summary

In this study, dynamic stability of a NMCT was investigated using four methods. The first two showed the dynamic stability of the transducer for elevated levels of temperature towards 60 °C, and the second employed a constant voltage method to drive the transducer at ambient room temperature. In both methods, a TMCT was used as a comparator, where it was shown that the dynamic stability can be strongly linked to the presence of Nitinol in the cascaded transducer. Based on the structural acoustic impedance, NMCT and TMCT were designed and manufactured. The dynamic results indicate that resonance stability is achieved within typical temperature ranges for resonant frequency, antiresonant frequency, and electromechanical coupling coefficient. Additionally, electric losses were introduced by testing both NMCT and TMCT under the same temperature conditions with voltage excitations ranging from 10 V_{RMS} to 50 V_{RMS}. It was observed that electric losses reduced resonance stability. Notably, as voltage increases, the range of temperature and frequency over which stability occurs also increases. In comparison to TMCT, NMCT's impedance and half-power bandwidth demonstrated greater sensitivity to voltage changes. Importantly, the presence of a power cut-off line in NMCT indicates that load power does not depend on temperature at lower temperatures. Furthermore, the self-heating experiment demonstrated that NMCT maintains resonance stability for both resonant frequency and vibration amplitude, even in the presence of unevenly distributed temperature fields.

The third and fourth methods, constituting power and current tracking, were then performed on the NMCT alone, demonstrating dynamic stability associated with frequency, electrical impedance, and vibration amplitude. It has been demonstrated that the time window for dynamic stability is significantly dependent on power and current, mainly attributable to the associated rates of heat generation. In general, the results indicate that dynamic stability of the NMCT can be achieved at ambient room temperature for both power and current tracking methods, for continuous operation across 300 s. It is evident that dynamic stability is highly dependent on power and current levels, but importantly there is strong practical application potential for a NMCT, with regards to exhibiting stable output performance. Future research will focus on investigating the performance and practical implementation of the Nitinol transducer for power ultrasonic applications, including in ultrasonic scalpel devices and for acoustic levitation. A major area of investigation for these applications will be the practical demonstration of resonance stability across different physical and environmental phenomena, such as fluctuating operating temperatures and elevated vibration amplitudes.

Chapter 6

Discussions

6.1 Lessons from Chapter 3, 4, and 5

Up to this point, previous chapters have explored the potential of implementing Nitinol into Langevin transducers. This analytical section integrates knowledge gained from Chapters 3, 4, and 5, drawing on both mathematical and experimental experiences. It not only improves the accuracy of predicting the transducer dynamics, but also provides insights that guide the fabrication and characterisation processes for future designs. As a result, this analysis is essential to correlate prototype development with practical applications.

6.1.1 Mathematical Modelling

In Chapter 3, 1D and 3D electromechanical models are developed, via the linear piezoelectricity theory. Both models demonstrate consistency to the experimental results. However, the 1D model has a lower accuracy than the 3D model when the L/D ratio is higher than 12.5. This limits that the 1D model is only applicable with the long-beam shaped Langevin configuration. This limitation means transducers designed in Chapters 4 and 5 have small L/D ratios, only the 3D model was considered and applied throughout these chapters. As the influences of temperature fields were not considered in the 3D model, it is only capable in solving transducer dynamics at room temperature. However, the design and operation of the Nitinol Langevin transducer are highly influenced by transducer temperature. Therefore, the development of a thermo-electro-mechanical model is essential. In terms of two operational situations, isothermal and self-heating, the model is required to be designed specifically. For isothermal condition, the temperature is a constant across the entire transducer, meaning the heat transfer is not involved, whereas the self-heating is based on the heat transfer mechanism.

Taking the isothermal condition as an example, the mechanical and thermal fields under discussion are not completely coupled. According to linear thermoelasticity in the weak coupling form, the constitutive equation of isotropic materials, including traditional metals and Nitinol,

is given as [233]:

$$\sigma = 2\mu\varepsilon + \lambda \mathbf{tr}(\varepsilon)\mathbf{1} - (3\lambda + 2\mu)\alpha(\vartheta - \vartheta_0)\mathbf{1} \tag{6.1}$$

where α is the thermal expansion coefficient, and ϑ and ϑ_0 are observed temperature and reference temperature respectively. Accordingly, the strain energy density function ψ for isotropic materials is introduced, considering $\sigma = \frac{\partial \psi}{\partial \varepsilon}$, as given:

$$\psi = \mu|\varepsilon|^2 + \frac{\lambda}{2}(\mathbf{tr}(\varepsilon))^2 - (3\lambda + 2\mu)\alpha(\vartheta - \vartheta_0)\mathbf{tr}(\varepsilon) \tag{6.2}$$

Weak coupling constitutive equations of piezoelectric material are given as follows based on linear thermoelasticity, linear piezoelectricity, and pyroelectricity [234, 235]. It should be pointed out that the mechanical and thermal fields exhibit a weak coupling, whereas the mechanical and electrical fields are fully coupled. Therefore, the constitutive equations for piezoelectric materials are given as:

$$\begin{aligned} \sigma &= \mathbb{C} : \varepsilon + \mathbf{e}^T \nabla\phi + \Lambda(\vartheta - \vartheta_0) \\ \mathbf{D} &= \mathbf{e} : \varepsilon - \chi\nabla\phi + \mathbf{p}(\vartheta - \vartheta_0) \end{aligned} \tag{6.3}$$

where Λ is the stress-temperature modulus tensor and $\mathbf{p}$ is the pyroelectricity tensor. The strain energy density function is derived considering $\sigma = \frac{\partial \psi}{\partial \varepsilon}$ and $\mathbf{D} = \frac{\partial \psi}{\partial \nabla\phi}$:

$$\psi = \frac{1}{2}\varepsilon : \mathbb{C} : \varepsilon + \varepsilon : \mathbf{e}\nabla\phi - \frac{1}{2}\chi\nabla\phi\nabla\phi + \varepsilon : \Lambda(\vartheta - \vartheta_0) + \nabla\phi\mathbf{p}(\vartheta - \vartheta_0) \tag{6.4}$$

The finite element process outlined in Chapter 3 allows for determining the dynamics of the Nitinol Langevin transducer under isothermal conditions according to the above constitutive equations. However, this model requires temperature-dependent material properties. Due to the difficulties in characterising the properties of Nitinol and piezoelectric materials as they strongly relate to temperature, solving the model and comparing it with experimental results present challenges. Consequently, developing the thermo-electro-mechanical model for the Nitinol Langevin transducer is lagged until a complete set of material properties is available, which is not time-wise achievable in this research. The 3D electromechanical model, thus, is favoured here to simulate Nitinol Langevin transducers exclusively at room temperature.

6.1.2 Material Selection and Characterisation

In the Nitinol Langevin transducer, material selection is a significant step that primarily involves choosing Nitinol, piezoelectric, and, optionally, traditional metal materials. Nitinol is prioritised not only for its phase transformation behaviours, which modify its elastic properties, but also for its ability to regulate the response of transducers to varying temperatures. The transformation temperatures, particularly M_F and A_F, serve as key indicators for when the transducer begins or completes the tuning of its dynamics. DSC is utilised to accurately measure these transformation

temperatures. The results illustrate the transformation processes and highlight the appearance of the R-phase, which should be avoided as it impedes the formation of the final phases in the processes.

Investigating the role of Nitinol's elastic properties in Langevin transducer dynamics can be conducted through mechanical testing under cyclic thermal loadings. This is further complicated by the fact that the pre-stress is applied to the Nitinol in the configuration. Material characterisation should be performed under a defined isobaric condition, since pressure shifts the phase transformation temperatures, an established result in the literature [61]. Additionally, the influences of frequency and cyclic pre-stresses are further complicating factors [236, 237]. Therefore, the elastic modulus of Nitinol is estimated iteratively using FEA in this study to describe the transducer dynamics in general terms, consistent with the approach employed in Chapters 4 and 5.

The hard type piezoelectric ceramic is the primary choice as its high mechanical quality factor and low elastic, piezoelectric, and dielectric losses are preferred in high-power applications [238]. While the manufacturer of the piezoelectric ceramic material can provide material properties at room temperature, multiple parameters related to the stiffness tensor at elevated temperatures remain unknown. At elevated temperatures, the stiffness, piezoelectric and permittivity tensors can be obtained by fitting measured impedance spectra across different geometries with optimisation algorithms, such as Levenberg–Marquardt, Nelder–Mead [239]. Even so, constraints in thermal control and high temperature capability make experimental characterisation challenging.

In accordance with the pre-designed configuration, typical metals have been selected. As discussed in Chapter 4, the Nitinol Langevin transducer features end masses made of Nitinol, except the pre-stress bolt, which is the only standard metal used. Conversely, in the cascade transducer presented in Chapter 5, aluminium end masses were utilised to create a gradient of acoustic impedance throughout the structure. This gradient enhances the vibration amplitude at the end sections of the transducer. In practical applications, the end effector is typically connected to the transducer, making the acoustic impedance gradient an essential consideration for achieving optimal performance. Moreover, the elastic modulus, Poisson's ratio, and density of standard metals are key parameters for determining the resonant frequency of transducers, which must be carefully calibrated alongside the phase transformation of Nitinol. Thus, selecting metals is crucial to meeting the desired requirement of resonant frequency. Notably, the transducer dimension is a consideration since it is decided by the choice of metals, particularly when there are dimensional constraints.

6.1.3 Transducer Design and Manufacturing

As mentioned above, the transducer design relies heavily on material selection, which drives the design process. The design of a Nitinol Langevin transducer is generally identical to that

of a traditional Langevin configuration. Applying the designed transducer to practical applications requires an end effector or a sonotrode, which was not included in Chapters 4 and 5. As limited knowledge regarding the material properties in this research, particularly for Nitinol and piezoelectric ceramics at various temperatures, the design can currently be conducted at room temperature. Initial material properties for Nitinol were obtained iteratively from the first investigative design [240]. With the assistance of the 3D electromechanical model proposed in Chapter 3, the designed vibration modal parameters at room temperature, such as resonant frequency and mode shape, are achieved by adjusting the dimensions and alignments of each transducer segment. It has to be noted that the positioning of Nitinol is favoured away from antinodes since the high strain at these points potentially causes phase transformations, for example, from B2 to de-twinned B19', thereby complicating the dynamic response.

Manufacturing is the subsequent step once all dimensions of the segments have been finalised. For standard metals like titanium and aluminium, as utilised in Chapters 4 and 5, traditional machining methods such as turning and drilling are employed to shape the segments into the desired geometries and dimensions. However, due to the work-hardening characteristics of Nitinol, these conventional methods are not suitable. In Chapters 4 and 5, Nitinol segments were manufactured using a sinker EDM, which has proven to be an effective method that ensures dimensional accuracy while minimising failures. However, this manufacturing process is time-consuming, even for relatively simple geometries, like the ring-shaped samples discussed in previous chapters. This limitation affects the design flexibility of Nitinol Langevin transducers. One suggestion from the author is to explore the use of 3D printing techniques in metal when dealing with Nitinol if more complex geometries are involved.

6.1.4 Transducer Characterisation

Chapters 4 and 5 follow the experimental procedures outlined in Chapter 3. EIA was initially employed to identify the local resonant frequencies corresponding to the longitudinal modes. Given that the designed transducers feature beam-shaped geometries, the longitudinal modes manifest as dominant peaks within the impedance spectra, which were used in determining the optimal pre-stress value. Once the transducers were settled, EMA utilised 3D LDV and scanning LDV to measure the vibration mode shapes. Following this, a harmonic system was used to analyse the dynamic responses and nonlinearity of the transducers. At this point, all static characterisations were taken at room temperature. As the temperature variation triggers adaptive and stable resonance of Nitinol Langevin transducers, two approaches were proposed to apply thermal loading: isothermal and self-heating conditions.

6.1.4.1 Isothermal Condition

As conducted in Chapters 4 and 5, the dynamics of Nitinol Langevin transducers were measured under isothermal conditions. An impedance analyser and a PiezoDrive collected electrical impedance spectra at static temperatures for longitudinal modes at low and high excitations, respectively. The experimental oven and climate chamber ensured an even distribution of temperature fields across the transducer. Analysis of the stepwise results revealed that Nitinol transducers can adjust their resonance, particularly frequency and impedance, in response to changes in ambient temperature. The purpose of maintaining isothermal conditions was to investigate how the Nitinol transducer reacts to a stable temperature environment while minimising the impact of heat transfer on transducer dynamics. However, all data collected above focused on the electrical responses of the transducers. To examine the mechanical responses, a harmonic system was integrated into the experimental chamber, as described in Chapter 4. The mechanical responses of the Nitinol transducer aligned closely with the electrical responses, displaying similar patterns of resonance shifts and nonlinear phenomena concerning temperatures and voltages. Thus, the isothermal methods discussed here are recommended for the characterisation of future prototypes of Nitinol Langevin transducer, when the ambient temperature is the thermal load.

6.1.4.2 Self-heating Condition

In contrast to isothermal conditions, self-heating conditions are defined by the internal heat source, which is the increasing dielectric heating of piezoelectric units during operation. Since the properties of piezoelectric materials are temperature-dependent, the dynamics of the transducer consequently change over time. Through a typical transducer configuration, such as the cascaded structure discussed in Chapter 5, the heat generated by the piezoelectric units can be passively transferred and accumulated in the Nitinol segment. This mechanism allows for the application of thermal loading to the transducer, which in turn triggers variations in the modulus of Nitinol. In this scenario, the temperature of the Nitinol remains comparatively lower than that of the piezoelectric components. Therefore, the configuration must be designed to ensure that variations in the modulus of Nitinol due to modest temperature changes can contribute to transducer dynamics. This requires positioning the Nitinol in places of the structure that are most sensitive to such modulus changes. Subsequently, the transducer's electrical parameters can be monitored over time through continuous operation using PiezoDrive. Mechanical parameters, including vibration amplitude and velocity, can be measured using a 1D LDV in the time domain.

6.2 How to Drive in Adaptive Resonance or Stable Resonance Conditions?

In the context of the resonance behaviours exhibited by Nitinol Langevin transducers, as examined in the previous chapters, one may question the underlying factors that result in adaptive and stable resonance. From the perspective of resonant frequency, it is established that in Langevin transducers without Nitinol, the longitudinal frequencies exhibit a decrease with rising temperatures, as demonstrated in Chapter 5. Consequently, the observed increase in frequency (adaptive resonance) and the plateau of frequency (stable resonance) within the Nitinol transducer can be attributed to changes in the material properties of Nitinol at elevated temperatures, particularly concerning elastic moduli, as informed by elasticity in mechanics. The stable resonance in the self-heating transducer aligns with this explanation, while no martensitic transformation is involved. This section discusses the changes in Nitinol moduli due to phase transformations, which laterally prove that temperature-dependent moduli of a single austenitic phase also achieve resonance tuneability.

6.2.1 Position- and Volume-Dependent Tuneability

The interaction between the piezoelectric material and Nitinol indicates that the greater the contribution of Nitinol to the dynamics of the transducer relative to the piezoelectric units, the more pronounced the adaptive resonance, and vice versa. Two principal structural factors influence resonance behaviour: the axial distance of the Nitinol segment from the nodal position and the volume ratio of Nitinol to the entire configuration. Given the complexities associated with the temperature-dependent properties of piezoelectric ceramics, the impact of Nitinol on resonance characteristics will be discussed solely in a decoupled manner, through the use of FEA. Taking the L1 mode as a representative case, the transducer model is simplified to a bar geometry with a circular cross-section, as depicted in Figure 6.1.

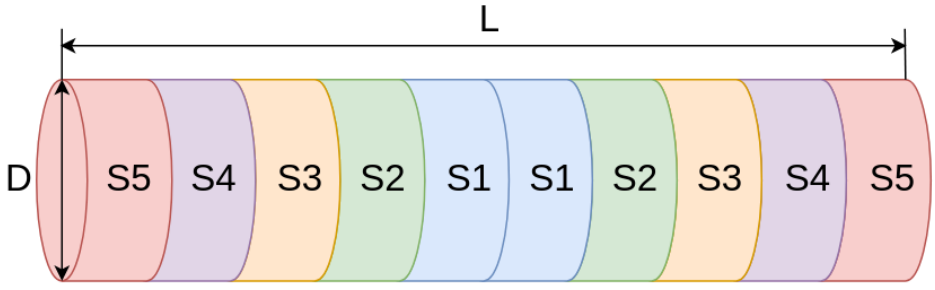

Figure 6.1: Simplified transducer with a bar-shaped geometry featuring five segment pairs.

As illustrated in Figure 6.1, the entire transducer, with a diameter D and a length L, has been segmented into five pairs, each highlighted in various colours. Each segment corresponds to a specific distance from the nodal position and consists of two symmetrical areas to the central

section on the axis. By incorporating Nitinol material into alternating segments, eigenfrequencies can be analysed to determine which areas exhibit the highest sensitivity to variations in elastic moduli. The model is designed with a 25 mm diameter, aligned with all Nitinol transducers proposed in this thesis, and a 100 mm length. Titanium has been selected as the material for the remaining segments. The modulus of Nitinol is defined as 40 GPa for martensite and 75 GPa for austenite, falling in the ranges mentioned in Chapter 3.

In Table 6.1, the frequency variations resulting from the martensite to austenite transformation of Nitinol are presented in percentage format, with the introduction of Nitinol effectively tuning the resonant frequency. Notably, frequency variation is maximised when Nitinol is positioned at S1, and the closer the distance of Nitinol to the nodal position is, the more tuneability the transducer will have. This finding emphasises that the resonant frequency of the L1 mode is particularly sensitive to modulus changes at its nodal position.

Table 6.1: Position of Nitinol versus the resonant frequency in the L1 mode of a bar-shaped model, where L=100 mm and D=25 mm.

Nitinol position	Frequency (kHz) (martensite)	Frequency (kHz) (austenite)	Frequency variation (%)
S1	18.908	22.802	20.594
S2	19.774	22.928	15.950
S3	20.759	23.046	11.017
S4	21.956	23.167	5.516
S5	22.950	23.250	1.307

To further explore the influence of Nitinol volume on transducer tuneability, the integration of Nitinol across multiple segments within the model is investigated. The results presented in Table 6.2 indicate that an increased volume of Nitinol within the model correlates with enhanced tuneability, achieving maximum effect when the entire model is composed of Nitinol. However, it is notable that the relationship is not linear. A convergence in tuneability occurs when Nitinol is allocated to segments S1, S2, S3, and S4, where the volume ratio of Nitinol reaches 80 %. Additionally, due to Nitinol's comparatively low modulus in both martensitic and austenitic phases versus standard metals, the introduction of Nitinol decreases the resonant frequency for the L1 mode.

Table 6.2: Volume of Nitinol versus the resonant frequency in the L1 mode of a bar-shaped model, where L=100 mm and D=25 mm.

Nitinol position	Frequency (kHz) (martensite)	Frequency (kHz) (austenite)	Frequency variation (%)
S1+S2	15.920	20.859	31.024
S1+S2+S3	14.276	19.325	35.367
S1+S2+S3+S4	13.208	18.061	36.743
S1+S2+S3+S4+S5	12.398	16.977	36.933

6.2.2 Configuration-Dependent Tuneability

In Tables 6.3 and 6.4, the model is modified to a 15 mm diameter, resulting in an increased L/D ratio. The results indicate that the larger the L/D ratio, the greater the tuneability. However, the impact of the L/D ratio on tuneability is significantly less than that of position and volume. This can be improved by optimising the dimensions and configurations of a Nitinol Langevin transducer.

Table 6.3: Position of Nitinol versus the resonant frequency in the L1 mode of a bar-shaped model, where L=100 mm and D=15 mm.

Nitinol position	Frequency (kHz) (martensite)	Frequency (kHz) (austenite)	Frequency variation (%)
S1	18.932	22.869	20.795
S2	19.715	22.973	16.525
S3	20.729	23.094	11.409
S4	21.963	23.217	5.710
S5	22.991	23.301	1.348

Table 6.4: Volume of Nitinol versus the resonant frequency in the L1 mode of a bar-shaped model, where L=100 mm and D=15 mm.

Nitinol position	Frequency (kHz) (martensite)	Frequency (kHz) (austenite)	Frequency variation (%)
S1+S2	15.962	20.930	31.124
S1+S2+S3	14.319	19.389	35.408
S1+S2+S3+S4	13.248	18.117	36.753
S1+S2+S3+S4+S5	12.432	17.024	36.937

6.2.3 Material-Dependent Tuneability

When the material of the remaining segments is changed to stainless steel, the tuneability of the transducer is significantly enhanced when adjusting the positions of the Nitinol, as shown in Tables 6.5. However, this phenomenon is not observed when increasing the volume fraction of Nitinol in Table 6.6. The results suggest that the type of material for the remaining segment directly impacts the tuneability, most likely the acoustic impedance. A design strategy recommends using a material with high acoustic impedance when the volume of Nitinol is limited to less than 40%, thereby maximising tuned resonant frequencies.

Table 6.5: Position of Nitinol versus the resonant frequency in the L1 mode of a bar-shaped model with stainless steel as remaining segments, where L=100 mm and D=25 mm.

Nitinol position	Frequency (kHz) (martensite)	Frequency (kHz) (austenite)	Frequency variation (%)
S1	15.848	19.842	25.202
S2	17.436	21.024	20.578
S3	19.444	22.614	16.303
S4	22.634	24.759	9.389
S5	26.203	26.521	1.213

Table 6.6: Volume of Nitinol versus the resonant frequency in the L1 mode of a bar-shaped model with stainless steel as remaining segments, where L=100 mm and D=25 mm.

Nitinol position	Frequency (kHz) (martensite)	Frequency (kHz) (austenite)	Frequency variation (%)
S1+S2	13.085	17.355	32.632
S1+S2+S3	12.135	16.422	35.328
S1+S2+S3+S4	12.016	18.117	36.753

6.2.4 Mode-Dependent Tuneability

Throughout the previous chapters, tuneability has been found in longitudinal modes but also OP modes in modal coupling. This modal coupling is likely a result of the different ways in which various modes respond to temperature changes. This is demonstrated in Tables 6.7 and 6.8 for the 1st bending mode (B1), and Tables 6.9 and 6.10 for the 1st torsional mode. The B1 and T1 modes demonstrate higher tuneability compared to the L1 mode, explaining why different modes can be coupled through the martensitic transformation of Nitinol. Certainly, these differences in tuneability are minor, so that resonant frequencies of different modes must be sufficiently close to perform the modal coupling.

Table 6.7: Position of Nitinol versus the resonant frequency in the B1 mode of a bar-shaped model, where L=100 mm and D=25 mm.

Nitinol position	Frequency (kHz) (martensite)	Frequency (kHz) (austenite)	Frequency variation (%)
S1	6.983	8.472	21.323
S2	7.623	8.871	16.371
S3	8.467	9.330	10.193
S4	9.085	9.455	4.072
S5	8.955	9.028	0.815

Table 6.8: Volume of Nitinol versus the resonant frequency in the B1 mode of a bar-shaped model, where L=100 mm and D=25 mm.

Nitinol position	Frequency (kHz) (martensite)	Frequency (kHz) (austenite)	Frequency variation (%)
S1+S2	5.917	7.770	31.317
S1+S2+S3	5.512	7.467	35.468
S1+S2+S3+S4	5.250	7.180	36.762
S1+S2+S3+S4+S5	4.840	6.628	36.942

Table 6.9: Position of Nitinol versus the resonant frequency in the T1 mode of a bar-shaped model, where L=100 mm and D=25 mm.

Nitinol position	Frequency (kHz) (martensite)	Frequency (kHz) (austenite)	Frequency variation (%)
S1	11.606	14.065	21.187
S2	12.042	14.122	17.273
S3	12.689	14.208	11.971
S4	13.483	14.295	6.022
S5	14.151	14.355	1.442

Table 6.10: Volume of Nitinol versus the resonant frequency in the T1 mode of a bar-shaped model, where L=100 mm and D=25 mm.

Nitinol position	Frequency (kHz) (martensite)	Frequency (kHz) (austenite)	Frequency variation (%)
S1+S2	9.795	12.863	31.322
S1+S2+S3	8.791	11.911	35.491
S1+S2+S3+S4	8.135	11.127	36.779
S1+S2+S3+S4+S5	7.634	10.454	36.940

These analyses reveal that the positioning of the Nitinol segment, the ratio of Nitinol volume, the L/D ratio, and other materials present in the transducer assembly influence the tuneability of the resonant frequency for the L1 mode, along with the discussion about tuneability for bending and torsional modes. In Chapter 4, the Nitinol transducers were designed with Nitinol as end masses, thereby maximising the volume of Nitinol. This configuration results in a frequency increase due to Nitinol, which surpasses the frequency decrease attributable to the piezoelectric elements, thereby achieving tuneable resonance. Conversely, although Nitinol was positioned at the nodal location in Chapter 5, its limited volume restricted the ability to induce significant shifts in resonant frequency with temperature. Consequently, when the effects of Nitinol counterbalance those of the piezoelectric material, stable resonance is attained, either under isothermal or self-heating conditions. This discussion forms part of a broader investigation due to numerous additional factors likely to influence tuneability, including the thermal hysteresis of Nitinol and the pre-stress applied to the structure, which will be examined in future work.

6.3 How to Bridge the Gap between Prototypes and Applications?

The transducer prototypes discussed in Chapters 4 and 5 exhibit promising capabilities in adaptive and stable resonance, indicating their potential applicability in real-world applications. Adaptive and stable resonance mechanisms primarily rely upon resonant frequency tuning, given the transducer frequency is critical in performing applications. For instance, adaptive resonance can be leveraged in surgical instruments designed for tissue dissection, where the operating frequency can be adjusted to accommodate different tissue types, with lower frequencies for hard tissues and higher frequencies for soft tissues. The inherent flexibility of the Nitinol Langevin transducer allows it to execute multiple functions through a single device under varying operational conditions. Nonetheless, the transducer necessitates an external heat source to maintain a consistent temperature, which could be addressed by designing a compact temperature chamber around the transducer or by integrating the entire application setup within an oven or climate chamber. However, these solutions introduce additional control requirements. Furthermore, the tuning capability of the prototype from Chapter 4 is limited to less than 20 %, which may not fulfil the criteria for operational frequencies ranging from approximately 20 kHz for hard tissues to 55 kHz for soft tissues. Hence, further investigations are required to optimise the tuning capabilities by engineering the transducer configuration and modifying the phase transformation behaviours of Nitinol.

In Chapter 5, the cascade transducer can operate under isothermal conditions while maintaining stable resonance across a broad temperature window. However, similar to the adaptive resonance system, the design of the temperature control mechanism needs careful consideration for applications, which will be discussed in future work. Currently, the most practical approach involves the employment of self-heating transducers, which eliminate the need for additional external efforts to maintain transducer temperature isothermally. In this scenario, temperature is passively transferred and accumulated within the Nitinol segment, thereby triggering the martensite phase transformation. As a result, the stable resonance decreases the demands on the tracking system, as the resonant frequency remains nearly constant over time. This stable resonance is advantageous for various power ultrasonics applications, enhancing predictability in transducer dynamics and application performance. One application that relies heavily on frequency stability is ultrasonic levitation, where frequency fluctuations directly impact the wavelength of transmitted sound waves, posing challenges in establishing standing waves within the medium. Preliminary experiments have been conducted, revealing the potential application of ultrasonic levitation utilising the Nitinol cascade transducer described in Chapter 5, as depicted in Figure 6.2.

A selection of solid objects, including a plastic plate, polyurethane foam, rubber ball, and capacitor, were successfully levitated within the levitation system, demonstrating the feasibility

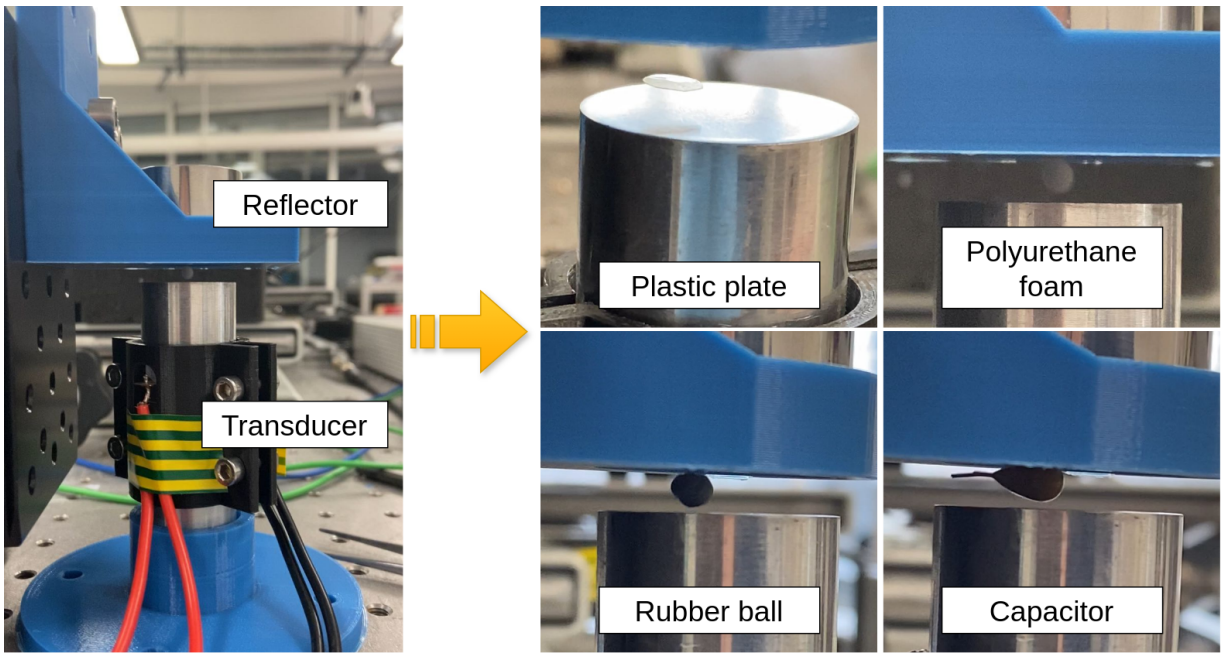

Figure 6.2: Preliminary ultrasonic levitation system and levitated objects, including a plastic plate, polyurethane foam, rubber ball, and capacitor.

of employing the Nitinol Langevin transducer in ultrasonic levitation. In the subsequent chapter, fluid droplets will be utilised to illustrate how stable resonance enhances ultrasonic levitation, as their geometric characteristics can more effectively reflect unstable resonance behaviours. The next chapter will employ the cascade configuration with an attached sonotrode to perform ultrasonic levitation of droplets and will evaluate the influence of stable resonance by contrasting the results with those obtained using a traditional transducer vibrating at a closely matched vibration frequency.

Chapter 7

A Case Study on Acoustic Levitation

As detailed in Chapter 4 and Chapter 5, it is evident that the Nitinol Langevin transducer can exhibit resonance tuneability and stability depending on microstructures of Nitinol, even with modest temperature changes. Analysis of the transducer dynamics demonstrated that variations in Nitinol and PZT properties contribute to observed phenomena. However, all transducers were designed as prototypes rather than real applications, resulting in simple and symmetric configurations. An application strongly reliant on the operating frequency is preferred to apply the Nitinol Langevin transducer to practical, based on analysis in Chapter 6. In this Chapter, a Nitinol Langevin transducer for droplet levitation is proposed, where the cascaded configuration was designed by attaching a sonotrode to amplify the mechanical outputs. Inspired by resonance stability in Chapter 5, the transducer here was engineered to vibrate at its resonance with a constant frequency for a certain period during self-heating, which is beneficial for stabilising the nodal positions in the standing wave field. This consequently has the potential to trap objects with a stable position and geometry. The objective is to investigate how a stable acoustic field generated by a Nitinol Langevin transducer improves the behaviours of levitated droplets, such as volumetric evaporation with time.

It is well-known that solids, liquids, and living creatures can be levitated and manipulated by strong acoustic fields [44, 241, 242]. This study examines explicitly liquid droplets, which are commonly utilised in chemical analysis [243], partly due to their geometric responses to radiation pressures that enable the observation of effects resulting from varying acoustic fields. Ultrasonic transducers are typically used in levitation to generate acoustic radiation, whether configured in arrays or as a single device [244–246]. A standing wave is formed within the medium by coupling travelling waves of identical frequency from either multiple transducers or a single transducer used in conjunction with transducers or a reflector. When a single Langevin transducer is employed for acoustic levitation in air, a reflector is necessary to reflect the transmitted acoustic waves [46, 247]. The standing wave is achieved by ensuring the distance between the transducer and the reflector is set to an integer multiple of half the wavelength in the medium [248]. Objects can be trapped or manipulated at the nodal points, where acoustic inten-

sity is minimised. It has to be noted that the establishment of the standing wave and the intensity of the radiation pressures is influenced by variations in the transducer vibration amplitude [249]. Given that the amplitude is a function of frequency [180], the application is significantly dependent on frequency, potentially underscoring the importance of utilising Nitinol Langevin transducers for their resonance stability.

To examine the repeatability of resonance stability in designing a Nitinol Langevin transducer, a different type of commercial hard PZT, referred to as PIC181, was utilised to build the transducer discussed in this chapter. Additionally, a titanium Langevin transducer was tailored with a resonant frequency closely matching that of the Nitinol transducer, both employing a cascaded configuration to facilitate a comparison of their dynamic responses during operation. The characterisation processes followed the methodologies outlined in previous chapters, including modal identification, harmonic analysis, and self-heating tests conducted both with and without loads. Subsequently, three types of liquid droplets, including water, isopropyl alcohol (IPA), and acetone, were selected for the levitation experiments, with their acoustic behaviours recorded using both a standard commercial camera and a high-speed imaging (HSI) system.

7.1 Transducer Design and Fabrication

Here, a cascaded Langevin transducer utilising Nitinol is designed and fabricated to showcase its stable dynamics under self-heating conditions. The Nitinol ring-shaped component, discussed in Chapter 5, has been repurposed as the middle mass of the newly designed transducer. The phase transition behaviours of the material are detailed in Table 4.18. Notably, the resonance stability exhibited by a Nitinol Langevin transducer represents a distinctive dynamic phenomenon compared to conventional transducers. This stability appears to arise from a defined combination of materials and structural dimensions, suggesting that repeatability is crucial. To achieve this, the materials employed in the transducer from Chapter 5 have been substituted, excluding the Nitinol component. In the revised design, the transducer adopts a cascaded configuration, with titanium serving as the front mass and stainless steel positioned as the back mass. For the PZT stacks, PIC181 ceramic rings have been chosen, as they exhibit dynamic responses to temperature that are comparable to those of the PZ26 material. All components are securely fastened using an A2 tool steel central pre-stress bolt, tightened via a constant torque value to guarantee a reliable connection.

In the field of power ultrasonics, attaching a sonotrode to the transducer is common to enhance vibration amplitudes [152]. The design of the sonotrode is closely linked to the dynamics of the transducer. Typically, the sonotrode and transducer are designed independently to simplify FEA simulations and enable the attachment of different sonotrodes to a single transducer [250]. For instance, when achieving a second longitudinal mode, also referred to as a full wavelength mode, for the entire device, the transducer and the sonotrode must be engineered to resonate in

their first longitudinal mode at the same frequency. If their resonant frequencies are not aligned, while the device may still perform a second longitudinal mode, the vibration amplitude and output energy will degrade. This chapter focuses on designing the device to operate at 30 kHz in its second longitudinal mode. Consequently, both the Nitinol transducer and the sonotrode vibrate at 30 kHz in their first longitudinal mode. To demonstrate the resonance stability of the Nitinol Langevin transducer, a titanium transducer with a cascaded configuration that also vibrates at 30 kHz in its first longitudinal mode has been fabricated for comparative analysis of their dynamic responses when installed to the same sonotrode. Both Nitinol and titanium transducers are designed and constructed with close structural parameters across all configuration aspects, highlighting that the primary difference in resonance response with temperature between the two lies in the materials used for the middle masses. Aluminium has been chosen as the sonotrode material due to its relatively low acoustic impedance, as detailed in Table 3.1, which facilitates the dynamic output at the tip of the sonotrode. Given the function of the transducer in the second longitudinal mode along with the sonotrode, two nodal positions are established: one at the sonotrode and another at the centre of the middle mass. However, due to the difficulties associated with fabricating the Nitinol middle mass into complex configurations, the nodal position at the sonotrode was selected to apply the clamped boundary condition. The assembled Nitinol and titanium transducers, equipped with the aluminium sonotrode, are depicted in Figure 7.1.

Both transducers underwent pre-stressing to obtain a relatively low electrical impedance at resonance. Due to the difficulty of holding the sonotrode by a collet during the assembly process, the sonotrode was not involved in recording the impedance spectra using EIA. As both transducers were designed to operate in their first longitudinal mode close to 30 kHz, Figure 7.2 illustrates the resonant frequencies and the impedance characteristics around 30 kHz for each transducer at various pre-stress values. The results indicate that at a pre-stress value of 12.5 Nm for both transducers, the electrical impedance was nearly minimised, and the resonant frequencies aligned, suggesting that this pre-stress value is optimal for both devices.

The transducers were subsequently aged for one week to facilitate releasing internal stresses within the transducer assembly, especially the piezoelectric ceramics. This procedure aims to promote stable dynamic performance during the characterisation process. Using EIA, the impedance-frequency and phase-frequency spectra were measured, which allowed for the initial identification of the resonant frequency in the second longitudinal mode from the series resonance observed at local minimum values. These results are illustrated in Figure 7.3.

The frequency difference between resonance and anti-resonance, the phase window, represents the frequency range between the two zero phase points. This concept has been extensively utilised to assess the compatibility and stability of transducers in phase-lock-loop control systems [251]. As illustrated in Figure 7.3, the Nitinol Langevin transducer exhibits a narrower phase window than the titanium transducer. The frequency margin is influenced by both the coupling factor of the PZT materials and the configuration of the transducer. To assess trans-

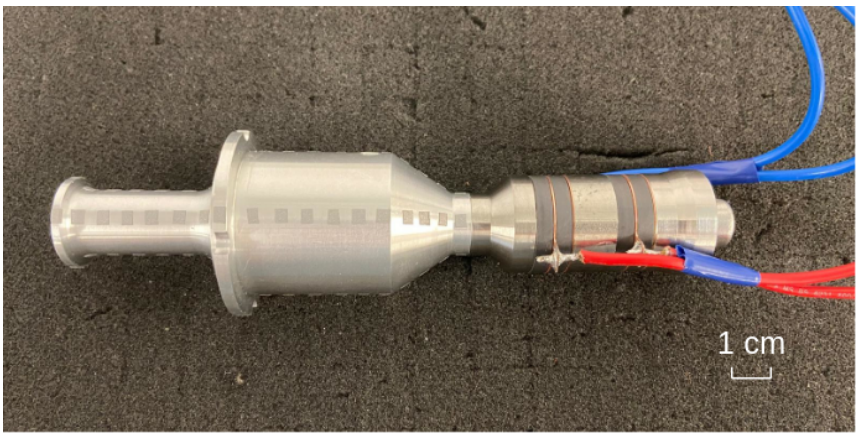

(a)

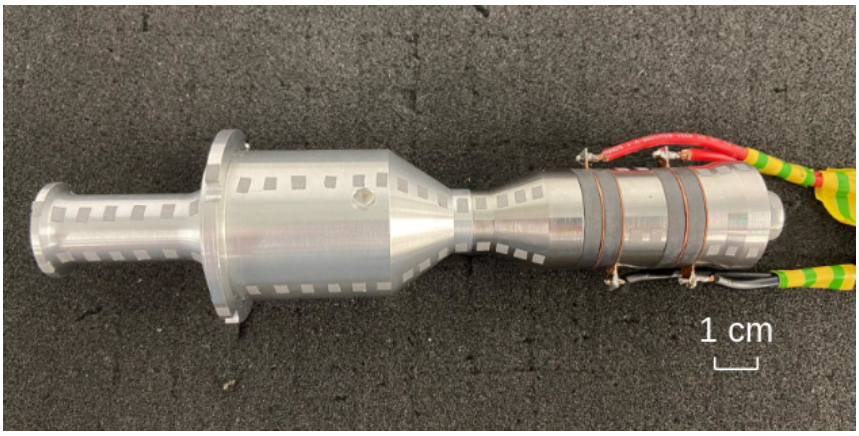

(b)

Figure 7.1: Manufactured (a) Nitinol Langevin transducer and (b) titanium Langevin transducer, each equipped with a sonotrode.

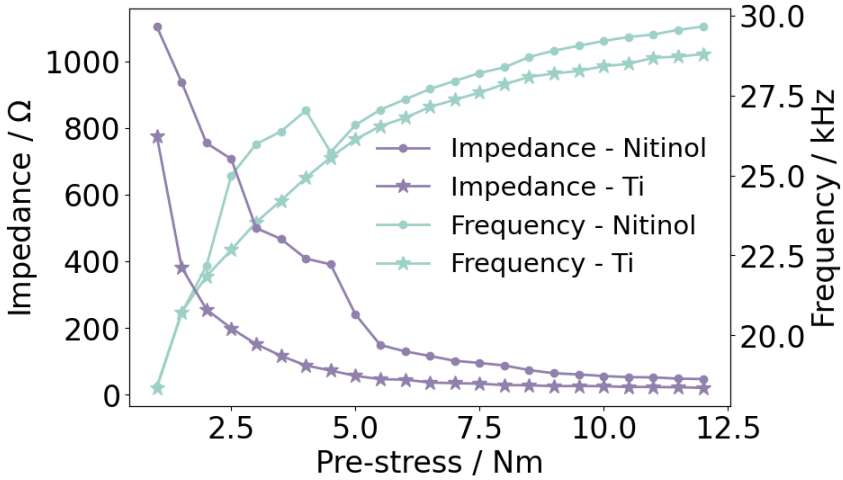

Figure 7.2: The resonant frequency and impedance of the local resonance at 30 kHz for the Nitinol Langevin transducer and the titanium Langevin transducer, without equipping a sonotrode for both configurations.

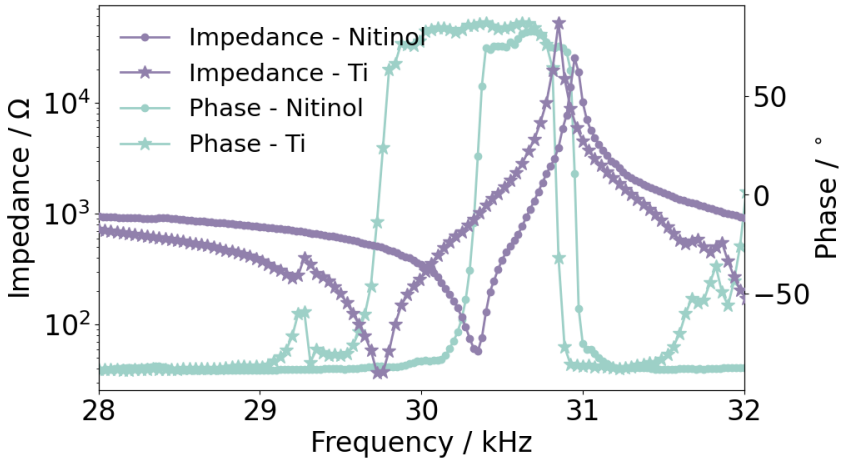

Figure 7.3: The impedance spectra of the local resonance near 30 kHz for both transducers, each with a sonotrode attached.

ducer performance using this margin, the effective electromechanical coupling factor is employed [252], which is calculated as follows:

$$k_{eff}^2 = (f_p^2 - f_s^2)/f_p^2 \tag{7.1}$$

where k_{eff} is the effective electromechanical coupling factor, f_s is the serial resonant frequency (resonance), and f_p is the parallel resonant frequency (anti-resonance). The coefficient k_{eff}^2 indicates the output mechanical energy as a ratio of the input electrical energy. A decline in this coefficient suggests that, with a constant input of electrical energy, the mechanical output becomes less effective [252], particularly in vibration amplitude. Consequently, a wider phase window of the titanium transducer is associated with greater efficiency in converting electrical energy into mechanical energy. This highlights the impact of the material properties of titanium and Nitinol on the transducer's energy conversion capabilities.

7.2 Transducer Characterisation at Room Temperature

7.2.1 Modal Identification

While the impedance-frequency relationship provides an initial estimate of the vibration mode based on empirical observations, it does not yield the dynamic information necessary for understanding the mode shape. A modal identification process is required to match the mode shape accurately with the local resonance identified in the impedance spectra. This process is typically carried out using LDV, as Chapter 3 outlines. However, because the dimensions of the transducers with sonotrode exceed the measurement capabilities of scanning LDV, only 3D LDV has been utilised in this section to obtain mode shapes. The primary advantage of using 3D LDV is its capability to measure mode shapes within a 3D structure, thus capturing any asymmetries

across the structure resulting from manufacturing inconsistencies. The dynamic properties of the transducer for the second longitudinal mode, mainly including resonant frequency and vibration mode shape, have been measured at room temperature and compared with FEA conducted in Abaqus afterwards.

Before conducting the characterisations, the phase microstructure of the Nitinol mass was initialised to austenite by heating the transducer to 60 °C, which exceeds the A_F of the Nitinol and maintaining this temperature for 10 minutes to ensure complete transition to the austenite phase [183]. Following this, the transducer was allowed to cool to room temperature above the M_S of the material, as confirmed by the DSC results shown in Figure 4.18. The longitudinal mode shapes for both transducers were then assessed using 3D LDV, with the results presented in Figure 7.4(a) for the Nitinol Langevin transducer and in Figure 7.4(b) for the titanium Langevin transducer. An excitation voltage of 10 $V_{P\text{-}P}$ was used for the 3D LDV measurements. The differences in the resonances measured through EIA and EMA are attributed to the nature of the measurement techniques, the resetting of the Nitinol microstructure, and the varying excitation applied [253].

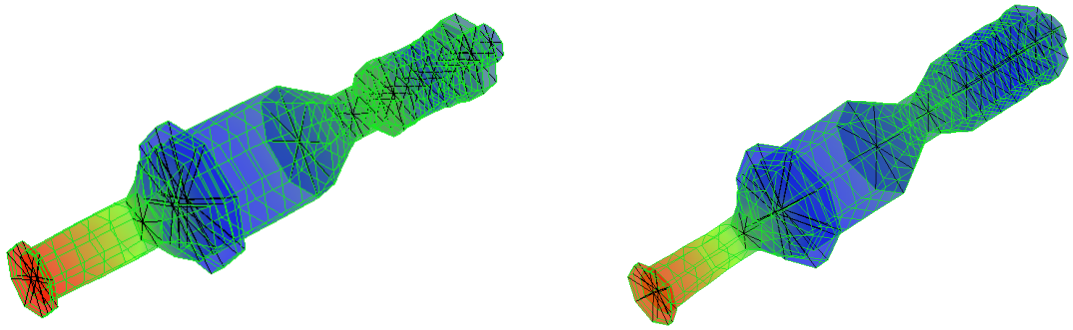

(a) (b)

Figure 7.4: The 3D LDV results of the second longitudinal mode for (a) the Nitinol Langevin transducer in the austenitic state at 30.76 kHz and (b) the titanium Langevin transducer at 30.45 kHz

Accurately measuring the mechanical properties of Nitinol presents considerable challenges [189], as they are heavily influenced by temperature and applied stress. Consequently, the design process was carried out iteratively [216]. As illustrated in Figure 7.5, both the resonant frequency and mode shape depicted in Figure 7.4 show a close correlation with the FEA results. Additionally, the mode shape and electric potential for both transducers at their resonant frequencies are given based on the proposed mathematical model, as shown in Figure 7.6. The elastic modulus of Nitinol in its austenitic phase was found to be approximately 73 GPa through this iterative approach [216], utilising FEA. This value is notably consistent with expectations for austenitic Nitinol proposed in Chapter 5.

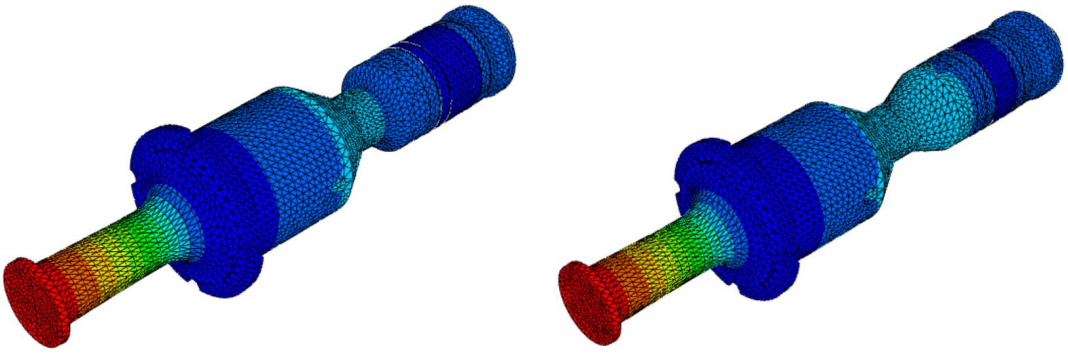

(a) (b)

Figure 7.5: FEA results of the second longitudinal mode for (a) the Nitinol Langevin transducer in the austenitic state at 30.650 kHz and (b) the titanium Langevin transducer at 30.483 kHz.

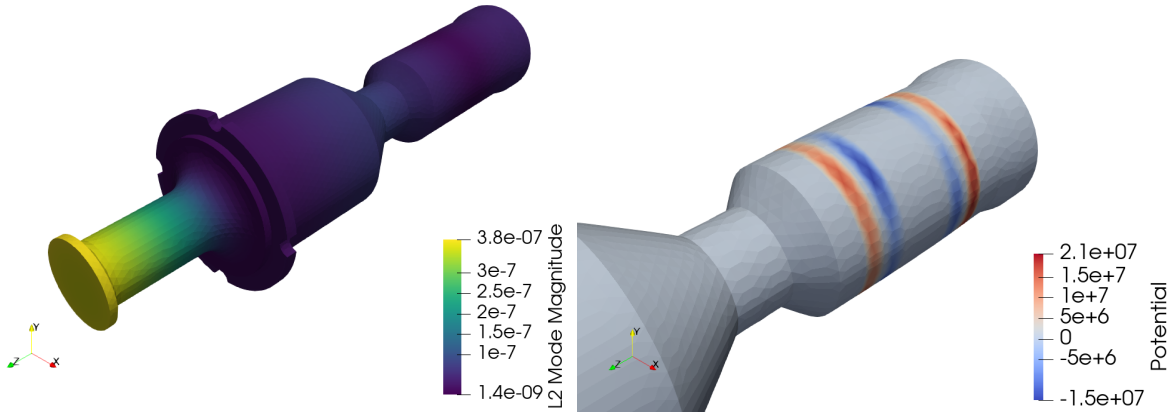

(a) (b)

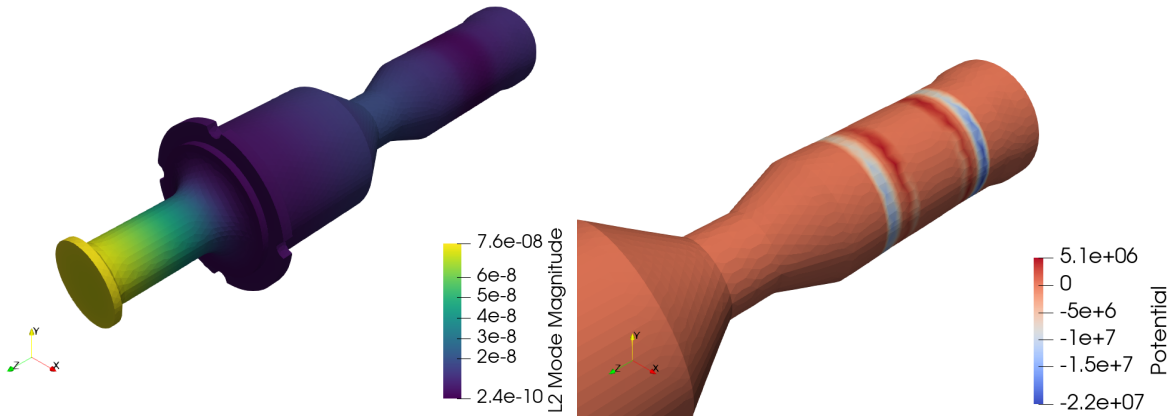

(c) (d)

Figure 7.6: (a) Mode shape and (b) electric potential of the Nitinol Langevin transducer at 30.718 kHz under free-short boundary condition, and (c) mode shape and (d) electric potential of the titanium Langevin transducer at 30.544 kHz under free-short boundary condition, all solved by using proposed 3D mathematical model with an eigenfrequency analysis.

7.2.2 Harmonic Analysis

The vibration amplitude responses of the designed transducers are inherently dependent on frequency and voltage due to the nature of piezoelectric materials, and these responses were measured using a harmonic analysis system. Once the mode shapes of both transducers were identified, frequency sweeping windows were established around 30 kHz to capture the responses of the L2 mode. Given that the dynamics of the transducers are certainly influenced by temperature, as previously discussed, obtaining amplitude responses at various temperatures is essential. The 1D LDV is limited to performing at constant temperatures across the transducer by utilising the oven, whereas the self-heating condition leads to an uneven temperature distribution on the transducer, causing discrepancies in situations. Consequently, the harmonic analysis was conducted exclusively at room temperature. As detailed in Chapter 5, the Nitinol Langevin transducer exists in one of two microstructures at room temperature due to hysteresis in the material, with variances arising from the heating or cooling cycles applied. Since this chapter focuses on resonance stability under self-heating conditions, the Nitinol Langevin transducer is operated in the heating cycle. It has been established that resonance stability in a cascaded configuration with similar dimensions occurs at around 20 V_{RMS}. Consequently, measurements for both transducers were conducted with voltage increments from 10 $V_{P\text{-}P}$ to 60 $V_{P\text{-}P}$ in 10 $V_{P\text{-}P}$ steps, as depicted in Figure 7.7. Although the voltage levels are relatively low for levitation using a Langevin transducer, typically exceeding 100 $V_{P\text{-}P}$ [244], it has been demonstrated that droplets, such as water, can be levitated within this voltage range [254].

The harmonic analysis results for both transducers, illustrated in Figure 7.7, indicate that irrespective of the voltage levels applied, both transducers exhibit similar vibration amplitude responses with respect to frequency. Given their close resonant frequencies at room temperature, the dynamics of both transducers are comparable when considering variations in temperature and voltage. The Nitinol Langevin transducer shows increased amplitude and decreased frequency as voltage rises, mirroring the behaviour observed in the titanium transducer. This observation is consistent with findings from the previous study outlined in Chapter 5, suggesting that the austenite phase does not significantly influence the non-linear behaviour of the transducers. Additionally, a further investigation was carried out by sweeping impedance as a function of frequency at the same voltage levels as the harmonic analysis since the vibration amplitude response is linked to the electrical properties of the transducers. The impedance results are shown in Figure 7.8 using the PiezoDrive system.

The voltage does not significantly influence the impedance of the Nitinol transducer, whereas the impedance of the titanium transducer increases with rising voltage. This aligns with the findings presented in Chapter 5, where a similar cascaded configuration was employed. To evaluate the performance of the transducers at higher voltages, the figure of merit outlined in the IEEE standard has been utilised [155], which is based on the impedance spectra. The formula for calculating the figure of merit is as follows:

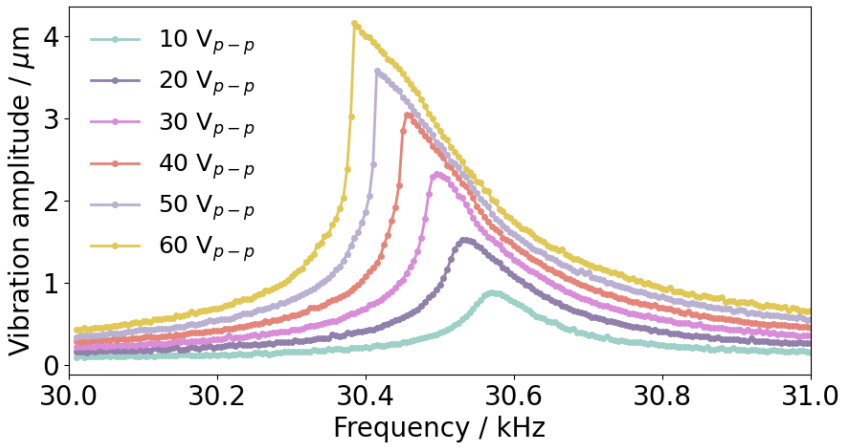

(a)

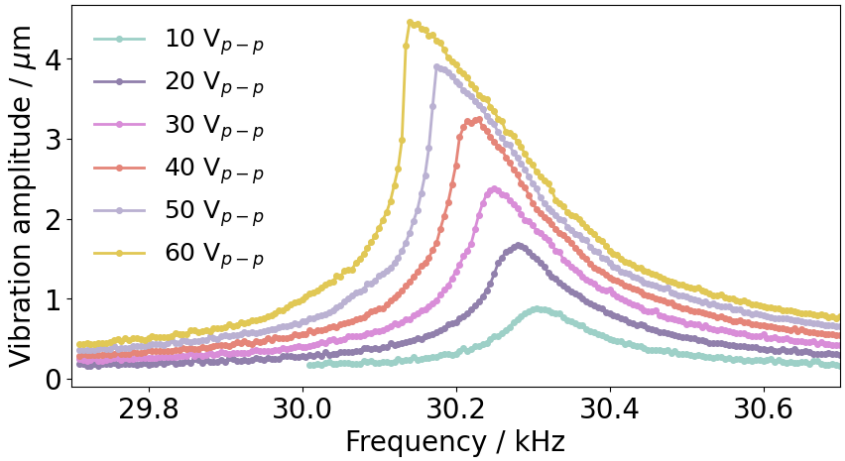

(b)

Figure 7.7: Vibration amplitude spectra of the L2 mode for (a) the Nitinol Langevin transducer and (b) the titanium Langevin transducer at room temperature with applied voltages from 10 $V_{P\text{-}P}$ to 60 $V_{P\text{-}P}$, using the harmonic system.

$$M = k_{eff}^2 Q/(l - k_{eff}^2) \tag{7.2}$$

Where M is the figure of merit, Q is the mechanical quality factor defined as the resonant frequency f_r divided by the 3 dB resonance bandwidth Δf, and l is the length of the resonator. The figure of merit for both transducers with applied voltage from 10 $V_{P\text{-}P}$ to 60 $V_{P\text{-}P}$ is shown in Figure 7.9.

The figure of merit acts as a measure of transducer performance, with higher values indicating enhanced performance [155,255]. As shown in Figure 7.9, the figure of merit for the titanium transducer decreases as voltage increases, while the Nitinol transducer shows a relatively stable figure of merit. The lower value observed for the Nitinol transducer is likely attributed to energy consumption associated with the Nitinol phase transition. The conversion of electrical energy into mechanical energy within the piezoelectric material manifests as strain, which causes the

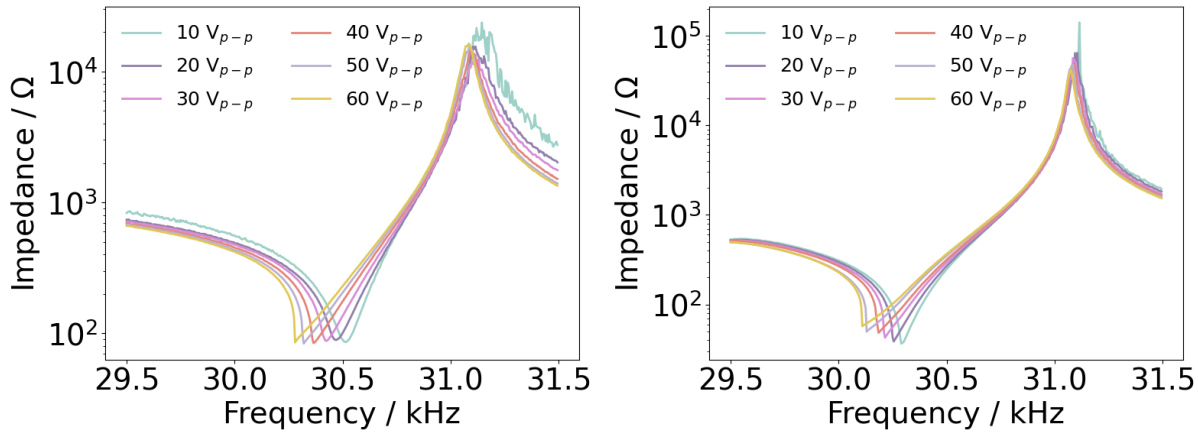

Figure 7.8: Impedance spectra of the L2 mode for (a) the Nitinol Langevin transducer and (b) the titanium Langevin transducer at room temperature with applied voltages from 10 $V_{P\text{-}P}$ to 60 $V_{P\text{-}P}$, using PiezoDrive.

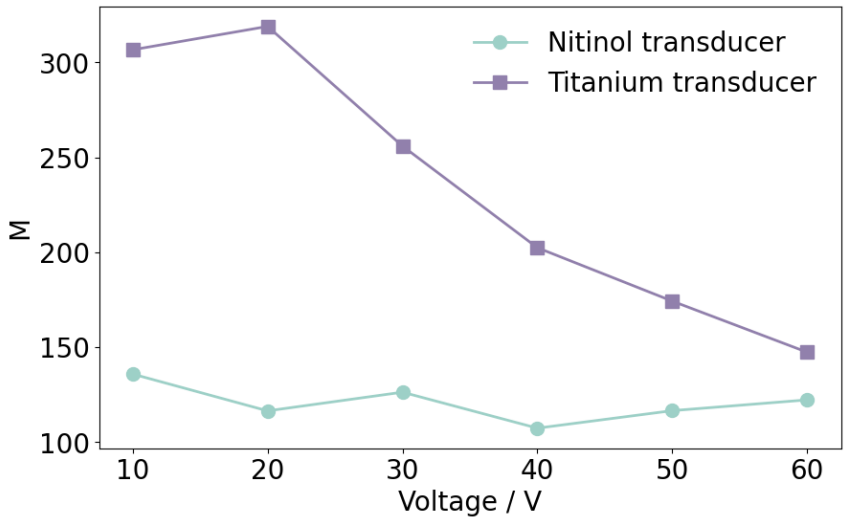

Figure 7.9: Figure of merit for Nitinol and titanium transducers with applied voltages ranging from 10 $V_{P\text{-}P}$ to 60 $V_{P\text{-}P}$ at room temperature.

Nitinol material to undergo a partial phase transition from austenite to detwinned martensite. This transition may contribute to energy losses in the mechanical output. Although the figure of merit for the Nitinol transducer is comparatively lower than that of the titanium transducer, it exhibits considerable resistance to voltage fluctuations. This resilience may result from high voltage facilitating the phase transition process due to increased strain, subsequently altering the material properties and affecting the transducer's dynamics. The reliable performance of the Nitinol transducer enables it to be a promising candidate for applications subject to voltage variations.

7.3 Self-heating with Unloaded Condition

Previous experiments and analyses have provided measurements at room temperature to conclude a systematic evaluation of the dynamic behaviours of the Nitinol Langevin transducer at room temperature. In practical ultrasonic applications, high electric potentials are typically applied, generating heat through dielectric heating from the AC voltage applied to piezoelectric components [256, 257]. During continuous operation of the Nitinol transducer, the PZT stacks serve as the main heat source, with the heat generated being transferred and accumulated to the middle mass of the Nitinol based on the cascaded configuration. It has been noted that changes in the elastic properties of Nitinol and piezoelectric materials contribute to dynamic stability during continuous operation. A continuous self-heating experiment lasting 300 s was conducted at ambient room temperature to confirm this behaviour in the Nitinol transducer discussed in this chapter. Given the strong correlation observed between resonance stability and applied voltages in previous studies of the Nitinol transducer, the transducers examined in this chapter were characterised with varying electric potentials ranging from 10 $V_{P\text{-}P}$ to 60 $V_{P\text{-}P}$ in increments of 10 $V_{P\text{-}P}$. Testing was halted if the temperature of the PZT stacks exceeded 60 °C. Thermal imaging was employed alongside PiezoDrive to assess heat increments and dynamic stability. The phase tracking method ensured that the transducers vibrated at their zero-phase electrical resonances. Throughout the experiments, the temperatures of the PZT stacks and the middle mass were typically monitored, and resonant frequency and electrical impedance were measured. The frequency variations were then quantified in percentage format over time, with the results presented in Figure 7.10.

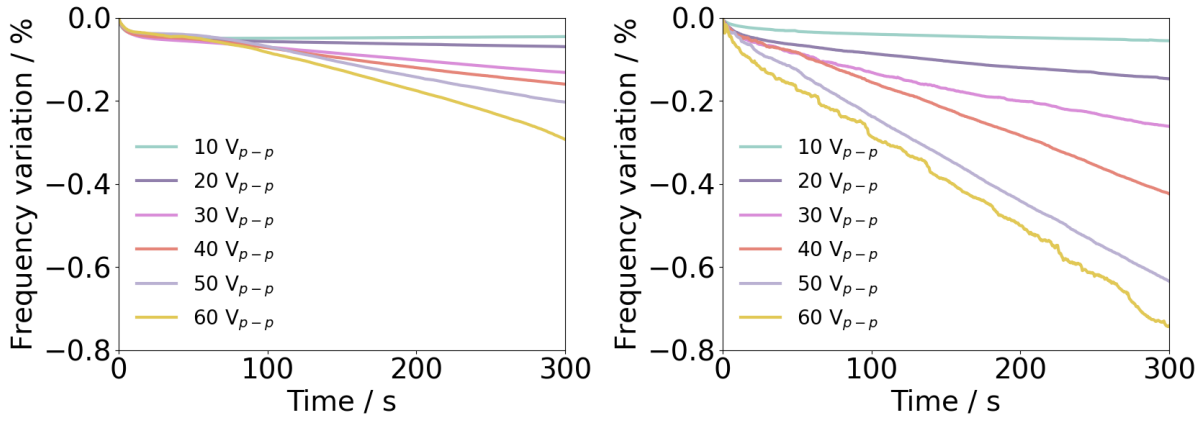

Figure 7.10: Frequency variations in the second longitudinal mode of vibration for the (a) Nitinol and (b) titanium transducers with the phase tracking method, for a 300 s continuous operation and set voltages ranging from 10 $V_{P\text{-}P}$ to 60 $V_{P\text{-}P}$ in 10 $V_{P\text{-}P}$ steps, measured by PiezoDrive.

It is evident that the resonant frequency of the titanium transducer decreases linearly over time, while the resonant frequency of the Nitinol transducer remains relatively stable within the time range of 0 s to 100 s for voltages exceeding 50 $V_{P\text{-}P}$. In this self-heating sce-

nario, although the material properties of aluminium, titanium, and stainless steel, including elastic modulus, Poisson's ratio, density, and thermal expansion coefficient, are temperature-dependent [258–260], the mechanical properties of these materials show minimal variation near room temperature. In contrast, the material properties of PIC181 are significantly affected by temperature [261, 262], which accounts for the frequency decrease observed in the titanium transducer in Figure 7.10(b). Figure 7.10(a) illustrates that the Nitinol Langevin transducer exhibits dynamic stability at higher voltage levels under self-heating conditions. These results strongly indicate the physical stiffening of the Nitinol middle mass likely contributes dynamic effects that counterbalance the changes in the elastic modulus of the PIC181 piezoelectric ceramic rings. The reduced frequency variation of the Nitinol transducer, following the resonance stability state, is due to the PIC181 having a greater influence on the transducer dynamics, thus behaving similarly to the titanium transducer. This finding is consistent with the dynamics discussed in Chapter 5. To characterise the voltage that optimises frequency stability, voltages ranging from 52 $V_{P\text{-}P}$ to 58 $V_{P\text{-}P}$, in 2 $V_{P\text{-}P}$ increments, were applied to the Nitinol transducer, as depicted in Figure 7.11.

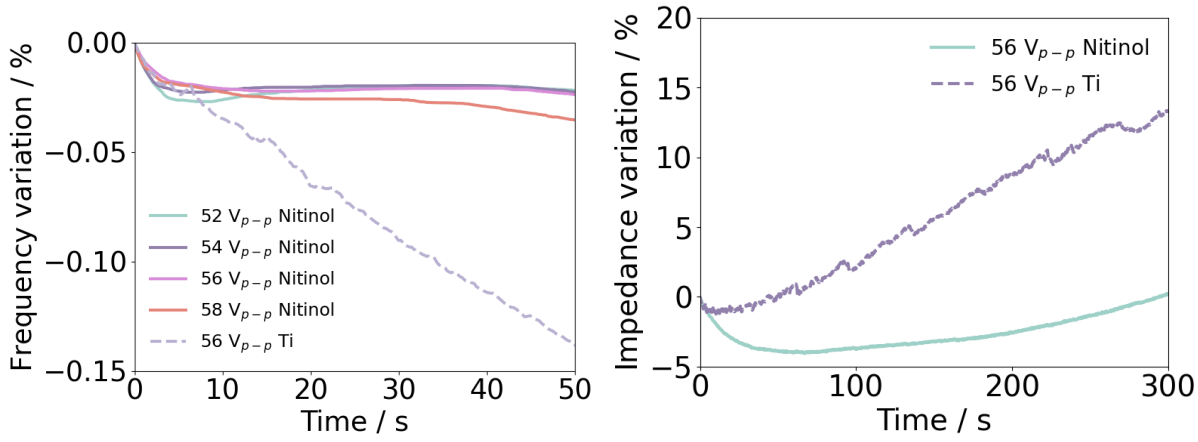

(a) (b)

Figure 7.11: (a) Frequency variations in the second longitudinal mode for the Nitinol and titanium transducers using the phase tracking method, within the frequency stability window from 0 s to 50 s and set voltages ranging from 52 $V_{P\text{-}P}$ to 58 $V_{P\text{-}P}$ in 2 $V_{P\text{-}P}$ steps, as measured by PiezoDrive, and (b) impedance variations for both transducers at 56 $V_{P\text{-}P}$, which was recorded for 300 s

In Figure 7.11(a), results of the Nitinol transducer demonstrate frequency stability during the first 50 s when the voltage is maintained between 50 $V_{P\text{-}P}$ and 60 $V_{P\text{-}P}$, reaching its maximum stability at 56 $V_{P\text{-}P}$. The frequency variations for the Nitinol transducer remain below 0.05 % overall. In contrast, the resonant frequency of the titanium transducer exhibits a decrease over time under continuous operation, regardless of the excitation levels. Therefore, only the results at 56 $V_{P\text{-}P}$ are presented for comparison. This observed behaviour is primarily attributed to changes in the material properties of PIC181, which significantly affect frequency. An increase

in the input voltage generates greater dielectric heating within the PIC181 stacks, resulting in a higher rate of heat production over time, along with fluctuating conductive heat transferred to the Nitinol middle mass. As such, the distinct responses of Nitinol and PIC181 likely exert different influences on the transducer dynamics as functions of voltage and time, with the frequencies displaying nonlinearity. It is important to note that the rapid decline in frequency observed during the first few seconds is mainly due to the time lag associated with the phase-tracking process. In Figure 7.11(b), the impedance changes for the Nitinol and titanium transducers first decrease, followed by a steady increase over time. This aligns with observations made in Chapter 5. A possible reason for the initial decrease is the phase tracking delays of the PiezoDrive system. Additionally, compared to Chapter 5, equipping a sonotrode has not led to any noticeable effects on the vibration of transducers.

Considering that the Nitinol transducer exhibits optimal resonance stability at 56 $V_{P\text{-}P}$, the dynamics have been characterised and explicitly analysed at this voltage level in the following sections. Initially, a harmonic analysis was performed to assess the vibration amplitude of both transducers at 56 $V_{P\text{-}P}$, as illustrated in Figure 7.12, which complements Figure 7.7. The results indicate that the vibration frequencies and amplitudes are closely aligned, making the dynamics of these transducers comparable in a mechanical sense.

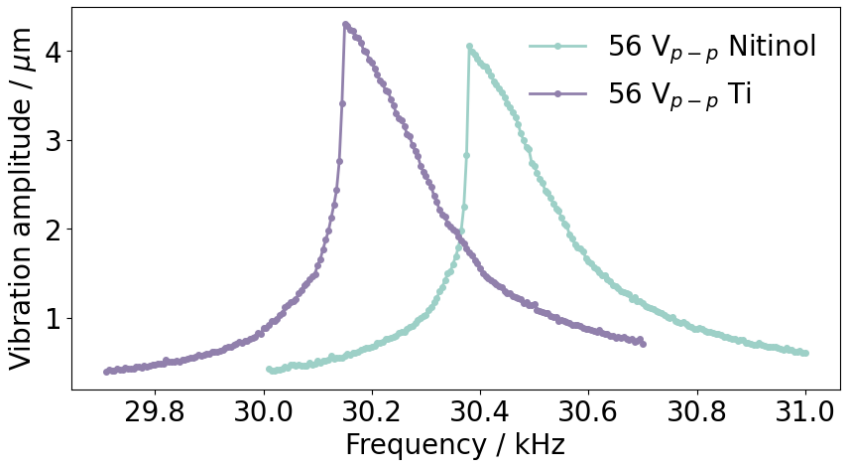

Figure 7.12: Vibration amplitude spectra of the L2 mode for (a) the Nitinol Langevin transducer and (b) the titanium Langevin transducer at room temperature with applied voltages from 10 $V_{P\text{-}P}$ to 60 $V_{P\text{-}P}$, using the harmonic system.

During the continuous operation, the thermal imager captured temperature profiles across the transducers, demonstrating the temperature variations experienced by each component. The emissivity for each material was adjusted according to Table 5.4. The results for both transducers are presented in Figure 7.13, which illustrates the maximum temperatures recorded for the PZT stacks.

As shown in Figure 7.13, there is an accumulation of heat in the middle masses, while the temperatures of all other components remain relatively close to room temperature. This phe-

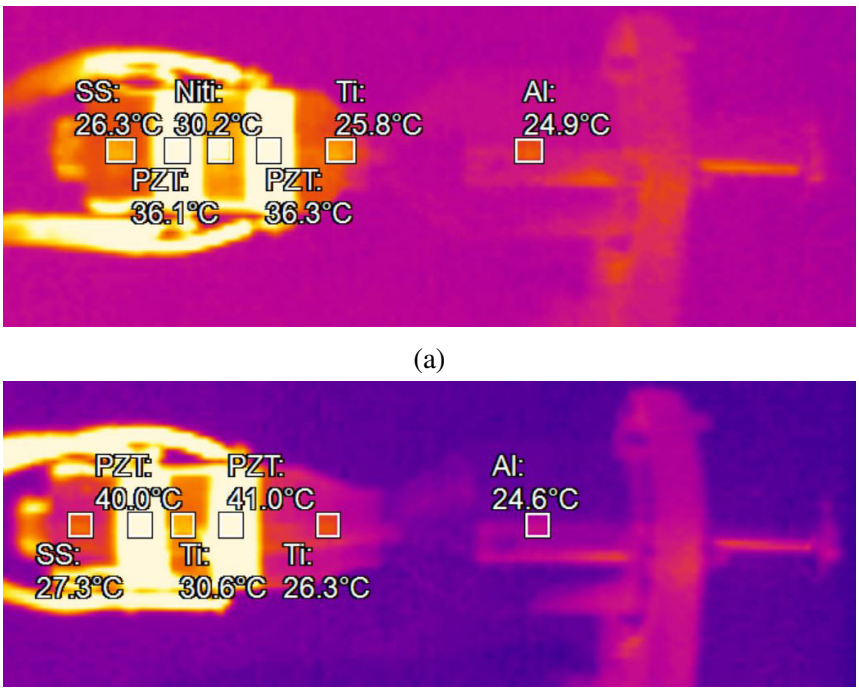

Figure 7.13: Thermal imaging profiles for (a) the Nitinol transducer and (b) the titanium transducer, where the measured maximum temperatures of the PZT stacks are demonstrated.

nomenon suggests that self-heating conditions considerably affect the temperature distribution within the PZT stacks and the middle masses of the transducers. Since conventional metallic materials show minimal changes in their properties near room temperature [258, 259, 263, 264], it is the PZT and Nitinol materials that play a role in influencing the dynamic behaviour of the transducers due to their thermal responses. Admittance loops were utilised to evaluate the impact of temperature variations on the electrical properties derived from the impedance spectra. Impedance spectra were collected at 5° intervals for the PZT stacks, using a 56 $V_{P\text{-}P}$ excitation. It is important to mention that impedance-frequency sweeping cannot be conducted when the transducer is being operated. Consequently, the sweep was performed by pausing the operation at the designated temperatures of the PZT stacks during the heating process, while measurements in the cooling process were taken under ambient cooling conditions. The results of the admittance loops are presented in Figure 7.14.

As depicted in Figure 7.14, the temperature ranges during testing differ between the two transducers. Because each transducer generates heat differently during continuous operation, there are distinct maximum temperatures in each transducer's PZT stacks. Specifically, the temperatures recorded for the Nitinol and titanium transducers reached up to 35°C and 40°C, respectively. For Langevin transducers utilised in power ultrasonics, the frequency and conductance at zero phase resonance are typically the most critical parameters to be interpolated from the admittance loops, represented by the intersection points between the admittance loops and the conductance axis. Notably, both transducers exhibited increased zero phase conductance

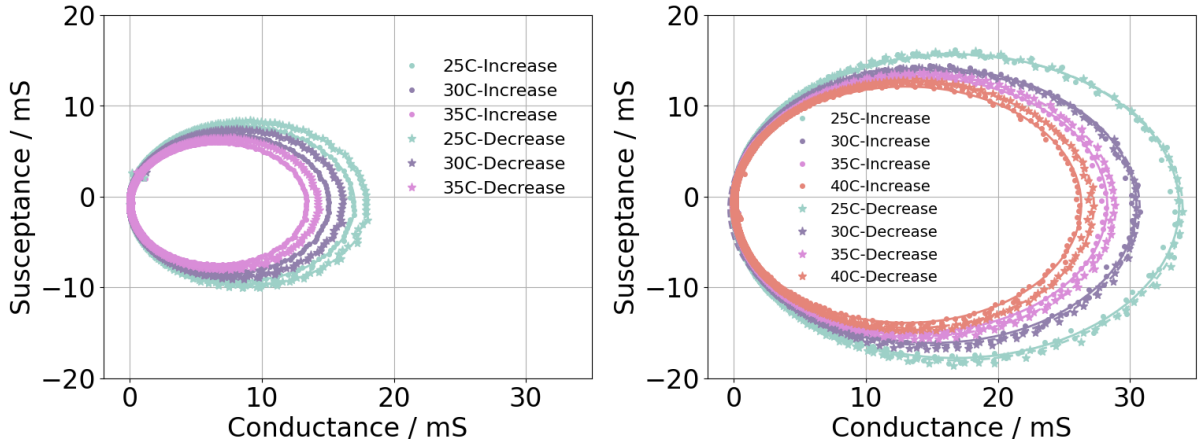

(a) (b)

Figure 7.14: Admittance loops for (a) the Nitinol Langevin transducer and (b) the titanium Langevin transducer with PZT stack temperatures varying from 25°C to 35°C and from 25°C to 40°C, respectively. Both were characterised under an applied voltage of 56 $V_{P\text{-}P}$ during both heating and cooling processes.

with rising temperature. This phenomenon is primarily attributed to the temperature-dependent properties of the PZT material rather than those of Nitinol. However, as shown by the impedance data in Figure 7.11, at a constant voltage of 56 $V_{P\text{-}P}$, the impedance of the Nitinol transducer initially decreases before increasing, indicating opposite trends in conductance. The increase in conductance with temperature is linked to the PZT stacks in the Nitinol transducer reaching 25°C after 50 s. This suggests that the initial decrease in zero-phase impedance, or the corresponding increase in conductance during the first 50 s, is not reflected in Figure 7.14. Furthermore, differences in the admittance loops during the heating and cooling processes are evident, primarily due to the hysteresis exhibited by the electrical properties of the PZT material [262]. Although Nitinol also exhibits thermal hysteresis [188], demonstrating this effect would require a broader temperature range and higher voltages to assess its contribution. However, such conditions are beyond the scope of this chapter, which focuses on resonance stability achievable only at 56 $V_{P\text{-}P}$. To further assess the influence of temperature on transducer performance, the figure of merit has been utilised, as shown in Figure 7.15.

In Figure 7.15, both transducers show a degradation in performance as temperature increases, with the Nitinol transducer generally exhibiting lower performance than the titanium transducer. Additionally, the figure of merit for both transducers is higher during the cooling phase compared to the heating phase, which can be attributed to the thermal hysteresis observed in the PZT and Nitinol. The performance of both transducers is closely related to temperature variations in the components, particularly the middle mass and PZT stacks. While this results in a compromise in the performance of the Nitinol transducer, its frequency stability is optimised at 56 $V_{P\text{-}P}$ during the first 50 s of operation. Its resonance impedance remains unaffected by changes in voltage. These measured dynamic characteristics allow the Nitinol transducer in the cascaded

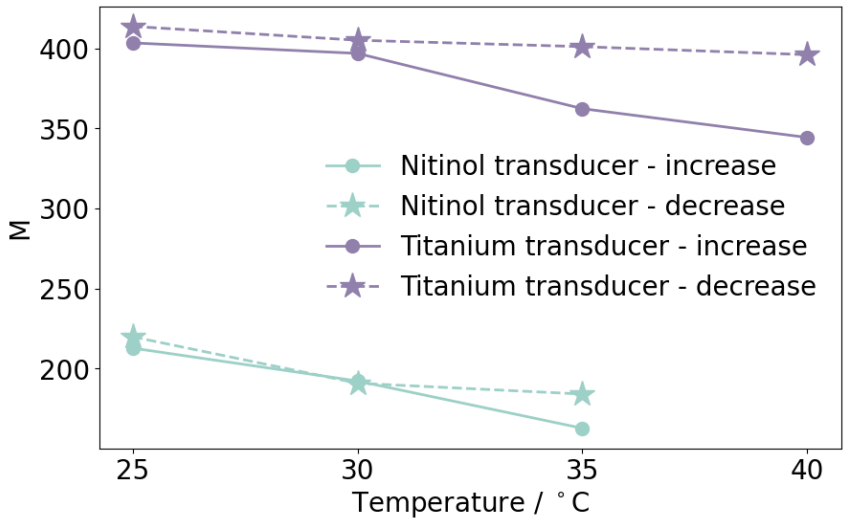

Figure 7.15: Figure of merit for Nitinol and titanium transducers with PZT stack temperatures varying from 25°C to 35°C and from 25°C to 40°C, respectively. Both were characterised under an applied voltage of 56 $V_{P\text{-}P}$ during both heating and cooling processes.

configuration to be operated under various driving conditions, facilitating an evaluation of dynamic stability for levitation, discussed in the following section.

7.4 Levitation for Liquid Droplets

As detailed in the previous section, the resonance stability of the Nitinol Langevin transducer has been proven to be optimised at 56 $V_{P\text{-}P}$ for the first 50 s continuous operation, indicating the phenomenon is replicable with different component materials from Chapter 5. In this section, Nitinol and titanium transducers are applied to the ultrasonic levitation application for liquid droplets, aiming to demonstrate the potential of using resonance stability in the industry.

7.4.1 Design of the Reflector

A reflector is typically employed in an ultrasonic levitation system using a Langevin transducer, playing a crucial role in establishing the standing wave [46, 247]. The reflector is positioned opposite the transducer to reflect the sound waves generated by the transducer. At the nodes of standing waves, minimal acoustic radiation force is produced, while at the anti-nodes, the radiation force is significantly higher. As a result, objects such as particles and droplets can be captured and manipulated at the nodes [265]. Therefore, in this section, the design of the reflector is focused on facilitating the formation of standing waves for both the Nitinol and titanium transducers.

The reflector is designed with a concave-shaped geometry to effectively reflect and converge the acoustic waves transmitted by the transducer. This configuration has been widely adopted

for single-axis levitation using Langevin transducers [266, 267]. The focused acoustic energy creates standing wave patterns between the transducer and the reflector, which trap particles at the pressure nodes. The material of the reflector influences the amount of acoustic energy reflected, as described in (3.2). In this case, the reflector is constructed from stainless steel due to its high acoustic impedance, as shown in Table 3.1, maximising the reflection of sound waves. The designed and installed reflector is illustrated in Figure 7.16, respectively. To investigate droplet behaviour with different transducers, the reflector and transducer are positioned coaxially to ensure a symmetric acoustic field around the droplet, stabilising its geometry. While levitation can also be achieved by placing the reflector off-axis and at a tilted angle [268], such configurations introduce complexities in analysing the acoustic field.

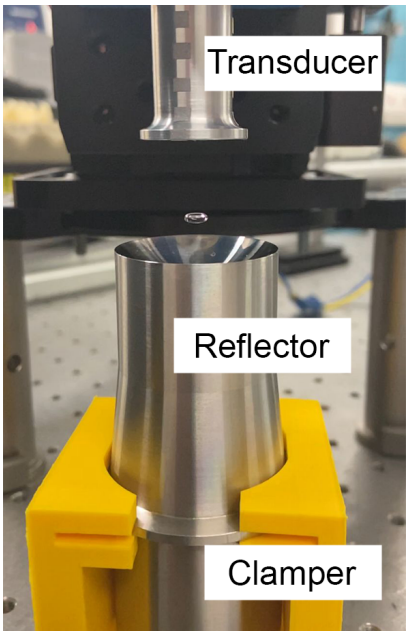

Figure 7.16: Installed reflector in the levitation setup.

7.4.2 Simulation of Acoustic Field

To conduct the levitation experiments, the acoustic field between the transducer and the reflector must first be simulated. It allows the user to comprehend and engineer the behaviours of the levitation system without using extensive optical experiments to visualise the actual acoustic field. It reveals whether a standing wave is created between the transducer and the reflector at specific distances. Furthermore, it predicts the locations of pressure nodes and anti-nodes, guiding where and how an object can be levitated.

Two commonly employed methods for simulating the acoustic field are FEM [269] and the Finite Difference Method (FDM) [270]. The key distinction between these two approaches is that FEM determines the unknowns at the element nodes based on the weak form of the governing equations, whereas FDM calculates unknowns on a grid using the strong form represented

by differential equations. The accuracy of FEM is influenced by the choice of shape functions and element orders, while the accuracy of FDM is determined by the grid spacing and the order of the finite difference approximation [271]. In this section, both methods which can be used to simulate the acoustic field are detailed.

7.4.2.1 Helmholtz Equation in Acoustics

The Helmholtz equation addresses physical problems that involve partial differential equations in both spatial and temporal dimensions, especially wave propagation in acoustics [272]. In ultrasonic levitation, the 3D acoustic field is typically reduced to a 2D form when the levitation system is axisymmetric. From this point, the Helmholtz equation in a 2D domain is presented in an inhomogeneous and dimensionless format, as given:

$$p_{,tt} - c^2 \Delta p = f \quad in \quad \Omega \subseteq \mathbb{R}^2 \tag{7.3}$$

where p is the scalar acoustic pressure or displacement, c is the propagation speed of the wave in the medium, f is the inhomogeneous force term, and Δ is the Laplacian in the 2D bonded open set Ω, defined as:

$$\Delta = \frac{\partial}{\partial x^2} + \frac{\partial}{\partial y^2} \tag{7.4}$$

Boundary conditions for the wave equation determine the behaviour of the wave upon reaching the boundaries of the domain. In acoustics, the typical boundary conditions include Dirichlet, Neumann, Robin, and periodic boundaries. This section focus solely on the application of Dirichlet boundary and absorbing boundary conditions (ABC), as outlined below:

$$\begin{aligned} \text{Dirichlet boundary condition:} \quad & p = \alpha \\ \text{ABC:} \quad & \frac{\partial p}{\partial t} + c\nabla p = 0 \end{aligned} \tag{7.5}$$

where α is a given number, and when it is zero, the boundary reflects the wave perfectly.

As both FEM and FDM uses the central difference approximation to calculate discretised time domain, the Courant-Friedrichs–Lewy condition (CFL) is prescribed for those terms of the finite difference approximation. In the 2D explicit case here, the CFL condition is required to be met:

$$\Delta t \leq \frac{\Delta x \Delta y}{c(\Delta x + \Delta y)} \tag{7.6}$$

7.4.2.2 Finite Element Method

From (7.3), the variation of the dimensionless potential energy W and kinetic energy T are expressed as:

$$\begin{aligned} W &= \frac{1}{2}\iint_{\Omega} c^2(\nabla p)^2 \mathrm{d}\Omega \\ T &= \frac{1}{2}\iint_{\Omega} (p_{,t})^2 \mathrm{d}\Omega \end{aligned} \tag{7.7}$$

In the simulation of the wave propagation, the inhomogeneous force f input energy into the system, making it a non conservative system. The force energy is given:

$$Q = \iint_{\Omega} f \cdot p \mathrm{d}\Omega \tag{7.8}$$

where Q is the work done by the external force. Then the displacement or the pressure p is governed by extended Hamiltonian for non-conservative systems [273], it can be shown that:

$$\delta \int_{t_0}^{t_1} [Q + W - T] = 0 \tag{7.9}$$

Substituting (7.7) and (7.8) into (7.9), the variational equation can be obtained that:

$$\int_{t_0}^{t_1} [\iint_{\Omega} f \cdot \delta p \mathrm{d}\Omega + \frac{1}{2}\iint_{\Omega} c^2 \nabla p \cdot \delta(\nabla p) \mathrm{d}\Omega - \frac{1}{2}\iint_{\Omega} p_{,t} \cdot \delta(p_{,t}) \mathrm{d}\Omega] = 0 \tag{7.10}$$

By applying integration by parts to (7.10) with respect to p, the equation is rewritten as:

$$\begin{aligned} &\int_{t_0}^{t_1} \iint_{\Omega} f \cdot \delta p \mathrm{d}\Omega \mathrm{d}t \\ &+ \frac{1}{2}\int_{t_0}^{t_1} [(c^2 \nabla p \cdot \delta p)|_{\Omega} - \iint_{\Omega} c^2 \Delta p \cdot \delta p \mathrm{d}\Omega] \mathrm{d}t \\ &- \frac{1}{2}\iint_{\Omega} [(p_{,t} \cdot \delta p)|_{t_0}^{t_1} - \int_{t_0}^{t_1} p_{,tt} \cdot \delta p \mathrm{d}t] \mathrm{d}\Omega = 0 \end{aligned} \tag{7.11}$$

Using the finite element setup which is detailed in Chapter 3, the standard finite element equation can be then derived as:

$$\mathbf{M} p_{,tt} - \mathbf{K} p = \mathbf{Q} \tag{7.12}$$

where global mass matrix $\mathbf{M}$ and stiffness matrix $\mathbf{K}$ are assembled from elemental mass and stiffness matrices:

$$\begin{aligned} \mathbf{M}^{(e)} &= \iint_{\Omega} N^{(e)}(x,y)^{\mathrm{T}} N^{(e)}(x,y) \mathrm{d}\Omega \\ \mathbf{K}^{(e)} &= c^2 \iint_{\Omega} \nabla N^{(e)}(x,y)^{\mathrm{T}} \nabla N^{(e)}(x,y) \mathrm{d}\Omega \end{aligned} \tag{7.13}$$

To simulate the wave propagation, the time variable is required to be dicretised into steps. As the p variable is in its second derivative with respect to time, the second-order central difference

approximation is introduced as shown that:

$$p_{,tt}(t) \approx \frac{p(t+\Delta t) - 2p(t) + p(t-\Delta t)}{(\Delta t)^2} \tag{7.14}$$

Substituting (7.14) into (7.12), $p(t+\Delta t)$ can be expressed:

$$p(t+\Delta t) = (\Delta t)^2 \mathbf{M}^{-1}(\mathbf{Q} - \mathbf{K}p(t)) + 2p(t) - p(t-\Delta t) \tag{7.15}$$

where $p(t-\Delta t)$ is calculated by the Taylor series from the initial values, therefore obtaining values for further iterations:

$$p(t-\Delta t) = p(t) - \Delta t \cdot p_{,t}(t) + \frac{(\Delta t)^2}{2} \cdot p_{,tt}(t) \tag{7.16}$$

The domain Ω is the 2D space between the transducer and the reflector, where the medium is air with a 340 m/s acoustic speed, and the wavelength of the transducer is set to $\lambda = 11.2$ mm. Triangle elements with three Gauss quadrature points are used. By applying the Dirichlet boundary condition to the arc boundary and ABC to left and right open boundaries, the numerical solutions of the Helmholtz equation by using FEM are shown as Figure 7.17.

7.4.2.3 Finite Difference Method

Unlike FEM, FDM uses the central difference approximation for both spacial domain and time. Here, the second-order central difference approximation is used, and (7.3) is rewritten as:

$$\begin{aligned} &\frac{p(x,y,t+\Delta t) - 2p(x,y,t) + p(x,y,t-\Delta t)}{(\Delta t)^2} \\ &- c^2 \frac{p(x+\Delta x,y,t) - 2p(x,y,t) + p(x-\Delta x,y,t)}{(\Delta x)^2} \\ &- c^2 \frac{p(x,y+\Delta y,t) - 2p(x,y,t) + p(x,y-\Delta y,t)}{(\Delta y)^2} = f(x,y,t) \end{aligned} \tag{7.17}$$

when $\Delta x = \Delta y$, $p(x,y,t+\Delta)$ can be obtained from (7.17):

$$\begin{aligned} &p(x,y,t+\Delta t) = \\ &C^2[p(x+\Delta x,y,t) + p(x-\Delta x,y,t) + p(x,y+\Delta y,t) + p(x,y-\Delta y,t) - 4p(x,y,t)] \\ &+ 2p(x,y,t) - p(x,y,t-\Delta t) + (\Delta t)^2 f(x,y,t) \end{aligned} \tag{7.18}$$

where

$$C = c\frac{\Delta t}{\Delta x} = c\frac{\Delta t}{\Delta y} \tag{7.19}$$

The construction of the domain in FDM differs significantly from that in FEM, particularly concerning the curved edges of the reflector. In FEM, irregular edges are represented by

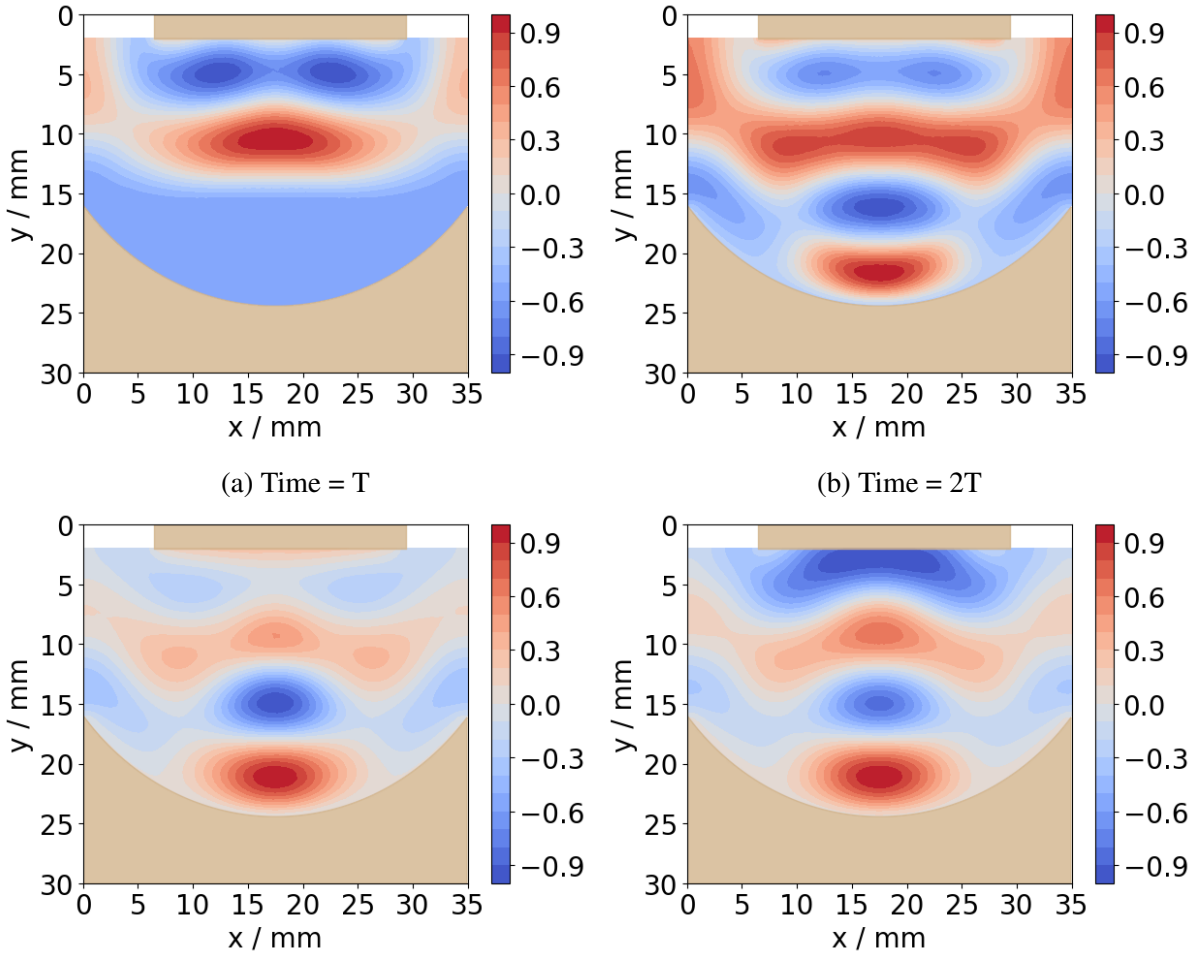

(a) Time = T

(b) Time = 2T

(c) Time = 3T

(d) Time = 4T

Figure 7.17: Numerical simulation of the Helmholtz equation in air within the domain Ω by using FEM at time frames (a) T, (b) 2T, (c) 3T, and (d) 4T, where $T = \lambda/c$ and λ = 11.2 mm.

refining the mesh size to closely approximate the geometry. In contrast, FDM typically approximates curved boundaries with a staircase-like pattern, as the mesh is structured in a mosaic grid, generally composed of square or rectangular shapes to comply with the central difference approximation algorithm [274, 275]. This approach inevitably introduces some errors, which can be reduced by further refining the mesh size. Despite this limitation, the low computational costs associated with FDM make it a popular choice for simulating acoustic fields.

The numerical solutions obtained from FEM and FDM are generally consistent, although differences primarily arise in the waveforms and pressure distributions. Both methods have factors that can lead to inaccuracies, such as large element sizes in FEM and staircase-like approximations of curved boundaries in FDM. Refining the element size can enhance the results. However, finer element sizes necessitate more time steps to be calculated according to the CFL stability condition. In the numerical setup discussed for FEM and FDM, the computation time for 801 frames is approximately 21 minutes for FEM and 1 minute for FDM. Therefore, refining the mesh in FEM is not advisable due to the exponentially increased time costs. The calculated

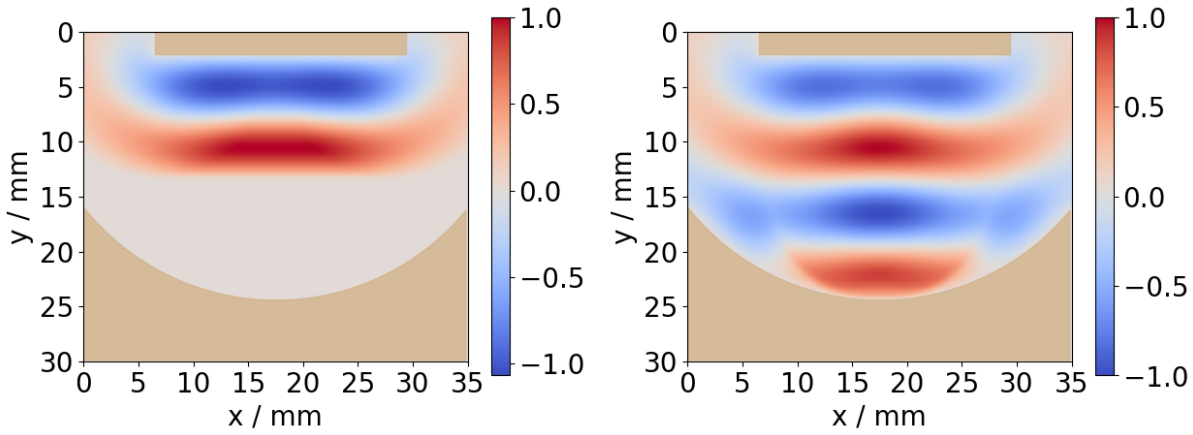

(a) Time = T

(b) Time = 2T

(c) Time = 3T

(d) Time = 4T

Figure 7.18: Numerical simulation of the Helmholtz equation in air within the domain Ω by using FDM at time frames (a) T, (b) 2T, (c) 3T, and (d) 4T, where $T = \lambda/c$ and λ = 11.2 mm.

results with 10 T are wrapped within the levitation setup, as illustrated in Figure 7.19, where the droplet position is close to the middle simulated node used to levitate droplets in subsequent experiments. The positional offset occurs because introducing a droplet affects the properties of the acoustic field, necessitating a slightly greater distance between the transducer and reflector to establish a standing wave. As a result, the actual distance between the transducer and reflector was adjusted slightly during the experiment.

7.4.3 Self-Heating and Droplet Evaporation

This section discusses the levitation performance of both Nitinol and titanium transducers. The observation time window was set to 300 s, and three types of droplets were used in the experiments: water, isopropyl alcohol (IPA), and acetone. A 56 $V_{P\text{-}P}$ voltage was applied to both transducers. Although this voltage is relatively low compared to most levitation systems, it has been demonstrated to be sufficient for inducing levitation of the droplets here [254]. Pre-tests were performed to show that the introduction of droplets minimally affects the transducer fre-

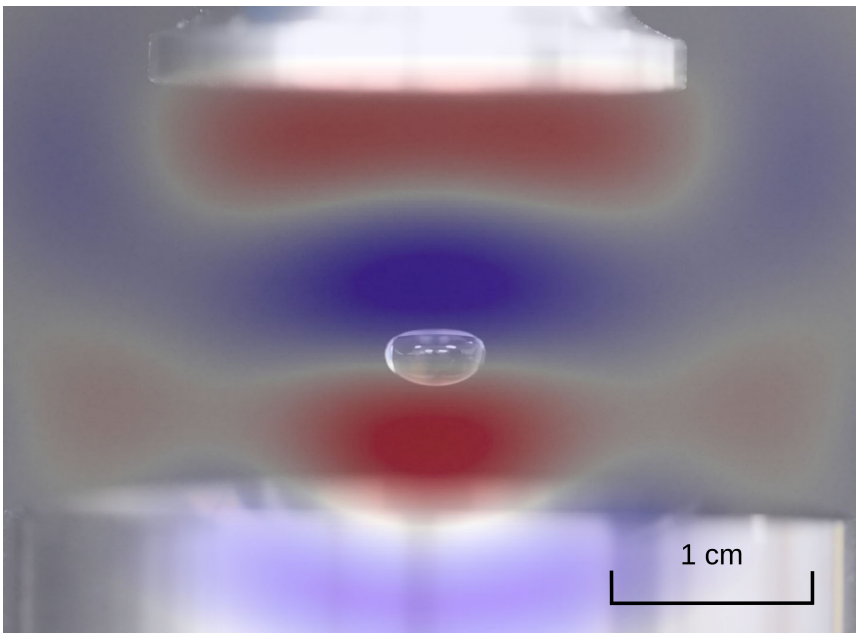

Figure 7.19: Wrapped levitation experiment conducted with a simulated acoustic field at 10 T.

quency, which is a crucial factor for the stability of the acoustic field. The variation in frequency, expressed as a percentage, is presented in Figure 7.20, where droplets of approximately 10 μL each of water, IPA, and acetone were utilised.

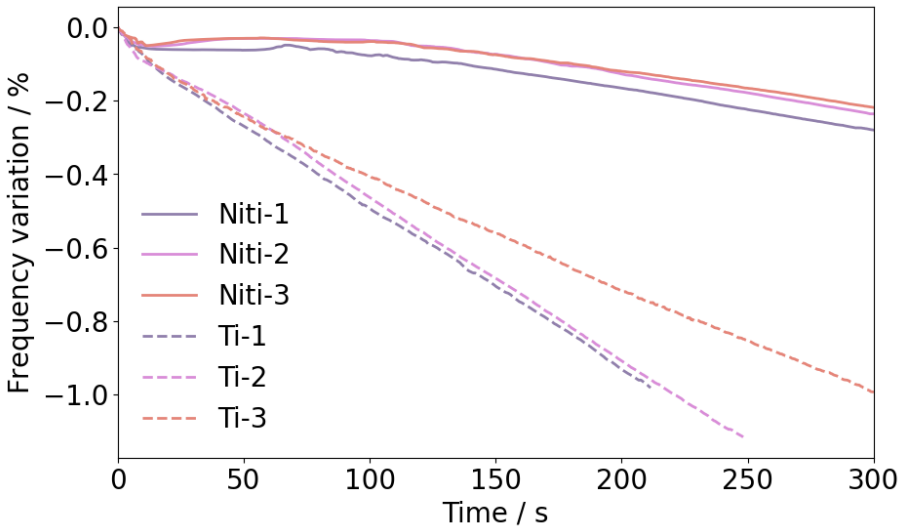

Figure 7.20: Frequency variations in the second longitudinal mode for the Nitinol and titanium transducers in preliminary tests for levitating droplets at a set voltage as 56 $V_{P\text{-}P}$, recorded by PiezoDrive over 300 s.

As illustrated in Figure 7.20, the frequency variation for both transducers remains consistent with that observed under unloaded conditions, indicating the formation of a standing wave, and the introduction of small droplets has minimal impact on the transducer frequencies over time. The Nitinol transducer demonstrates high frequency stability, with only a 60 Hz shift after 300 s

continuous operation, whereas the titanium transducer experiences a shift of approximately 300 Hz. Furthermore, the results indicate that this stable frequency is reproducible regardless of the type of droplets introduced. For Langevin transducers operating at their resonant frequency, the electrical impedance is more sensitive to load changes, which refers to the levitated droplets. The variations in impedance were also monitored during the pre-tests, as shown in Figure 7.21.

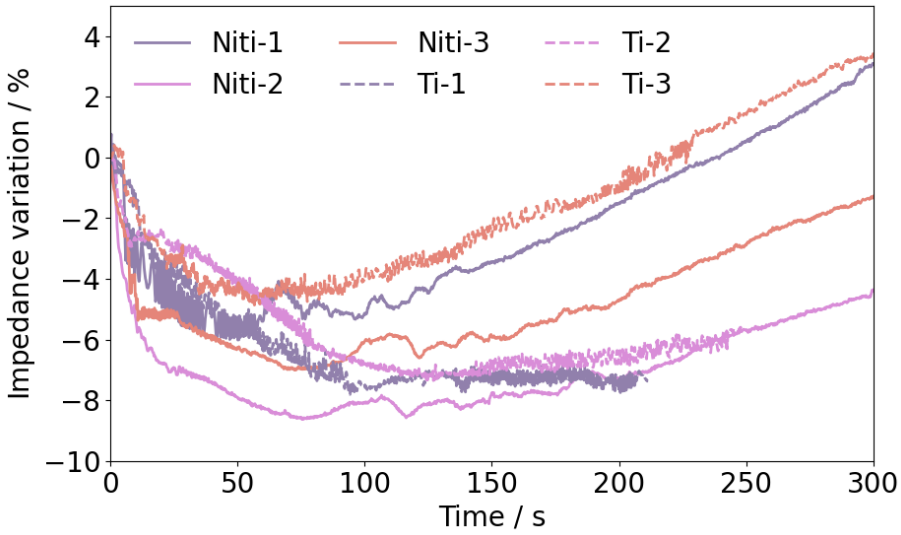

Figure 7.21: Impedance variations in the second longitudinal mode for the Nitinol and titanium transducers in preliminary tests for levitating droplets at a set voltage as 56 $V_{P\text{-}P}$, recorded by PiezoDrive over 300 s.

Generally, the impedance responses for both transducers correlate well with the results presented in Figure 7.20. However, introducing droplets has affected the impedance, resulting in minor fluctuations over time. Notably, these fluctuations correspond to the unstable position and geometry of the droplets within the acoustic field, suggesting that the instability of the droplets impacts the loaded condition of the transducer. Since the fluctuations in impedance are relatively small, no significant changes in heat generation have been observed.

Preliminary tests revealed notable differences in the behaviour of Nitinol and titanium transducers under loaded conditions. The Nitinol transducer vibrated at a relative stable resonant frequency, even when subjected to load, though it experienced slight impedance variations due to unstable droplets. On the other hand, dynamics of the titanium transducer remained unchanged by loading, maintaining frequency and impedance responses similar to those observed in its unloaded state. With both transducers operating at resonant frequencies close to 30 kHz, the levitation system was initially positioned with a 2λ distance between the transducer and the reflector, followed by fine adjustments at the start of the experiment. Three types of droplets, water, IPA, and acetone, were introduced into the standing wave field. The selection of different droplets was crucial due to their varying viscosities and surface tensions, which influence droplet volumes and sizes, respectively. The viscosity and surface tension of water, IPA, and acetone at 20°C are shown in Table 7.1 [276, 277].

Table 7.1: Viscosity and surface tension of water, IPA, and acetone at 20°C.

Liquids	Viscosity (mPa·s)	Surface tension (mN/m)
Water	1	72.7
IPA	2.3703	21.7
Acetone	0.3311	23.7

Since precise droplet volume control was challenging, experiments were repeated, and results were selected for droplets with volumes around 10 μL. Surgical needles were utilised instead of pipettes, as pipette tips disrupted the stability of the standing waves, leading to failures in the introduction of droplets to the acoustic field. In order to investigate the evaporation of three types of droplets during levitation, the droplets were observed over the period. Frames were captured at different intervals, allowing for the visualization of the 2D geometry of droplets. The contrast of these images was adjusted and converted to greyscale. The droplet volume was then calculated by revolving the fitted ellipse, which was identified by detecting the droplet edge using OpenCV. The results related to evaporation are presented in Figure 7.22.

From Figure 7.22, the irregular curves suggest that the droplet volumes vary rapidly over time. One of the reasons is the instability of the geometry of droplets [278]. Also, the non elliptical geometry, as a result of varying surface tension due to frequency and acoustic intensity [279, 280], introduces errors when calculating the volume. This accounts for instances where the volume exceeds 100%. Consequently, the volume depicted in the figure should be viewed as an approximation rather than an exact measurements. As illustrated in Figure 7.22(a), the titanium transducer levitated water droplets for a shorter duration than the Nitinol transducer. One possible explanation for this is that the frequency of the titanium transducer decreases over time due to its high temperature, making it challenging to maintain a standing wave when the distance between the transducer and the reflector remains constant. They naturally fall when the radiation force becomes insufficient to hold the droplets. In contrast, the Nitinol transducer exhibits a longer levitation time, as its consistent frequency response ensures a reliable radiation force acting on the droplets. However, it is difficult to draw definitive conclusions about the evaporation rate of water droplets with either transducer based on the figure. The evaporation rate of water at room temperature is relatively low, even though elevated radiation pressure could potentially expedite the process.

In Figure 7.22(b), both transducers successfully levitated the IPA droplets for 300 s, maintaining a stable levitation status. It was observed that all droplets exhibited a linear decrease in volume over time. However, the final droplet volumes for the Nitinol transducer ranged between 60 % and 80 %, while the titanium transducer resulted in volumes below 60 %. This difference can be attributed to the stable frequency of the Nitinol transducer, which contributes to a consistent droplet geometry. In contrast, the titanium transducer experiences unstable radiation forces due to decreasing frequencies, leading to an inconsistent geometry. These changes in geometry ultimately result in variations in the evaporation rate.

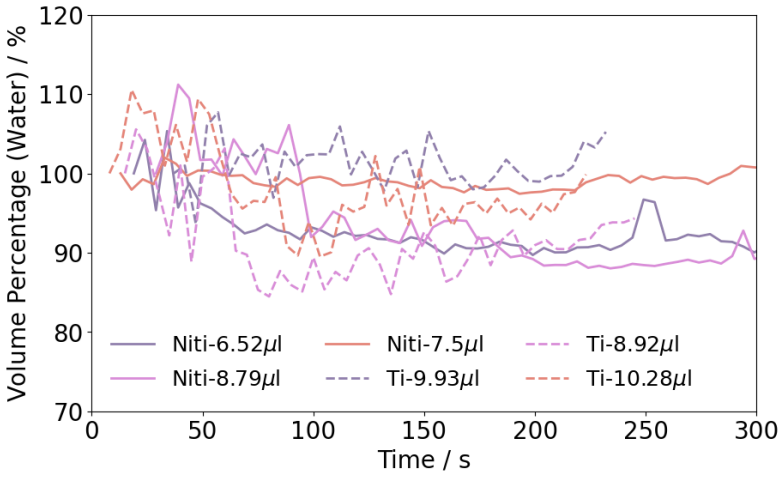

(a)

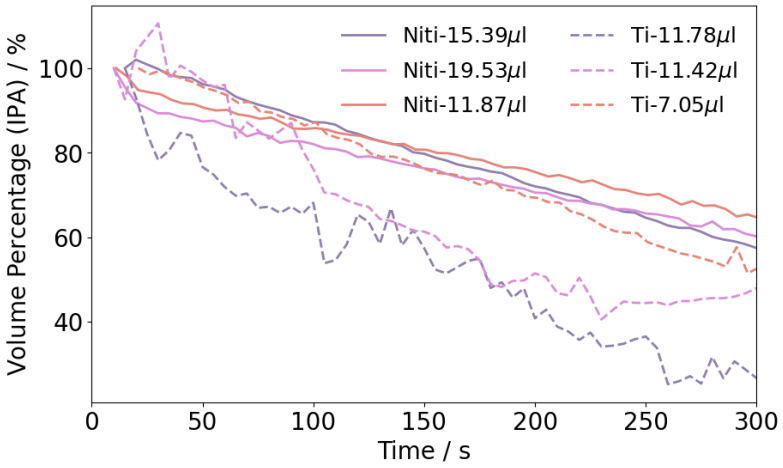

(b)

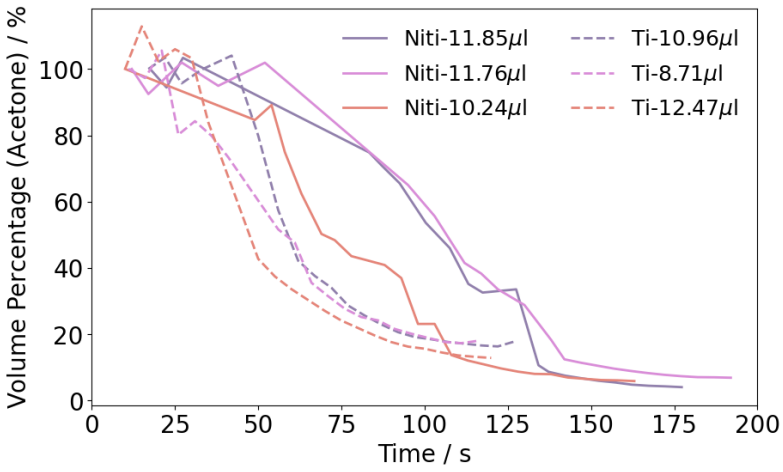

(c)

Figure 7.22: Volume percentage of levitated droplets for (a) water, (b) IPA, and (c) acetone, using the Nitinol and titanium transducers at a set voltage of 56 $V_{P\text{-}P}$, recorded by PiezoDrive over 300 s.

As depicted in Figure 7.22(c), both transducers could not maintain the levitation of acetone droplets to 300 s. This is attributed to the high evaporation rate of acetone, leading to a rapid volume decrease. When the droplets are introduced, they alter the distance between the transducer and reflector needed to establish the standing wave. If the volume changes significantly, the initial conditions may not generate sufficient radiation pressure to support the new volume. Additionally, changing transducer frequency is another factor in creating an unstable acoustic field. It has to note that the experiments can be divided into three phases for both transducers. The first phase involves rapid changes in geometry and volume, followed by a high evaporation rate during the second phase. The final phase is marked by minimal evaporation before the droplets eventually fall. Notably, the Nitinol transducer outperformed the titanium transducer in duration across all three phases, which its stable radiation force can explain.

Based on the experiments conducted, all three droplets exhibited varying behaviours during levitation, mainly when influenced by different transducers, where these droplets differ in viscosity and evaporation rates. The Nitinol transducer was able to levitate water and acetone for longer durations while it effectively maintained IPA droplets with a lower evaporation rate. These outcomes can be attributed to the stable frequency of the Nitinol transducer, which ensures consistent radiation pressure. However, droplet oscillations were observed throughout the experiments. To investigate the nature of these oscillations and assess whether the Nitinol transducer aids in maintaining droplet geometry, HSI has been conducted, with results discussed in the following section.

7.4.4 High-Speed Imaging

The high-speed test was performed using a HSI system (Fastcam SA-Z 2100 K, Photron, UK) where droplets were illuminated by synchronous 10 ns laser pulses at 640 nm (CAVILUX Smart, Cavitar, Finland), aiming to capture the complete oscillation period of the droplets. The capture interval was set to every 30 s. However, to optimise video file storage, the number of frames was limited to 30000 frames, allowing for the entire observation of the vibration modes of the liquids. Although the vibration frequency of the droplets is around 30 kHz, matching the frequency produced by the transducer, the complete mode could still be captured as long as the frame rate is close to 30 kHz. This high-speed test was carried out using both Nitinol and titanium transducers with water, IPA, and acetone at a different time for one oscillation, as illustrated in Figure 7.23, 7.24, 7.25, D.1, D.2, and D.3.

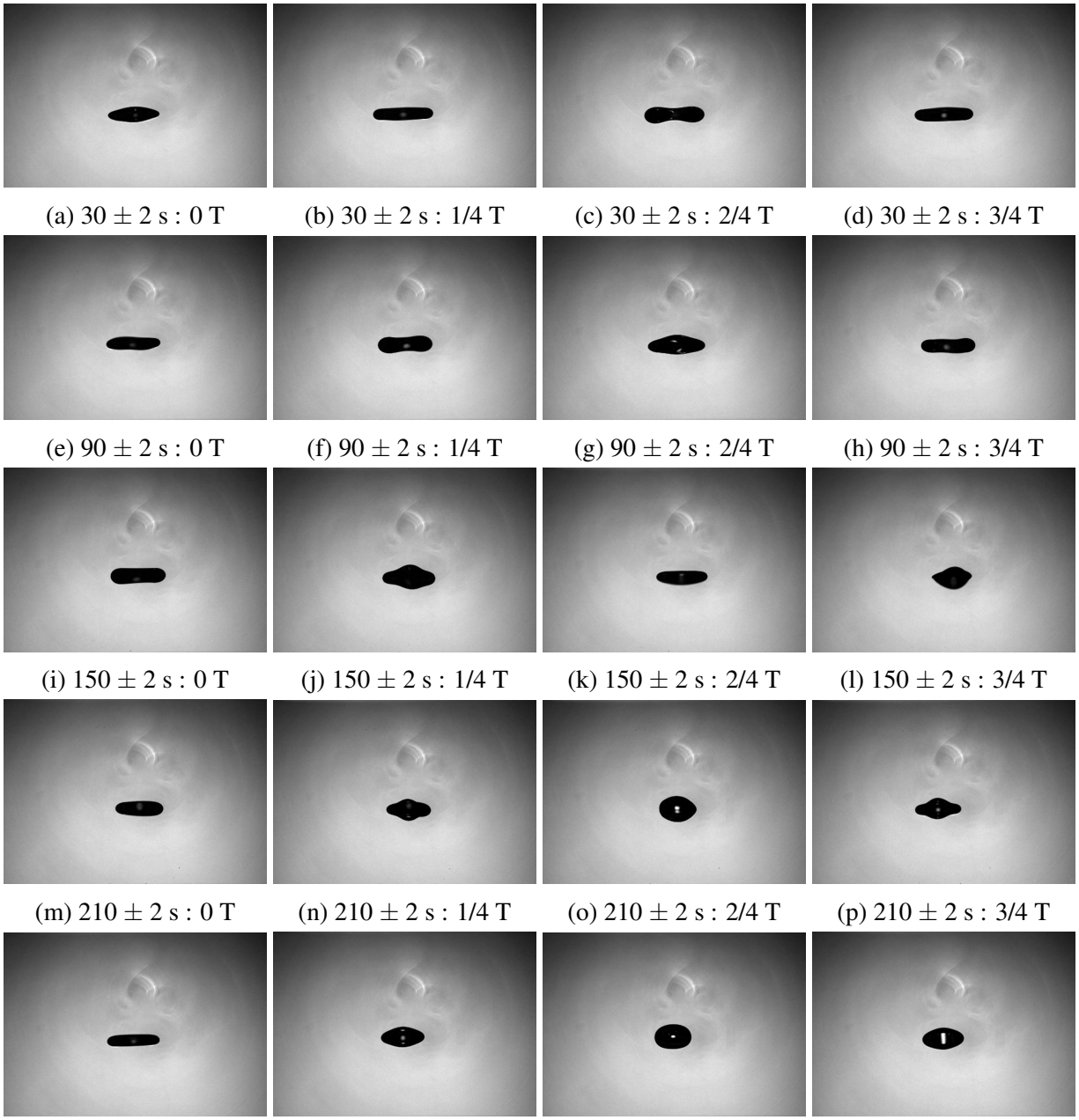

(a) 30 ± 2 s : 0 T (b) 30 ± 2 s : 1/4 T (c) 30 ± 2 s : 2/4 T (d) 30 ± 2 s : 3/4 T

(e) 90 ± 2 s : 0 T (f) 90 ± 2 s : 1/4 T (g) 90 ± 2 s : 2/4 T (h) 90 ± 2 s : 3/4 T

(i) 150 ± 2 s : 0 T (j) 150 ± 2 s : 1/4 T (k) 150 ± 2 s : 2/4 T (l) 150 ± 2 s : 3/4 T

(m) 210 ± 2 s : 0 T (n) 210 ± 2 s : 1/4 T (o) 210 ± 2 s : 2/4 T (p) 210 ± 2 s : 3/4 T

(q) 270 ± 2 s : 0 T (r) 270 ± 2 s : 1/4 T (s) 270 ± 2 s : 2/4 T (t) 270 ± 2 s : 3/4 T

Figure 7.23: The full vibration mode for levitated water droplets, where the shadowed region indicates section geometry, at 30 s, 90 s, 150 s, 210 s, and 270 s based on the Nitinol Langevin transducer, conducted at a set voltage of 56 $V_{P\text{-}P}$ and recorded by a HSI system.

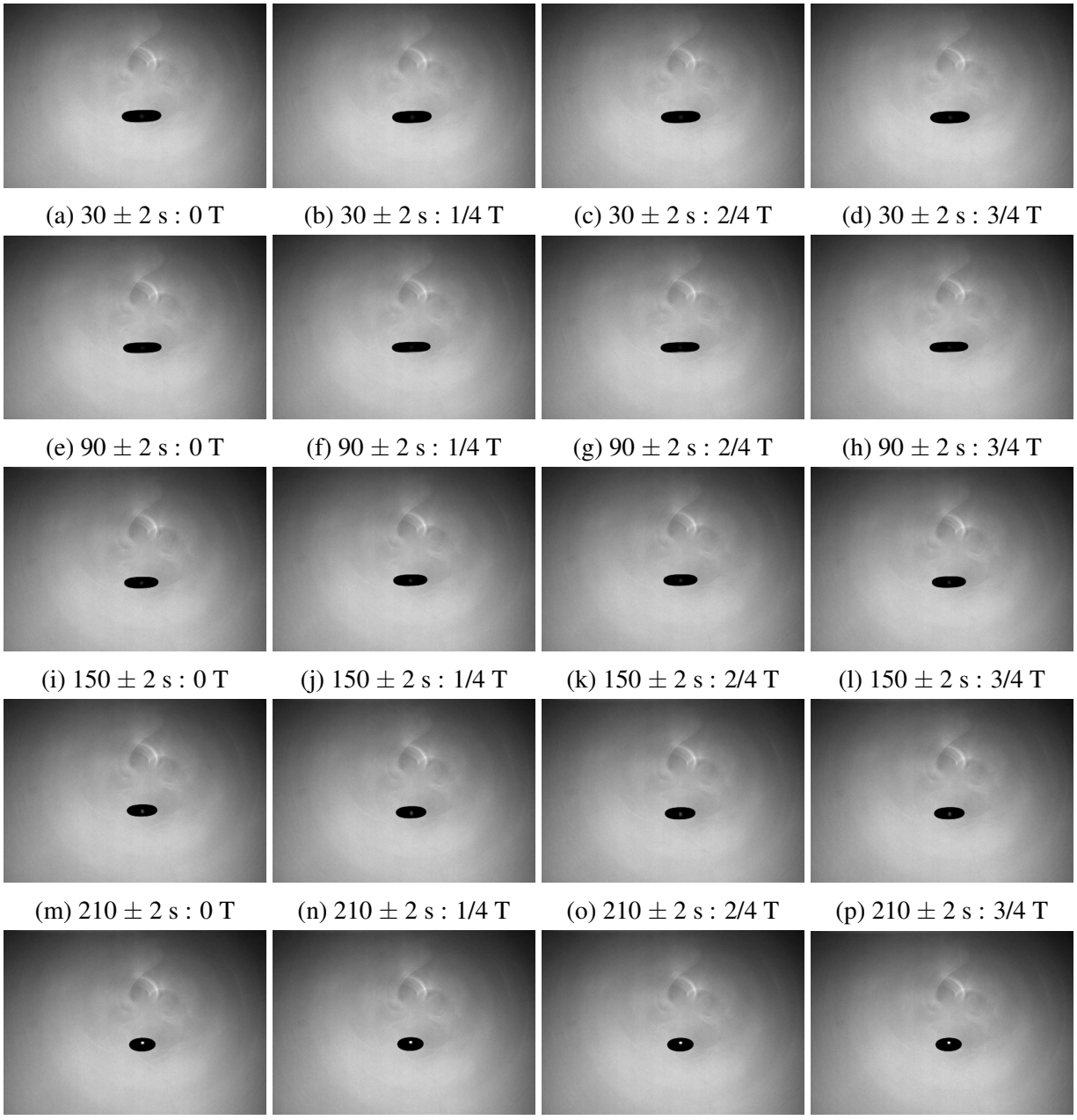

(a) 30 ± 2 s : 0 T (b) 30 ± 2 s : 1/4 T (c) 30 ± 2 s : 2/4 T (d) 30 ± 2 s : 3/4 T

(e) 90 ± 2 s : 0 T (f) 90 ± 2 s : 1/4 T (g) 90 ± 2 s : 2/4 T (h) 90 ± 2 s : 3/4 T

(i) 150 ± 2 s : 0 T (j) 150 ± 2 s : 1/4 T (k) 150 ± 2 s : 2/4 T (l) 150 ± 2 s : 3/4 T

(m) 210 ± 2 s : 0 T (n) 210 ± 2 s : 1/4 T (o) 210 ± 2 s : 2/4 T (p) 210 ± 2 s : 3/4 T

(q) 270 ± 2 s : 0 T (r) 270 ± 2 s : 1/4 T (s) 270 ± 2 s : 2/4 T (t) 270 ± 2 s : 3/4 T

Figure 7.24: The full vibration mode for levitated IPA droplets, where the shadowed region indicates section geometry, at 30 s, 90 s, 150 s, 210 s, and 270 s based on the Nitinol Langevin transducer, conducted at a set voltage of 56 $V_{P\text{-}P}$ and recorded by a HSI system.

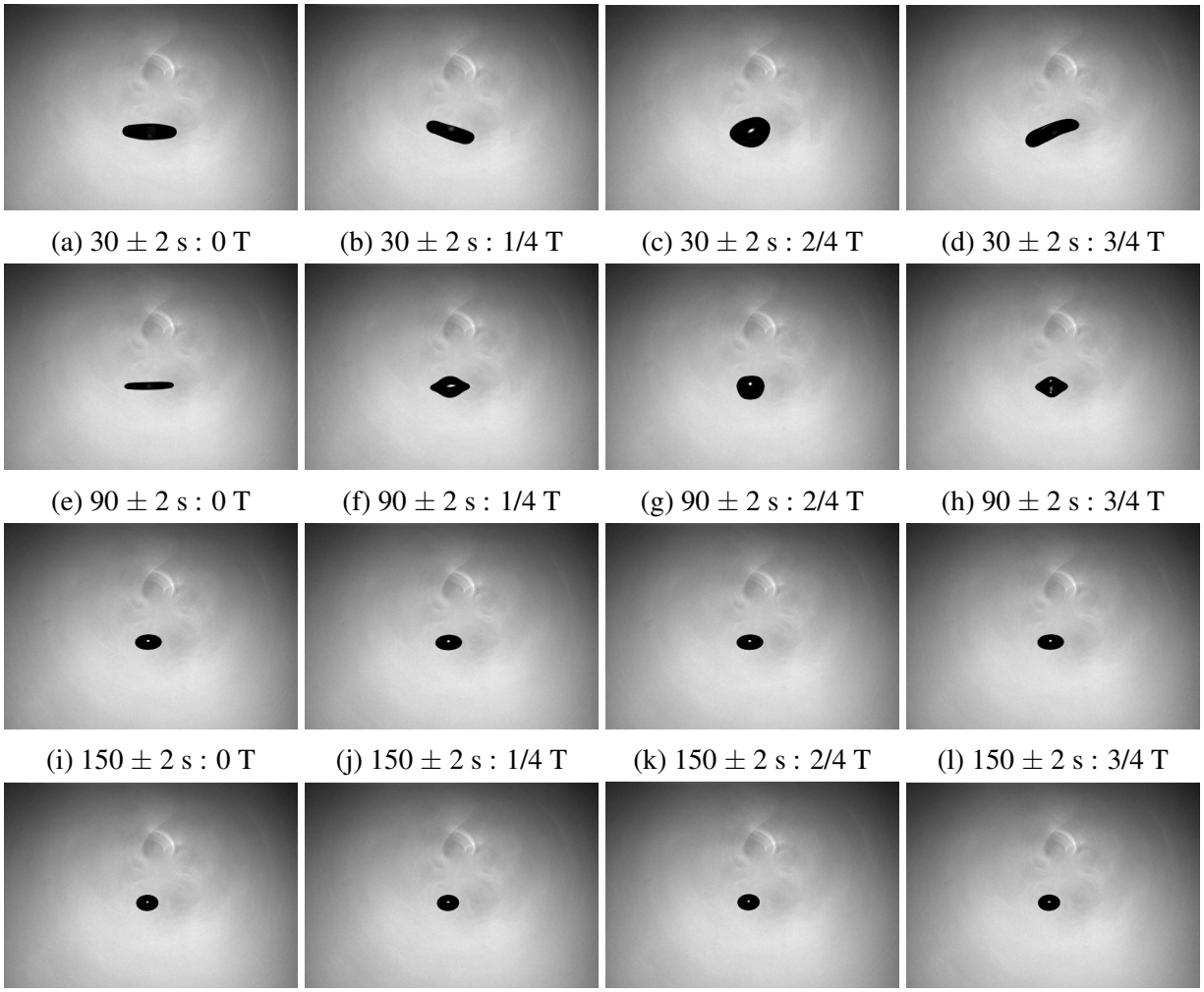

(a) 30 ± 2 s : 0 T (b) 30 ± 2 s : 1/4 T (c) 30 ± 2 s : 2/4 T (d) 30 ± 2 s : 3/4 T

(e) 90 ± 2 s : 0 T (f) 90 ± 2 s : 1/4 T (g) 90 ± 2 s : 2/4 T (h) 90 ± 2 s : 3/4 T

(i) 150 ± 2 s : 0 T (j) 150 ± 2 s : 1/4 T (k) 150 ± 2 s : 2/4 T (l) 150 ± 2 s : 3/4 T

(m) 210 ± 2 s : 0 T (n) 210 ± 2 s : 1/4 T (o) 210 ± 2 s : 2/4 T (p) 210 ± 2 s : 3/4 T

Figure 7.25: The full vibration mode for levitated acetone droplets, where the shadowed region indicates section geometry, at 30 s, 90 s, 150 s, 210 s, and 270 s based on the Nitinol Langevin transducer, conducted at a set voltage of 56 $V_{P\text{-}P}$ and recorded by a HSI system.

When the droplets are water, their geometry continuously changes regardless of the transducer used. This is likely due to the low viscosity of water, which makes it more susceptible to the effects of the acoustic field. In contrast, the geometry of the IPA droplets remained consistently stable throughout the tests. For the acetone droplets, the geometry fluctuated during the first 30 s before stabilising for the remainder of the experiment. One reason the droplets struggle to maintain their geometry and position is that introducing them to the acoustic field increases their kinetic energy due to the radiation pressure acting on them, pushing the droplets toward the node [281]. This results in an unstable state until they settle. It was observed that the droplets vibrated while their vibration modes changed over time. This can be attributed to alterations in the volume of the droplets due to evaporation and variations in transducer frequencies. To further investigate the dynamic behaviours of these droplets levitated by the Nitinol and titanium transducers, temporal variations in vertical position and section area of the droplets are analysed using OpenCV, as shown in Figures 7.26, 7.27 and 7.28.

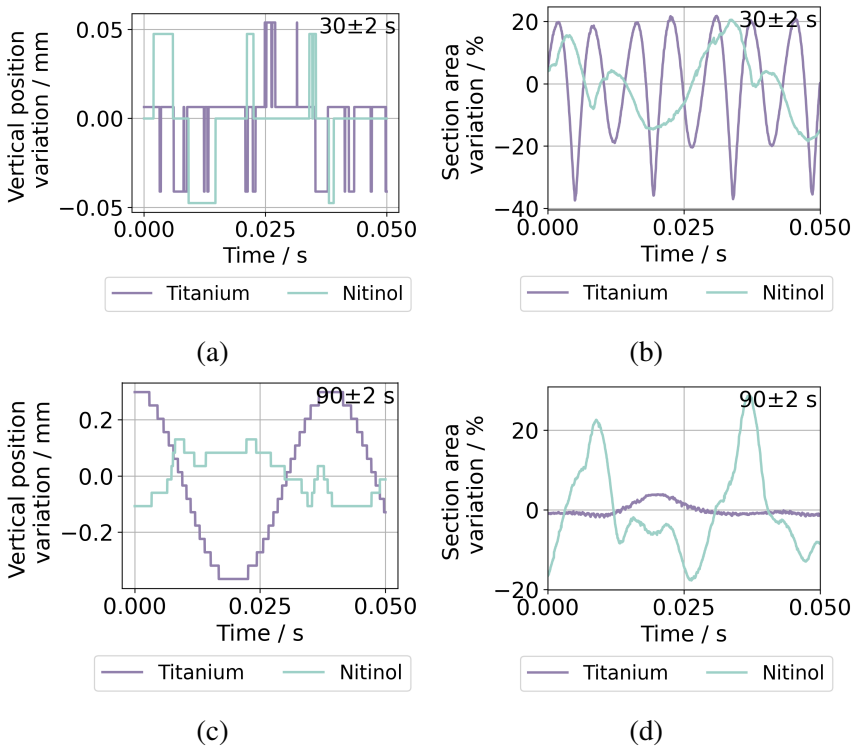

Figure 7.26: Temporal variations in vertical position and section area for water (a-d) at 30±2 s and 90±2 s intervals.

As shown in Figures 7.26, 7.27 and 7.28, the vertical position curves exhibit a stepped, discontinuous pattern due to minimal vertical displacement spanning only a few pixels, with each step representing one pixel in the captured video. At approximately 30 s, the Nitinol transducer demonstrates larger or comparable vertical displacements for water and acetone compared to the titanium transducer, while both maintain stable positions for IPA. This behaviour likely results from introducing droplets into the acoustic field, creating perturbations. The weaker acoustic

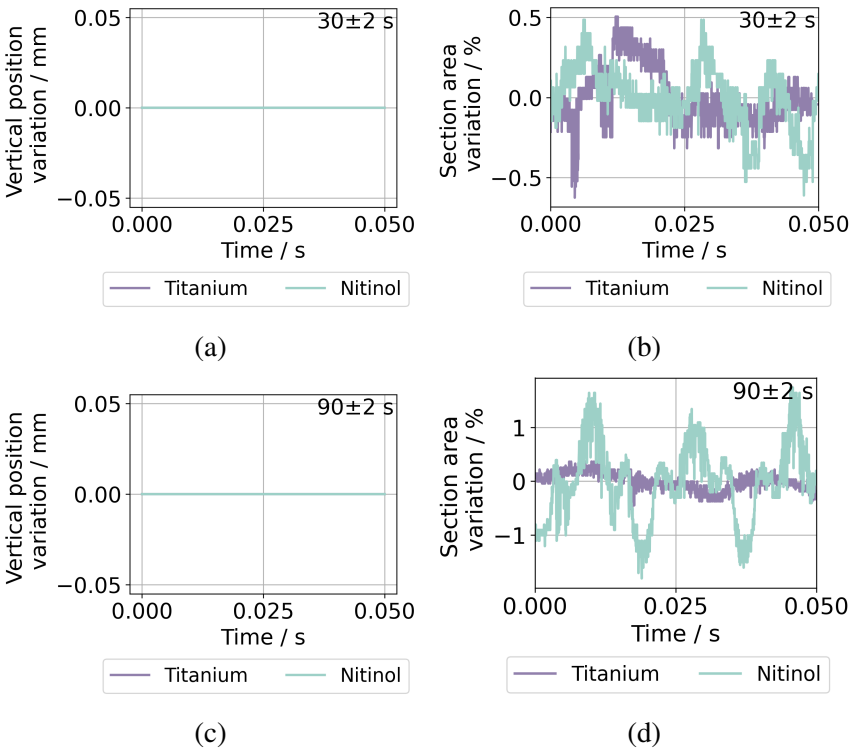

Figure 7.27: Temporal variations in vertical position and section area for IPA (a-d) at 30±2 s and 90±2 s intervals.

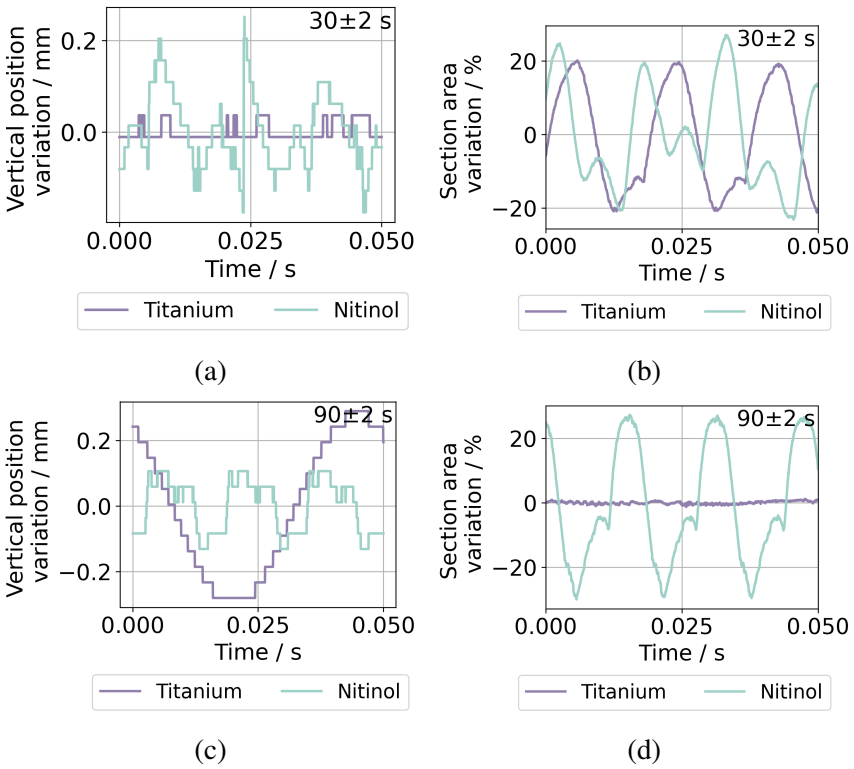

Figure 7.28: Temporal variations in vertical position and section area for acetone (a-d) at 30±2 s and 90±2 s intervals.

radiation of the Nitinol transducer, due to high electrical impedance, results in low resistance to these perturbations. Additionally, both transducers exhibit similar section area variations during this period. However, at 90 s, the Nitinol transducer outperforms the titanium transducer by reducing vertical displacements for both water and acetone droplets. Neither transducer shows measurable displacement for IPA droplets at this time point. Notably, while the Nitinol transducer maintains more stable vertical positions, it exhibits greater section area variations compared to the titanium transducer. These findings confirm that the stable resonance enhances levitation by reducing vertical displacements, though it does not necessarily produce more stable droplet geometry. This investigation discloses that the Nitinol transducer improves levitation duration through reduced temporal frequency variation, therefore extending the levitation duration, decreasing evaporation rates, and stabilising vertical displacement in acoustic levitation applications.

7.5 Summary

In this chapter, Nitinol was integrated into the cascaded transducer design to replicate the resonance stability observed in Chapter 5. The chapter details the design process for both Nitinol and titanium Langevin transducers equipped with an attached sonotrode, with dimensions optimised through FEA. Given that resonance in ultrasonic levitation is highly dependent on frequency, the dimensions of both transducers were tailored to vibrate at close resonant frequencies in their L2 mode. Manufactured components were assembled with optimal pre-stress values. After allowing the transducers to settle for a week, their dynamics at room temperature were characterised, including modal identification and harmonic analysis. The experimental findings were in good agreement with the simulation results. To validate the resonance stability of the Nitinol Langevin transducer, tests were conducted under self-heating conditions without any applied loads. In comparison to the frequency response of the titanium transducer, the Nitinol transducer exhibited high frequency stability over time, while the frequency of the titanium transducer decreased almost linearly.

A reflector was designed and manufactured to create the levitation system, featuring a concave surface that reflects ultrasonic waves emitted from the transducer, thereby generating standing waves. Water, IPA, and acetone were used in the levitation experiments to investigate the resonance stability of droplet behaviour in the acoustic field. Preliminary tests indicated that the Nitinol transducer maintained stable frequencies under load, with droplet volumes around 10 μL. Each liquid was levitated three times to observe evaporation over time. The results indicated that the Nitinol transducer resulted in longer levitation times for water and acetone and lower evaporation rates for IPA and acetone. This can be attributed to the interaction between droplet properties, such as surface tension and viscosity, and the frequency of the transmitted transducer waves. The stable frequency of the Nitinol transducer likely contributes to a steady standing

wave field, which helps maintain consistent radiation pressure on the droplets. In contrast, the frequency decrease observed with the titanium transducer led to an unstable field, resulting in shorter levitation times. Furthermore, a HSI examined the droplet geometry during levitation with both transducers. The results demonstrated that the titanium transducer produces more stable droplet geometry than the Nitinol transducer. This is likely due to the relatively lower electrical impedance of the titanium transducer, which generates a generally higher radiation force, thus reducing variation in droplet geometry.

Chapter 8

Conclusions

This thesis presents the design, fabrication, and characterisation of Langevin transducers integrated with Nitinol, a shape memory alloy. Driven by practical devices that require adaptive operation, the thesis targets resonance tuning. It explores and develops tuneable designs and establishes correlations between resonance behaviour and Nitinol's temperature dependent properties. The experimental results demonstrated that integrating Nitinol enabled controllable tuning of fundamental resonance parameters, including resonant frequency and electrical impedance. These tuneable dynamics were observed in the forms of resonance tuneability, modal coupling, and resonance stability, with the latter two appearing as variants of tuneable resonance.

Several prototype transducers were developed, featuring varying configurations and Nitinol transformation behaviours. The design process incorporated mathematical modelling to simulate the dynamic responses of the transducers. A 1D transducer model based on the Timoshenko-Ehrenfest beam theory was constructed within a linear piezoelectric framework. This approach offered computational efficiency over full 3D finite element models, such as those implemented in Abaqus FEA. It did not require a complete set of material properties in a 3D domain, an advantage when extending it to a thermo-electro-mechanical model for Nitinol Langevin transducers, where temperature-dependent properties for both Nitinol and PZT are challenging. However, the accuracy of the 1D model declined significantly when the L/D ratio exceeded 12.5 due to limitations in considering complex geometries and cross-sectional variations. Consequently, a 3D electromechanical model was employed by using Abaqus. The development of these models significantly enhanced the author's understanding of the interplay between solid mechanics and transducer dynamics, laying the groundwork for future temperature-dependent and nonlinear modelling of Nitinol-based ultrasonic devices.

The fabrication of prototypes followed established procedures for conventional Langevin transducers, except for the Nitinol component. EDM was employed to machine the Nitinol elements due to its ability to provide high quality surface finish and minimal thermal input. The prototypes were validated statically through EIA and LDV, confirming their resonant frequencies, mode shapes, and electrical impedance characteristics under pre-stress at room tempera-

ture. Given the difficulty of experimentally measuring the temperature and pressure dependent properties of Nitinol, a reverse optimisation was applied using FEA to approximate these properties. However, the accuracy of this method remains limited by uncertainties in the properties of other transducer components. Therefore, a model with known material properties under conditions representative of those within a Langevin transducer is preferred to simulate resonance behaviours.

Thermal loading was experimentally applied to the prototypes under both isothermal and self-heating conditions. EIA results confirmed that the Nitinol-integrated Langevin transducers could tune their resonance characteristics in response to temperature. Resonance tuneability, modal coupling, and resonance stability were observed in relation to the distance to nodal position and volume fraction of Nitinol, which FEA validated in Chapter 6. The likely reason for resonance tuneability is the increase in Nitinol moduli due to the phase transformation that overwhelms the properties changes of PZT on the transducer resonances, showing opposite frequency shifting to conventional Langevin transducers. Modal coupling experiments revealed temperature-dependent frequency shifts in multiple vibration modes, with two adjacent OP modes becoming coupled at low temperatures (around -25°C). This phenomenon indicates that the phase transformations of Nitinol influence vibration modes in different ways. Certainly, further investigation is required to increase its effective operating temperature near room temperature so that it can be applied to typical applications such as ultrasonic motors. Resonance stability was observed under both thermal loading conditions, though the underlying mechanisms differed: under isothermal conditions, martensitic transformation appeared to counterbalance the temperature-induced frequency variation of the PZT elements, while under self-heating conditions, the stable resonance was attributed to the intrinsic temperature-dependent properties of Nitinol in its austenitic phase. These findings suggest that resonance behaviours of a Langevin transducer can be actively controlled by incorporating shape memory alloys, achieving multi-frequency and tuneable ultrasonic devices to adapt to changing environments.

A Nitinol prototype was fabricated with a more complex configuration and an alternative piezoelectric material to investigate the repeatability of stable resonance under self-heating and apply it to applications. This prototype was integrated into an acoustic levitation system, where frequency stability is essential for maintaining consistent droplet geometry and reducing evaporation rate. Compared to a conventional Langevin transducer of similar design and frequency, the Nitinol-integrated transducer exhibited superior resonance stability during continuous operation. As a result, lower evaporation rates and longer levitation durations were achieved for various liquids, including water, acetone, and IPA. This application of the developed prototype in levitation demonstrates the practical potential of Nitinol-based Langevin transducers, opening avenues for further research and application in areas requiring adaptive ultrasonic actuation.

Chapter 9

Future Research Directions

In addition to the work presented in this thesis, several directions for future studies are briefly outlined in the following sections.

9.1 Material Characterisation and Manufacturing

Despite some attempts to characterise Nitinol properties at various temperatures, there are challenges associated with material characterisation, which will be addressed in future studies. Firstly, it is essential to measure the stress-strain relationship of Nitinol in isothermal and isobaric environments. This data validates whether the phase transformation from an austenitic phase to a de-twinned martensitic phase happens during the pre-stress process, in which the temperature-dependent elastic moduli also facilitate an accurate finite element model. Moreover, phase transformation behaviours have to be monitored under cyclic thermal loading, as well-documented in the literature [66]. This knowledge helps in evaluating the longevity of a Nitinol Langevin transducer.

Recalling the work hardening experienced in manufacturing Nitinol, EDM is a proven method. Alternatively, additive manufacturing for Nitinol can reduce the machining effort needed for segments, allowing for more intricate geometries. The feasibility of this method has been reported in the literature [221]. However, one downside may be encountered is a low elastic modulus for the final printed product and imperfections in the microstructures.

9.2 Mathematical Modelling

Mathematical models developed in this thesis are based on linear piezoelectricity. However, temperature triggers the phase transformation of Nitinol Langevin transducers, and consequently, tuneable resonance. An electromechanical model alone cannot accurately simulate this tuneable resonance with temperature. Therefore, the temperature field will be implemented into future developed models. A semi-coupled thermo-electro-mechanical model will be utilised to simulate

the resonance tuneability, modal coupling, and resonance stability in isothermal environments. In contrast, a fully coupled model, considering heat transfer, will simulate stable resonance under self-heating conditions. Future models will include damping parameters such as mechanical, coupling, and dielectric damping, which will enable a more accurate simulation of the losses in the designed transducers. The implementation of this model for the Nitinol Langevin transducer follows the complete material characterisations discussed in the previous section.

9.3 Optimisation of Transducer Configuration

As discussed in Chapter 6, the volume fraction and position of Nitinol influence the tuneablity of the transducer from a linear elasticity perspective. This indicates that the tuneability can be engineered to its maximum. While the theoretical maximum frequency variation ratio exceeds 30%, as shown in Table 6.4, the tuneable transducer described in Section 4.1 achieves frequency tunings of approximately 15% and 10% in modes L1 and L3, respectively. Indeed, configuration is one of the factors that defines tuneability, and can be optimised by adjusting the dimensional parameters of the transducer. For example, a Langevin transducer can be modified by varying diameters across the structure to make typical positions more sensitive to stiffness. When strategically placing Nitinol at these key positions while maximising its volume fraction, the tuneability is potentially enhanced. Moreover, the configuration can be tailored to accommodate other vibration modes in addition to longitudinal ones, such as torsional and bending modes. Different levels of tuneability will be observed, as demonstrated in Section 4.3, where it is manifested that various modes respond differently to martensitic transformation.

9.4 Applications under Isothermal Conditions

In Chapter 7, the Nitinol Langevin transducer was operated under self-heating conditions and stable resonance was observed. In this scenario, the temperature of the Nitinol middle mass did not increase prominently and remained consistently lower than that of the PZT stacks. As a result, the property changes of Nitinol with temperature were limited and insufficient to trigger martensitic transformation. In order to leverage phase transformation for applications, a wider temperature range is necessary so that an external facility, like a mini oven, is designed to apply thermal loading to the Nitinol segment. This controlled facility creates isothermal environments, thus allowing resonance tuneability and model coupling to be achieved. However, due to self-heating during operation, temperature interplays between Nitinol and PZT segments increase the complexity of transducer dynamics. Therefore, positioning the Nitinol segment away from the PZT elements to mitigate this phenomenon is suggested.

9.5 Exploration of Alternative Smart Materials

Finally, this research focused on Nitinol, however, alternative SMAs are candidates and could offer enhanced or tailored tuneable resonances. For example, Cu-based shape memory alloys have sharp martensitic phase transformations, meaning that the transducer does not require a wide temperature range to trigger martensitic transformations. Also, the low cost and favourable machinability of Fe-based SMAs can significantly improve the manufacturing process for integrating SMAs into a Langevin transducer.

Appendix A

Material Properties for Simulations

This appendix provides the material properties of the materials used in this thesis, including isotropic and piezoelectric materials.

A.1 Isotropic Materials

Table A.1: Material properties of isotropic materials used in this thesis.

Materials	Elastic modulus (E / GPa)	Poisson's ratio (ν)	Density (ρ / (kg/m^3))
Stainless steel (304)	210	0.3	7800
Ti6Al4V	116	0.32	4506
Aluminium alloy (6082)	70	0.35	2700
Copper	115	0.31	8942

A.2 Piezoelectric Materials

A.2.1 PZ26

Stiffness Matrix

$$\begin{aligned}\mathbb{C} &\equiv \begin{bmatrix} C_{11} & C_{12} & C_{13} & 0 & 0 & 0 \\ C_{12} & C_{11} & C_{13} & 0 & 0 & 0 \\ C_{13} & C_{13} & C_{33} & 0 & 0 & 0 \\ 0 & 0 & 0 & C_{44} & 0 & 0 \\ 0 & 0 & 0 & 0 & C_{44} & 0 \\ 0 & 0 & 0 & 0 & 0 & C_{66} \end{bmatrix} \\ &= \begin{bmatrix} 1.68\text{E}11 & 1.10\text{E}11 & 9.99\text{E}10 & 0 & 0 & 0 \\ 1.10\text{E}11 & 1.68\text{E}11 & 9.99\text{E}10 & 0 & 0 & 0 \\ 9.99\text{E}10 & 9.99\text{E}10 & 1.23\text{E}11 & 0 & 0 & 0 \\ 0 & 0 & 0 & 3.01\text{E}10 & 0 & 0 \\ 0 & 0 & 0 & 0 & 3.01\text{E}10 & 0 \\ 0 & 0 & 0 & 0 & 0 & 2.88\text{E}10 \end{bmatrix}\end{aligned} \tag{A.1}$$

Piezoelectric Matrix

$$\begin{aligned}\mathbf{e} &\equiv \begin{bmatrix} 0 & 0 & 0 & 0 & e_{15} & 0 \\ 0 & 0 & 0 & e_{15} & 0 & 0 \\ e_{31} & e_{31} & e_{33} & 0 & 0 & 0 \end{bmatrix} \\ &= \begin{bmatrix} 0 & 0 & 0 & 0 & 9.86 & 0 \\ 0 & 0 & 0 & 9.86 & 0 & 0 \\ -2.8 & -2.8 & 14.7 & 0 & 0 & 0 \end{bmatrix}\end{aligned} \tag{A.2}$$

Permittivity Matrix

$$\begin{aligned}\chi &\equiv \begin{bmatrix} \chi_{11} & 0 & 0 \\ 0 & \chi_{11} & 0 \\ 0 & 0 & \chi_{33} \end{bmatrix} \\ &= \begin{bmatrix} 7.3312\text{E}-9 & 0 & 0 \\ 0 & 7.3312\text{E}-9 & 0 \\ 0 & 0 & 6.1979\text{E}-9 \end{bmatrix}\end{aligned} \tag{A.3}$$

A.2.2 PIC181

Stiffness Matrix

$$\mathbb{C} \equiv \begin{bmatrix} C_{11} & C_{12} & C_{13} & 0 & 0 & 0 \\ C_{12} & C_{11} & C_{13} & 0 & 0 & 0 \\ C_{13} & C_{13} & C_{33} & 0 & 0 & 0 \\ 0 & 0 & 0 & C_{44} & 0 & 0 \\ 0 & 0 & 0 & 0 & C_{44} & 0 \\ 0 & 0 & 0 & 0 & 0 & C_{66} \end{bmatrix}$$
$$= \begin{bmatrix} 1.37\text{E}11 & 7.44\text{E}10 & 7.21\text{E}10 & 0 & 0 & 0 \\ 7.44\text{E}10 & 1.37\text{E}11 & 7.21\text{E}10 & 0 & 0 & 0 \\ 7.21\text{E}10 & 7.21\text{E}10 & 1.24\text{E}11 & 0 & 0 & 0 \\ 0 & 0 & 0 & 2.80\text{E}10 & 0 & 0 \\ 0 & 0 & 0 & 0 & 2.80\text{E}10 & 0 \\ 0 & 0 & 0 & 0 & 0 & 3.16\text{E}10 \end{bmatrix} \tag{A.4}$$

Piezoelectric Matrix

$$\mathbf{e} \equiv \begin{bmatrix} 0 & 0 & 0 & 0 & e_{15} & 0 \\ 0 & 0 & 0 & e_{15} & 0 & 0 \\ e_{31} & e_{31} & e_{33} & 0 & 0 & 0 \end{bmatrix}$$
$$= \begin{bmatrix} 0 & 0 & 0 & 0 & 13.3262 & 0 \\ 0 & 0 & 0 & 13.3262 & 0 & 0 \\ -6.3441 & -6.3441 & 15.6108 & 0 & 0 & 0 \end{bmatrix} \tag{A.5}$$

Permittivity Matrix

$$\chi \equiv \begin{bmatrix} \chi_{11} & 0 & 0 \\ 0 & \chi_{11} & 0 \\ 0 & 0 & \chi_{33} \end{bmatrix}$$
$$= \begin{bmatrix} 1.3281\text{E}-8 & 0 & 0 \\ 0 & 1.3281\text{E}-8 & 0 \\ 0 & 0 & 1.0625\text{E}-8 \end{bmatrix} \tag{A.6}$$

Appendix B

Harmonic Analysis under Isothermal Conditions

This appendix provides harmonic analysis results under isothermal conditions for the Nitinol Langevin transducer studied in Chapter 4. The vibration amplitude and impedance responses with respect to frequency demonstrate the tuneability of the transducer with temperature.

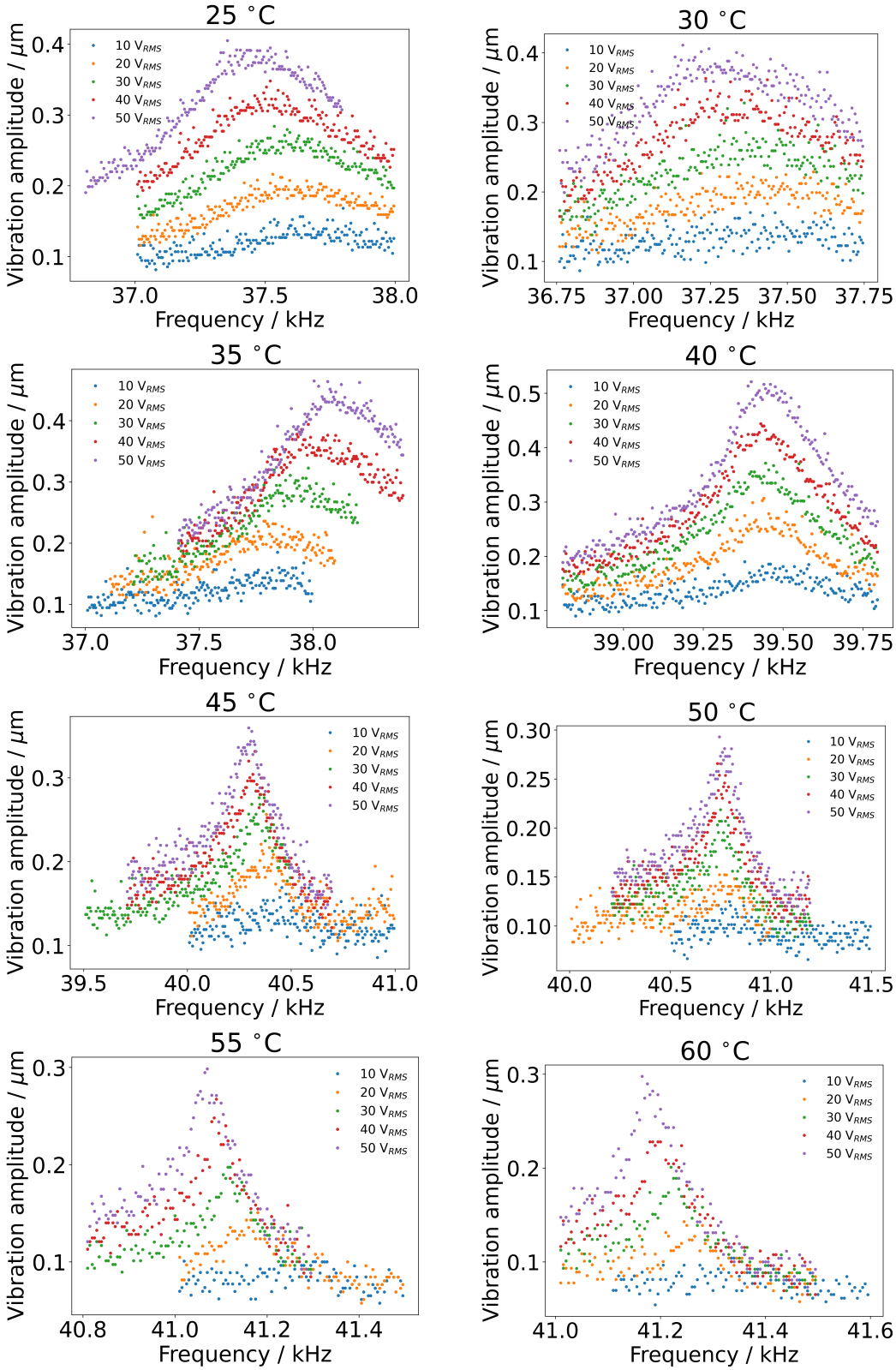

Figure B.1: Vibration amplitude spectra of the L3 mode for the Nitinol Langevin transducer under static temperatures within a 25°C to 60°C temperature window with applied voltages of 10 V_{RMS} to 50 V_{RMS}.

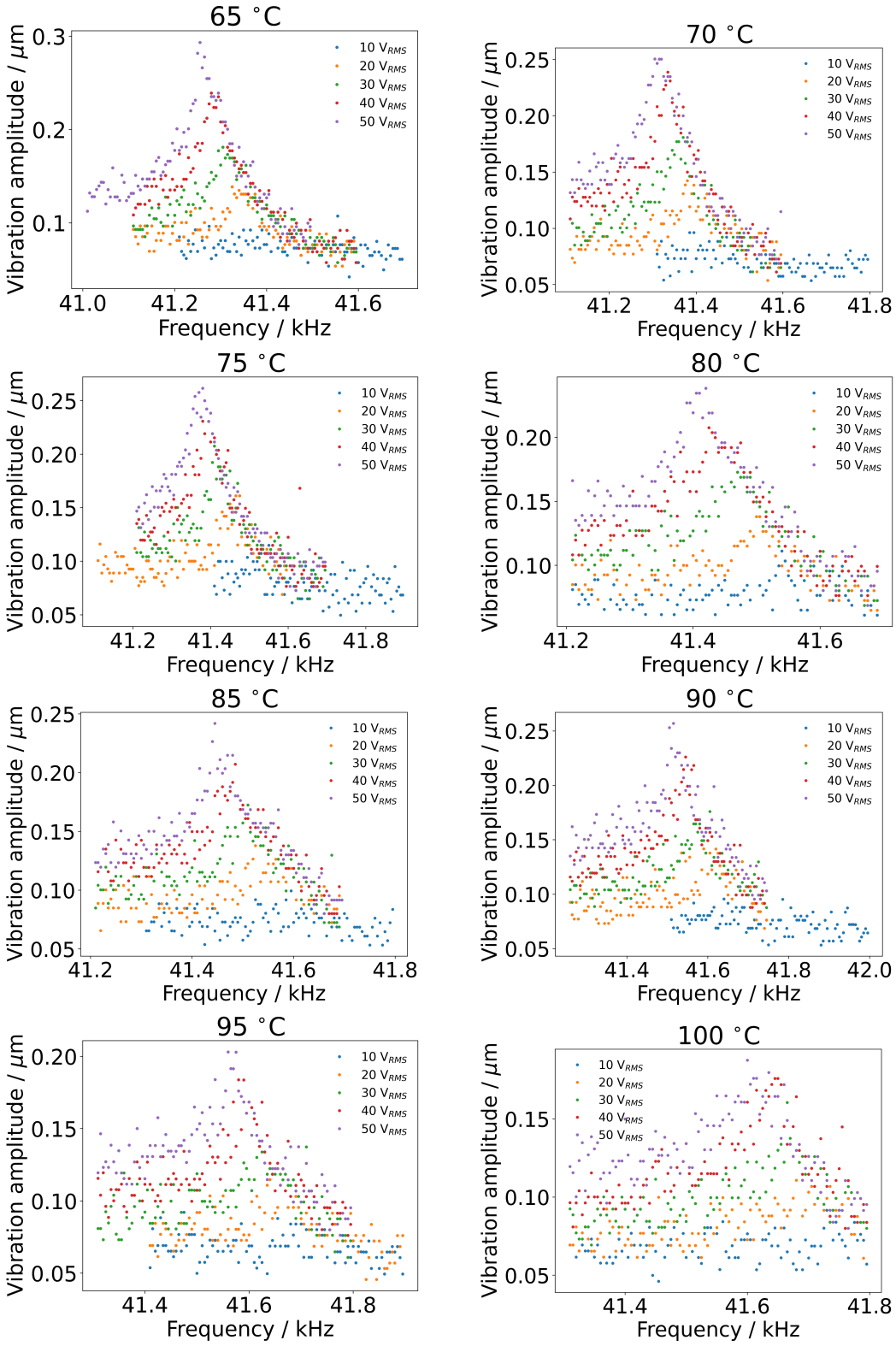

Figure B.2: Vibration amplitude spectra of the L3 mode for the Nitinol Langevin transducer under static temperatures within a 65°C to 100°C temperature window with applied voltages of 10 V_{RMS} to 50 V_{RMS}.

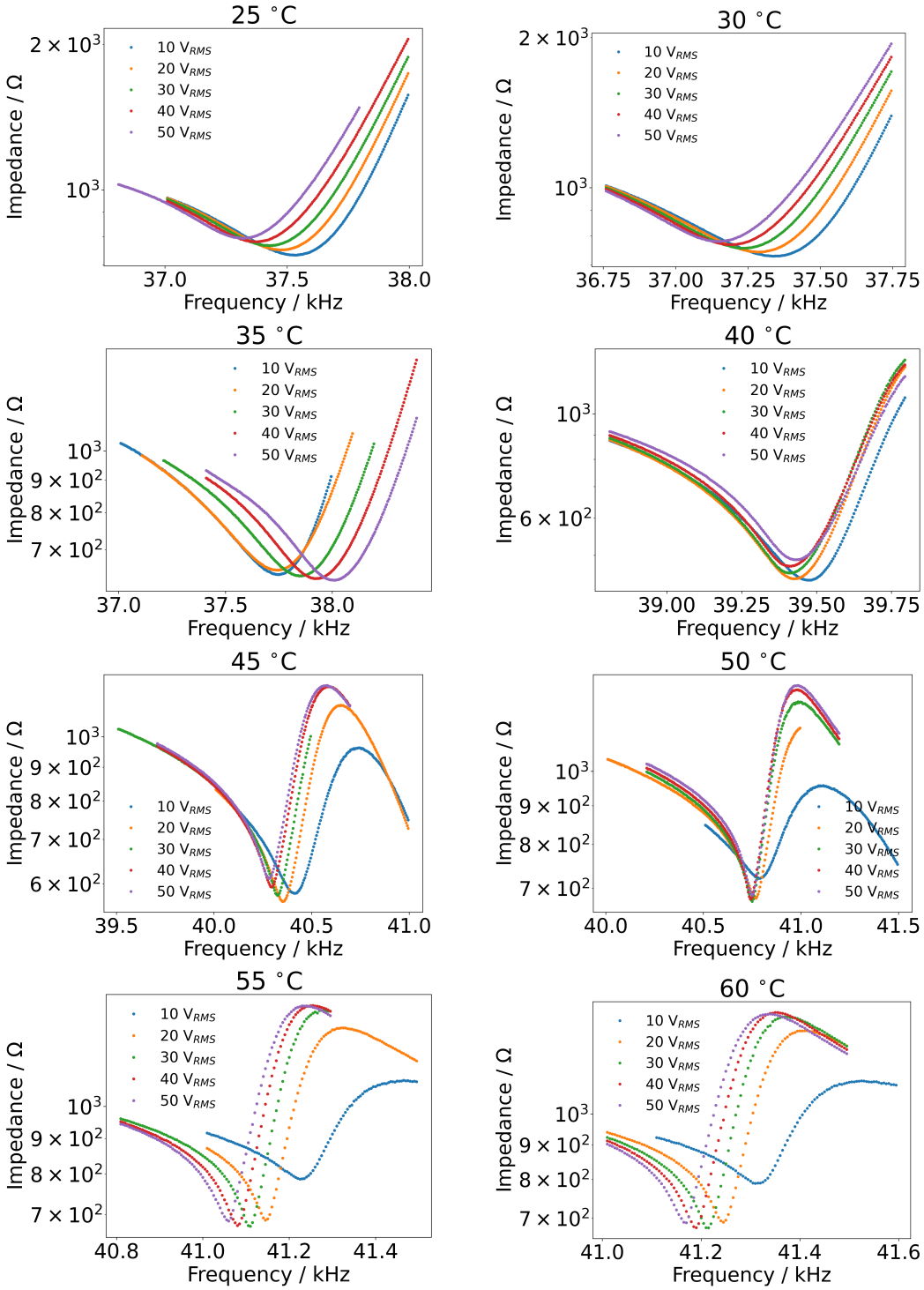

Figure B.3: Impedance spectra of the L3 mode for the Nitinol Langevin transducer under static temperatures within a 25°C to 60°C temperature window with applied voltages of 10 V_{RMS} to 50 V_{RMS}.

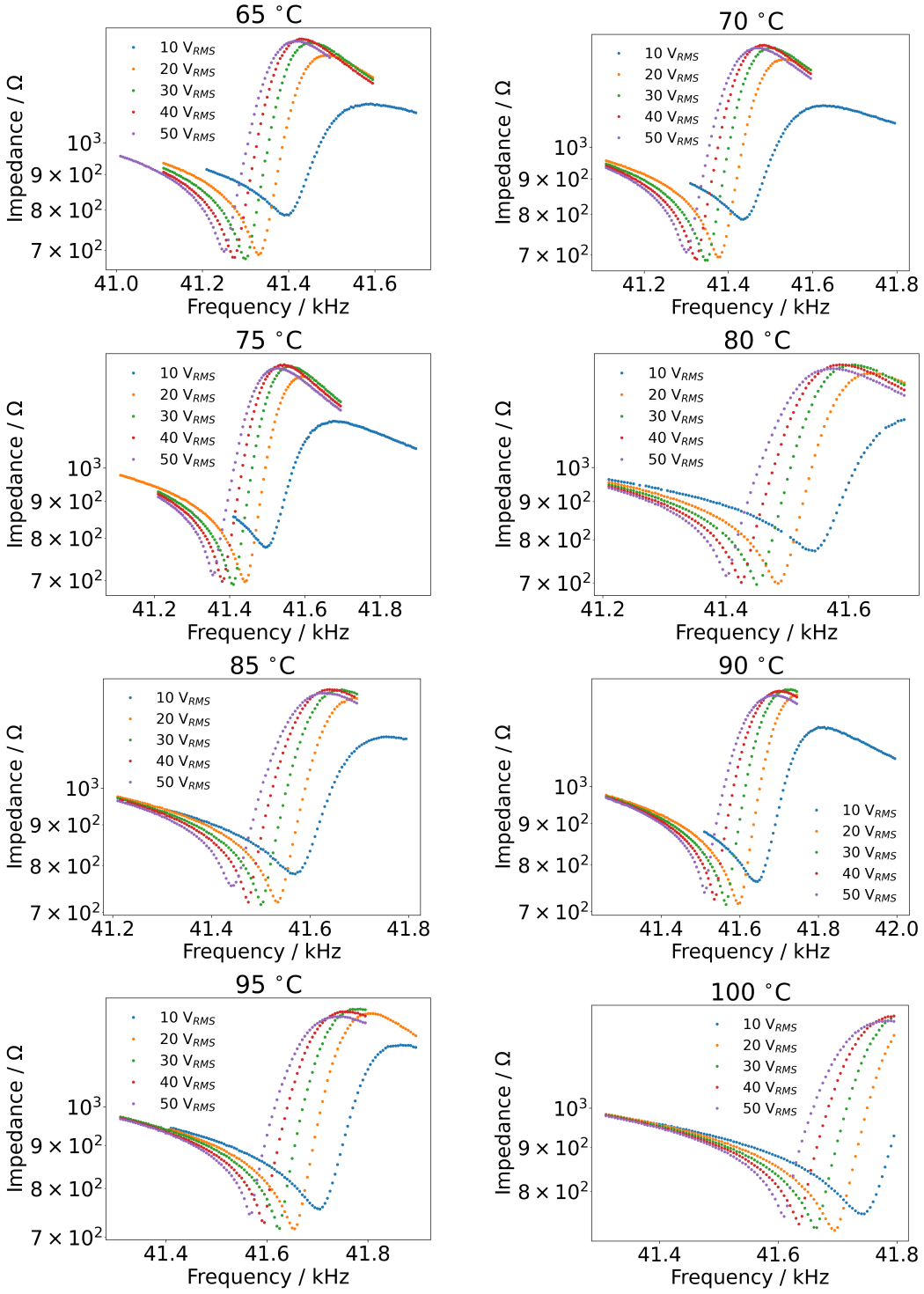

Figure B.4: Impedance spectra of the L3 mode for the Nitinol Langevin transducer under static temperatures within a 65°C to 100°C temperature window with applied voltages of 10 V_{RMS} to 50 V_{RMS}.

Appendix C

3D Models for Stable Resonance

This appendix provides the vibration mode shape and electric potential of the Nitinol Langevin transducer studied in Chapter 4. The modal information has been simulated using the proposed 3D electromechanical model, which applies a free-short boundary condition. The frequency input of the single-frequency analysis used in the simulations is derived from Abaqus results.

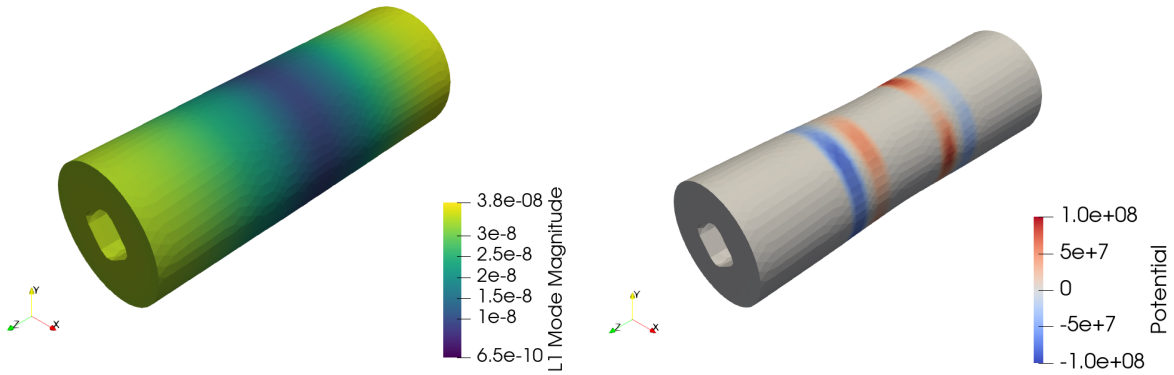

(a) (b)

Figure C.1: (a) Mode shape and (b) electric potential of the L1 mode for the NMCT in the heating cycle at 28.769 kHz under free-short boundary condition.

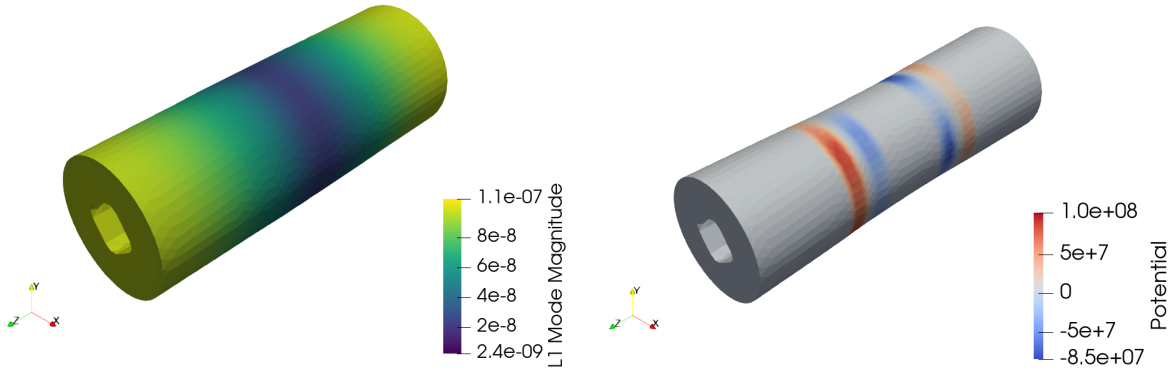

(a) (b)

Figure C.2: (a) Mode shape and (b) electric potential of the L1 mode for the NMCT in the cooling cycle at 29.642 kHz under free-short boundary condition.

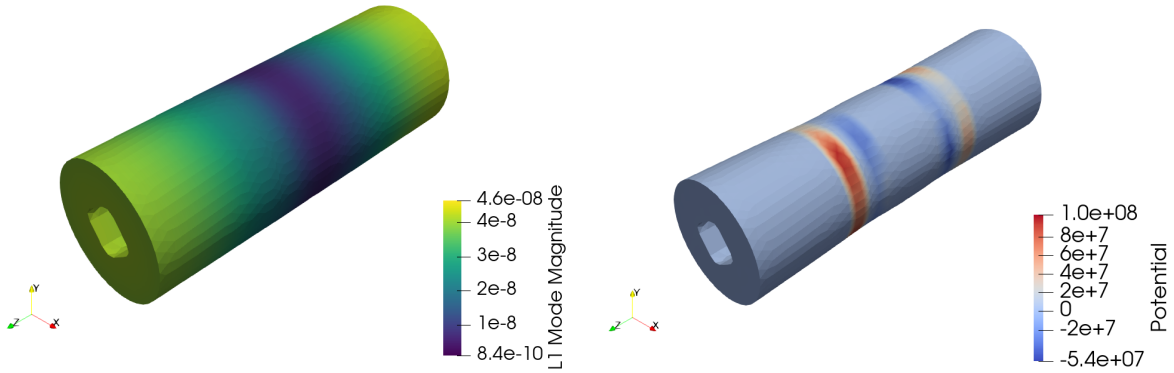

(a) (b)

Figure C.3: (a) Mode shape and (b) electric potential of the L1 mode for the TMCT at 31.363 kHz under free-short boundary condition.

Appendix D

High-Speed Imaging

This appendix provides the HSI results for droplets levitated by the titanium Langevin transducer discussed in Chapter 7. Water, IPA, and acetone have been utilised, and their geometric sections have been recorded over time.

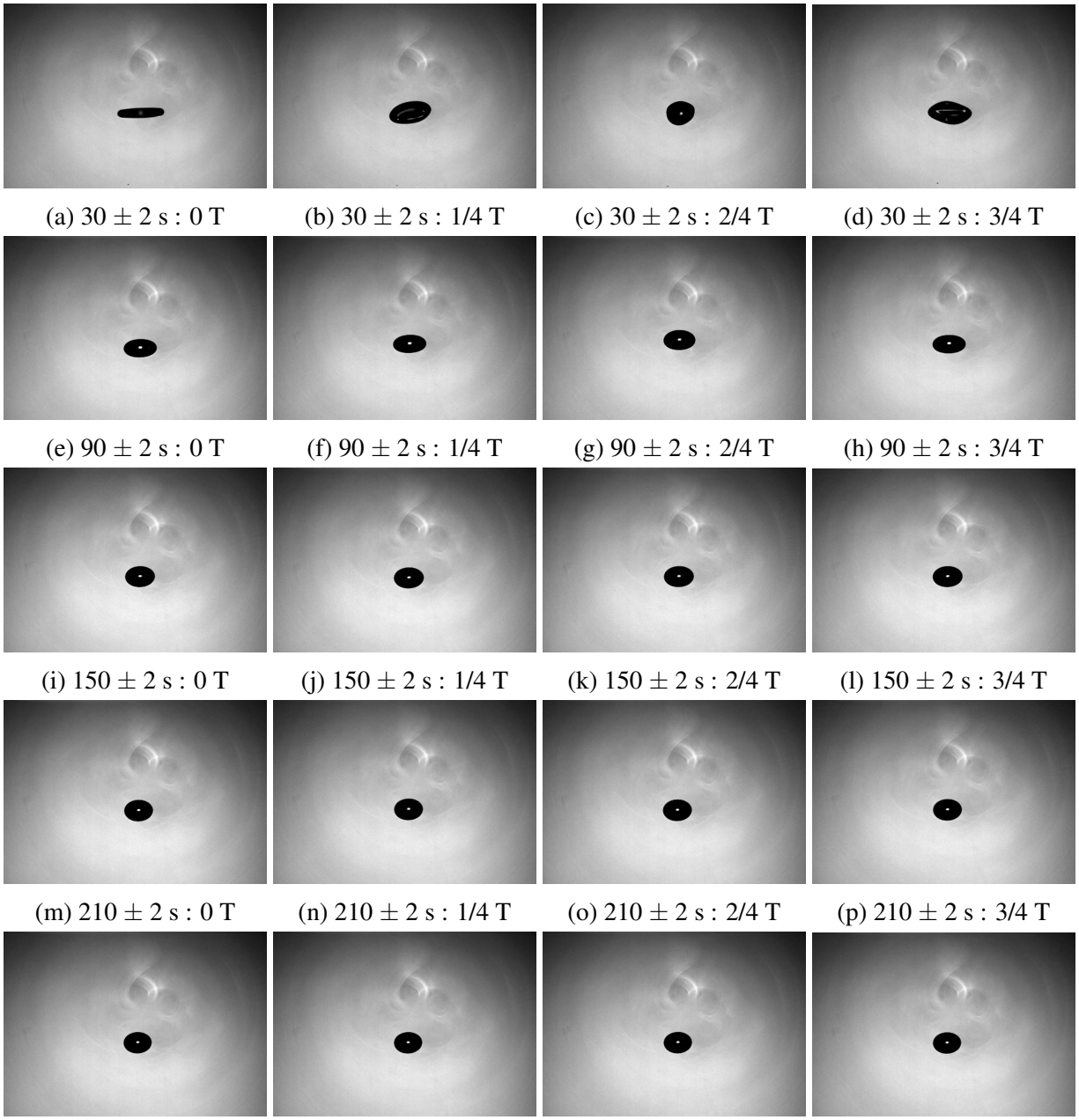

(a) 30 ± 2 s : 0 T (b) 30 ± 2 s : 1/4 T (c) 30 ± 2 s : 2/4 T (d) 30 ± 2 s : 3/4 T

(e) 90 ± 2 s : 0 T (f) 90 ± 2 s : 1/4 T (g) 90 ± 2 s : 2/4 T (h) 90 ± 2 s : 3/4 T

(i) 150 ± 2 s : 0 T (j) 150 ± 2 s : 1/4 T (k) 150 ± 2 s : 2/4 T (l) 150 ± 2 s : 3/4 T

(m) 210 ± 2 s : 0 T (n) 210 ± 2 s : 1/4 T (o) 210 ± 2 s : 2/4 T (p) 210 ± 2 s : 3/4 T

(q) 270 ± 2 s : 0 T (r) 270 ± 2 s : 1/4 T (s) 270 ± 2 s : 2/4 T (t) 270 ± 2 s : 3/4 T

Figure D.1: The full vibration mode for levitated water droplets, where the shadowed region indicates section geometry, at 30 s, 90 s, 150 s, 210 s, and 270 s based on the titanium Langevin transducer, conducted at a set voltage of 56 $V_{P\text{-}P}$ and recorded by a HSI system.

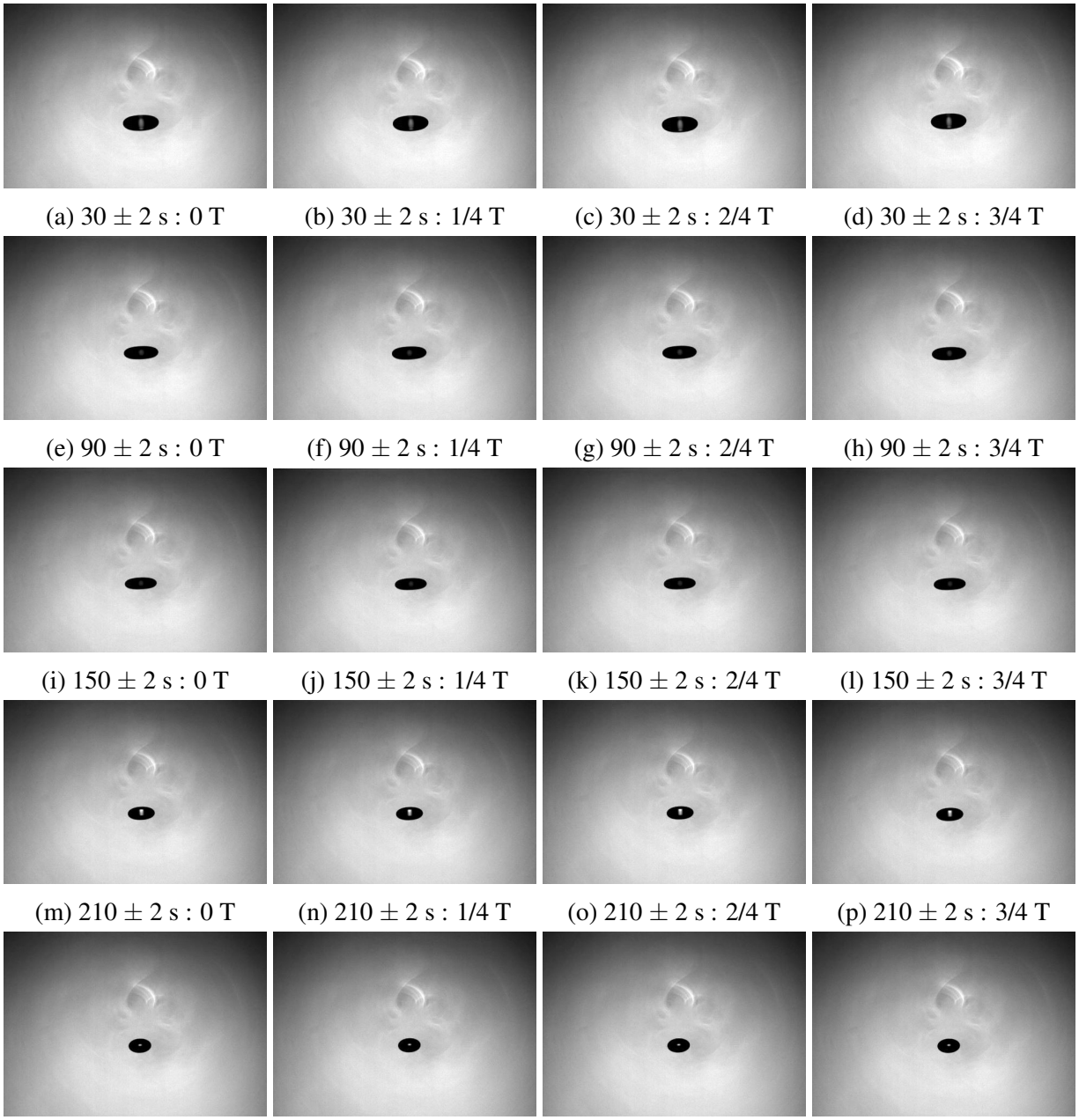

(a) 30 ± 2 s : 0 T (b) 30 ± 2 s : 1/4 T (c) 30 ± 2 s : 2/4 T (d) 30 ± 2 s : 3/4 T

(e) 90 ± 2 s : 0 T (f) 90 ± 2 s : 1/4 T (g) 90 ± 2 s : 2/4 T (h) 90 ± 2 s : 3/4 T

(i) 150 ± 2 s : 0 T (j) 150 ± 2 s : 1/4 T (k) 150 ± 2 s : 2/4 T (l) 150 ± 2 s : 3/4 T

(m) 210 ± 2 s : 0 T (n) 210 ± 2 s : 1/4 T (o) 210 ± 2 s : 2/4 T (p) 210 ± 2 s : 3/4 T

(q) 270 ± 2 s : 0 T (r) 270 ± 2 s : 1/4 T (s) 270 ± 2 s : 2/4 T (t) 270 ± 2 s : 3/4 T

Figure D.2: The full vibration mode for levitated IPA droplets, where the shadowed region indicates section geometry, at 30 s, 90 s, 150 s, 210 s, and 270 s based on the titanium Langevin transducer, conducted at a set voltage of 56 $V_{P\text{-}P}$ and recorded by a HSI system.

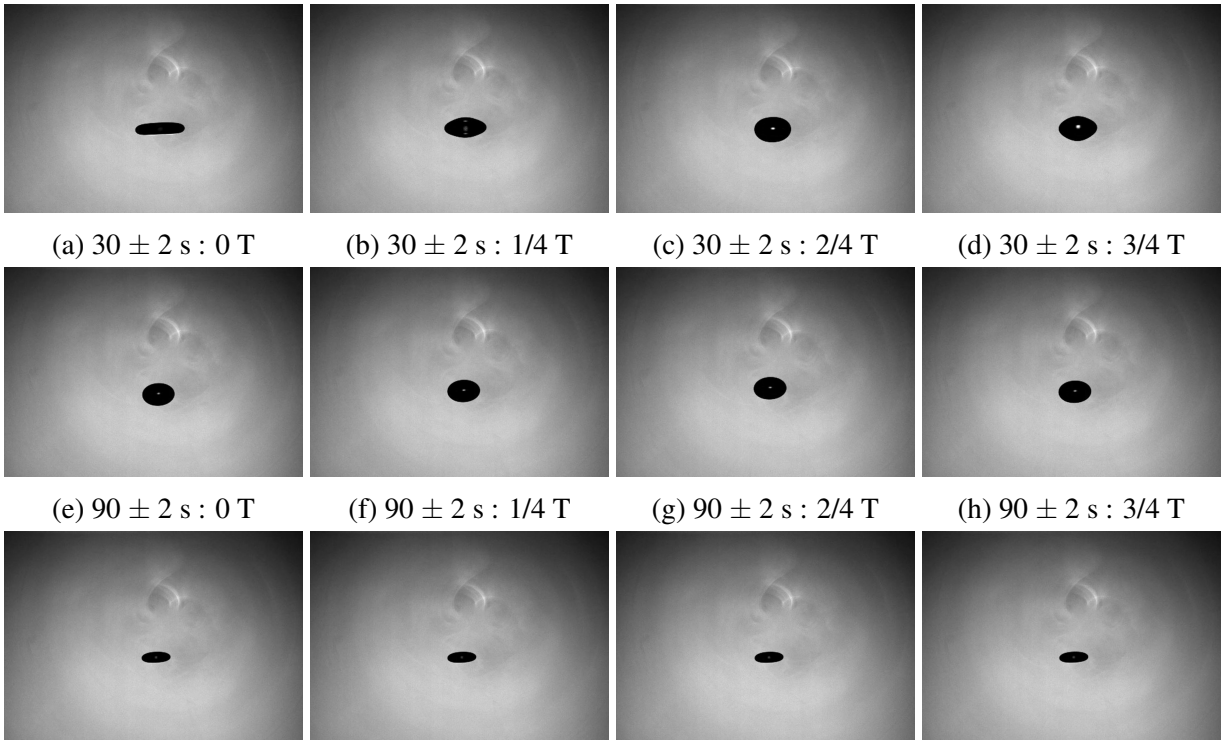

(a) 30 ± 2 s : 0 T (b) 30 ± 2 s : 1/4 T (c) 30 ± 2 s : 2/4 T (d) 30 ± 2 s : 3/4 T

(e) 90 ± 2 s : 0 T (f) 90 ± 2 s : 1/4 T (g) 90 ± 2 s : 2/4 T (h) 90 ± 2 s : 3/4 T

(i) 150 ± 2 s : 0 T (j) 150 ± 2 s : 1/4 T (k) 150 ± 2 s : 2/4 T (l) 150 ± 2 s : 3/4 T

Figure D.3: The full vibration mode for levitated acetone droplets, where the shadowed region indicates section geometry, at 30 s, 90 s, and 150 s based on the titanium Langevin transducer, conducted at a set voltage of 56 $V_{P\text{-}P}$ and recorded by a HSI system.

Appendix E

List of publications

E.1 Journal

- Liu, Y., Hafezi, M. and Feeney, A. (2024) A cascaded Nitinol Langevin transducer for resonance stability at elevated temperatures. Ultrasonics, 137, 107201.
- Liu, Y., Nguyen, L.T.K., Li, X., and Feeney, A. (2024) A Timoshenko-Ehrenfest beam model for simulating Langevin transducer dynamics. Applied Mathematical Modelling, 131, 363-380.
- Liu, Y., Hafezi, M. and Feeney, A. (2024) Dynamic stability of a nitinol Langevin ultrasonic transducer under power and current tracking conditions. Applied Acoustics, 225, 110188.
- Adams, S., Hamilton, A., Hafezi, M., Liu, Y., Somerset, W. E., Kang, L., Dixon, S. and Feeney, A. (2025) Stereolithography for tailoring the dynamics of flexural ultrasonic transducers. IEEE Sensors Journal. (Accepted for Publication)
- Hamilton, A., Chambers, J., Adams, S., Liu, Y., Hafezi, M., and Feeney, A. (2025). The Dynamics of Flexural Ultrasonic Transducers with Nitinol Plates. IEEE Sensors Journal. (Accepted for Publication)

E.2 Conference

- Liu, Y., Hafezi, M. and Feeney, A. Active Modal Coupling of a Nitinol Langevin Transducer. In:2023 IEEE International Ultrasonics Symposium (IUS), Montreal, Canada, 3-8 September 2023.
- Liu, Y., Hafezi, M. and Feeney, A. Fabrication and Characterisation of a Nitinol Langevin Transducer. In:2023 IEEE International Ultrasonics Symposium (IUS), Montreal, Canada, 3-8 September 2023.

- Liu, Y., Hafezi, M. and Feeney, A. Fabrication and Dynamic Characterisation of a Nitinol Langevin Transducer. 17th International Conference on Advances in Experimental Mechanics, Glasgow, UK, 30 Aug-01 Sept 2023.

Bibliography

[1] D. Dance, S. Christofides, A. Maidment, I. McLean, K. Ng, Diagnostic Radiology Physics, Non-serial Publications, INTERNATIONAL ATOMIC ENERGY AGENCY, Vienna, 2014.

[2] T. G. Leighton, What is ultrasound?, Progress in biophysics and molecular biology 93 (1-3) (2007) 3–83. doi:10.1016/j.pbiomolbio.2006.07.026.

[3] T. D. Rossing, Introduction to acoustics, Springer handbook of acoustics (2014) 1–7doi:10.1007/978-1-4939-0755-7_1.

[4] H. Moller, C. S. Pedersen, Hearing at low and infrasonic frequencies, Noise and health 6 (23) (2004) 37–57.

[5] P. G. Stelmachowicz, K. A. Beauchaine, A. Kalberer, W. Jesteadt, Normative thresholds in the 8-to 20-khz range as a function of age, The Journal of the Acoustical Society of America 86 (4) (1989) 1384–1391. doi:10.1121/1.398698.

[6] A. Rodríguez Valiente, A. Trinidad, J. García Berrocal, C. Górriz, R. Ramírez Camacho, Extended high-frequency (9–20 khz) audiometry reference thresholds in 645 healthy subjects, International journal of audiology 53 (8) (2014) 531–545. doi:10.3109/14992027.2014.893375.

[7] F. Duck, T. Leighton, Frequency bands for ultrasound, suitable for the consideration of its health effects, The Journal of the Acoustical Society of America 144 (4) (2018) 2490–2500. doi:10.1121/1.5063578.

[8] J. Gallego-Juarez, Piezoelectric ceramics and ultrasonic transducers, Journal of Physics E: Scientific Instruments 22 (10) (1989) 804. doi:10.1088/0022-3735/22/10/001.

[9] K. Yamamoto, P. M. King, X. Wu, T. J. Mason, E. M. Joyce, Effect of ultrasonic frequency and power on the disruption of algal cells, Ultrasonics sonochemistry 24 (2015) 165–171. doi:https://doi.org/10.1016/j.ultsonch.2014.11.002.

[10] Y. Kuang, Y. Jin, S. Cochran, Z. Huang, Resonance tracking and vibration stablilization for high power ultrasonic transducers, Ultrasonics 54 (1) (2014) 187–194. doi:https://doi.org/10.1016/j.ultras.2013.07.001.

[11] J. A. Gallego-Juárez, K. F. Graff, M. Lucas, Power ultrasonics: applications of high-intensity ultrasound, Woodhead Publishing, 2023. doi:10.1016/C2013-0-16435-5.

[12] K. Graff, J. Sheehan, Power ultrasonic transducers: principles and design, in: Power ultrasonics, Elsevier, 2023, pp. 83–108. doi:https://doi.org/10.1016/B978-1-78242-028-6.00006-5.

[13] W. Shao, X. Li, Z. Li, P. Li, X. Zhu, Y. Cui, J. Shen, Multifrequency ultrasonic transducers based on dual vibration and harmonic mode, Sensors and Actuators A: Physical 333 (2022) 113228. doi:https://doi.org/10.1016/j.sna.2021.113228.

[14] P. Harkness, M. Lucas, A. Cardoni, Coupling and degenerating modes in longitudinal–torsional step horns, Ultrasonics 52 (8) (2012) 980–988. doi:https://doi.org/10.1016/j.ultras.2012.05.002.

[15] A. Feeney, Nitinol cymbal transducers for tuneable ultrasonic devices, Ph.D. thesis, University of Glasgow (2014).

[16] A. Feeney, M. Lucas, Smart cymbal transducers with nitinol end caps tunable to multiple operating frequencies, IEEE Transactions on Ultrasonics, Ferroelectrics, and Frequency Control 61 (10) (2014) 1709–1719. doi:10.1109/TUFFC.2013.006231.

[17] M. Ruzzene, A. Baz, Control of wave propagation in periodic composite rods using shape memory inserts, J. Vib. Acoust. 122 (2) (2000) 151–159. doi:10.1115/1.568452.

[18] A. Baz, S. Poh, J. Ro, J. Gilheany, Control of the natural frequencies of nitinol-reinforced composite beams, Journal of Sound and Vibration 185 (1) (1995) 171–185. doi:https://doi.org/10.1006/jsvi.1994.0370.

[19] T.-G. Park, D.-S. Jeong, M.-H. Kim, T.-K. Song, A study on the rotary-type ultrasonic motor using a longitudinal–torsional vibration converter, Materials chemistry and physics 98 (1) (2006) 1–4. doi:10.1016/j.matchemphys.2004.09.049.

[20] F. Bejarano, A. Feeney, R. Wallace, H. Simpson, M. Lucas, An ultrasonic orthopaedic surgical device based on a cymbal transducer, Ultrasonics 72 (2016) 24–33. doi:10.1016/j.ultras.2016.07.004.

[21] A. Mathieson, D. A. DeAngelis, Analysis of lead-free piezoceramic-based power ultrasonic transducers for wire bonding, IEEE Transactions on Ultrasonics, Ferroelectrics, and Frequency Control 63 (1) (2015) 156–164. doi:10.1109/TUFFC.2015.2496216.

[22] H. Al-Budairi, M. Lucas, P. Harkness, A design approach for longitudinal–torsional ultrasonic transducers, Sensors and Actuators A: Physical 198 (2013) 99–106. doi:10.1016/j.sna.2013.04.024.

[23] C.-H. Yun, T. Ishii, K. Nakamura, S. Ueha, K. Akashi, A high power ultrasonic linear motor using a longitudinal and bending hybrid bolt-clamped langevin type transducer, Japanese Journal of Applied Physics 40 (5S) (2001) 3773. doi:10.1143/JJAP.40.3773.

[24] T. Harada, N. Ishikawa, T. Kanda, K. Suzumori, Y. Yamada, K.-I. Sotowa, Droplet generation using a torsional langevin-type transducer and a micropore plate, Sensors and Actuators A: Physical 155 (1) (2009) 168–174. doi:https://doi.org/10.1016/j.sna.2009.08.007.

[25] A. Cornogolub, P.-J. Cottinet, L. Petit, Analytical modeling of curved piezoelectric, langevin-type, vibrating transducers using transfer matrices, Sensors and Actuators A: Physical 214 (2014) 120–133. doi:10.1016/j.sna.2014.04.003.

[26] J. Kim, J. Lee, Acoustic and thermal characterization of therapeutic ultrasonic langevin transducers under continuous-and pulsed wave excitations, Sensors 22 (22) (2022) 9006. doi:10.3390/s22229006.

[27] A. Feeney, M. Lucas, A comparison of two configurations for a dual-resonance cymbal transducer, IEEE Transactions on Ultrasonics, Ferroelectrics, and Frequency Control 65 (3) (2018) 489–496. doi:10.1109/TUFFC.2018.2793310.

[28] Y. Song, Y. Shen, A metasurface radar for steering ultrasonic guided waves, Journal of Sound and Vibration 538 (2022) 117260. doi:https://doi.org/10.1016/j.jsv.2022.117260.

[29] R. Cleary, X. Li, M. Lucas, Incorporating direct metal laser sintered complex shaped ti-6al-4v components in ultrasonic surgical devices, The Journal of the Acoustical Society of America 150 (3) (2021) 2163–2173. doi:10.1121/10.0006379.

[30] F. Balle, D. Eifler, Statistical test planning for ultrasonic welding of dissimilar materials using the example of aluminum-carbon fiber reinforced polymers (cfrp) joints, Materialwissenschaft und Werkstofftechnik 43 (4) (2012) 286–292. doi:https://doi.org/10.1002/mawe.201200943.

[31] F. Balle, G. Wagner, D. Eifler, Ultrasonic metal welding of aluminium sheets to carbon fibre reinforced thermoplastic composites, Advanced Engineering Materials 11 (1-2) (2009) 35–39. doi:https://doi.org/10.1002/adem.200800271.

[32] D. Grewell, A. Benatar, Welding of plastics: fundamentals and new developments, International polymer processing 22 (1) (2007) 43–60. doi:10.3139/217.0051.

[33] H. Daniels, Ultrasonic welding, Ultrasonics 3 (4) (1965) 190–196. doi:https://doi.org/10.1016/0041-624X(65)90169-1.

[34] S. Krüger, G. Wagner, D. Eifler, Ultrasonic welding of metal/composite joints, Advanced engineering materials 6 (3) (2004) 157–159. doi:https://doi.org/10.1002/adem.200300539.

[35] G. Wagner, F. Balle, D. Eifler, Ultrasonic welding of aluminum alloys to fiber reinforced polymers, Advanced Engineering Materials 15 (9) (2013) 792–803. doi:https://doi.org/10.1002/adem.201300043.

[36] F. Lionetto, F. Balle, A. Maffezzoli, Hybrid ultrasonic spot welding of aluminum to carbon fiber reinforced epoxy composites, Journal of Materials Processing Technology 247 (2017) 289–295. doi:https://doi.org/10.1016/j.jmatprotec.2017.05.002.

[37] P. touch, https://dental.mectron.com/no/products/piezosurgeryr/units/piezosurgeryr-touch/.

[38] H. . S. . E. . J. M. U. . Ireland, https://www.jnjmedtech.com/en-GB/product/harmonic-1100-shears.

[39] T. T. S. O. M. Systems, https://www.olympus.co.uk/medical/en/Products-and-solutions/Products/Product/THUNDERBEAT-Type-S.html.

[40] Z. Yuan, C. Lu, C. Liu, X. Bai, L. Zhao, S. Feng, Y. Liu, Ultrasonic tweezer for multifunctional droplet manipulation, Science Advances 9 (16) (2023) eadg2352. doi:10.1126/sciadv.adg2352.

[41] R. Hirayama, D. Martinez Plasencia, N. Masuda, S. Subramanian, A volumetric display for visual, tactile and audio presentation using acoustic trapping, Nature 575 (7782) (2019) 320–323. doi:https://doi.org/10.1038/s41586-019-1739-5.

[42] R. Hirayama, G. Christopoulos, D. Martinez Plasencia, S. Subramanian, High-speed acoustic holography with arbitrary scattering objects, Science advances 8 (24) (2022) eabn7614. doi:10.1126/sciadv.abn7614.

[43] M. A. Andrade, T. S. Ramos, J. C. Adamowski, A. Marzo, Contactless pick-and-place of millimetric objects using inverted near-field acoustic levitation, Applied Physics Letters 116 (5) (2020). doi:https://doi.org/10.1063/1.5138598.

[44] M. A. Andrade, A. L. Bernassau, J. C. Adamowski, Acoustic levitation of a large solid sphere, Applied Physics Letters 109 (4) (2016). doi:https://doi.org/10.1063/1.4959862.

[45] M. A. Andrade, F. T. Okina, A. L. Bernassau, J. C. Adamowski, Acoustic levitation of an object larger than the acoustic wavelength, The Journal of the Acoustical Society of America 141 (6) (2017) 4148–4154. doi:10.1121/1.4984286.

[46] S. Baer, M. A. Andrade, C. Esen, J. C. Adamowski, G. Schweiger, A. Ostendorf, Analysis of the particle stability in a new designed ultrasonic levitation device, Review of Scientific Instruments 82 (10) (2011). doi:https://doi.org/10.1063/1.3652976.

[47] A. M. Alanazi, Non-destructive testing of steel-lined concrete structure using multiple agents with deep prior, Scientific Reports 15 (1) (2025) 31275. doi:https://doi.org/10.1038/s41598-025-16978-3.

[48] H. Kazari, M. Kabir, A. Mostavi, D. Ozevin, Multi-frequency piezoelectric micromachined ultrasonic transducers, IEEE Sensors Journal 19 (23) (2019) 11090–11099. doi:10.1109/JSEN.2019.2935158.

[49] S. Lin, Analysis of multifrequency langevin composite ultrasonic transducers, IEEE transactions on ultrasonics, ferroelectrics, and frequency control 56 (9) (2009) 1990–1998. doi:10.1109/TUFFC.2009.1275.

[50] X. Meng, S. Lin, Analysis of a cascaded piezoelectric ultrasonic transducer with three sets of piezoelectric ceramic stacks, Sensors 19 (3) (2019) 580. doi:https://doi.org/10.3390/s19030580.

[51] K. MJ, N. Chubachi, Theoretical and experimental characteristics analysis of multi-frequency composite langevin-type ultrasonic transducer, IEEJ Transactions on Electronics, Information and Systems 114 (1) (1994) 42–50.

[52] A. Feeney, M. Lucas, Differential scanning calorimetry of superelastic nitinol for tunable cymbal transducers, Journal of Intelligent Material Systems and Structures 27 (10) (2016) 1376–1387. doi:10.1177/1045389X15591383.

[53] R. Meyer Jr, R. Newnham, Flextensional transducers with shape memory caps for tunable devices, Journal of intelligent material systems and structures 11 (3) (2000) 199–205. doi:10.1106/M9B2-FK6D-DR38-2JVL.

[54] J. M. Jani, M. Leary, A. Subic, M. A. Gibson, A review of shape memory alloy research, applications and opportunities, Materials & Design (1980-2015) 56 (2014) 1078–1113. doi:10.1016/j.matdes.2013.11.084.

[55] Y. Liu, H. Xiang, Apparent modulus of elasticity of near-equiatomic niti, Journal of alloys and compounds 270 (1-2) (1998) 154–159. doi:10.1016/S0925-8388(98)00500-3.

[56] K. Suresh, D. Lahiri, A. Agarwal, S. Suwas, Microstructure dependent elastic modulus variation in niti shape memory alloy, Journal of Alloys and Compounds 633 (2015) 71–74. doi:10.1016/j.jallcom.2015.01.301.

[57] P. Šittner, L. Heller, J. Pilch, C. Curfs, T. Alonso, D. Favier, Young's modulus of austenite and martensite phases in superelastic niti wires, Journal of materials engineering and performance 23 (2014) 2303–2314. doi:10.1007/s11665-014-0976-x.

[58] O. Benafan, R. Noebe, S. Padula Ii, A. Garg, B. Clausen, S. Vogel, R. Vaidyanathan, Temperature dependent deformation of the b2 austenite phase of a niti shape memory alloy, International Journal of Plasticity 51 (2013) 103–121. doi:10.1016/j.ijplas.2013.06.003.

[59] G. Laplanche, J. Pfetzing-Micklich, G. Eggeler, Orientation dependence of stress-induced martensite formation during nanoindentation in niti shape memory alloys, Acta materialia 68 (2014) 19–31. doi:10.1016/j.actamat.2014.01.006.

[60] M. Thomasová, P. Sedlák, H. Seiner, M. Janovská, M. Kabla, D. Shilo, M. Landa, Young's moduli of sputter-deposited niti films determined by resonant ultrasound spectroscopy: Austenite, r-phase, and martensite, Scripta materialia 101 (2015) 24–27. doi:10.1016/j.scriptamat.2015.01.00.

[61] J. W. Mwangi, L. T. Nguyen, V. D. Bui, T. Berger, H. Zeidler, A. Schubert, Nitinol manufacturing and micromachining: A review of processes and their suitability in processing medical-grade nitinol, Journal of manufacturing processes 38 (2019) 355–369. doi:https://doi.org/10.1016/j.jmapro.2019.01.003.

[62] P. Chen, Y. Liu, N. Min, M. Wang, X. Cai, M. Jin, X. Jin, Enhanced two way shape memory effect in nanocrystalline niti shape memory alloy wires, Scripta Materialia 236 (2023) 115669. doi:https://doi.org/10.1016/j.scriptamat.2023.115669.

[63] M. Mohri, M. Nili-Ahmadabadi, Phase transformation and structure of functionally graded ni–ti bi-layer thin films with two-way shape memory effect, Sensors and Actuators A: Physical 228 (2015) 151–158. doi:10.1007/978-0-387-47685-8.

[64] Q. Meng, Z. Wu, R. Bakhtiari, B. S. Shariat, H. Yang, Y. Liu, T.-h. Nam, A unique "fishtail-like" four-way shape memory effect of compositionally graded niti, Scripta Materialia 127 (2017) 84–87. doi:https://doi.org/10.1016/j.scriptamat.2016.09.007.

[65] K. Melton, Ni-ti based shape memory alloys, Engineering aspects of shape memory alloys 344 (1990) 21–25.

[66] D. Hartl, D. Lagoudas, Shape memory alloys: modeling and engineering applications (2008).

[67] C. Chu, C. Chung, P. Lin, Dsc study of the effect of aging temperature on the reverse martensitic transformation in porous ni-rich niti shape memory alloy fabricated by combustion synthesis, Materials letters 59 (4) (2005) 404–407. doi:https://doi.org/10.1016/j.matlet.2004.08.036.

[68] X. Wang, S. Kustov, B. Verlinden, J. Van Humbeeck, Fundamental development on utilizing the r-phase transformation in niti shape memory alloys, Shape memory and superelasticity 1 (2015) 231–239. doi:https://doi.org/10.1007/s40830-015-0007-2.

[69] J. Uchil, K. K. Ganesh, K. Mahesh, Simple thermal actuator using r-phase transformation of nitinol, in: Smart Structures and Materials 2002: Smart Structures and Integrated Systems, Vol. 4701, SPIE, 2002, pp. 435–442. doi:10.1117/12.474680.

[70] S. Robertson, A. Mehta, A. Pelton, R. Ritchie, Evolution of crack-tip transformation zones in superelastic nitinol subjected to in situ fatigue: A fracture mechanics and synchrotron x-ray microdiffraction analysis, Acta Materialia 55 (18) (2007) 6198–6207. doi:https://doi.org/10.1016/j.actamat.2007.07.028.

[71] I. Müller, On the size of the hysteresis in pseudoelasticity, Continuum mechanics and thermodynamics 1 (1989) 125–142. doi:https://doi.org/10.1007/BF01141998.

[72] S. Miyazaki, H. Kim, Basic characteristics of titanium–nickel (ti–ni)-based and titanium–niobium (ti–nb)-based alloys, in: Shape Memory and Superelastic Alloys, Elsevier, 2011, pp. 15–42. doi:https://doi.org/10.1533/9780857092625.1.15.

[73] S. Nemat-Nasser, W.-G. Guo, Superelastic and cyclic response of niti sma at various strain rates and temperatures, Mechanics of materials 38 (5-6) (2006) 463–474. doi:https://doi.org/10.1016/j.mechmat.2005.07.004.

[74] N. Agarwal, J. Ryan Murphy, T. S. Hashemi, T. Mossop, D. O'Neill, J. Power, A. Shayegh, D. Brabazon, Effect of heat treatment time and temperature on the microstructure and shape memory properties of nitinol wires, Materials 16 (19) (2023) 6480. doi:https://doi.org/10.3390/ma16196480.

[75] T. Duerig, K. Bhattacharya, The influence of the r-phase on the superelastic behavior of niti, Shape Memory and Superelasticity 1 (2015) 153–161. doi:https://doi.org/10.1007/s40830-015-0013-4.

[76] R. Georges Sabat, B. K. Mukherjee, W. Ren, G. Yang, Temperature dependence of the complete material coefficients matrix of soft and hard doped piezoelectric lead zirconate titanate ceramics, Journal of Applied Physics 101 (6) (2007). doi:10.1063/1.2560441.

[77] K. Uchino, S. Hirose, Loss mechanisms in piezoelectrics: how to measure different losses separately, IEEE Transactions on Ultrasonics, ferroelectrics, and frequency control 48 (1) (2001) 307–321. doi:10.1109/58.896144.

[78] M. H. Amini, A. N. Sinclair, T. W. Coyle, A new high-temperature ultrasonic transducer for continuous inspection, IEEE transactions on Ultrasonics, Ferroelectrics, and Frequency control 63 (3) (2016) 448–455. doi:10.1109/TUFFC.2016.2519348.

[79] T. Wang, Q. Quan, D. Tang, Z. Yang, J. Huang, F. Guo, L. Meng, Z. Zhao, Z. Deng, Effect of hyperthermal cryogenic environments on the performance of piezoelectric transducer, Applied Thermal Engineering 193 (2021) 116725. doi:10.1016/j.applthermaleng.2021.116725.

[80] D. Yamaguchi, T. Kanda, K. Suzumori, An ultrasonic motor for cryogenic temperature using bolt-clamped langevin-type transducer, Sensors and Actuators A: Physical 184 (2012) 134–140. doi:10.1016/j.sna.2012.06.024.

[81] A. Kárpáti, Translation or compilation? contributions to the analysis of sources of boethius' de institutione musica, Studia Musicologica Academiae Scientiarum Hungaricae 29 (Fasc. 1/4) (1987) 5–33. doi:https://doi.org/10.2307/902171.

[82] J. B. Egan, MARIN MERSENNE:'TRAITE DE L'HARMONIE UNIVERSELLE': CRITICAL TRANSLATION OF THE SECOND BOOK, Indiana University, 1962.

[83] G. Galilei, Two new sciences, Dover New York, 1914.

[84] P. Gouk, The role of acoustics and music theory in the scientific work of robert hooke, Annals of Science 37 (5) (1980) 573–605. doi:https://doi.org/10.1080/00033798000200401.

[85] M. J. Osler, Pierre gassendi, A companion to early modern philosophy (2002) 80–95doi:10.1002/9780470998847.ch6.

[86] E. Rossi, Beyond the saggi: Experiments on sound in the manuscripts of the accademia del cimento, Physis: International Journal for the History of Science: LIX, 2, 2024 (2024) 409–430doi:10.1400/298754.

[87] B. S. Finn, Laplace and the speed of sound, Isis 55 (1) (1964) 7–19.

[88] K. A. Kaproth-Joslin, R. Nicola, V. S. Dogra, The history of us: from bats and boats to the bedside and beyond: Rsna centennial article, Radiographics 35 (3) (2015) 960–970. doi:https://doi.org/10.1148/rg.2015140300.

[89] H. Greven, From johann august ephraim goeze to ernst marcus: A ramble through the history of early tardigrade research (1773 until 1929), in: Water bears: The biology of tardigrades, Springer, 2019, pp. 1–55. doi:https://doi.org/10.1007/978-3-319-95702-9_1.

[90] S. Marguet, Doppler effect, in: The Physics of Nuclear Reactors, Springer, 2018, pp. 333–385. doi:https://doi.org/10.1007/978-3-319-59560-3.

[91] R. B. Lindsay, The story of acoustics, The Journal of the Acoustical Society of America 39 (4) (1966) 629–644. doi:https://doi.org/10.1121/1.1909936.

[92] L. A. Orloff, Head and neck ultrasonography: essential and extended applications, Plural Publishing, 2017.

[93] H. S. Klickstein, Pierre curie—an appreciation of his scientific achievements., Journal of Chemical Education 24 (6) (1947) 278.

[94] J. Erhart, Experiments to demonstrate piezoelectric and pyroelectric effects, Physics Education 48 (4) (2013) 438. doi:10.1088/0031-9120/48/4/438.

[95] A. Von Hippel, R. Breckenridge, F. Chesley, L. Tisza, High dielectric constant ceramics, Industrial & Engineering Chemistry 38 (11) (1946) 1097–1109. doi:10.1021/ie50443a009.

[96] T. J. Scarpa, Electroacoustic sandwich transducers, uS Patent 3,140,859 (Jul. 14 1964).

[97] W. P. Mason, Piezoelectricity, its history and applications, The journal of the Acoustical Society of America 70 (6) (1981) 1561–1566. doi:https://doi.org/10.1121/1.387221.

[98] R. Boucher, J. Kreuter, The electroacoustic horn—a new high-intensity sound source, The Journal of the Acoustical Society of America 46 (6A) (1969) 1406–1409. doi:https://doi.org/10.1121/1.1911873.

[99] A. Hulst, On a family of high-power transducers, in: Ultrasonics International Conference Proceedings, 1973.

[100] Y. Kagawa, T. Yamabuchi, Finite element simulation of a composite piezoelectric ultrasonic transducer, IEEE Transactions on Sonics and Ultrasonics 26 (2) (1979) 81–87. doi:10.1109/T-SU.1979.31071.

[101] Y. Koike, M. Kihara, J. Satonobu, K. Nakamura, S. Ueha, A peripherally bolted torsional langevin vibrator with large diameter, Journal of the Acoustical Society of Japan (E) 18 (5) (1997) 239–246. doi:10.1250/ast.18.239.

[102] K. Adachi, M. Tsuji, H. Kato, Elastic contact problem of the piezoelectric material in the structure of a bolt-clamped langevin-type transducer, The Journal of the Acoustical Society of America 105 (3) (1999) 1651–1656. doi:https://doi.org/10.1121/1.426704.

[103] K. Takeda, H. Tanaka, T. Tsuchiya, S. Kaneko, Molecular movement during welding for engineering plastics using langevin transducer equipped with half-wave-length step horn, Ultrasonics 36 (1-5) (1998) 75–78. doi:https://doi.org/10.1016/S0041-624X(97)00077-2.

[104] M. Y. Baraya, M. Hossam, Design of an electromechanical system for measuring and monitoring micro-ultrasonic amplitude of langevin transducer, The International Journal of Advanced Manufacturing Technology 107 (2020) 2953–2965. doi:https://doi.org/10.1007/s00170-020-04922-w.

[105] A. Yazdian, M. R. Karafi, An analytical approach to design horns and boosters of ultrasonic welding machines, SN Applied Sciences 4 (6) (2022) 166. doi:https://doi.org/10.1007/s42452-022-05044-6.

[106] M. S. M. Shimanuki, M. A. M. Aoyagi, Y. T. Y. Tomikawa, Single-resonance longitudinal and torsional vibrator combination-type motor: Improvement of motor characteristics, Japanese journal of applied physics 33 (5S) (1994) 3075. doi:10.1143/JJAP.33.3075.

[107] R. Kurniawan, S. Ali, K. M. Park, C. P. Li, T. J. Ko, Development of a three-dimensional ultrasonic elliptical vibration transducer (3d-uevt) based on sandwiched

piezoelectric actuator for micro-grooving, International journal of precision engineering and manufacturing 20 (2019) 1229–1240. doi:https://doi.org/10.1007/s12541-019-00126-9.

[108] J. Deng, Y. Liu, J. Liu, D. Xu, Y. Wang, Development of a planar piezoelectric actuator using bending–bending hybrid transducers, IEEE Transactions on Industrial Electronics 66 (8) (2018) 6141–6149. doi:10.1109/TIE.2018.2873123.

[109] J. Wu, Y. Mizuno, K. Nakamura, A rotary ultrasonic motor operating in torsional/bending modes with high torque density and high power density, IEEE Transactions on Industrial Electronics 68 (7) (2020) 6109–6120. doi:10.1109/TIE.2020.3000112.

[110] J. Wu, Y. Mizuno, K. Nakamura, Vibration characteristics of polymer-based langevin transducers, Smart Materials and Structures 27 (9) (2018) 095013. doi:10.1088/1361-665X/aad530.

[111] K. Honda, Multi-frequency ultrasonic transducer, uS Patent 4,490,640 (Dec. 25 1984).

[112] S. Lin, C. Xu, Analysis of the sandwich ultrasonic transducer with two sets of piezoelectric elements, Smart materials and structures 17 (6) (2008) 065008. doi:10.1088/0964-1726/17/6/065008.

[113] Z. Liao, S. Zhang, Y. Liu, X. Li, C. Liu, Y. Wu, A dual-frequency ultrasonic aspirator (dfua) based on a novel langevin transducer, in: 2023 IEEE International Ultrasonics Symposium (IUS), IEEE, 2023, pp. 1–4. doi:10.1109/IUS51837.2023.10307718.

[114] G. Kurdyumov, Diffusionless (martensitic) transformations in alloys, Zh. tekh. fiz 18 (8) (1948) 999–1025.

[115] G. Kurdyumov, L. Khandros, On the thermoelastic equilibrium on martensitic transformations, in: Dokl. Akad. Nauk SSSR, Vol. 66, 1949, pp. 211–214. doi:https://doi.org/10.1016/0036-9748(77)90263-0.

[116] A. W. McReynolds, Effects of stress and deformation on the martensite transformation, Journal of Applied Physics 20 (10) (1949) 896–907. doi:https://doi.org/10.1063/1.1698251.

[117] J. Bowles, J. Mackenzie, The crystallography of martensite transformations iii. face-centred cubic to body-centred tetragonal transformations, Acta Metallurgica 2 (2) (1954) 224–234. doi:https://doi.org/10.1016/0001-6160(54)90163-7.

[118] C. Chen, Some characteristics of the martensite transformation of cu-al-ni alloys, JOM 9 (1957) 1202–1203.

[119] W. J. Buehler, J. V. Gilfrich, R. C. Wiley, Effect of low-temperature phase changes on the mechanical properties of alloys near composition tini, Journal of applied physics 34 (5) (1963) 1475–1477. doi:https://doi.org/10.1063/1.1729603.

[120] F. Laves, H. Wallbaum, Die kristallstruktur von ni3ti und si2ti:(zwei neue typen.), Zeitschrift für Kristallographie-Crystalline Materials 101 (1-6) (1939) 78–93.

[121] F. E. Wang, W. J. Buehler, S. J. Pickart, Crystal structure and a unique“martensitic”transition of tini, Journal of Applied Physics 36 (10) (1965) 3232–3239. doi:https://doi.org/10.1063/1.1702955.

[122] C. Jackson, H. Wagner, R. Wasilewski, The alloy with a memory, 55-nitinol: its physical metallurgy, properties, and applications, Tech. rep., NASA (1972).

[123] H. U. Schuerch, Certain physical properties and applications of nitinol, Tech. rep., NASA (1968).

[124] W. B. Cross, A. H. Kariotis, F. J. Stimler, Nitinol characterization study, Tech. rep., NASA (1969).

[125] L. M. Schetky, Shape-memory alloys, Scientific American 241 (5) (1979) 74–83. doi:https://doi.org/10.1002/0471238961.1908011619030805.a01.

[126] K. Melton, O. Mercier, Fatigue of niti thermoelastic martensites, Acta Metallurgica 27 (1) (1979) 137–144. doi:https://doi.org/10.1016/0001-6160(79)90065-8.

[127] J. G. Boyd, D. C. Lagoudas, A thermodynamical constitutive model for shape memory materials. part i. the monolithic shape memory alloy, International journal of plasticity 12 (6) (1996) 805–842. doi:https://doi.org/10.1016/S0749-6419(96)00030-7.

[128] C. Trepanier, M. Tabrizian, L. Yahia, L. Bilodeau, D. L. Piron, Effect of modification of oxide layer on niti stent corrosion resistance, Journal of biomedical materials research 43 (4) (1998) 433–440. doi:10.1002/(sici)1097-4636(199824)43:4<433::aid-jbm11>3.0.co;2-#.

[129] S. A. Shabalovskaya, On the nature of the biocompatibility and on medical applications of niti shape memory and superelastic alloys, Bio-medical materials and engineering 6 (4) (1996) 267–289.

[130] H. Hou, E. Simsek, T. Ma, N. S. Johnson, S. Qian, C. Cissé, D. Stasak, N. Al Hasan, L. Zhou, Y. Hwang, et al., Fatigue-resistant high-performance elastocaloric materi-

als made by additive manufacturing, Science 366 (6469) (2019) 1116–1121. doi:10.1126/science.aax7616.

[131] K. Weinert, V. Petzoldt, Machining of niti based shape memory alloys, Materials science and engineering: A 378 (1-2) (2004) 180–184. doi:https://doi.org/10.1016/j.msea.2003.10.344.

[132] M. H. Elahinia, M. Hashemi, M. Tabesh, S. B. Bhaduri, Manufacturing and processing of niti implants: A review, Progress in materials science 57 (5) (2012) 911–946. doi:https://doi.org/10.1016/j.pmatsci.2011.11.001.

[133] R. Pflueger, H. Nita, S. Bacich, R. Siegel, G. Bond, E. DeCastro, Ultrasonic angioplasty device incorporating improved transmission member and ablation probe, uS Patent 5,304,115 (Apr. 19 1994).

[134] S. Poh, A. Baz, J. Gilheany, Active control of sound radiated from nitinol-reinforced composite plates, The Journal of the Acoustical Society of America 88 (S1) (1990) S149–S149. doi:https://doi.org/10.1121/1.2028662.

[135] Y. Liu, L. T. K. Nguyen, X. Li, A. Feeney, A timoshenko-ehrenfest beam model for simulating langevin transducer dynamics, Applied Mathematical Modelling 131 (2024) 363–380. doi:https://doi.org/10.1016/j.apm.2024.04.019.

[136] D. A. DeAngelis, G. W. Schulze, Optimizing piezoelectric ceramic thickness in ultrasonic transducers, in: Proceedings of the 39th Annual Symposium of the Ultrasonic Industry Association, 2010, pp. 1–9. doi:10.1109/UIA.2010.5506062.

[137] V. T. Rathod, A review of acoustic impedance matching techniques for piezoelectric sensors and transducers, Sensors 20 (14) (2020) 4051. doi:https://doi.org/10.3390/s20144051.

[138] N. Hiremath, V. Kumar, N. Motahari, D. Shukla, An overview of acoustic impedance measurement techniques and future prospects, Metrology 1 (1) (2021) 17–38. doi:https://doi.org/10.3390/metrology1010002.

[139] I. Ibanez, B. Zeqiri, M. Hodnett, M. Frota, Cavitation-erosion measurements on engineering materials, Engineering Science and Technology, an International Journal 23 (6) (2020) 1486–1498. doi:10.1016/j.jestch.2020.06.001.

[140] A. A. Mohammed, S. M. Haris, M. Z. Nuawi, Utilizing hilbert–huang transform in detection some of mechanical properties of the refractory metals, Mechanical Systems and Signal Processing 68-69 (2016) 449–461. doi:10.1016/j.ymssp.2015.07.024.

[141] E. Ginzel, B. Turnbull, Determining approximate acoustic properties of materials, NDT. net Dec 2016 (2016) 1–10.

[142] M. Gorostiaga, M. Wapler, U. Wallrabe, Optimizing piezoelectric receivers for acoustic power transfer applications, Smart Materials and Structures 27 (7) (2018) 075024. doi:10.1088/1361-665X/aabf09.

[143] T. R. Kelley, Lead-free versus pzt: Acoustic characterization of ultrasonic immersion transducers fabricated with lead-free nbt-bt piezoceramic, The Journal of Engineering 2023 (6) (2023) e12282. doi:10.1049/tje2.12282.

[144] J. Bian, Y. Wang, Z. Liu, M. Shen, H. Zhao, Y. Sun, J. Zhu, Ultra-wideband underwater acoustic transducer with a gradient impedance matching layer, Applied Acoustics 175 (2021) 107789. doi:https://doi.org/10.1016/j.apacoust.2020.107789.

[145] J. D. Boles, P. L. Acosta, Y. K. Ramadass, J. H. Lang, D. J. Perreault, Evaluating piezoelectric materials for power conversion, in: 2020 IEEE 21st Workshop on Control and Modeling for Power Electronics (COMPEL), IEEE, 2020, pp. 1–8. doi:10.1109/TPEL.2021.3114350.

[146] Y. Ji, A. Chen, Y. Chen, X. Han, B. Li, Y. Gao, C. Liu, J. Xie, A state-of-the-art review of concrete strength detection/monitoring methods: With special emphasis on pzt transducers, Construction and Building Materials 362 (2023) 129742. doi:https://doi.org/10.1016/j.conbuildmat.2022.129742.

[147] M. Elhadrouz, T. B. Zineb, E. Patoor, Finite element analysis of a multilayer piezoelectric actuator taking into account the ferroelectric and ferroelastic behaviors, International journal of engineering science 44 (15-16) (2006) 996–1006. doi:https://doi.org/10.1016/j.ijengsci.2006.05.013.

[148] C. Kadapa, M. Hossain, A robust and computationally efficient finite element framework for coupled electromechanics, Computer Methods in Applied Mechanics and Engineering 372 (2020) 113443. doi:https://doi.org/10.1016/j.cma.2020.113443.

[149] S. Yarlagadda, M. H. Chan, H. Lee, G. A. Lesieutre, D. W. Jensen, R. S. Messer, Low temperature thermal conductivity, heat capacity, and heat generation of pzt, Journal of intelligent material systems and structures 6 (6) (1995) 757–764. doi:https://doi.org/10.1177/1045389X95006006.

[150] L. Wang, V. Hofmann, F. Bai, J. Jin, J. Twiefel, A novel additive manufactured three-dimensional piezoelectric transducer: Systematic modeling and experimental validation,

Mechanical Systems and Signal Processing 114 (2019) 346–365. doi:https://doi.org/10.1016/j.ymssp.2018.05.025.

[151] X. Ma, Y. Yang, J. Qiu, J. Zhang, P. Vasiljev, J. Wu, D. Mazeika, L. Zhao, S. Borodinas, J. Liu, A novel rotary ultrasonic motor based on multiple langevin transducers: design, simulation, and experimental investigation, Smart Materials and Structures 33 (5) (2024) 055001. doi:10.1088/1361-665X/ad37b4.

[152] A. Pérez-Sánchez, J. Segura, C. Rubio-Gonzalez, L. A. Baldenegro-Pérez, J. Soto-Cajiga, Numerical design and analysis of a langevin power ultrasonic transducer for acoustic cavitation generation, Sensors and Actuators A: Physical 311 (2020) 112035. doi:https://doi.org/10.1016/j.sna.2020.112035.

[153] H. Alves, Instrument for measuring prestress in piezoceramics during bolt-clamped langevin-type transducers preloading, in: 2024 52nd Annual Ultrasonic Industry Association Symposium (UIA), IEEE, 2024, pp. 1–7. doi:10.23919/UIA60812.2024.10716020.

[154] D. A. DeAngelis, G. W. Schulze, Performance of pzt8 versus pzt4 piezoceramic materials in ultrasonic transducers, Physics Procedia 87 (2016) 85–92, 44th Annual Symposium of the Ultrasonic Industry Association, UIA 44th Symposium, 20-22 April 2015, Washington, DC, USA and of the 45th Annual Symposium of the Ultrasonic Industry Association, UIA 45th Symposium, 4-6 April 2016, Washington, DC, USA. doi:https://doi.org/10.1016/j.phpro.2016.12.014.

[155] Ieee standard on piezoelectricity, ANSI/IEEE Std 176-1987 (1988). doi:10.1109/IEEESTD.1988.79638.

[156] C. Wang, S. Kitipornchai, C. Lim, M. Eisenberger, Beam bending solutions based on nonlocal timoshenko beam theory, Journal of Engineering Mechanics 134 (6) (2008) 475–481. doi:https://doi.org/10.1061/(ASCE)0733-9399(2008)134:6(475).

[157] N. Van Rensburg, A. Van der Merwe, Natural frequencies and modes of a timoshenko beam, Wave motion 44 (1) (2006) 58–69. doi:https://doi.org/10.1016/j.wavemoti.2006.06.008.

[158] S. S. Rao, Vibration of continuous systems, John Wiley & Sons, 2019. doi:10.1002/9780470117866.

[159] J. Hutchinson, Shear coefficients for timoshenko beam theory, J. Appl. Mech. 68 (1) (2001) 87–92. doi:https://doi.org/10.1115/1.1349417.

[160] J. Banerjee, A. Ananthapuvirajah, Coupled axial-bending dynamic stiffness matrix for beam elements, Computers & Structures 215 (2019) 1–9. doi:https://doi.org/10.1016/j.compstruc.2019.01.007.

[161] K.-J. Bathe, Finite element procedures, Klaus-Jurgen Bathe, 2006.

[162] C. Pozrikidis, Introduction to finite and spectral element methods using MATLAB, CRC press, 2005. doi:https://doi.org/10.1201/b17067.

[163] L. N. Trefethen, Spectral methods in MATLAB, SIAM, 2000. doi:https://doi.org/10.1137/1.9780898719598.

[164] H. Georgi, The physics of waves, Prentice Hall Englewood Cliffs, NJ, 1993.

[165] H. Allik, T. J. Hughes, Finite element method for piezoelectric vibration, International journal for numerical methods in engineering 2 (2) (1970) 151–157. doi:https://doi.org/10.1002/nme.1620020202.

[166] S.-T. Gu, L. Qin, Variational principles and size-dependent bounds for piezoelectric inhomogeneous materials with piezoelectric coherent imperfect interfaces, International Journal of Engineering Science 78 (2014) 89–102. doi:https://doi.org/10.1016/j.ijengsci.2014.02.010.

[167] A. V. Mezheritsky, Efficiency of excitation of piezoceramic transducers at antiresonance frequency, IEEE transactions on ultrasonics, ferroelectrics, and frequency control 49 (4) (2002) 484–494. doi:10.1109/58.996567.

[168] A. Mathieson, A. Feeney, A. Tweedie, M. Lucas, Ultrasonic biopsy needle based on the class iv flextensional configuration, in: 2015 IEEE International Ultrasonics Symposium (IUS), IEEE, 2015, pp. 1–4. doi:10.1109/ULTSYM.2015.0213.

[169] J. Cai, Y. Wang, D. Jiang, S. Zhang, Y. A. Gu, L. Lou, F. Gao, T. Wu, Beyond fundamental resonance mode: high-order multi-band aln pmut for in vivo photoacoustic imaging, Microsystems & nanoengineering 8 (1) (2022) 116. doi:https://doi.org/10.1038/s41378-022-00426-7.

[170] B.-H. Lee, J.-M. Lee, J.-E. Baek, J.-Y. Sim, An estimation method of an electrical equivalent circuit considering acoustic radiation efficiency for a multiple resonant transducer, Electronics 10 (19) (2021) 2416. doi:https://doi.org/10.3390/electronics10192416.

[171] A. Ballo, A. D. Grasso, M. Privitera, Demystifying regulating active rectifiers for energy harvesting systems: a tutorial assisted by verilog-a models, IEEE Access 11 (2023) 43891–43908. doi:10.1109/ACCESS.2023.3272504.

[172] F. A. Firestone, A new analogy between mechanical and electrical systems, The Journal of the Acoustical Society of America 4 (3) (1933) 249–267. doi:https://doi.org/10.1121/1.1915605.

[173] M. W. Hooker, Properties of pzt-based piezoelectric ceramics between-150 and 250 c, Tech. rep., NASA (1998).

[174] K. Nakamura, Ultrasonic transducers: Materials and design for sensors, actuators and medical applications, Elsevier, 2012.

[175] M. Wild, M. Bring, E. Halvorsen, L. Hoff, K. Hjelmervik, The challenge of distinguishing mechanical, electrical and piezoelectric losses, The Journal of the Acoustical Society of America 144 (4) (2018) 2128–2134. doi:10.1121/1.5057443.

[176] R. J. Allemang, D. L. Brown, Experimental Modal Analysis Methods, Springer New York, New York, NY, 2020. doi:10.1007/978-1-4939-6503-8_36-2.

[177] T. Rossing, Modal Analysis, Springer New York, New York, NY, 2007. doi:10.1007/978-0-387-30425-0_28.
URL https://doi.org/10.1007/978-0-387-30425-0_28

[178] A. Mathieson, A. Cardoni, N. Cerisola, M. Lucas, The influence of piezoceramic stack location on nonlinear behavior of langevin transducers, IEEE transactions on ultrasonics, ferroelectrics, and frequency control 60 (6) (2013) 1126–1133. doi:10.1109/TUFFC.2013.2675.

[179] Y. Liu, R. Ozaki, T. Morita, Investigation of nonlinearity in piezoelectric transducers, Sensors and Actuators A: Physical 227 (2015) 31–38. doi:https://doi.org/10.1016/j.sna.2015.03.036.

[180] N. P. Alvarez, A. Cardoni, N. Cerisola, E. Riera, M. A. B. Andrade, J. C. Adamowski, Nonlinear dynamic modeling of langevin-type piezoelectric transducers, in: Actuators, Vol. 4, MDPI, 2015, pp. 255–266. doi:https://doi.org/10.3390/act4040255.

[181] A. C. Mathieson, Nonlinear characterisation of power ultrasonic devices used in bone surgery, Ph.D. thesis, University of Glasgow (2012).

[182] M. Stewart, M. G. Cain, Measurement and modelling of self-heating in piezoelectric materials and devices, in: Characterisation of Ferroelectric Bulk Materials and Thin Films, Springer, 2014, pp. 147–189. doi:https://doi.org/10.1007/978-1-4020-9311-1_7.

[183] Y. Liu, M. Hafezi, A. Feeney, Dynamic stability of a nitinol langevin ultrasonic transducer under power and current tracking conditions, Applied Acoustics 225 (2024) 110188. doi:https://doi.org/10.1016/j.apacoust.2024.110188.

[184] S.-A. Li, C. Li, Fpga implementation of adaptive kalman filter for industrial ultrasonic applications, Microsystem Technologies 27 (2021) 1611–1618. doi:https://doi.org/10.1007/s00542-019-04456-6.

[185] Z. Wang, J. Everaerts, E. Salvati, A. M. Korsunsky, Evolution of thermal and mechanical properties of nitinol wire as a function of ageing treatment conditions, Journal of Alloys and Compounds 819 (2020) 153024. doi:https://doi.org/10.1016/j.jallcom.2019.153024.

[186] A. Shamimi, B. Amin-Ahmadi, A. Stebner, T. Duerig, The effect of low temperature aging and the evolution of r-phase in ni-rich niti, Shape Memory and Superelasticity 4 (2018) 417–427. doi:https://doi.org/10.1007/s40830-018-0193-9.

[187] N. Agarwal, D. Bourke, M. A. Obeidi, D. Brabazon, Influence of laser powder bed fusion and ageing heat treatment parameters on the phase structure and physical behavior of ni-rich nitinol parts, Journal of Materials Research and Technology 30 (2024) 4527–4541. doi:https://doi.org/10.1016/j.jmrt.2024.04.198.

[188] J. Eaton-Evans, J. Dulieu-Barton, E. Little, I. Brown, Observations during mechanical testing of nitinol, Proceedings of the Institution of Mechanical Engineers, Part C: Journal of Mechanical Engineering Science 222 (2) (2008) 97–105. doi:https://doi.org/10.1243/09544062JMES79.

[189] M. Thomasová, H. Seiner, P. Sedlák, M. Frost, M. Ševčík, I. Szurman, R. Kocich, J. Drahokoupil, P. Šittner, M. Landa, Evolution of macroscopic elastic moduli of martensitic polycrystalline niti and niticu shape memory alloys with pseudoplastic straining, Acta Materialia 123 (2017) 146–156. doi:10.1016/j.actamat.2016.10.024.

[190] S. Rajagopalan, A. Little, M. Bourke, R. Vaidyanathan, Elastic modulus of shape-memory niti from in situ neutron diffraction during macroscopic loading, instrumented indentation, and extensometry, Applied Physics Letters 86 (8) (2005). doi:10.1063/1.1863437.

[191] M. F.-X. Wagner, Microstructural and mechanical challenges in biomedical niti, in: Journal of Physics: Conference Series, Vol. 240, IOP Publishing, 2010, p. 012004. doi:10.1088/1742-6596/240/1/012004.

[192] Q. Mei, L. Zhang, K. Tsuchiya, H. Gao, T. Ohmura, K. Tsuzaki, Grain size dependence of the elastic modulus in nanostructured niti, Scripta Materialia 63 (10) (2010) 977–980. doi:10.1016/j.scriptamat.2010.07.018.

[193] K. Chu, B. Wang, Q. Li, Y. Onuki, F. Ren, Grain size effect on the temperature-dependence of elastic modulus of nanocrystalline niti, Journal of Alloys and Compounds 934 (2023) 167907. doi:10.1016/j.jallcom.2022.167907.

[194] S. Spinner, A. G. Rozner, Elastic properties of niti as a function of temperature, The Journal of the Acoustical Society of America 40 (5) (1966) 1009–1015. doi:10.1121/1.1910180.

[195] D. Bradley, Sound propagation in near-stoichiometric ti-ni alloys, Journal of the Acoustical Society of America 37 (4) (1965) 700–702. doi:10.1121/1.1909397.

[196] M. Thomasová, H. Seiner, P. Sedlák, M. Frost, M. Ševčík, I. Szurman, R. Kocich, J. Drahokoupil, P. Šittner, M. Landa, Evolution of macroscopic elastic moduli of martensitic polycrystalline niti and niticu shape memory alloys with pseudoplastic straining, Acta Materialia 123 (2017) 146–156. doi:https://doi.org/10.1016/j.actamat.2016.10.024.

[197] K. R. Labs, https://www.kelloggsresearchlabs.com/product/rods/.

[198] S. D. C. Velmurugan, V. Senthilkumar, D. Arulkirubakaran, Machining of niti-shape memory alloys-a review, Machining Science and Technology 22 (3) (2018) 355–401. doi:10.1080/10910344.2017.1365894.

[199] R. Chaudhari, J. J. Vora, V. Patel, L. López de Lacalle, D. Parikh, Surface analysis of wire-electrical-discharge-machining-processed shape-memory alloys, Materials 13 (3) (2020) 530. doi:https://doi.org/10.3390/ma13030530.

[200] J. F. Liu, Y. B. Guo, T. M. Butler, M. Weaver, Crystallography, compositions, and properties of white layer by wire electrical discharge machining of nitinol shape memory alloy, Materials & Design 109 (2016) 1–9.
URL https://api.semanticscholar.org/CorpusID:138926129

[201] J. Liu, C. Li, X. Fang, J. Jordon, Y. Guo, Effect of wire-edm on fatigue of nitinol shape memory alloy, Materials and Manufacturing Processes 33 (16) (2018) 1809–1814. doi:https://doi.org/10.1080/10426914.2018.1512125.

[202] Y. Liao, Y. Yu, Study of specific discharge energy in wedm and its application, International Journal of Machine Tools and Manufacture 44 (12-13) (2004) 1373–1380. doi:https://doi.org/10.1016/j.ijmachtools.2004.04.008.

[203] W. Theisen, A. Schuermann, Electro discharge machining of nickel–titanium shape memory alloys, Materials Science and Engineering: A 378 (1-2) (2004) 200–204. doi:10.1016/j.msea.2003.09.115.

[204] R. Chaudhari, Y. Shah, S. Khanna, V. K. Patel, J. Vora, D. Y. Pimenov, K. Giasin, Experimental investigations and effect of nano-powder-mixed edm variables on performance measures of nitinol sma, Materials 15 (20) (2022) 7392. doi:10.3390/ma15207392.

[205] R. Chaudhari, J. Vora, L. López de Lacalle, S. Khanna, V. K. Patel, I. Ayesta, Parametric optimization and effect of nano-graphene mixed dielectric fluid on performance of wire electrical discharge machining process of ni55. 8ti shape memory alloy, Materials 14 (10) (2021) 2533. doi:10.3390/ma14102533.

[206] A. F. Mansor, A. I. Azmi, M. Z. M. Zain, R. Jamaluddin, Parametric evaluation of electrical discharge coatings on nickel-titanium shape memory alloy in deionized water, Heliyon 6 (8) (2020). doi:https://doi.org/10.1016/j.heliyon.2020.e04812.

[207] V. N. Kulkarni, V. Gaitonde, S. Karnik, M. Manjaiah, J. P. Davim, Machinability analysis and optimization in wire edm of medical grade nitinol memory alloy, Materials 13 (9) (2020) 2184. doi:https://doi.org/10.3390/ma13092184.

[208] A. N. Bucsek, H. M. Paranjape, A. P. Stebner, Myths and truths of nitinol mechanics: elasticity and tension–compression asymmetry, Shape Memory and Superelasticity 2 (2016) 264–271. doi:https://doi.org/10.1007/s40830-016-0074-z.

[209] T. Duerig, A. Pelton, K. Bhattacharya, The measurement and interpretation of transformation temperatures in nitinol, Shape Memory and Superelasticity 3 (2017) 485–498. doi:https://doi.org/10.1007/s40830-017-0133-0.

[210] D. Lega, A. Antonini, A. Ciccioli, S. Brutti, P. Lenzuni, Low scan rate dsc study of the monoclinic-tetragonal transition in zirconia, Thermochimica acta 524 (1-2) (2011) 18–22. doi:https://doi.org/10.1016/j.tca.2011.06.004.

[211] D. Vojtech, L. Joska, J. Leitner, Influence of a controlled oxidation at moderate temperatures on the surface chemistry of nitinol wire, Applied Surface Science 254 (18) (2008) 5664–5669. doi:https://doi.org/10.1016/j.apsusc.2008.03.014.

[212] R. Sidharth, A. Mohammed, H. Sehitoglu, Functional fatigue of niti shape memory alloy: effect of loading frequency and source of residual strains, Shape Memory and Superelasticity 8 (4) (2022) 394–412. doi:https://doi.org/10.1007/s40830-022-00397-8.

[213] T. Birk, S. Biswas, J. Frenzel, G. Eggeler, Twinning-induced elasticity in niti shape memory alloys, Shape Memory and Superelasticity 2 (2016) 145–159. doi:https://doi.org/10.1007/s40830-016-0064-1.

[214] M. Xia, P. Liu, Q. Sun, Grain size effects on young's modulus and hardness of nanocrystalline niti shape memory alloy, Advances in Shape Memory Materials: In Commemoration of the Retirement of Professor Hisaaki Tobushi (2017) 203–210doi:https://doi.org/10.1007/978-3-319-53306-3_15.

[215] A. Mathieson, A. Cardoni, N. Cerisola, M. Lucas, Understanding nonlinear vibration behaviours in high-power ultrasonic surgical devices, Proceedings of the Royal Society A: Mathematical, Physical and Engineering Sciences 471 (2176) (2015) 20140906. doi:10.1098/rspa.2014.0906.

[216] Y. Liu, M. Hafezi, A. Feeney, A cascaded nitinol langevin transducer for resonance stability at elevated temperatures, ULTRASONICS 137 (2024) 107201. doi:https://doi.org/10.1016/j.ultras.2023.107201.

[217] R. V. Sukesha, N. Kumar, Effect of electric field and temperature on dielectric constant and piezoelectric coefficient of piezoelectric materials: A review, Integrated Ferroelectrics 167 (1) (2015) 154–175. arXiv:https://doi.org/10.1080/10584587.2015.1107383, doi:10.1080/10584587.2015.1107383.
URL https://doi.org/10.1080/10584587.2015.1107383

[218] J. Wang, H. Sehitoglu, Martensite modulus dilemma in monoclinic niti-theory and experiments, International Journal of Plasticity 61 (2014) 17–31. doi:https://doi.org/10.1016/j.ijplas.2014.05.005.

[219] X. Wang, Chapter 2 - analysis of a single degree of freedom piezoelectric vibration energy harvester system using the transfer function, integration, state space, and frequency response methods, in: X. Wang (Ed.), Frequency Analysis of Vibration Energy Harvesting Systems, Academic Press, 2016, pp. 15–42. doi:https://doi.org/10.1016/B978-0-12-802321-1.00002-9.

[220] Z. Wu, W. Liu, Z. Tong, Y. Cai, C. Sun, L. Lou, Tuning characteristics of aln-based piezoelectric micromachined ultrasonic transducers using dc bias voltage, IEEE Transactions on Electron Devices 69 (2) (2022) 729–735. doi:10.1109/TED.2021.3137766.

[221] J. W. Mwangi, V. D. Bui, K. Thuesing, S. Hahn, M. F.-X. Wagner, A. Schubert, Characterization of the arcing phenomenon in micro-edm and its effect on key mechanical properties of medical-grade nitinol, Journal of Materials Processing Technology 275 (2020) 116334. doi:10.1016/j.jmatprotec.2019.116334.

[222] Y. Feng, J. Qiao, L. Li, Acoustic behavior of composites with gradient impedance, Materials & Design 193 (2020) 108870. doi:10.1016/j.matdes.2020.108870.

[223] X. Wang, W. Xia, X. Wu, Y. Wei, C. Huang, In-situ investigation of dynamic deformation in niti shape memory alloys under laser induced shock, Mechanics of Materials 114 (2017) 69–75. doi:10.1016/j.mechmat.2017.06.009.

[224] H. Daneshpajooh, M. Choi, Y. Park, T. Scholehwar, E. Hennig, K. Uchino, Compressive stress effect on the loss mechanism in a soft piezoelectric Pb(Zr,Ti)O3, Review of Scientific Instruments 90 (7) (2019) 075001. doi:10.1063/1.5096905.

[225] K. Uchino, Y. Zhuang, S. O. Ural, Loss determination methodology for a piezoelectric ceramic: new phenomenological theory and experimental proposals, Journal of Advanced Dielectrics 1 (01) (2011) 17–31. doi:10.1142/S2010135X11000033.

[226] P. Gardonio, M. J. Brennan, On the origins and development of mobility and impedance methods in structural dynamics, Journal of Sound and vibration 249 (3) (2002) 557–573. doi:10.1006/jsvi.2001.3879.

[227] M. Schmid, E. Benes, W. Burger, V. Kravchenko, Motional capacitance of layered piezoelectric thickness-mode resonators, IEEE transactions on ultrasonics, ferroelectrics, and frequency control 38 (3) (1991) 199–206. doi:10.1109/58.79604.

[228] D. Rizos, G. Feltrin, M. Motavalli, Structural identification of a prototype pre-stressable leaf-spring based adaptive tuned mass damper: Nonlinear characterization and classification, Mechanical systems and signal processing 25 (1) (2011) 205–221. doi:10.1016/j.ymssp.2010.07.001.

[229] A. Lei, R. Xu, L. M. Borregaard, M. Guizzetti, O. Hansen, E. V. Thomsen, Impedance based characterization of a high-coupled screen printed pzt thick film unimorph energy harvester, Journal of Microelectromechanical Systems 23 (4) (2014) 842–854. doi:10.1109/JMEMS.2013.2295625.

[230] M. Takasaki, Y. Maruyama, T. Mizuno, Resonance frequency tracing system for langevin type ultrasonic transducers, in: 2007 International Conference on Mechatronics and Automation, IEEE, 2007, pp. 3817–3822. doi:10.1109/ICMA.2007.4304183.

[231] N. Wongdamnern, N. Triamnak, A. Ngamjarurojana, Y. Laosiritaworn, S. Ananta, R. Yimnirun, Comparative studies of dynamic hysteresis responses in hard and soft pzt ceramics, Ceramics international 34 (4) (2008) 731–734. doi:10.1016/j.ceramint.2007.09.048.

[232] A. Wellendorf, L. von Damnitz, A. W. Nuri, D. Anders, S. Trampnau, Determination of the temperature-dependent resonance behavior of ultrasonic transducers using the finite-element method, Journal of Vibration Engineering & Technologies 12 (2) (2024) 1277–1290. doi:https://doi.org/10.1007/s42417-023-00906-8.

[233] L. Anand, S. Govindjee, Continuum mechanics of solids, Oxford University Press, 2020. doi:https://doi.org/10.1093/oso/9780198864721.001.0001.

[234] V. Piefort, Finite element modelling of piezoelectric active structures, Ph. D. thesis. Bruxelles, Belgium: Université Libre de Bruxelles, Department ... (2001).

[235] R. Melnik, Modelling coupled dynamics: Piezoelectric elements under changing temperature conditions, International communications in heat and mass transfer 30 (1) (2003) 83–92. doi:https://doi.org/10.1016/S0735-1933(03)00010-1.

[236] D. Catoor, Z. Ma, S. Kumar, Cyclic response and fatigue failure of nitinol under tension–tension loading, Journal of Materials Research 34 (20) (2019) 3504–3522. doi:https://doi.org/10.1557/jmr.2019.254.

[237] S. Robertson, A. Pelton, R. Ritchie, Mechanical fatigue and fracture of nitinol, International Materials Reviews 57 (1) (2012) 1–37. doi:10.1179/1743280411Y.0000000009.

[238] T. Tsurumi, H. Kakemoto, S. Wada, Dielectric, elastic and piezoelectric losses of pzt ceramics in the resonance state, in: Proceedings of the 13th IEEE International Symposium on Applications of Ferroelectrics, 2002. ISAF 2002., IEEE, 2002, pp. 375–378. doi:10.1109/ISAF.2002.1195947.

[239] N. G. Fenu, N. Giles-Donovan, M. R. Sadiq, S. Cochran, Full set of material properties of lead-free pic 700 for transducer designers, IEEE Transactions on Ultrasonics, Ferroelectrics, and Frequency Control 68 (5) (2020) 1797–1807. doi:10.1109/TUFFC.2020.3044790.

[240] Y. Liu, M. Hafezi, A. Feeney, Fabrication and characterisation of a nitinol langevin transducer, in: 2023 IEEE International Ultrasonics Symposium (IUS), IEEE, 2023, pp. 1–4. doi:10.1109/IUS51837.2023.10308112.

[241] D. Zang, J. Li, Z. Chen, Z. Zhai, X. Geng, B. P. Binks, Switchable opening and closing of a liquid marble via ultrasonic levitation, Langmuir 31 (42) (2015) 11502–11507. doi:10.1021/acs.langmuir.5b02917.

[242] W. Xie, C. Cao, Y. Lü, Z. Hong, B. Wei, Acoustic method for levitation of small living animals, Applied Physics Letters 89 (21) (2006). doi:https://doi.org/10.1063/1.2396893.

[243] S. Santesson, S. Nilsson, Airborne chemistry: acoustic levitation in chemical analysis, Analytical and bioanalytical chemistry 378 (2004) 1704–1709. doi:https://doi.org/10.1007/s00216-003-2403-2.

[244] A. Marzo, A. Barnes, B. W. Drinkwater, Tinylev: A multi-emitter single-axis acoustic levitator, Review of Scientific Instruments 88 (8) (2017). doi:https://doi.org/10.1063/1.4989995.

[245] J. Li, P. Liu, H. Ding, W. Cao, Modeling characterization and optimization design for pzt transducer used in near field acoustic levitation, Sensors and Actuators A: Physical 171 (2) (2011) 260–265. doi:https://doi.org/10.1016/j.sna.2011.06.020.

[246] S. Inoue, S. Mogami, T. Ichiyama, A. Noda, Y. Makino, H. Shinoda, Acoustical boundary hologram for macroscopic rigid-body levitation, The Journal of the Acoustical Society of America 145 (1) (2019) 328–337. doi:https://doi.org/10.1121/1.5087130.

[247] Z. Hong, W. Xie, B. Wei, Acoustic levitation with self-adaptive flexible reflectors, Review of Scientific Instruments 82 (7) (2011). doi:https://doi.org/10.1063/1.3610652.

[248] B. W. Drinkwater, Dynamic-field devices for the ultrasonic manipulation of microparticles, Lab on a Chip 16 (13) (2016) 2360–2375. doi:https://doi.org/10.1039/C6LC00502K.

[249] H. Li, Y. Wang, Y. Li, W. Sun, Y. Shen, Q. Zeng, The levitation and driving performance of a contact-free manipulation device actuated by ultrasonic energy, International Journal of Mechanical Sciences 225 (2022) 107358. doi:https://doi.org/10.1016/j.ijmecsci.2022.107358.

[250] H. Lais, P. S. Lowe, L. C. Wrobel, T.-H. Gan, Investigation of ultrasonic sonotrode design to improve the performance of ultrasonic fouling removal, IEEE Access 7 (2019) 148897–148912. doi:10.1109/ACCESS.2019.2946702.

[251] D. A. De Angelis, G. W. Schulze, T. J. Palumbo, Optimizing the phase window of ultrasonic transducers, in: 2024 52nd Annual Ultrasonic Industry Association Symposium (UIA), IEEE, 2024, pp. 1–9. doi:10.23919/UIA60812.2024.10716029.

[252] A. Caronti, R. Carotenuto, M. Pappalardo, Electromechanical coupling factor of capacitive micromachined ultrasonic transducers, The Journal of the Acoustical Society of America 113 (1) (2003) 279–288. doi:10.1121/1.1527958.

[253] A. Feeney, L. Kang, S. Dixon, Higher order modal dynamics of the flexural ultrasonic transducer, Journal of Physics D: Applied Physics 55 (7) (2021) 07LT01. doi:10.1088/1361-6463/ac3352.

[254] R. Boullosa, A. Pérez-López, R. Dorantes-Escamilla, An ultrasonic levitator, Journal of applied research and technology 11 (6) (2013) 857–865. doi:https://doi.org/10.1016/S1665-6423(13)71592-X.

[255] W. J. Marshall, G. A. Brigham, Determining equivalent circuit parameters for low figure of merit transducers, Acoustics Research Letters Online 5 (3) (2004) 106–110. doi:https://doi.org/10.1121/1.1756031.

[256] Y. Yao, Y. Pan, S. Liu, Study on heat pipe heat dissipation of high-power ultrasonic transducer, Ultrasonics 120 (2022) 106654. doi:10.1016/j.ultras.2021.106654.

[257] D. Powell, J. Mould, G. Wojcik, Dielectric and mechanical absorption mechanisms for time and frequency domain transducer modeling, in: 1998 IEEE Ultrasonics Symposium. Proceedings (Cat. No. 98CH36102), Vol. 2, IEEE, 1998, pp. 1019–1024. doi:10.1109/ULTSYM.1998.764978.

[258] N. Torić, J. Brnić, I. Boko, M. Brčić, I. W. Burgess, I. Uzelac, Experimental analysis of the behaviour of aluminium alloy en 6082aw t6 at high temperature, Metals 7 (4) (2017) 126. doi:https://doi.org/10.3390/met7040126.

[259] A. Saini, B. Pabla, S. Dhami, Developments in cutting tool technology in improving machinability of ti6al4v alloy: A review, Proceedings of the Institution of Mechanical Engineers, Part B: Journal of Engineering Manufacture 230 (11) (2016) 1977–1989. doi:https://doi.org/10.1177/0954405416640.

[260] M. Fukuhara, A. Sanpei, Elastic moduli and internal frictions of inconel 718 and ti-6al-4v as a function of temperature, Journal of materials science letters 12 (14) (1993) 1122–1124. doi:https://doi.org/10.1007/BF00420541.

[261] B. Koc, J. Homberg, S. Schlack, Material properties of hard and soft piezoelectric ceramics at cryogenic temperatures, in: ACTUATOR 2024; International Conference and Exhibition on New Actuator Systems and Applications, VDE, 2024, pp. 195–198.

[262] M. Marsilius, K. G. Webber, E. Aulbach, T. Granzow, Comparison of the temperature-dependent ferroelastic behavior of hard and soft lead zirconate titanate ceramics, Journal of the American Ceramic Society 93 (9) (2010) 2850–2856. doi:10.1111/j.1551-2916.2010.03801.x.

[263] A. K. Gain, L. Zhang, S. Lim, Tribological behavior of ti–6al–4v alloy: Subsurface structure, damage mechanism and mechanical properties, Wear 464 (2021) 203551. doi:https://doi.org/10.1016/j.wear.2020.203551.

[264] J. Chen, B. Young, Stress–strain curves for stainless steel at elevated temperatures, Engineering structures 28 (2) (2006) 229–239. doi:https://doi.org/10.1016/j.engstruct.2005.07.005.

[265] D. Sukhanov, S. Rosliakov, Particle levitation and control in midair using wideband ultrasonic waves, Applied Acoustics 178 (2021) 108004. doi:https://doi.org/10.1016/j.apacoust.2021.108004.

[266] M. A. Andrade, N. Pérez, J. C. Adamowski, Analysis of a non-resonant ultrasonic levitation device, Physics Procedia 70 (2015) 68–71. doi:https://doi.org/10.1016/j.phpro.2015.08.044.

[267] W. Xie, B. Wei, Dependence of acoustic levitation capabilities on geometric parameters, Physical Review E 66 (2) (2002) 026605. doi:https://doi.org/10.1103/PhysRevE.66.026605.

[268] M. A. Andrade, N. Pérez, J. C. Adamowski, Particle manipulation by a non-resonant acoustic levitator, Applied physics letters 106 (1) (2015). doi:https://doi.org/10.1063/1.4905130.

[269] M. A. Andrade, F. Buiochi, J. C. Adamowski, Finite element analysis and optimization of a single-axis acoustic levitator, IEEE transactions on ultrasonics, ferroelectrics, and frequency control 57 (2) (2010) 469–479. doi:10.1109/TUFFC.2010.1427.

[270] S. Yadav, A. Gupta, Finite difference study to evaluate the resonance condition of the standing wave acoustic levitation system, Journal of Vibration Engineering & Technologies 12 (2) (2024) 1923–1929. doi:https://doi.org/10.1007/s42417-023-00953-1.

[271] Z. Li, Z. Qiao, T. Tang, Numerical solution of differential equations: introduction to finite difference and finite element methods, Cambridge University Press, 2017. doi:https://doi.org/10.1017/9781316678725.

[272] R. Fitzgerald, Helmholtz equation as an initial value problem with application to acoustic propagation, The Journal of the Acoustical Society of America 57 (4) (1975) 839–842. doi:https://doi.org/10.1121/1.380516.

[273] F. T. Tveter, Hamilton's equations of motion for non-conservative systems, Celestial Mechanics and dynamical astronomy 60 (1994) 409–419. doi:https://doi.org/10.1007/BF00692025.

[274] T. Liszka, J. Orkisz, The finite difference method at arbitrary irregular grids and its application in applied mechanics, Computers & Structures 11 (1-2) (1980) 83–95. doi:https://doi.org/10.1016/0045-7949(80)90149-2.

[275] Z. Jomaa, C. Macaskill, The embedded finite difference method for the poisson equation in a domain with an irregular boundary and dirichlet boundary conditions, Journal of Computational Physics 202 (2) (2005) 488–506. doi:https://doi.org/10.1016/j.jcp.2004.07.011.

[276] J. A. Dean, Lange's handbook of chemistry, McGraw-Hill, 1999.

[277] H. E. White, Modern College Physics, D. Van Nostrand Company Inc New York, 1948.

[278] C. Lee, A. Anilkumar, T. Wang, Static shape and instability of an acoustically levitated liquid drop, Physics of Fluids A: Fluid Dynamics 3 (11) (1991) 2497–2515. doi:https://doi.org/10.1063/1.858192.

[279] E. Trinh, Compact acoustic levitation device for studies in fluid dynamics and material science in the laboratory and microgravity, Review of scientific instruments 56 (11) (1985) 2059–2065. doi:https://doi.org/10.1063/1.1138419.

[280] Z. Hong, J. Yin, W. Zhai, N. Yan, W. Wang, J. Zhang, B. W. Drinkwater, Dynamics of levitated objects in acoustic vortex fields, Scientific reports 7 (1) (2017) 7093. doi:https://doi.org/10.1038/s41598-017-07477-1.

[281] N. Pérez, M. A. Andrade, R. Canetti, J. C. Adamowski, Experimental determination of the dynamics of an acoustically levitated sphere, Journal of Applied Physics 116 (18) (2014). doi:10.1063/1.4901579.